# Modeling and experimental validation of high temperature steam and carbon dioxide co-electrolysis

Jérôme Aicart

## To cite this version:

Jérôme Aicart. Modeling and experimental validation of high temperature steam and carbon dioxide co-electrolysis. Other. Université de Grenoble, 2014. English. NNT : 2014GRENI095 . tel-01284476

HAL Id: tel-01284476
https://theses.hal.science/tel-01284476
Submitted on 7 Mar 2016

UNIVERSITÉ DE GRENOBLE

# THÈSE

Pour obtenir le grade de

## DOCTEUR DE L'UNIVERSITÉ DE GRENOBLE

Spécialité : **Ingénierie – Matériaux Mécanique Énergétique Environnement Procédés Production**

Arrêté ministériel : 7 août 2006

Présentée par

## Jérôme AICART

Thèse dirigée par **Laurent DESSEMOND**
et codirigée par **Jérôme LAURENCIN** et **Marie PETITJEAN**

préparée au sein du **CEA LITEN** et du **LEPMI**
dans **l'École Doctorale IMEP2**

# Modélisation et Validation Expérimentale de la Co-Électrolyse de la Vapeur d'Eau et du Dioxyde de Carbone à Haute Température

Thèse soutenue publiquement le **03 Juin 2014**,
devant le jury composé de :

**M. Gilles CABOCHE**
Professeur, Université de Bourgogne, Président du Jury
**M. Olivier LOTTIN**
Professeur, Université de Lorraine LEMTA, Rapporteur
**Mme. Armelle RINGUEDE**
Docteur, Chimie ParisTech, Rapporteur
**M. Jan VAN HERLE**
Docteur, EPFL Lausanne, Examinateur
**M. Yann BULTEL**
Professeur, Grenoble-INP LEPMI, Examinateur
**Mme. Sandra CAPELA**
Docteur, GDF SUEZ, Membre invité
**M. Laurent DESSEMOND**
Professeur Grenoble-INP LEPMI, Directeur de thèse
**M. Jérôme LAURENCIN**
Docteur, CEA LITEN, Co-encadrant de thèse
**Mme. Marie PETITJEAN**
Docteur, CEA LITEN, Co-encadrant de thèse

# Abstract

This work investigates the high temperature co-electrolysis of $H_2O$ and $CO_2$ in Solid Oxide Cells. A detailed model was developed, encompassing electrochemical, chemical, thermal and mass transfer phenomena, and introducing a macroscopic representation of the co-electrolysis mechanism. This model allows predicting the performances and outlet compositions in single cell and stack environments. An experimental validation protocol was implemented on two types of commercial Cathode Supported Cells, ranging from polarization curves, obtained in single and co-electrolysis modes, to micro gas analyses. These tests aimed both at determining the different exchange current densities, representative of the kinetics of electrochemical reactions, and validating the simulated cell global behavior and mechanism proposed. Comprehensive analysis of the simulations led to the identification of limiting processes and paths for optimization, as well as to the establishment of co-electrolysis operating maps.

# Résumé

Cette étude porte sur la co-électrolyse de $H_2O$ et $CO_2$ à $800°C$ dans une cellule à oxydes solides. Un modèle détaillé a été développé afin de rendre compte des phénomènes électrochimiques, chimiques, thermiques et de transferts de matière, et introduisant une représentation macroscopique du mécanisme de co-électrolyse. Il permet d’estimer les performances et les compositions en sortie de cellule. Un protocole expérimental, visant à valider les principales hypothèses de ce modèle, a été appliqué à deux types de cellule commerciale à cathode support. À partir de courbes de polarisations, obtenues en électrolyse et en co-électrolyse, ainsi que d’analyses gaz, les densités de courant d’échange, illustrant les cinétiques électrochimiques, ont pu être estimées, et le mécanisme proposé a pu être validé. L’analyse des simulations a permis l’identification des processus limitant la co-électrolyse, la proposition de voies d’optimisation et l’établissement des cartographies de fonctionnement.

*« Le monde est composé de flèches et de molécules, et d'électricité, comme le Big-Bang tu vois, et tout ça ensemble, ça forme l'Univers. »*

*Jean-Claude Van Damme*

**« Trèfle à Quatre Feuilles »**

Grille de nickel assurant le contact électrique avec la cellule électrochimique.
Marque laissée par la combustion de l'hydrogène dans l'air passant par une fissure en forme d'étoile.

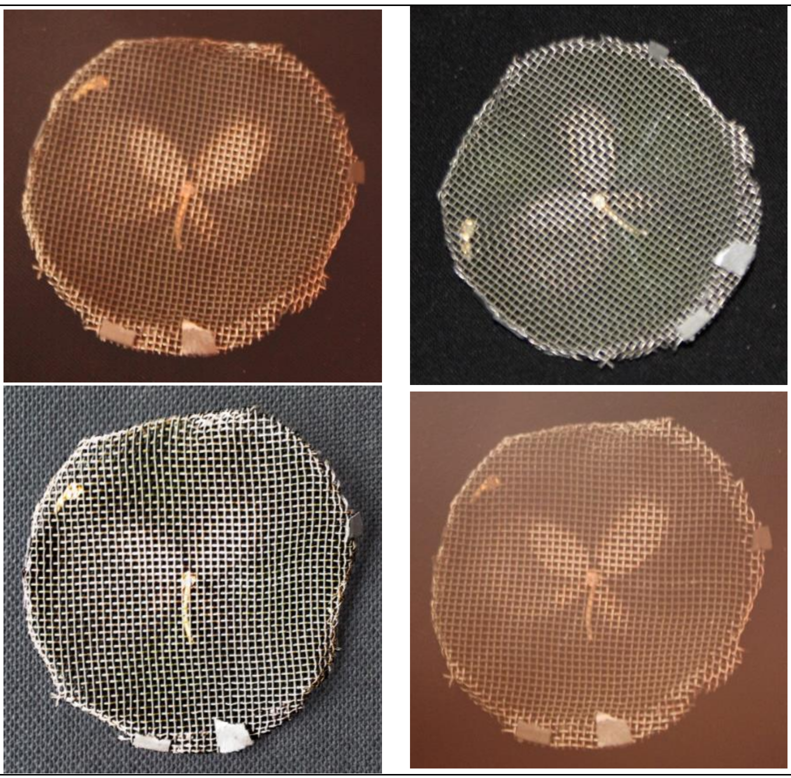

**« Four-Leaf Clover »**

Nickel grid providing electrical contact with the electrochemical cell.
Mark left by the combustion of hydrogen in air flowing through a star shaped crack.

*The journey is the reward.*

*Chinese Proverb*

# Acknowledgements

# -

# Remerciements

Ces travaux s'étant déroulés principalement au CEA de Grenoble, je tiens au préalable à remercier **Mme Julie MOUGIN**, pour son accueil au sein du laboratoire LTH.

Mes plus vifs remerciements vont également à **Mme Armelle RINGUEDE** et **M. Olivier LOTTIN** pour avoir accepté de rapporter ce travail, à **M. Jan VAN HERLE**, **M. Yann BULTEL** et **Mme Sandra CAPELA** pour leur participation au jury de soutenance, ainsi qu'à **M. Gilles CABOCHE** pour l'avoir présidé.

Je voudrais remercier « du fond du cœur » **Marie PETITJEAN**, **Jérôme LAURENCIN**, ainsi que mon directeur de thèse **Laurent DESSEMOND**, pour l'encadrement exceptionnel dont j'ai bénéficié durant ces trois années. Vous avez su me faire confiance en me laissant la liberté et l'autonomie que je cherchais, tout en restant présents, actifs et réactifs.

Votre bonne humeur, entente et investissement sous-tendent ce travail, votre plus grande qualité ayant sans doute été de m'avoir supporté tout au long de ce périple. Dans les moments de joie comme dans ceux de doutes et de galères, bien nombreux, vous avez été d'un soutien inébranlable. Et bien que vos travaux individuels s'inscrivent dans des contextes différents, vous êtes parvenus à être continuellement d'accord, ce qui n'était parfois pas une mince affaire.

Ces travaux n'auraient jamais pu être ce qu'ils sont sans le dévouement infaillible d'une bien belle équipe de techniciens. Je cite **Benoit SOMMACAL** pour son aide précieuse dans la mise en place du banc, **Michel PLANQUE** pour ses talents de dessinateur, **André CHATROUX** pour son habileté à murmurer à l'oreille des automates, ou encore **Lionel TALLOBRE** pour sa contribution soutenue qui nous a permis d'obtenir des mesures chromatographiques de grande qualité. Et bien sûr Pascal **GIROUD** ! Un simple signe de ponctuation ne suffit pas, bien sûr, à exprimer toute ma gratitude. Tes petits doigts de fée m'ont sorti de nombreuses situations délicates, dont la liste justifierait un second manuscrit. Après tout, « il n'y a pas de problème, il n'y a que des solutions ».

Je n'oublie pas **Bertrand MOREL**, pour ses conseils éclairés lors de nos nombreuses discussions autour des bancs. J'ai beaucoup appris de toi et de ton souci constant d'une expérience bien maîtrisée. Ma sympathie va également à **Stéphane DI IORIO** et à **Karine COUTURIER**, pour leurs remarques pertinentes et avisées, leur jovialité et leur expertise, tant sur les oxydes solides que sur la trompette ou le violon.

Ma plus grande gratitude va également à **Magali REYTIER**, pour son implication, son investissement, et sa fantastique force de proposition. A chaque obstacle, tu avais plus de solutions que je ne pouvais explorer. Je te souhaite plein de belles réussites et beaucoup de courage pour avoir pris la tête de la joyeuse bande du LPH.

Ma chaleureuse reconnaissance va également à **Sarah LORAUX**, pour sa rigueur et son soutien, qui débordent largement ses missions de secrétariat. Nous avons parfois bravé les intempéries, et ces moments partagés étaient pour moi une vraie bouffée d'oxygène.

Je ne peux citer individuellement tous ceux qui, lors de discussions de couloirs, de collaborations ponctuelles ou informelles, ou simplement grâce à la cohésion qui existe dans ce laboratoire, m'ont apporté réflexions et bénéfices constructifs. Je vous remercie donc tous infiniment, membres du LTH, du D2 et d'ailleurs ! Je garderai en mémoire, preuve de l'ambiance générale, les « tourments » de trouver une table de 20 le midi.

Comment continuer ces remerciements sans parler du bureau des thésards. En partageant le fameux bureau D2-214 avec toi, **Myriam DE SAINT JEAN**, et toi, **François USSEGLIO-VERETTA**, la pièce semblait bien plus grande. Je vous souhaite réussite et succès pour votre soutenance prochaine.

Ensuite, je souhaiterais exprimer ma reconnaissance à **Élisabeth DJURADO** ainsi qu'à l'ensemble du personnel de l'équipe IES du LEPMI. En m'accueillant parmi vous durant quelques mois, j'ai beaucoup appris à vos côtés, notamment la facette académique de la recherche, inconnue pour moi jusqu'alors.

Je voudrais également faire part de ma gratitude à **Romain SOULAS**. Tu as transformé une conversation autour d'un verre en clichés MEB et analyses chimiques de mes cellules, tout en m'expliquant ce que tu faisais. Que ne l'ai-je su avant !

Et parce que le CEA finissait par fermer le soir, merci à Bob, Clairette, Coco, Elise, Ju, Junior, Mathilde, Rem, Seb, Serguei et tous les autres, pour votre soutien et votre amitié. Sans vous, j'aurais probablement été plus reposé certains matins…

Enfin, j'adresse toute mon affection à ma famille, Lucile, Pauline, Patrick et Christine, pour leur confiance, leur tendresse et leur soutien sans faille durant ces 3 années, ainsi que les 25 qui les ont précédées. Pour ne citer que quelques détails parmi l'immensité du tout, Lucile, ton expertise a métamorphosé la présentation, la faisant passer de « oh mais quelle horreur ! » à ce qu'elle est devenue, et Maman, ce pot était magnifique.

Enfin, à tous ceux que j'ai pu oublier, et à vous tous déjà évoqués, un grand merci pour votre contribution, quelle qu'elle ait pu être, dans ce qui s'est avéré être une grande et très belle aventure.

# Table of Contents

# Chapter 3 - Tools……………………………………p.52

# Chapter 5 - Simulation Results & Discussion….p.120

# Chapter 6 - Conclusion……………………………p.152

# Chapter 7 - Appendix……………………………p.158

# Table of Figures

# Chapter 1 - Introduction

# Chapter 2 - State of the Art

# Chapter 3 - Tools

# Chapter 4 - Model Validation

# Chapter 5 - Simulation Results & Discussion

# Chapter 7 - Appendix

# Table of Tables

# Chapter 1 - Introduction

# Chapter 2 - State of the Art

# Chapter 3 - Tools

# Chapter 4 - Model Validation

# Chapter 5 - Simulation Results & Discussion

# Chapter 7 - Appendix

# Table of Symbols

### Variables

| | | |
|---|---|---|
| $T$ | Temperature | $K$ |
| $P$ | Pressure | $Pa$ |
| $R$ | Gas constant | 8.314 $J.mol^{-1}.K^{-1}$ |
| $F$ | Faraday constant | 96485 $C.mol^{-1}$ |
| $\sigma$ | Stefan-Boltzmann constant | $5.64 \times 10^{-8}$ $W.m^{-2}.K^{-4}$ |
| $R_i$ | Resistance | $\Omega.cm^2$ |
| $N_i$ | Molar flux | $mol.s^{-1}.m^{-2}$ |
| $F_i$ | Flow rate | $NmL.min^{-1}.cm^{-2}$ |
| $n_i$ | Molar flow rate | $mol.s^{-1}$ |
| $D_i$ | Diffusion coefficient | $m^2.s^{-1}$ |
| $\varepsilon$ | Porosity | - |
| $\tau$ | Tortuosity factor | - |
| $y_i$ | Molar fraction | - |
| $M_i$ | Molar mass | $kg.mol^{-1}$ |
| $\bar{r}$ | Mean pore radius | $m$ |
| $\delta$ | Thickness | $m$ |
| $\sigma$ | Electrical conductivity | $\Omega^{-1}.m^{-1}$ |
| $I$ | Current | $A$ |
| $i$ | Current density | $A.m^{-2}$ |
| $i_0$ | Exchange current density | $A.m^{-2}$ |
| $v$ | Chemical reaction rate | $mol.s^{-1}.m^{-3}$ |
| $k$ | Kinetic constant | $mol.s^{-1}.bar^{-2}.m^{-3}$ |
| $E_a$ | Activation energy | $J.mol^{-1}$ |
| $S$ | Surface | $m^2$ |
| $\beta$ | Surface ratio | - |
| $U$ | Voltage | $V$ |
| $\eta$ | Overpotential | $V$ |
| $h$ | Heat transfer coefficient | $W.m^{-2}.K^{-1}$ |
| $\lambda$ | Thermal conductivity | $W.m^{-1}.K^{-1}$ |
| $H$ | Enthalpy | $J.mol^{-1}$ |
| $\varphi$ | Heat flux | $W.m^{-2}$ |
| $C_p$ | Heat capacity | $J.kg^{-1}$ |

### Upscripts / Subscripts

| | |
|---|---|
| $0$ | Initial / standard |
| $eff$ | Effective |
| $tot$ | Total |
| $exp$ | Experimental |
| $sim$ | Simulated |
| $out$ | Outlet, exiting the cell |
| $WGS$ | Water Gas Shift |
| $c$ | Cathode |
| $e$ | Electrolyte |
| $a$ | Anode |
| $\theta$ | Standard $P,T$ conditions |

# Chapter 1

# Introduction

# Chapter 1

# Introduction

## 1.1. From Fossil Carbonated Energies to Environmental Pressures

Icecap analyses over the past several hundreds of thousands of years have shown that there is a strong correlation between the amount of $CO_2$ in the atmosphere and average temperature changes around the globe. As shown in Figure 1-1, the overall climate alternates from hot to cold eras, and the temperature evolution follows remarkably the same pattern as the $CO_2$ and $CH_4$ contents, which fluctuate from 180 to 300 *ppmv* and from 300 to 750 *ppbv* respectively [1].

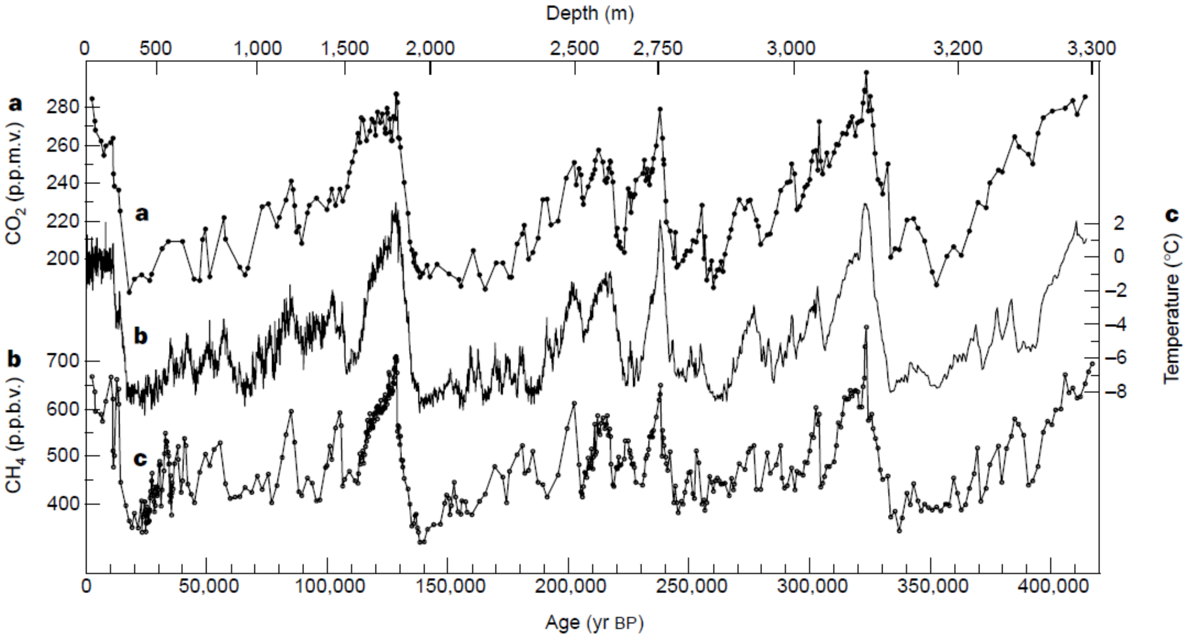

Figure 1-1: Correlation between atmospheric $CO_2$ concentration and global temperature changes [1].

Since the industrial revolution of the 19th century, atmospheric contents of GreenHouse Gases (GHG - $CO_2$, $CH_4$, $H_2O$, *etc.*) have increased tremendously. Similar observation can be made concerning $N_2O$, the main responsible for the destruction of the ozone layer. As shown on Figure 1-2, since the 1850s, the concentrations of $CO_2$, $N_2O$ and $CH_4$ in the atmosphere have steeply risen from a 2000 years long plateau at around 280 *ppm*, 220 *ppm* and 700 *ppb* respectively to astonishing levels at around 380 *ppm*, 320 *ppm* and 1800 *ppb* in 2000 [2, 3].

The $CO_2$ atmospheric content was 27% higher in 2000 than it has ever been over the past 400.000 years.

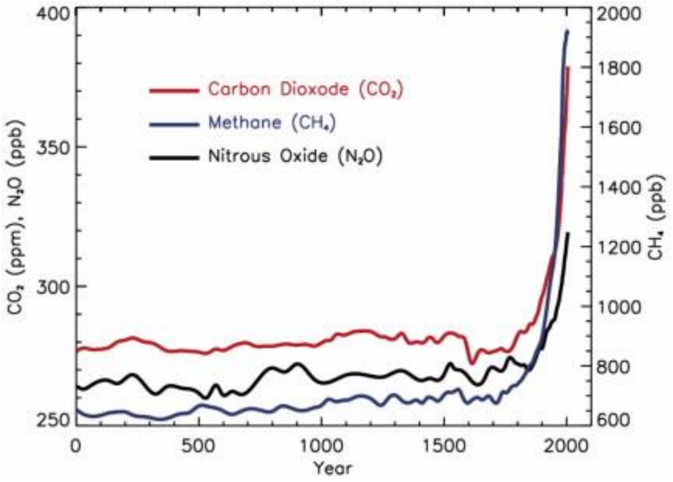

Figure 1-2:
Atmospheric concentrations of $CO_2$, $CH_4$ and $N_2O$ [2, 3].

On the basis of this astounding increase of greenhouse gases concentration in the atmosphere, climate models predict a global warming that could spread from 1.1°*C* to 6.4°*C* before the end of the current century, depending on different scenario and $CO_2$ emissions predictions [4].

Such an increase of the average global temperature could have unpredictable consequences: mass extinction of species, rise of see level, mass migrations of populations, natural disaster occurring more frequently, *etc.* Therefore, governments are trying to limit this temperature increase, for instance by reducing GHG emissions. However, due to a lack of global consensus and multi-country agreement, it seems that, within the 21st century, the world is heading toward a 4°*C* temperature increase [5].

Most of mankind $CO_2$ emissions are due to the massive use of fossil hydrocarbons to meet the global energy bill. Indeed, as shown in Figure 1-3, more than 85% of the ever increasing worldwide energy demand is provided by coal, oil and natural gas. Thus, these energy sources remain vital for the economic development and social stability of most countries.

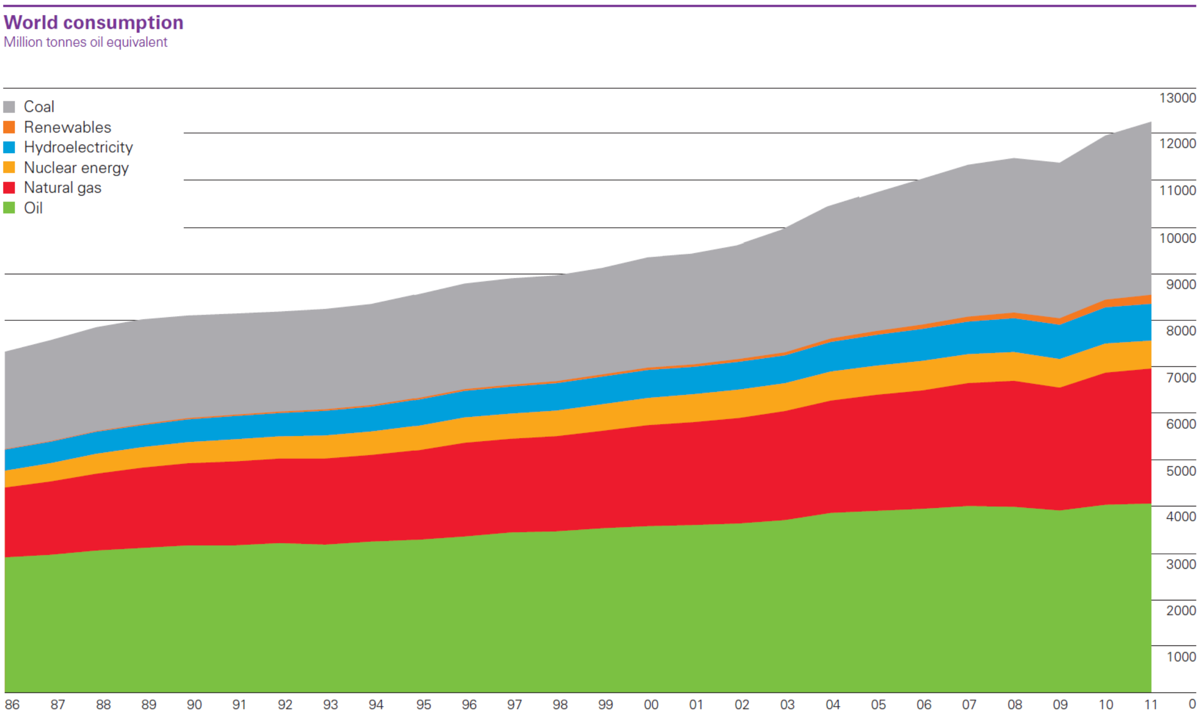

World primary energy consumption grew by 2.5% in 2011, less than half the growth rate experienced in 2010 but close to the historical average. Growth decelerated for all regions and for all fuels. Oil remains the world's leading fuel, accounting for 33.1% of global energy consumption, but this figure is the lowest share on record. Coal's market share of 30.3% was the highest since 1969.

Figure 1-3: Distribution of the world energy consumption **[6]**.

The price of oil (and therefore natural gas) has widely fluctuated throughout the past 150 years (Figure 1-4). It is currently sold for more than 100 *$/barrel* while the exchange rate was as low as 10 *current$/barrel* in 1970. Any price peak can often be related to social or military crises in the Middle East, such as the Iranian revolution in 1979, or more recently the invasion of Afghanistan or the Arab Spring. The correlation between crises and oil prices stem from the uneven worldwide distribution of the global oil reserves (Figure 1-4). Indeed, the Middle East and South and Central America own the large majority of the world currently known oil reserves, whereas Europe and Pacific Asia each have less than 30 years of estimated reserves. Nowadays, the impact of uneven oil reserves distribution is reinforced by a global depletion of resources, driven by a steadily increasing demand. Indeed, the known global oil stockpile is estimated to last roughly 60 years (Figure 1-4). As oil is depleted, the exploitation of the remaining wells will become more technical (deep under see level, underneath the polar ice cap, *etc.*). Unless massive new reserves are discovered, the oil prices are likely to keep increasing in the upcoming decades.

The oil cost and varying prices, along with the non-proportional distribution of the depleting oil reserves can induce stress on the energy supply of most countries. In turn, this can lead to diplomatic strains and eventually conflicts (*e.g.* Russia closing NG pipelines passing through

Ukraine in January 2009). Therefore, from a strategic point of view, it can be interesting for a government to rely on energy sources different from fossil hydrocarbons.

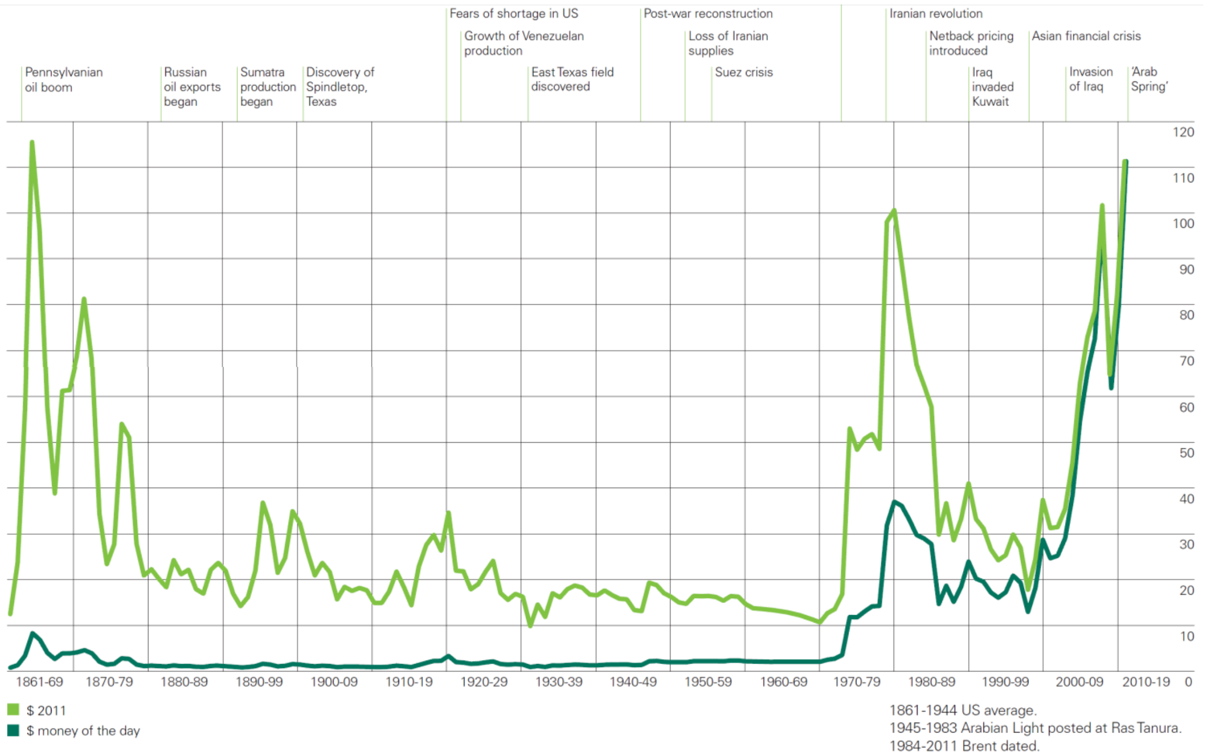

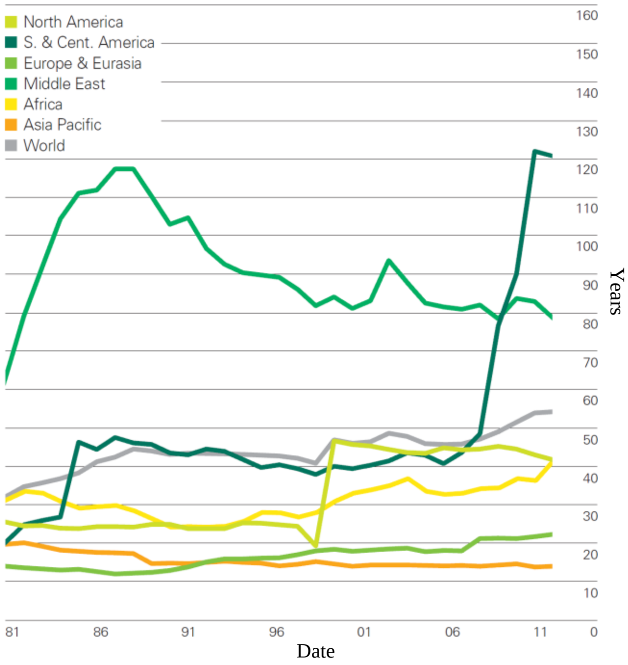

Figure 1-4:
Oil prices fluctuations over the past 150 years (up) and reserve to production ratios (left) **[6]**.

## 1.2. Integration of Carbon-Free Energies

To decrease their carbonated fuel dependence, governments consider massive integration of renewable energies in their global energy mix (Table 1-1).

| **Year** | 2010 | 2020 | 2030 |
|---|---|---|---|
| **Total (*TWh*)** | 3 335 | 3 540 | 3 706 |
| **RES (*TWh*)** | 715 | 1 217 | 1 689 |
| **RES/Total** | **21%** | **34%** | **46%** |

Table 1-1: Electricity production in Europe and evolution of Renewable Energy Sources (RES)

(Source: IEA and Minerve Project).

Because most of renewable energy sources are constituted by small production units which energy outputs fluctuate during the day/year, their integration on the global energy market remains a major technological issue. Therefore, the portion of these small varying electricity sources that cannot be directly injected in the global network (electrical grid) has to be stored (using batteries or hydro pumps) to avoid wastage. Similar observations can be made concerning nuclear energy. A nuclear reactor has a roughly constant energy output that cannot be easily modulated to match the electricity network demand. Thus, the overproduction is generally dumped or stored by pumping water. Without reliable and cost effective technologies for energy storage, fluctuations of electricity demand on the grid can only be managed using electrical sources generated from coal, natural gas or oil power plants, that offer a larger flexibility compared to renewable or nuclear technologies.

Regardless of their high cost, the available technologies for electricity storage have a low energy capacity and a time-span of only several hours – days at the most (Figure 1-5). However, this is not the case for power-to-gas technologies, which enable the storage of electricity under the form of a fuel. As a result, numerous projects are on-going worldwide to assess power-to-gas potential [7].

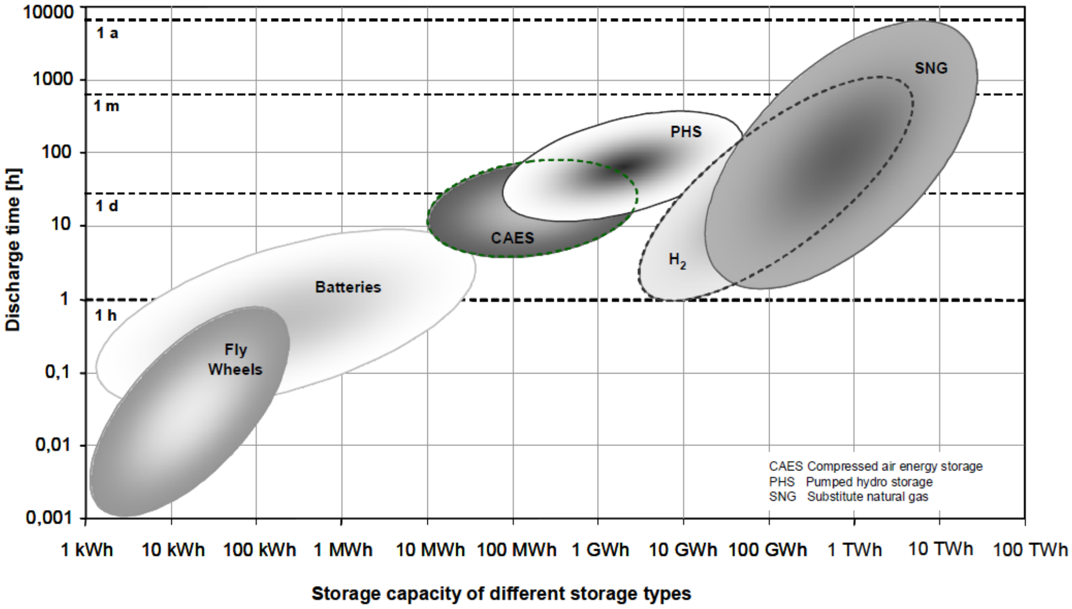

Figure 1-5: Current technologies for electricity storage [8].

“Power-to-Gas” (or “Power-to-Liquid”) consists in taking profit of the overproduction of carbon-free electricity (renewable or nuclear) at low cost, and optionally $CO_2$ from industrial facilities, to produce high value products such as hydrogen or synthetic methane (or methanol, DME, *etc.* in case of “Power-to-Liquid”), therefore storing electrical energy (Figure 1-6).

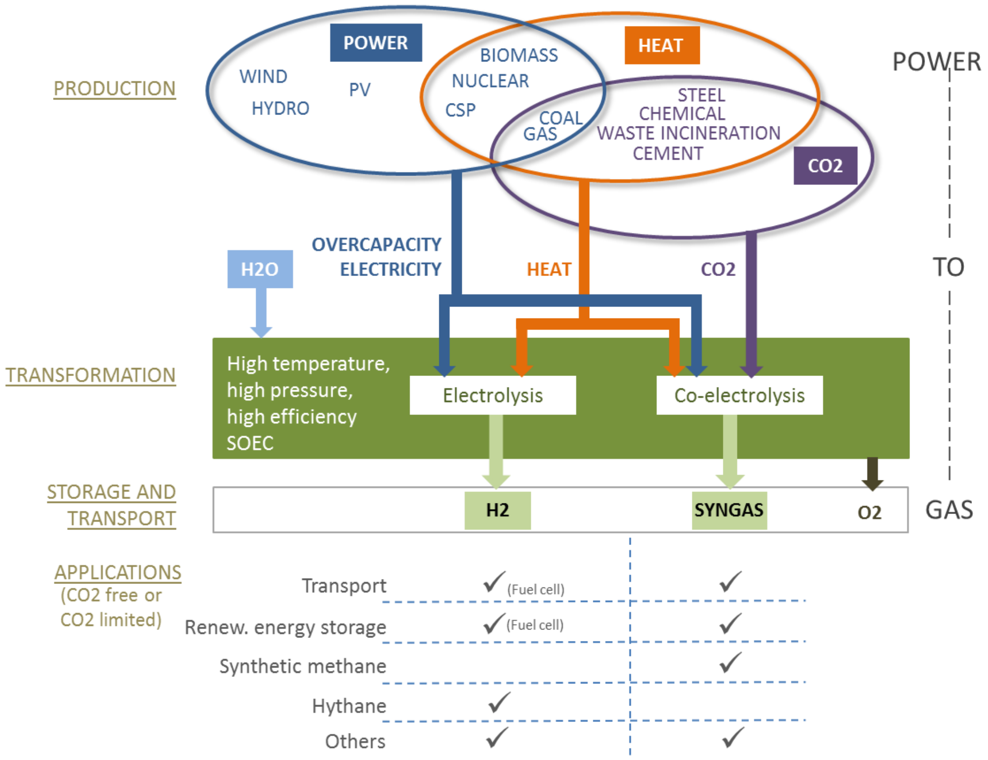

Figure 1-6: “Power to gas” ecosystem (European project Sophia).

There are a large number of applications and advantages in a “Power-to-Gas” vision, among which are the following examples:

- Hydrogen technologies and fuel cells are part of the European Strategic Energy Technology Plan (Europe 2020 and Europe 2050). Hydrogen produced by electrolysis and used for transport applications contributes to lowering GHG emissions and the dependence of Europe on fossil mobility fuel. Several car manufacturers have announced the commercialization of $H_2$ vehicles embracing Europe’s vision.
- Hythane makes storage and transport of hydrogen easy: in the near future, up to 20 *vol.%* hydrogen could be introduced in the existing natural gas network (making Hythane) for domestic applications. This would thus participate to the lowering of GHG emissions.
- The development of energy storage technologies favors the deployment of renewable energy by introducing flexibility to the electrical network, and helping offer to meet demand. Storage also allows for high electrical network efficiency by ensuring that all of the produced energy is consumed.
- Synthetic gas, also called syngas (*i.e.* $H_2$+CO), can be produced by electrolysis of $H_2O$ and $CO_2$ and further transformed into many end-products such as synthetic methane, methanol or dimethyl ether (DME). These products can be used as fuels or by industries (*e.g.* chemical industry). Co-electrolysis coupled with renewable or nuclear power is not only a way to produce syngas; it can also valorize $CO_2$ emitted by industries such as steel, cement, and domestic waste incineration, which are numerous and spread over Europe. Finally, oxygen by-product can further increase the added value of the co-electrolysis process, if used for oxy-combustion purposes for example.

Hydrogen produced via water electrolysis opens up excellent perspectives for both storing renewable/nuclear electricity and transport applications. Indeed, $H_2$ has an extremely high energy content per mass unit (although low energy content per volume unit), about three times as high as gasoline (Table 1-2). Such energy feature makes it a serious option to be used as a replacement fuel in “power to gas” scenarios.

| **Energy Vector** | **Energy content (GJ ton$^{-1}$) (NCV)** |
|---|---|
| Hard coal | 26 |
| Gasoline | 44 |
| Biodiesel | 37 |
| Hydrogen | 120 |

Table 1-2: Energy content of different vectors **[9]** (NCV: Net Calorific Value)

However, there are several technological barriers hampering immediate deployment of hydrogen. Most of them are linked to its low volumic energy content. Thus, hydrogen is usually pressurized or liquefied. Up to now, such costly operations generally make hydrogen economically irrelevant compared to current oil prices. Additional hydrogen storage options are also being developed. Among them, storing hydrogen in hydride powders has shown promising results [10], and the possibility to introduce up to 20 *vol.%* $H_2$ in the natural gas network could provide a stationary mass storage solution with easy implementation.

Electrochemical syngas is also relevant in “Power-to-Gas” scenario. Indeed, because it can be subsequently catalyzed into various synthetic fuels, it circumvents the challenges connected with handling, storing and transporting hydrogen. Additionally, if the syngas is produced from $CO_2$ captured in the air and carbon-free electricity, the overall cycle from fuel production to fuel consumption does not participate to $CO_2$ emissions.

## 1.3. Electrolysis Technologies

Electrolyzers are fuel cells operating in a reverse mode. Consequently, if fuel cells are electrochemical devices that convert the chemical energy contained in a fuel such as hydrogen into electricity, electrolyzers produce fuels from electricity. Historically, the first commercial use of fuel cells was to generate electricity for NASA space devices (probes, satellites, *etc.*) [11]. There are currently several types of fuel cell/electrolyzer, relying on different technologies and/or fuels [12–14]. In these devices, the basic components are the electrolyte, an electronic insulator exhibiting a sufficiently high ionic conductivity to transport ions from one electrode to the other, and the electronic conductive electrodes, where electrochemical reactions occur.

In an electrolyzer, water is electrochemically reduced at the cathode and oxygen is produced at the anode (Reactions (1-1) and (1-2)). The net reaction corresponds to the chemical production of hydrogen (Reaction (1-3)). Figure 1-7 presents the general scheme of a high temperature electrolyzer producing hydrogen from steam. Regardless of the electrolysis technology, the current collecting is ensured by using additional elements, called interconnects in the specific case of high temperature electrolysis.

$$H_2O + 2e^- \rightarrow H_2 + O^{2-} \qquad (1\text{-}1)$$

$$2O^{2-} \rightarrow O_2 + 4e^- \qquad (1\text{-}2)$$

$$H_2O \rightarrow H_2 + \frac{1}{2}O_2 \quad \left(\Delta_r H^0 = 286\ kJ.mol^{-1}\right)\ [15] \qquad (1\text{-}3)$$

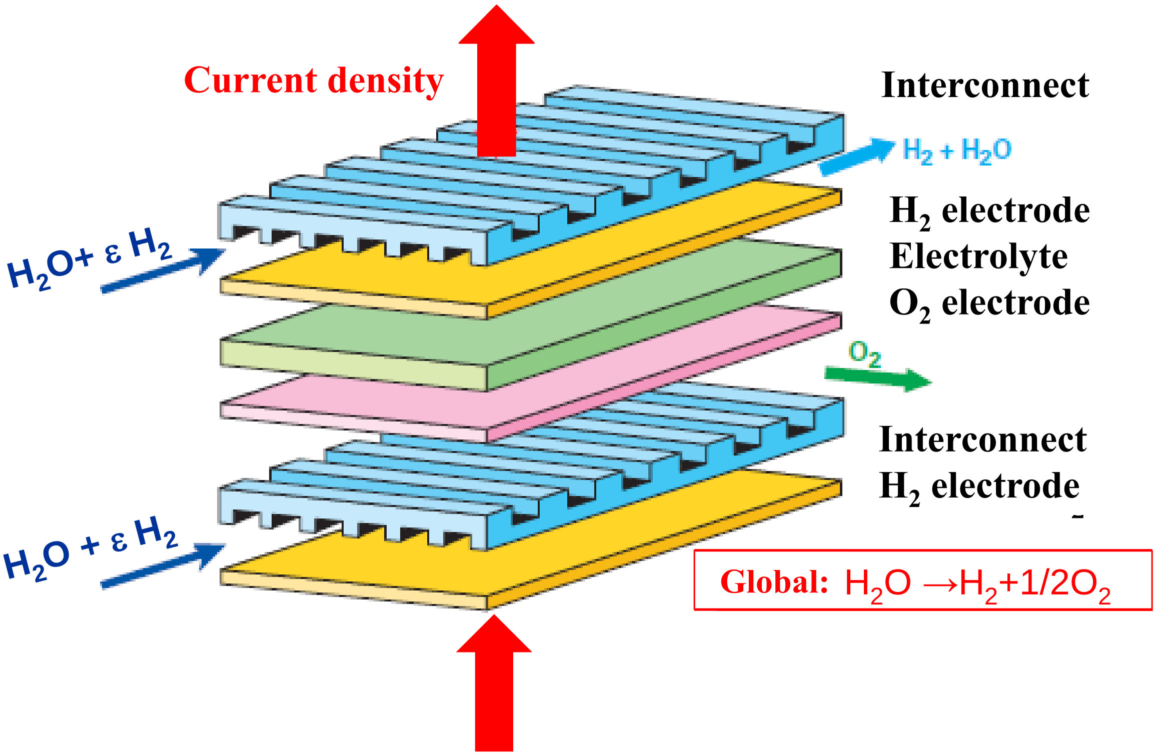

Figure 1-7: Typical components of electrolyzers: the example of SOEC technology.

However, electrolyzers are not the sole technology that can produce hydrogen. Table 1-3 summarizes the current technologies available, their efficiencies and market position.

| **Process** | **Source** | **Efficiency** [16] | [17] | **Technological readiness** |
|---|---|---|---|---|
| Steam reforming | Hydrocarbons | 70-85% | 60-85% | Commercial |
| Partial oxidation | Hydrocarbons | 60-75% | 60-85% | Commercial |
| Autothermal reforming | Hydrocarbons | 60-75% | 60-85% | Short-term |
| Biomass gasification | Biomass | 35-50% | N.A. | Commercial |
| Fermentation | Biomass | 60-80% | N.A. | Long term |
| Alkaline electrolysis | Water | 50-60% | N.A. | Commercial |
| Membrane electrolysis | Water | 55-70% | N.A. | Short-term |
| Photo-electrolysis | Water | 12.4% | ≈10% | Long term |
| **HTSE** | **Water** | **40-60%** | **>95%** | **Medium term** |

Table 1-3: Overview of some of hydrogen production technologies **[18, 19]**

It should be noted that most of the current hydrogen production comes from steam reforming of natural gas (Reaction (1-4)), thus relying on hydrocarbon energy and generating large amounts of greenhouse gases.

$$CH_4 + H_2O \leftrightarrow CO + 3H_2 \qquad \Delta_r H^\theta = 206.1\, kJ.mol^{-1} \text{ [20]} \qquad (1\text{-}4)$$

### 1.3.1. High Temperature Steam Electrolysis

Solid oxide materials used in SOECs (commonly Yttria Stabilized Zirconia - YSZ) become sufficiently conducting for ions at high temperatures (between 500-1000$°C$, usually 800$°C$). These operating temperatures allow to operate without expensive catalyzers: nickel is mostly used as high temperature (193 $\$.kg^{-1}$) compared to, for instance, platinum (44.000 $\$.kg^{-1}$) [21]. Moreover, like in Solid Oxide Fuel Cell (SOFC) mode, high temperatures promote the efficiency of electrochemical reactions by increasing kinetic rates, resulting in higher performances.

The High Temperature Steam Electrolysis (HTSE) consumes less electrical energy than electrolysis at room temperature because of favorable thermodynamic conditions. Indeed, energy demand is significantly lowered by the vaporization of water into steam. Moreover, steam electrolysis is increasingly endothermic with temperature, *i.e.* the required electrical power is reduced at high temperatures [22].

The electric energy required for the electrolysis process is equal to the variation of the Gibbs free energy $\Delta G$:

$$\Delta H(T) = \Delta G(T) + T\Delta S(T) \tag{1-5}$$

where $\Delta H$ is the enthalpy variation of the water splitting reaction (1-3), $T$ the absolute temperature and $\Delta S$ the entropy variation.

A shown in Figure 1-8, the decrease in electrical energy $\Delta G$ is steeper than the increase in total energy $\Delta H$. Therefore, since heat is cheaper than electricity, electrolysis at high temperatures reduces the cost of hydrogen production (3.1 $kWh.Nm^{-3}H_2$ for HTSE compared to 4.1 $kWh.Nm^{-3}H_2$ at low temperatures [19]). This is especially the case if the heat energy ($T\Delta S$) is supplied by an external heat source, such as nuclear power or renewable energy.

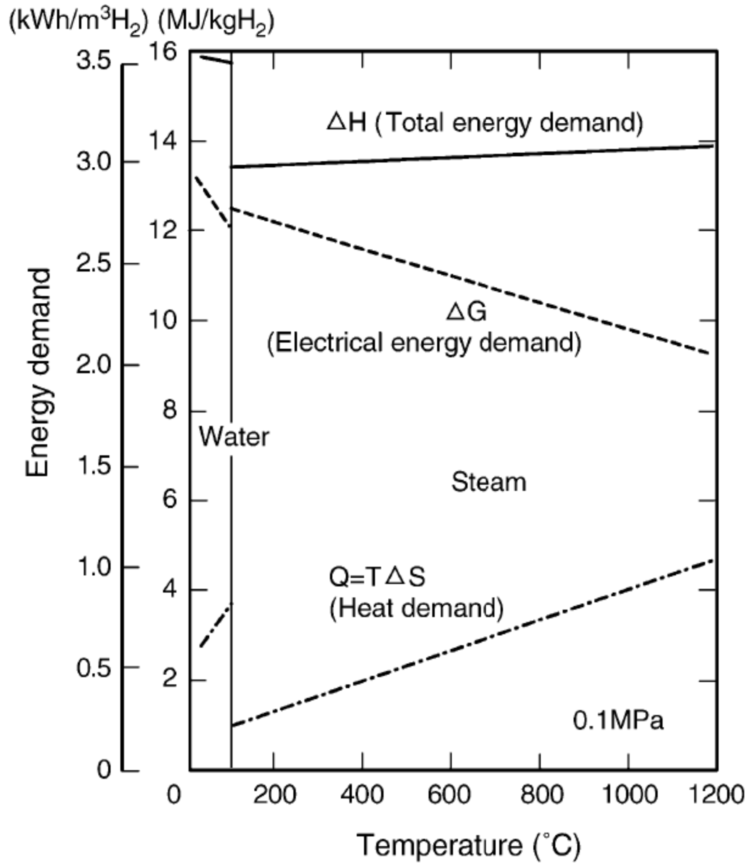

Figure 1-8:
Evolution of the total energy demand, electrical energy demand and heat demand with temperature for steam electrolysis [23]

For HTSE, the thermoneutral voltage of the cell $U_{th.neutral}$ corresponds to the potential at which the cell remains thermally stable compared to its equilibrium state at Open Circuit Voltage (OCV). At typical SOEC operating temperatures (*i.e.* 800°*C*), the thermoneutral potential is around 1.29 *V*, since the enthalpy variation of the reaction remains nearly unchanged (Figure 1-8). When the cell voltage $U_{cell}$ is equal to the thermoneutral potential, the heat provided by the irreversibilities in the cell is fully absorbed by the energy required for water splitting. In other words, enthalpy for $H_2O$ reduction $\Delta H$ is entirely provided by the electrical work $\Delta G$ and thus the entropy variation is nil. Furthermore, the cell can operate at thermal equilibrium with an electrical conversion efficiency equal to 100% (*i.e.* $\eta = {}^{\Delta H}\!/\!_{\Delta G} = 1$). Such operating conditions are of great interest for SOECs since neither heat generator nor exchanger are required.

In the endothermic mode, $U_{cell} < U_{th.neutral}$ (Figure 1-9) and the electrical energy supply $\Delta G$ is lower than the enthalpy variation $\Delta H$. Thus, additional heat is required to maintain the operating temperature. In this mode, electrical conversion efficiency is higher than 100% [24] (*i.e.* $\eta = {}^{\Delta H}\!/_{\Delta G} > 1$). If heat is provided at a temperature higher than the cell temperature, the mode is called allothermic.

When $U_{cell} > U_{th.neutral}$, the cell operates in the exothermic mode. It corresponds to an increase of the cell temperature because the electric energy supply $\Delta G$ exceeds the enthalpy variation $\Delta H$. In this mode, the electrical conversion efficiency is lower than 100% ($\eta = {}^{\Delta H}\!/_{\Delta G} < 1$).

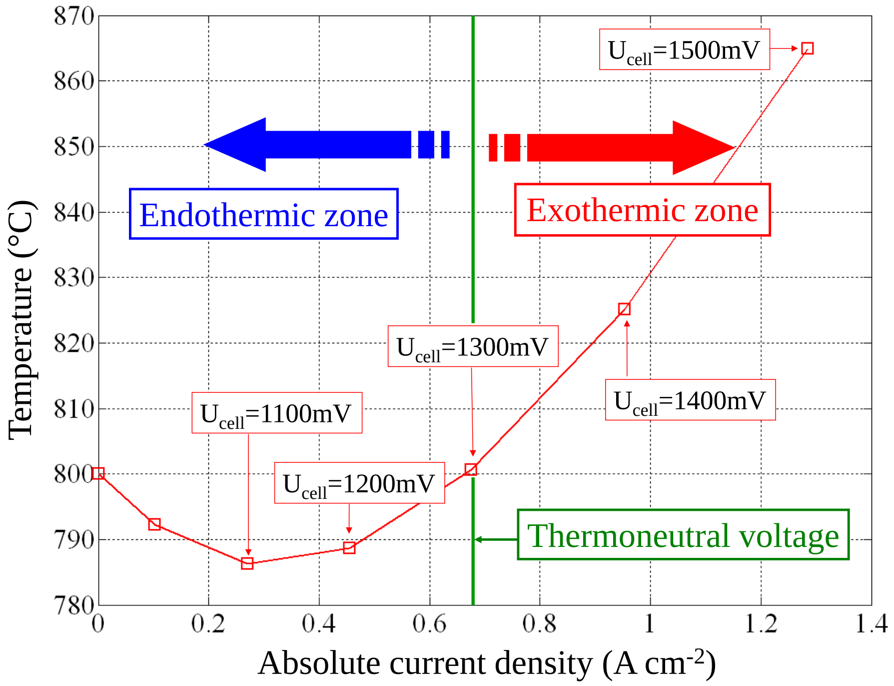

Figure 1-9: Temperature of an operating SRU - thermal operating modes for steam electrolysis [25].

Regardless of the operating mode, performances of a solid oxide cell (SOC) in specific conditions (composition of the gaseous inlet, temperature, *etc.*) are usually measured through polarization curves, corresponding to the evolution of the cell voltage as a function of the cell current density. By convention, and contrary to the SOFC mode where electricity is produced, the current density supplied to a SOEC is negative. Typical polarization curves in both operating modes are displayed in upcoming Figure 1-11.

The highest efficiencies displayed by SOCs are not their only advantage compared to other electrolysis technologies. Due to a wide fuel flexibility with their ability to operate with carbonated fuel such as natural gas, these systems have received a lot of attention these last decades. Indeed, SOCs are able to oxidize or produce CO [26, 27], whereas CO is usually considered as a poison for fuel cells operating at low temperature [28–30].

### 1.3.2. High Temperature Carbone Dioxide Electrolysis

In SOECs, carbon dioxide can be electrolyzed to carbon monoxide and oxygen. In this case, reaction (1-1) is replaced by reaction (1-6), corresponding to global reaction (1-7). It should be noted that at SOEC operating temperatures, both $H_2O$ and $CO_2$ electrolyzes require about the same amount of electrical energy (*i.e.* between 750-850°*C*, $\Delta G_{H_2O\ electrolysis} \approx \Delta G_{CO_2\ electrolysis}$). However, this operating mode usually exhibits lower performances compared to steam electrolysis [31–33]. Additionally, if the CO content is high enough (depending on operating temperature and pressure), carbon may be deposited at the cathode side according to the Boudouard reaction (1-8) and/or CO electro-reduction (1-9) at very high $CO_2$ conversion rates. If such reactions occur, the performances of standard cells would be seriously lowered.

$$CO_2 + 2e^- \rightarrow CO + O^{2-} \tag{1-6}$$

$$CO_2 \rightarrow CO + \frac{1}{2}O_2 \quad \left(\Delta_r H^\theta = 283\ kJ.mol^{-1}\right)\ \text{[15]} \tag{1-7}$$

$$2CO \rightarrow CO_2 + C \tag{1-8}$$

$$CO + 2e^- \rightarrow C + O^{2-} \tag{1-9}$$

Other current technologies can reduce $CO_2$ in CO, some of which are gathered in Table 1-4. If some of the presented efficiencies might seem high, it should be noted that most of these processes suffer (at varying extents) from low conversion rates, mass transfer limitations and/or low durability that might affect their economic potential.

In addition and contrary to $H_2$, CO is rarely if ever the desired end product. Consequently, many processes, which are out of the scope of this work, have been developed to convert $CO_2$ directly into a variety of fuels (*e.g.* methanol, methane, *etc.*). Therefore, Table 1-4 is not intended to reflect the current state of the art in $CO_2$ utilization.

| **Process** | **Efficiency** | **Ref.** |
|---:|:---:|:---:|
| Thermolysis | 5-50% | [34] |
| Thermochemical cycle | 16-25% | [35] |
| Alkaline Electrolysis | 80% | [36] |
| Molten carbonate electrolysis | 80-90% | [37] |
| **HT electrolysis** | **>100%** | * |

Table 1-4: Overview of some of the technologies of production of CO from $CO_2$ **[38]**.

* if the required additional heat is supplied by an external cheap source. Electrolysis efficiency is usually defined as the ratio of thermoneutral voltage to the operating voltage.

## 1.3.3. High Temperature $H_2O$ and $CO_2$ Co-Electrolysis

Weissbart *et al.* [39] first showed in 1967 that by adding $CO_2$ to steam at the cell inlet, both $H_2$ and CO can be produced within a SOEC. In this co-electrolysis mode, both reactions (1-1) and (1-7) could occur simultaneously. Furthermore, the Water Gas Shift (WGS) reaction (1-10) may also take place at the cathode side. The elementary chemical reactions and transport processes for single electrolyses and co-electrolysis of steam and carbon dioxide are shown in Figure 1-10.

$$CO + H_2O \leftrightarrow CO_2 + H_2 \qquad \left(\Delta_r H\left(800°C, 1\,atm\right) = 41\,kJ.mol^{-1}\right) [20] \tag{1-10}$$

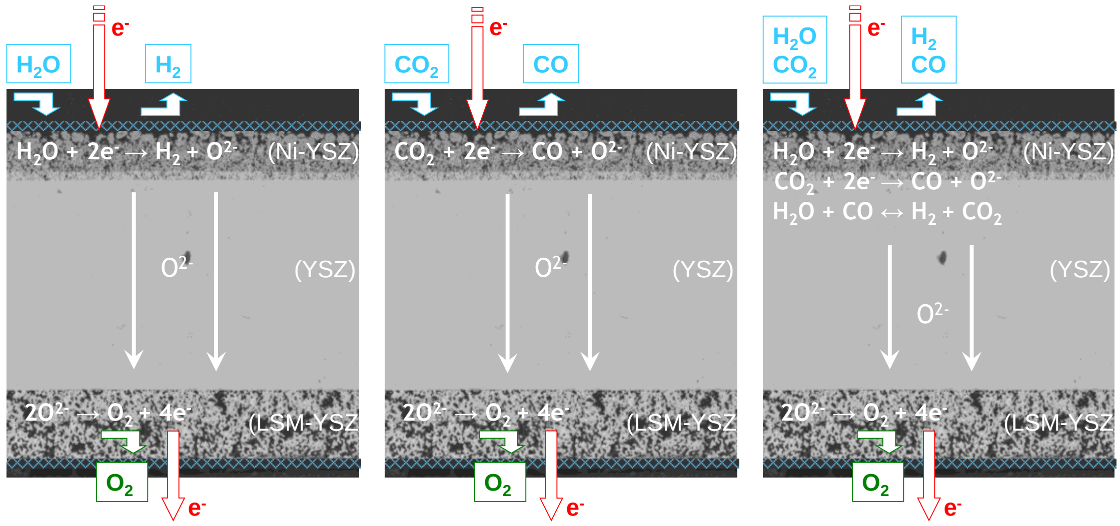

Figure 1-10: Principles of $H_2O$ electrolysis, $CO_2$ electrolysis and co-electrolysis.

Because it could produce syngas ($H_2$+CO) within the same apparatus, the co-electrolysis process has been widely investigated these past few years (since O'Brien *et al.* first papers in 2007, about 50 references in Scopus, although some technical reports were published in the 1960s [39–41]). Indeed, while the syngas can be directly oxidized to generate electricity in fuel cells [26], it also constitutes the chemical basis for the production of a variety of synthetic fuels [42] by catalytic processes (*e.g.* $CH_4$ [20], DME [43] *etc.* – Table 1-5) . Such fuels could be integrated in a $CO_2$ neutral energy cycle, provided that the initial carbon dioxide is recycled [15]. In addition, the complete route, (i) atmospheric $CO_2$ capture using solid sorbent, (ii) $H_2O$+$CO_2$ co-electrolysis and (iii) synthetic fuels production based on the Fischer-Tropsch process [44, 45], was identified as one of the most energy efficient and economically viable "Power-to-Gas" path [15].

| **End product** | **$CO/H_2$** (*via* co-electrolysis) | **$CO_2/H_2$** (*via* $H_2O$ electrolysis) |
|---|---|---|
| Methane | 1/3 | 1/4 |
| Methanol | 1/2 | 1/3 |
| DME (Dimethyl ether) | 1/1 | 1/2 |
| Diesel (*via* Fischer-Tropsch) | 1/2 | 1/3 |

Table 1-5: Synthetic fuels that can be produced via co-electrolysis of $H_2O$+$CO_2$ or steam electrolysis – Communication DTU Risø.

By ultimately producing substitute natural gas, co-electrolysis could also provide an environmentally friendly electricity storage option on a large scale (*cf.* Figure 1-5), that could be implemented without adapting the current natural gas distribution network. Although methane, the main component of natural gas, is usually produced through $CO_2$ methanation reaction (1-11), it can be alternately synthetized through CO methanation reaction (1-12). This last chemical reaction makes a more efficient use of $H_2$ in yielding $CH_4$ compared to $CO_2$ methanation. Furthermore, CO hydrogenates more easily than $CO_2$ [46]. Therefore, in methane production scenario, syngas produced by co-electrolysis appears advantageous. Nevertheless, it is worth noting that the thermal management of the highly exothermic CO methanation reaction is hardened compared to its counterpart, and the methanator is more likely to suffer from carbon deposition due to a lower oxygen content in the gas stream (Figure 2-1).

$$CO_2 + 4H_2 \rightarrow CH_4 + 2H_2O \quad \left(\Delta_r H^\theta = -165.0\ kJ.mol^{-1}\right)[46] \tag{1-11}$$

$$CO + 3H_2 \rightarrow CH_4 + H_2O \quad \left(\Delta_r H^\theta = -206.1\ kJ.mol^{-1}\right)[46] \tag{1-12}$$

However, since the regain of interest in $H_2O$ and $CO_2$ high temperature co-electrolysis is as recent as 2005, there is still much to be learned and understood. Indeed, the co-electrolysis process is much more complicated than single electrolysis mechanisms. In addition, there is currently no consensus concerning the electrochemical mechanism, and it is not clear whether the reverse WGS reaction contributes to CO production [47, 48].

# 1.4. Overview of a Solid Oxide Electrolysis Cell

There are many different physical phenomena occurring in a high temperature (co-) electrolyzer. This section strives to explicit each one of them. The complete associated mathematic equations will be detailed in Chapter 3.

## 1.4.1. Steady State

Due to the difference in oxygen partial pressures between anodic and cathodic compartments, both electrodes of a SOC are characterized by proper electrical potentials. When no electrical current flows through the cell, the OCV can be expressed by using the Nernst law:

$$U_{i=0}^{H_2-H_2O//O_2} = U_{H_2-H_2O//O_2}^{0}\left(T\right) + \frac{RT}{2F}\ln\frac{y_{H_2}^{int\_i=0}\sqrt{y_{O_2}^{int\_i=0}}}{y_{H_2O}^{int\_i=0}} \tag{1-13}$$

$$U_{i=0}^{CO-CO_2//O_2} = U_{CO-CO_2//O_2}^{0}\left(T\right) + \frac{RT}{2F}\ln\frac{y_{CO}^{int\_i=0}\sqrt{y_{O_2}^{int\_i=0}}}{y_{CO_2}^{int\_i=0}} \tag{1-14}$$

where $U^0$ is the standard potential, $R$ the gas constant, $T$ the temperature, $F$ the Faraday constant, $y_{i=H_2,H_2O,CO,CO_2}^{int\_i=0}$ the molar fractions at the cathode active sites at $i = 0$ and $y_{i=O_2}^{int\_i=0}$ the oxygen molar fraction calculated at the anode active sites at $i = 0$.

## 1.4.2. Overpotentials and Polarization Curves Decomposition

Under electrolysis operating conditions, the cell voltage is always higher than OCV because of electrode overpotentials and ohmic losses. In a SOEC, a sufficient cell voltage or current must be applied to trigger the non-spontaneous electrolysis processes. $H_2O$ and $CO_2$ are fed to the cathode and are transported through that porous layer to the cathode/electrolyte interface where they are reduced to $H_2$ and CO, respectively. These reactions result in the formation of oxygen ions $O^{2-}$. The as produced hydrogen and carbon monoxide are then transported out of the porous cathode and collected. The oxygen ions migrate through the dense electrolyte membrane and are oxidized to form $O_2$ at the anode/electrolyte interface. $O_2$ is transported out of the porous anode and the electrons are collected by the external circuit. To summarize, any electrolysis reaction implies mass transport of multi-components in a gas phase, mass transport through solid phases as well as charge transfer mechanisms. Accordingly, the understanding of the physico-chemical processes involved in co-electrolysis of steam and carbon dioxide requires a pertinent modeling and a reliable analysis.

The ohmic losses are related to the overall series resistance due to the contributions of both electrodes, electrolyte materials and the interconnects. The activation overpotentials are caused by slow charge transfer reactions and reflect the electrochemical activities of the electrodes. Concentration overpotentials originate from the slow mass transports of reactants and products through porous electrodes and the depletion/enrichment of reactants/products along the gas channels. The latter losses become predominant at high current densities. Accordingly, the cell voltage can be decomposed into a sum of the OCV and the different overpotentials [25, 49] (Figure 1-11).

For steam electrolysis, the cell voltage can be written:

$$U_{cell} = U_{i=0,OCV}^{H_2-H_2O//O_2} + R_{ohm}\left|i_{cell}\right| + \left(\left|\eta_{act,H_2-H_2O//O_2}^{anode}\right| + \left|\eta_{act,H_2-H_2O//O_2}^{cathode}\right|\right) + \left(\left|\eta_{conc,H_2-H_2O//O_2}^{anode}\right| + \left|\eta_{conc,H_2-H_2O//O_2}^{cathode}\right|\right) \quad (1\text{-}15)$$

where $R_{ohm}$ is the cell ohmic Area Specific Resistance (ASR), $i$ the current density, $\eta_{act}$ the activation overpotentials and $\eta_{conc}$ the concentration overpotentials.

The same type of expression prevails for carbon dioxide electrolysis:

$$U_{cell} = U_{i=0,OCV}^{CO-CO_2//O_2} + R_{ohm}\left|i_{cell}\right| + \left(\left|\eta_{act,CO-CO_2//O_2}^{anode}\right| + \left|\eta_{act,CO-CO_2//O_2}^{cathode}\right|\right) + \left(\left|\eta_{conc,CO-CO_2//O_2}^{anode}\right| + \left|\eta_{conc,CO-CO_2//O_2}^{cathode}\right|\right) \quad (1\text{-}16)$$

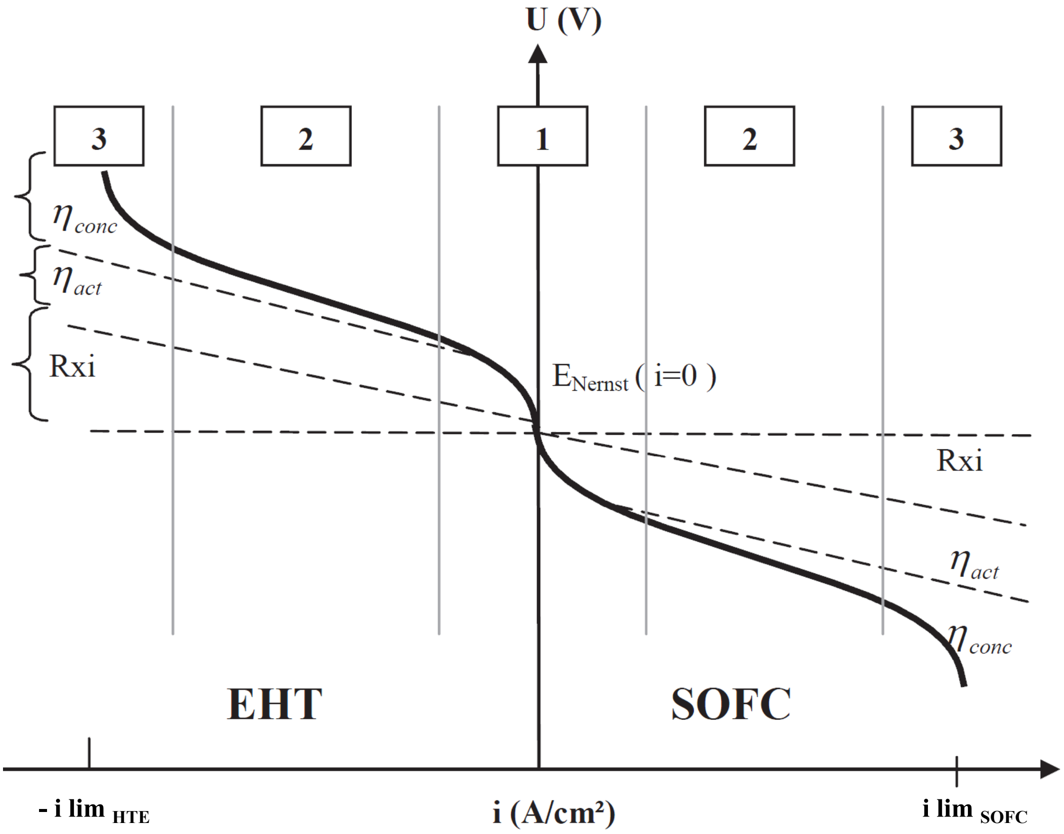

Figure 1-11: Typical decomposition of polarization curves in both SOFC and SOEC **[19]**.
*i-V* curves can usually be decomposed into 3 zones: zone 1 is mainly governed by activation, zone 2 by ohmic losses and zone 3 by mass transfer.
Due to mass transfer limitations, usually i lim $_{HTE}$ < i lim $_{SOFC}$

### 1.4.3. Electrochemical Reactions

The electrochemical reactions are likely to occur in the vicinity of the electrode/electrolyte interface. This assumption is well verified for sufficiently thick electrodes. Indeed, several studies have shown that the reaction zone spreads within the first 10-20 $\mu m$ of electrode thickness [50–53]. This originates from the low ionic conductivity of the electrode material compared to its electronic counterpart.

Due to their inherent irreversiblities, the electrochemical reactions induce a voltage increase called activation overpotentials. These overpotentials depend on the electrode exchange current densities, characterizing the electrochemical activity of materials. These last parameters are thermally activated and strongly depend on the density of available active sites. They are defined by the lines in the electrode where the ionic ($O^{2-}$) and electronic ($e^-$) charge carriers as well as gaseous species ($H_2$, $H_2O$, CO, $CO_2$, $O_2$) can meet. They correspond to the well-known Triple Phase Boundary lengths (TPBls), as illustrated in Figure 1-12. It is worth noting that the density of TPBls depends on the microstructure characteristics of the porous electrode.

At high current densities, the gas composition in the vicinity of the active sites is different from the inlet composition. Such difference also leads to a voltage increase denoted concentration overpotentials. It should be noted that optimizing an electrolysis process translates into minimizing the different overpotentials. Indeed, at a given current density, that determines the $H_2$ production in $H_2O$ electrolysis, a low cell voltage would increase the cell efficiency (*i.e.* the required electrical power would be reduced).

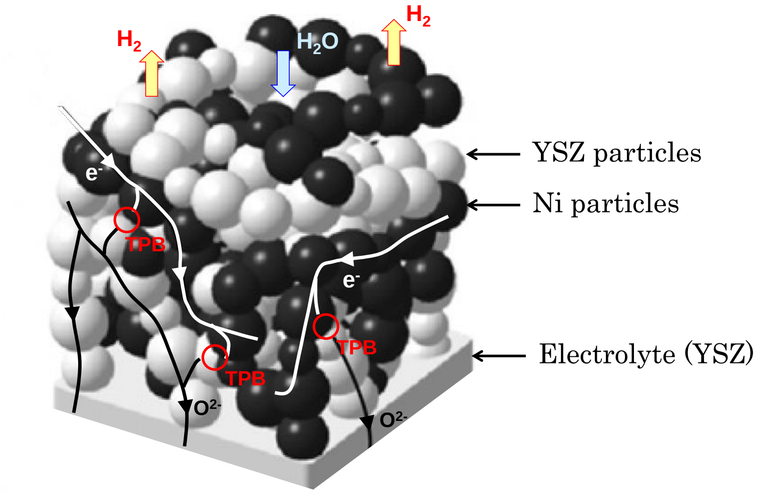

Figure 1-12:
Triple Phase Boudary
lengths (TPBl).

### 1.4.4. Mass Transport

For the sake of clarity, this section presents the mass transport phenomena in the specific case of SOEC cathode (fuel electrode). Similar observations can be made at the anode side.

To reach the electroactive area in the vicinity of the cathode/electrolyte interface, gases of the cathodic inlet stream first flow along the gas channel supplying reactants and collecting products of the electrochemical reaction(s). Then, gases are transported through the porous cathode to the electrolyte interface. The mass transfer is strongly dependent on the microstructure properties. Diffusion of gases can be described by using three parameters: the porosity, the ‘apparent’ tortuosity factor and the mean pore diameter. The porosity represents the ratio of the volume of voids to the total volume of the electrode. The ‘apparent’ tortuosity factor is used to describe the complex transport paths in a heterogeneous porous structure. It encompasses two contributions [54]: the geometrical tortuosity factor (Figure 1-13), and the constriction factor that accounts for bottleneck effects.

Figure 1-14 illustrates $H_2O$ and $H_2$ paths from the inlet to the outlet along a SOC operating in steam electrolysis, as well as the main mass transfer processes.

Models for mass transport inside a porous electrode are used to calculate the gas concentrations at the electrode/electrolyte interface and, thus, predict the related concentration overpotential. In a porous medium, the diffusion process can be divided into two diffusion mechanisms: molecular diffusion and Knudsen diffusion. In the former case, interactions between gas molecules are important and this mechanism can be considered as dominant for large pore sizes and high pressures. The Knudsen diffusion becomes predominant when the mean free path of gas species is larger than the pore size, *i.e.* the interactions between gas molecules and the solid phase dominate.

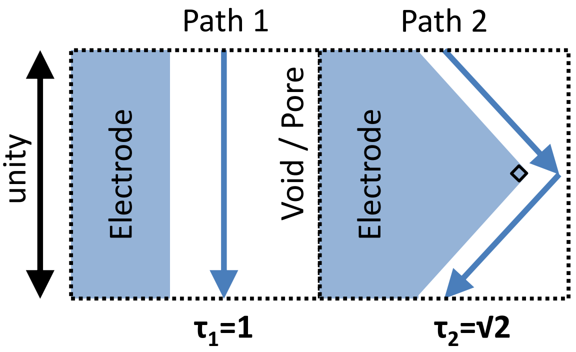

Figure 1-13:
Illustration of the geometrical
tortuosity factor.

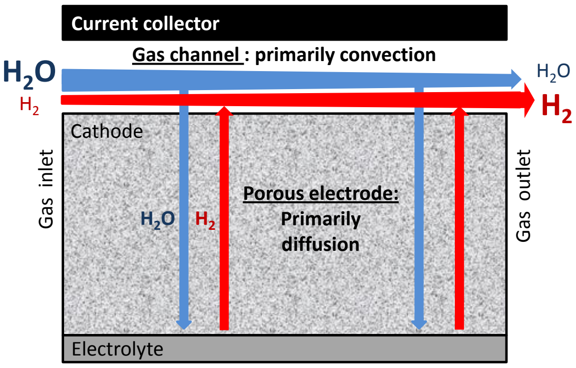

Figure 1-14: $H_2O$ and $H_2$ paths along the cell and trough the cathode in steam electrolysis and main mass transfer modes.

There are several models that describe the gas diffusion in porous media. The Fick model is the simplest and supposes that matter always moves from zones of high concentrations to those of lower ones (this is also the case for all diffusion models). The corresponding mass flow is proportional to the concentration gradient of the gas component. The extended Fick model takes into account Knudsen and molecular diffusions. The Stefan-Maxwell model neglects the Knudsen diffusion mechanism and is likely to be better predictive than the Fick model for multi-components diffusion processes. The Dusty Gas Model (DGM) includes the Stefan-Maxwell formulation and takes into account the Knudsen diffusion mechanism. Several reports have investigated the ability of each model to accurately predict the mass transport through SOC [55, 56]. Because of its good agreement with experimental measurements, especially under high polarization, the DGM has been used throughout most SOC modeling studies.

## 1.5. Objectives of the Study

This work aims at investigating the simultaneous co-electrolysis of $H_2O$ and $CO_2$ at high temperature, typically $800°C$. Tackling this fairly new field of SOC application that was co-electrolysis 3 years ago, this investigation should lead to the assessment of key outputs, relevant for system design and technology evaluation. To do so, one must thus predict, depending on operating conditions and cell materials and microstructure:

- cell performances (*i.e.* polarization curves),
- outlet composition,
- electrochemical and thermal behaviors in stack environments,
- operating maps.

Furthermore, as will be developed in the following chapter, a current lack of consensus exists on co-electrolysis mechanism and on the relative influence of the WGS reaction over global CO production. Thus, this work also aims at addressing these issues, through the determination of respective influences of chemistry over electrochemistry, and the formulation of a possible mechanism.

Finally, this study has provided scientific analysis of high temperature co-electrolysis in French Research National Agency (ANR) project DEMETER (ANR-1-SEED-0005-01) and European project MINERVE (KIC InnoEnergy, grant agreement 76_2012_IP35_MINERVE).

## 1.6. Methodology

A combined modeling and experimental approach has been developed and implemented to investigate the high temperature co-electrolysis of $H_2O$ and $CO_2$. Indeed, a well-adapted model should allow for fine analyses of the multiple and entangled phenomena occurring in an operating SOC.

Three separate models are used in this study, the first of which describes single $H_2O$ electrolysis. It was developed within the CEA/LITEN/LTH laboratory and published prior to this work [25]. From this peer-reviewed starting point, $CO_2$ electrolysis and co-electrolysis models were developed.

Single electrolysis models will be used to assess unknown parameters needed for modeling purposes (*e.g.* exchange current densities), by comparing simulations and experimental data obtained in the same well-chosen conditions. Indeed, the experimental protocols implemented will highlight modifications of cathodic overpotentials through composition, dilution ratio and flow changes.

Finally, using the previously determined inputs, the predictive co-electrolysis model will be experimentally validated, and the simulations analyzed to determine co-electrolysis operating maps. Figure 1-15 summarizes the global methodology implemented and applied in this work.

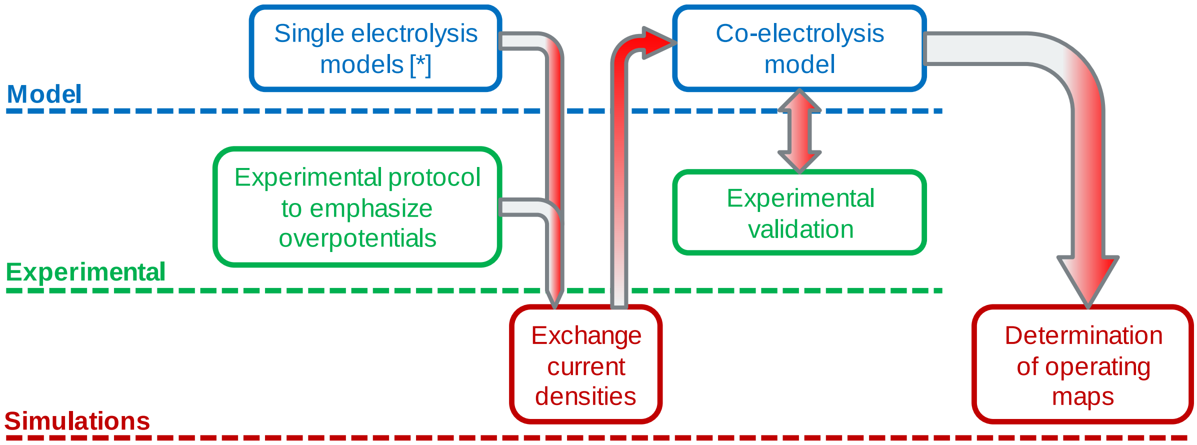

Figure 1-15: Summary of the methodology implemented.

[*] $H_2O$ electrolysis model was developed prior to this work [25].

## 1.7. References

1. J.-R. Petit, J. Jouzel, D. Raynaud, N. I. Barkov, J.-M. Barnola, I. Basile, M. Bender, J. Chappellaz, M. Davis, and G. Delaygue, Climate and atmospheric history of the past 420,000 years from the Vostok ice core, Antarctica, *Nature* 399, 429 (**1999**).
2. *IPCC Fourth Assessment Report, Chapter 2*, (**2007**).
3. *http://www.acs.org/content/acs/en/climatescience/greenhousegases/industrialrevolution.html*.
4. N. R. C. (US) C. on A. C. Choices, *Advancing the Science of Climate Change: America's Climate Choices*, National Academies Press (**2010**).
5. "World Bank. 2012. Turn Down the Heat: Why a 4°C Warmer World Must Be Avoided. © Washington, DC., (**2012**)
6. *BP Statistical Review of World Energy*, bp.com/statisticalreview (**2012**).
7. H. Iskov and N. B. Rasmussen, Global screening of projects and technologies for Power-to-Gas and Bio-SNG, *http://www.dgc.dk/sites/default/files/filer/publikationer/R1307_screening_projects.pdf* (**2013**)
8. M. Specht, U. Zuberbühler, F. Baumgart, B. Feigl, V. Frick, B. Stürmer, M. Sterner, and G. Waldstein, Storing Renewable Energy in the Natural Gas Grid Methane via Power-to-Gas (P2G): A Renewable Fuel for Mobility, (**2011**)
9. CEA, Energy Handbook, (**2012**).
10. G. Sandrock, A panoramic overview of hydrogen storage alloys from a gas reaction point of view, *J. Alloys Compd.* 293, 877 (**1999**).
11. *http://www.fuelcelltoday.com/about-fuel-cells/history*.
12. A. Kirubakaran, S. Jain, and R. K. Nema, A review on fuel cell technologies and power electronic interface, *Renew. Sustain. Energy Rev.* 13, 2430 (**2009**).
13. J. M. Andújar and F. Segura, Fuel cells: History and updating. A walk along two centuries, *Renew. Sustain. Energy Rev.* 13, 2309 (**2009**).
14. A. B. Stambouli, Fuel cells: The expectations for an environmental-friendly and sustainable source of energy, *Renew. Sustain. Energy Rev.* 15, 4507 (**2011**).
15. C. Graves, S. D. Ebbesen, M. Mogensen, and K. S. Lackner, Sustainable hydrocarbon fuels by recycling CO2 and H2O with renewable or nuclear energy, *Renew. Sustain. Energy Rev.* 15, 1 (**2011**).
16. J. D. Holladay, J. Hu, D. L. King, and Y. Wang, An overview of hydrogen production technologies, *Catal. Today* 139, 244 (**2009**).
17. A. Hauch, S. D. Ebbesen, S. H. Jensen, and M. Mogensen, Highly efficient high temperature electrolysis, *J. Mater. Chem.* 18, 2331 (**2008**).
18. F. Chauveau, *Synthèse et caractérisations électrochimiques de nouveaux matériaux pour anodes d'électrolyseurs à haute température*, (**2009**).
19. A. Mansuy, *Etude de la durabilité de cellules d'électrolyse de la vapeur d'eau à haute température: influence des paramètres de fonctionnement*, (**2012**)

20. J. Xu and G. F. Froment, Methane steam reforming, methanation and water-gas shift: I. Intrinsic kinetics, *AIChE J.* 35, 88 (**1989**).
21. *www.kitco.com* (**2013**).
22. S. Dutta, Technology assessment of advanced electrolytic hydrogen production, *Int. J. Hydrog. Energy* 15, 379 (**1990**).
23. R. Hino, K. Haga, H. Aita, and K. Sekita, 38. R&amp;D on hydrogen production by high-temperature electrolysis of steam, *Nucl. Eng. Des.* 233, 363 (**2004**).
24. J. E. O'Brien, Considerations for Thermal Water Splitting Processes and High Temperature Electrolysis, *Proc. 2008 Int. Mech. Eng. Congr. Expo.* (**2008**)
25. J. Laurencin, D. Kane, G. Delette, J. Deseure, and F. Lefebvre-Joud, Modelling of solid oxide steam electrolyser: Impact of the operating conditions on hydrogen production, *J. Power Sources* 196, 2080 (**2011**).
26. A. Weber, B. Sauer, A. C. Müller, D. Herbstritt, and E. Ivers-Tiffée, Oxidation of H2, CO and methane in SOFCs with Ni/YSZ-cermet anodes, *Solid State Ion.* 152–153, 543 (**2002**).
27. W. Oser, *Electrochemical method for conversion of carbon dioxide*, Google Patents (**1967**).
28. J. J. Baschuk and X. Li, Carbon monoxide poisoning of proton exchange membrane fuel cells, *Int. J. Energy Res.* 25, 695 (**2001**).
29. Q. Li, R. He, J.-A. Gao, J. O. Jensen, and N. J. Bjerrum, The CO Poisoning Effect in PEMFCs Operational at Temperatures up to 200°C, *J. Electrochem. Soc.* 150, A1599 (**2003**).
30. J.-M. Le Canut, R. M. Abouatallah, and D. A. Harrington, Detection of Membrane Drying, Fuel Cell Flooding, and Anode Catalyst Poisoning on PEMFC Stacks by Electrochemical Impedance Spectroscopy, *J. Electrochem. Soc.* 153, A857 (**2006**).
31. P. Kim-Lohsoontorn, N. Laosiripojana, and J. Bae, Performance of solid oxide electrolysis cell having bi-layered electrolyte during steam electrolysis and carbon dioxide electrolysis, *Curr. Appl. Phys.* 11, S223 (**2011**).
32. J. E. O'Brien, M. G. McKellar, C. M. Stoots, J. S. Herring, and G. L. Hawkes, Parametric study of large-scale production of syngas via high-temperature co-electrolysis, *Int. J. Hydrog. Energy* 34, 4216 (**2009**).
33. C. Graves, S. D. Ebbesen, and M. Mogensen, Co-electrolysis of CO2 and H2O in solid oxide cells: Performance and durability, *Solid State Ion.* 192, 398 (**2011**).
34. A. J. Traynor and R. J. Jensen, Direct Solar Reduction of CO $_2$ to Fuel: First Prototype Results, *Ind. Eng. Chem. Res.* 41, 1935 (**2002**).
35. A. Kogan, Direct solar thermal splitting of water and on-site separation of the products. III. Improvement of reactor efficiency by steam entrainment, *Int. J. Hydrog. Energy* 25, 739 (**2000**).
36. H. Noda, S. Ikeda, Y. Oda, K. Imai, M. Maeda, and K. Ito, Electrochemical reduction of carbon dioxide at various metal electrodes in aqueous potassium hydrogen carbonate solution., *Bull. Chem. Soc. Jpn.* 63, 2459 (**1990**).
37. V. Kaplan, E. Wachtel, K. Gartsman, Y. Feldman, and I. Lubomirsky, Conversion of CO[sub 2] to CO by Electrolysis of Molten Lithium Carbonate, *J. Electrochem. Soc.* 157, B552 (**2010**).
38. C. Graves, S. D. Ebbesen, M. Mogensen, and K. S. Lackner, Sustainable hydrocarbon fuels by recycling CO2 and H2O with renewable or nuclear energy, *Renew. Sustain. Energy Rev.* 15, 1 (**2011**).

39. J. Weissbart and W. Smart, Study of electrolytic dissociation of CO2-H2O using a solid oxide electrolyte. NASA CR-680., *NASA Contract. Rep. NASA CR U. S. Natl. Aeronaut. Space Adm.* 1 (**1967**).
40. W. Smart and J. Weissbart, Development of a CO2-H2O Solid Oxide Electrolysis System : First annual report, 29 March 1968–29 May 1969, *Moffett Field, CA: National Aeronautics and Space Administration, Ames Research Center* (**1969**).
41. L. Elikan, J. Morris, and C. Wu, Development of a solid electrolyte carbon dioxide and water reduction system for oxygen recovery, (**1972**).
42. I. Chorkendorff and J. W. Niemantsverdriet, *Concepts of modern catalysis and kinetics*, Wiley (**2003**)
43. T. Ogawa, N. Inoue, T. Shikada, O. Inokoshi, and Y. Ohno, Direct Dimethyl Ether (DME) synthesis from natural gas, *J. Nat. Gas Chem.* 22, 219 (**2003**).
44. M. E. Dry, The Fischer–Tropsch process: 1950–2000, *Fisch.-Tropsch Synth. Eve XXI Century* 71, 227 (**2002**).
45. W. L. Becker, R. J. Braun, M. Penev, and M. Melaina, Production of Fischer–Tropsch liquid fuels from high temperature solid oxide co-electrolysis units, *Energy* 47, 99 (**2012**).
46. J. Gao, Y. Wang, Y. Ping, D. Hu, G. Xu, F. Gu, and F. Su, A thermodynamic analysis of methanation reactions of carbon oxides for the production of synthetic natural gas, *RSC Adv.* 2, 2358 (**2012**).
47. C. Stoots, J. O'Brien, and J. Hartvigsen, Results of recent high temperature coelectrolysis studies at the Idaho National Laboratory, *Int. J. Hydrog. Energy* 34, 4208 (**2009**).
48. M. Ni, An electrochemical model for syngas production by co-electrolysis of H2O and CO2, *J. Power Sources* 202, 209 (**2012**).
49. J. Laurencin, F. Lefebvre-Joud, and G. Delette, Impact of cell design and operating conditions on the performances of SOFC fuelled with methane, *J. Power Sources* 177, 355 (**2008**).
50. J.-W. Kim, Polarization Effects in Intermediate Temperature, Anode-Supported Solid Oxide Fuel Cells, *J. Electrochem. Soc.* 146, 69 (**1999**).
51. S. B. Adler, Mechanism and kinetics of oxygen reduction on porous La1−xSrxCoO3−δ electrodes, *Solid State Ion.* 111, 125 (**1998**).
52. S. Primdahl and M. Mogensen, Oxidation of hydrogen on Ni/yttria-stabilized zirconia cermet anodes, *J. Electrochem. Soc.* 144, 3409 (**1997**).
53. E. Lay-Grindler, J. Laurencin, G. Delette, J. Aicart, M. Petitjean, and L. Dessemond, Micro modelling of solid oxide electrolysis cell: From performance to durability, *Int. J. Hydrog. Energy* 38, 6917 (**2013**).
54. F. Usseglio-Viretta, J. Laurencin, G. Delette, J. Villanova, P. Cloetens, and D. Leguillon, Quantitative microstructure characterization of a Ni–YSZ bi-layer coupled with simulated electrode polarisation, *J. Power Sources* 256, 394 (**2014**).
55. R. Suwanwarangkul, E. Croiset, M. W. Fowler, P. L. Douglas, E. Entchev, and M. A. Douglas, Performance comparison of Fick's, dusty-gas and Stefan–Maxwell models to predict the concentration overpotential of a SOFC anode, *J. Power Sources* 122, 9 (**2003**).
56. M. Andersson, J. Yuan, and B. Sundén, Review on modeling development for multiscale chemical reactions coupled transport phenomena in solid oxide fuel cells, *Appl. Energy* 87, 1461 (**2010**).

# Chapter 2

# State of the Art

# Chapter 2

# State of the Art

Co-electrolysis studies are relying on decades of experimental developments of materials and design optimization. Indeed, the high operating temperature yields rigorous and specific constraints concerning the different components of an electrolyzer. It is worth mentioning that specific materials have yet to be developed for the (co-)electrolysis mode. Indeed, the materials currently used have been developed for high temperature fuel cell applications.

Regardless of the wealth of information that actual cell testing has represented throughout several decades, the high temperature makes experimental works expensive and time consuming. Indeed, because the cell housing, Single Repeating Units (SRU) or stacks have to be maintained at around 800*°C*, it is quite more technical to equip the test bench with the different sensors required for fine investigations than it would be for low temperature systems. Additionally, SOC are complex devices to analyze due to the numerous physical phenomena involved. Therefore, modeling approaches have been widely adopted to investigate the multiphysics phenomena occurring inside a SOC. Experimental validation is required to strengthen a model ability to predict the SOC behavior. It is worth noting that most of these validations are performed by comparing experimental and simulated polarization curves.

This chapter will first detail the most common materials utilized in a SRU operating in high temperature electrolysis: electrolyte and electrodes materials. Then, experimental developments in steam electrolysis, $CO_2$ electrolysis and co-electrolysis will be overviewed. A section focused on degradation mechanisms will also be presented. Finally, relevant modeling studies of a SOEC operating in all electrolysis modes will be specified.

## 2.1. SOC Materials

The operating conditions for steam electrolysis or co-electrolysis induce high strains on the materials constituting the SOEC, the SRU (cell coupled with two half interconnects) or the stack (pileup of several SRUs). To be compatible with electrochemical processes, electrode materials must foremost present sufficiently high electrical conductivities. For oxygen ion conducting oxides, high ionic conductivities are reached above $600°C$. Thus, the different materials must exhibit compatible thermal expansion coefficients (TEC) along with good thermal cyclability to withstand start and stop cycles [1–3]. Indeed, different TEC values between adjacent cell layers induce mechanical stresses that can lead to cell failures. Additionally, since both electrodes are in contact with highly oxidant/reducing atmospheres at high temperature, electrodes and electrolyte should be chemically stable.

The main roles of the dense electrolyte membrane are to ensure the gas tightness between both electrode compartments, to avoid any recombination of hydrogen and oxygen, and to force the electrons in the outer circuit. Moreover, this membrane should be as thin as possible to minimize the ohmic losses. Both electrodes should exhibit high electrocatalytic activity, high ionic and electronic conductivities to promote the geometrical extent of the electrode reactions from the electrolyte interface and to improve the current collection, respectively.

These electrodes should have suitable porosity to promote the matter transport in the gas phase and provide sufficient reaction sites.

### 2.1.1. Electrolyte

The electrolyte is a key component in a SOC. Indeed, it must be an electronic insulator in a wide range of oxygen partial pressure to avoid any short circuit reducing the current efficiency. The most common electrolyte material is based on yttria doped zirconia. Since the ohmic loss should be as low as possible for a given electrolyte thickness, the chosen ionic conductor should exhibit the highest conductivity in the operating conditions. Accordingly, scandia-doped zirconia (ScSZ) can be regarded as an interesting material, especially if one refers to the results reported by the Idaho National Laboratory [4]. Indeed, this oxide exhibits a higher ionic conductivity than yttria stabilized zirconia (YSZ), but its manufacturability should be more expensive [5]. The stability of ScSZ remains also to be established since thermal cycling of a cell results in an Area Specific Resistance (ASR) degradation [4]. Moreover, the ionic conductivity of ScSZ can hugely degrade during isothermal ageing in SOFC mode at high temperatures [6]. If one refers strictly to the ionic conductivity value, ceria-based oxides, doped either by $Gd_2O_3$ (GDC) or $Sm_2O_3$ (SDC), can be regarded as promising electrolytes for electrolysis operation, at least for temperatures up to 700°*C*. The use of SDC as an electrolyte was found effective in lowering both cathode and anode overpotentials in an electrolysis mode [7]. But, the main problem is that cerium cations can be partly reduced in a reducing atmosphere or fully reduced under high applied voltages. Despite deteriorating the ionic transfer number, this reduction process could also lead to a mechanical failure of a cell [8]. Recently, the use of a bi-layered GDC/YSZ electrolyte was proposed to increase the performances compared to cells only involving YSZ or GDC [9]. But, as for ScSZ, the stability of such an assembly in operating conditions must be investigated. $LaGaO_3$ doped with strontium and magnesium (LSGM) could be used as an electrolyte for steam electrolysis [10] because the ionic conductivity of LSGM is higher than that of YSZ. However, the electronic conductivity of LSGM depends on its microstructure and thus on the sintering conditions [11]. Moreover, LSGM is likely to react with a nickel containing electrode to form additional phases [12], resulting in a loss of conductivity [13].

At this stage, taking into account the level of ionic conductivity, the chemical stability as well as economic reasons, the most common electrolyte material for SOECs remains YSZ with dopant contents between 3 and 10 *mol.%* [14]. Within a wide range of oxygen partial pressure, the purely ionic conductivity of YSZ is of the order of 0.03 $S.cm^{-1}$ at 700°*C* [15] and 0.2 $S.cm^{-1}$ at 1000°*C* [5]. As can be seen in Table 2-1 which gathers performances and degradation reports, high performances as well as low degradation rates can be obtained using cells based on YSZ. This observation is probably related to the fact that YSZ is the most commonly optimized (in terms of elaboration, microstructure, *etc.*) and tested material.

### 2.1.2. Fuel Electrode

The oxygen partial pressure at the cathode side of a SOEC is expected to vary between $10^{-12}$ and $10^{-16}$ *atm*. Therefore, materials like nickel and cobalt can be used [16]. Although Ni exhibits a high electrochemical activity for the oxidations of hydrogen and carbon monoxide, it is only an electronic conductor. Thus, the nickel particles must be mixed with an ion conducting material, the same material than the electrolyte such as YSZ, in order to increase the number of active sites. The addition of a ceramic material also allows to limit the coarsening of nickel particles and to adapt the TEC of the electrode to that of the electrolyte. Nevertheless, the electrode must be porous (porosity varying between 30 and 50 *vol.%*) to support the diffusion of steam (and/or carbon dioxide) and hydrogen (and/or carbon monoxide) during high temperature electrolysis. Depending on the elaboration conditions of the cermet Ni-YSZ, effective electronic conductivities as high as 800-1200 $S.cm^{-1}$ can be reached at 800°*C* [17], allowing an efficient collection of electrons in operating conditions. Accordingly, the cermet Ni-YSZ is presently the cathode material widely used in SOECs [10, 14], as shown in Table 2-1. In order to avoid the reoxidation of Ni to NiO, which can result in a mechanical failure of the cermet layer [18–20], small amounts of hydrogen are required at the cathode side (during operating steps without polarization, *i.e.* without $H_2$ production). Furthermore, some studies have reported on the degradation of the Ni-YSZ cermet during long-term wet conditions [21–23] . This is accompanied by a coarsening of the Ni particles in the cermet yielding a decrease in density of active sites (TPBls) [24].

It is worth mentioning that only few studies have been devoted to the use of new cathode materials in $H_2O$ (and/or $CO_2$) electrolysis applications. The electrochemical behavior of mixed conducting Ni-SDC was evaluated [25]. The results of Marina *et al.* [26] suggest that strontium-doped lanthanum titanate-ceria composites seem to be more active than Ni-YSZ. Recently, $La_{0.75}Sr_{0.25}Cr_{0.5}Mn_{0.5}O_3$ (LSCM) has been proposed as an alternative cathode material for steam electrolysis [27]. However, the current collection must be improved since the effective conductivity is low in reducing environments.

### 2.1.3. Oxygen Electrode

In SOEC mode, the oxygen electrode operates in a highly oxidizing atmosphere. Accordingly, only conducting oxides are suitable materials for such an electrode. Strontium-doped lanthanum manganite $La_{1-x}Sr_xMnO_3$ (LSM) is the oldest electrode material commercially used for SOFCs. In order to increase the number of active sites for the oxidation of oxygen ions, LSM is mixed with the electrolyte material and the most common material for an oxygen electrode is the composite LSM-YSZ [28–30]. Note that the TEC of LSM is close to that of YSZ, thus ensuring the integrity of the cell. Moreover, the chemical reactivity between LSM and YSZ is rather low especially at high $O_2$ partial pressure and this should extend the lifetime during operation.

Despite a good stability, LSM-based anodes may not appear optimal for high temperature electrolysis [31]. Thus, alternative materials for oxygen electrodes have been proposed over the past few years, including mixed ionic and electronic conductors (MIECs), like strontium-doped lanthanum ferrite (LSF) [32], strontium-doped lanthanum copper-ferrite (LSCuF) [10], strontium-doped lanthanum cobalt-ferrite (LSCoF) [33], strontium-doped lanthanum cobaltite (LSC) [34] and more recently strontium-doped barium cobalt-ferrite (BSCF) [35]. Among these materials, strontium-doped lanthanum cobaltite (LSC) and strontium-doped lanthanum cobalt-ferrite (LSCF) present lower polarization losses than LSM by operating as an SOEC anode [32, 36–38]. The performances of BSCF decrease during high temperature electrolysis because of a change in microstructure. The chemical stability of BSCF must be improved and durability studies must be performed prior to any application as a SOEC anode. Solid state reactions have been evidenced between LSC (LSCF) and YSZ, resulting in lower cell performances [39–41]. Such a reactivity is alleviated by adding a barrier diffusion layer between strontium-doped lanthanum based oxides and YSZ [42] such as CGO or YDC. Recently, a great interest has been devoted to the $K_2NiF_4$ structure type materials showing high electrocatalytic activity and ionic conductivity in SOEC operating conditions [43].

## 2.2. Recent Experimental Developments

### 2.2.1. Performances

SOFC have first been shown to operate in a reversed mode (*i.e.* SOEC) by Doenitz *et al.* on tubular cells [16, 44]. Up to now, several studies have been dedicated to assess performances and durability in electrolysis mode, both being the main elements of evaluation of the technology marketability. Table 2-1 summarizes some pertinent results concerning high temperature electrolysis of $H_2O$, $CO_2$ and co-electrolysis of $H_2O + CO_2$. It is worth mentioning that very few reports can be directly compared as the experimental conditions greatly differ.

Several studies demonstrated the technology feasibility of co-electrolysis on 10-cell stacks with total active surfaces varying from 640 $cm^2$ [45, 46] to 922 $cm^2$ [47]. As observed in Table 2-1, references on steam electrolysis greatly outnumber the combined studies of $CO_2$ electrolysis and co-electrolysis. Nevertheless, one can note that co-electrolysis performances are between those of steam and $CO_2$ electrolysis. But a consensus has yet to be found on whether or not co-electrolysis performances would be closer to steam or to $CO_2$ electrolysis. Indeed, various studies show that similar performances can be obtained in steam electrolysis or in co-electrolysis in specific operating conditions [48–50]. For instance, Graves *et al*. [50] reported that initial co-electrolysis performances (ASR = 0.22 $\Omega.cm^2$ at 850°*C* under 25/25/25/25 *vol.%* $H_2O/H_2/CO_2/CO$) on a cathode supported Ni-YSZ/YSZ/LSM-YSZ cell are very close to those obtained under steam (ASR = 0.20 $\Omega.cm^2$ at 850°*C* under 50/50 *vol.%* $H_2O/H_2$). This result seems to be consistent with other studies demonstrating the feasibility of the direct electro-reduction of $CO_2$ in CO at high temperature [48, 51–53]. However, according to Zhan *et al* [54], the co-electrolysis performances would be significantly lower than those obtained with pure steam. The reasons for this result would lie on an easier diffusion process of $H_2/H_2O$ compared to $CO/CO_2$ in a porous electrode and on a faster charge transfer for the steam reduction.

Nevertheless, only limited understanding and knowledge are available on the co-electrolysis elementary mechanisms. For instance, the amounts of CO produced by co-electrolysis and by the reverse WGS reaction would strongly depend on operating conditions (temperature, operating voltage, $H_2O/CO_2$ inlet ratio, *etc*.) [55].

| **Cell electrodes and thicknesses** | | | | | | **Active area** | | | **Mode** | **T** | **Composition** | **Flow** | **Performances*** | | **Degradation** | | | | **Ref.** |
|---|---|---|---|---|---|---|---|---|---|---|---|---|---|---|---|---|---|---|---|
| Fuel electrode | | Electrolyte | | $O_2$ electrode | | Cells | $S_{one\ cell}$ | $S_{tot}$ | | | | NmL. | $i^{(0)}$ | $U^{(1)}$ | $i$ | SC(2) | time | deg. | |
| *Material* | *µm* | *Material* | *µm* | *Material* | *µm* | *Nb.* | *cm²* | *cm²* | | *°C* | *%volume* | *min$^{-1}$cm$^{-2}$* | *A/cm²* | *V* | *A/cm²* | *%* | *h* | *%U.kh$^{-1}$* | |
| Ni-YSZ | 400+10(3) | 8YSZ | 10 | LSM-YSZ | 30-40 | 30 | 10×10 | 3.000 | $H_2O$ elec. | 800 | 80/20 $H_2O/H_2$ | | -0.3 | 1.58 | -0.15 | 62 | 1100 | 11.7 | [56] |
| Ni-YSZ | 1500 | 8YSZ | 10 | CGO/LSCF | 5+40 | 1 | Ø7.6 | 45 | $H_2O$ elec. | 772 | 80/9.2/10.8 $H_2O/H_2/N_2$ | 24.2 | -1.5 | 1.2 | -1 | 36 | 9300 | 3.8 | [57] |
| Ni-YSZ | 1500(4) | YSZ | | LSCF | | 2 | 80 | 160 | SOFC | 750 | 18/82 $H_2O/H_2$ | 10.6 | | | +0.5 | 40 | 3820 | -0.6 | [58] |
| | | | | | | | | | $H_2O$ elec. | 810 | 50/50 $H_2O/H_2$ | 27.5 | -0.8 | 1.2 | -0.3 | 15 | 2034 | -0.2 | |
| | | | | | | | | | Co-elec. | 760 | 25/25/50 $H_2O/CO_2/H_2$ | 27.5 | | | -0.3 | 15 | 174 | 1.0 | |
| Ni-YSZ/ScSZ | 680+15(3) | ScSZ | 20 | LSM-ScSZ | 15 | 1 | Ø1.3 | 1.33 | $CO_2$ elec. | 750 | 50/50 $CO_2/CO$ | 226 | -0.3 | 1.4 | | | | | [59] |
| Ni-YSZ/ScSZ | 680+15(3) | ScSZ | 20 | LSM-ScSZ | 15 | 1 | Ø1.3 | 1.33 | Co-elec. | 750 | 29/29/14/29 $H_2O/CO_2/H_2/Ar$ | 263 | -0.43 | 1.35 | | | | | [60] |
| Ni-YSZ | 300+15(3) | YSZ | 15 | LSM-YSZ | 20 | 1 | 4×4 | 16 | $H_2O$ elec. | 850 | 50/50 $H_2O/H_2$ | 26 | -1.15 | 1.25 | | | | | [50] |
| | | | | | | | | | Co-elec. | | 25/25/25/25 $H_2O/CO_2/H_2/CO$ | | -1 | 1.25 | | | | | |
| | | | | | | | | | $CO_2$ elec. | | 50/50 $CO_2/CO$ | | -0.85 | 1.25 | | | | | |
| | | | | | | | | | Co-elec. | | 45/45/10 $H_2O/CO_2/H_2$ | | | | -0.5 | 15 | 200 | 0.1*mV.h$^{-1}$* | |
| | | | | | | | | | | | | | | | -1 | 30 | 200 | 1*mV.h$^{-1}$* | |
| Ni-YSZ | 300+15(3) | YSZ | 15 | LSM-YSZ | 20 | 1 | 4×4 | 16 | $H_2O$ elec. | 850 | 50/25/25 $H_2O/H_2/Ar$ | | -1.05 | 1.3 | | | | | [61] |
| | | | | | | | | | Co-elec. | | 25/25/25/25 $H_2O/CO_2/CO/Ar$ | | -0.90 | 1.3 | | | | | |
| | | | | | | | | | $CO_2$ elec. | | 50/25/25 $CO_2/CO/Ar$ | | -0.84 | 1.3 | | | | | |
| Ni-YSZ | | YSZ | 150(5) | LSM | | 10 | 8×8 | 640 | $H_2O$ elec. | 800 | 55/22.5/22.5 $H_2O/H_2/N_2$ | 3.13 | -0.35 | 1.35 | | | | | [45] |
| | | | | | | | | | Co-elec. | 800 | 55/22.5/22.5 $H_2O/CO_2/N_2$ | | -0.35 | 1.35 | | | | | |
| | | | | | | | | | $CO_2$ elec. | 800 | 100 $CO_2$ | 2.34 | -0.12 | 1.3 | | | | | |
| Ni-YSZ | | YSZ | | LSM-YSZ | | 10 | 9.6×9.6 | 922 | $H_2O$ elec. | 850 | 50/50 $H_2O/H_2$ | 20 | -0.25 | 1.05 | -0.25 | 17 | 900 | 250*mV.kh$^{-1}$* | [47] |
| | | | | | | | | | Co-elec. | 850 | 45/45/10 $H_2O/CO_2/H_2$ | 6.5 | -0.65 | 1.2 | -0.5 | 60 | 800 | 190*mV.kh$^{-1}$* | |
| | | | | | | | | | | | | | | | -0.75 | 60 | 350 | 100*mV.kh$^{-1}$* | |

Table 2-1: Overview of some performances and degradations reports in recent literature

*: Performances taken at the maximum of a typical polarization curve

(0): In case of a stack, the indicated current density corresponds to the stack current divided by the active area of one cell

(1): In case of a stack, the indicated voltage corresponds to the stack voltage divided by the number of cell

(2): Steam conversion for steam electrolysis, $CO_2$ conversion in $CO_2$ electrolysis, $H_2$ conversion in SOFC, global conversion ($H_2O+CO_2$) for co-electrolysis

(3): Functional layer (4): Total average cell thickness (5): Electrolyte supported cell

## 2.2.2. Durability and Degradation

### 2.2.2.1. Experimental Reports

There are large discrepancies in experimental conditions and degradation reports, regardless of the operating mode (Table 2-1). Still, degradation rates experienced by cells operating in co-electrolysis seem to be more severe than for steam electrolysis, as investigated by Nguyen *et al.* [58]. These authors compared the voltage evolution of a two Ni-YSZ/YSZ/CGO/LSCF cells stack operating in $H_2O$ electrolysis, $CO_2$ electrolysis and co-electrolysis, and showed that the voltage degradation is a bit higher in co-electrolysis compared to steam electrolysis. At 760°*C* and 15% reactant utilization, degradations rates comprised between 0.5 and 1.5%.$kh^{-1}$ for 50/50 *vol.%* $H_2/H_2O$ steam electrolysis and between 1.0 and 6.1%.$kh^{-1}$ ($\Delta U/U$) for 25/25/50 *vol.%* $H_2O/CO_2/H_2$ co-electrolysis were recorded. Furthermore, whatever the operating mode, degradation rates have been reported to level off after a few hundred hours of operation [62, 47, 58].

It should be noted that some research groups have investigated performances and degradations of cells fed with $CO_2$+$H_2$ inlet mixture [58]. However, it is unclear if such inlet mixtures would lead to $CO_2$ electrolysis or $H_2O$ electrolysis subsequent to the WGS reaction. Most probably, the reality would lie somewhere between these two extremes. For that reason, these reports are not included in Table 2-1 and this section.

Over long term measurements, cells operating in co-electrolysis should degrade following some of the same mechanisms, if not all, than in steam electrolysis. Since the present work is not focused on durability, the degradation mechanisms are not detailed here. The reader can refer to references [10, 14, 63–65] for an overview on the most liable phenomena that could drive the degradation in electrolysis performances.

Only a short report is presented in the next section on the risk of carbon deposition that arises in the specific cases of $CO_2$ or co-electrolysis operations.

#### 2.2.2.2. Carbon Deposition

During $CO_2$ electrolysis or co-electrolysis operation, carbon deposition may occur. This phenomenon is governed by local gas composition in the cathode, and operating conditions (temperature, pressure, inlet gas flow, conversion rate). Figure 2-1 displays a ternary C-O-H diagram under 1 *atm* with the carbon deposition regions depending on the temperature [66]. In $CO/CO_2$ mixtures under atmospheric pressure, only CO contents superior to 85% would favor carbon deposition. It should be noted that the local CO content is to be considered when evaluating carbon deposition. Indeed, in case of $CO_2$ electrolysis, high global conversion rates would translate into higher CO contents in the vicinity of active sites. This arises from the diffusion process limitation through the cathode: as $CO_2$ is consumed near the electrolyte interface, its concentration is a decreasing function of the electrode thickness (considering the thickness takes its origin at the gas channel/cathode interface). Shi *et al.* [59] have indeed measured that carbon deposition is a decreasing function of the distance from the electrolyte interface.

The addition of steam in co-electrolysis operation significantly reduces risks associated with carbon deposition. However, at higher current density, if diffusion is hindered by insufficient porosity, local reducing atmosphere can favor carbon deposition near the electrolyte [67]. As previously stated (section 1.4), it becomes obvious here that if carbon deposition occurs (Reactions (1-10) and (1-11)), the catalyst (commonly nickel) could be deactivated. The density of TPBls would thus be decreased, severely impacting electrochemical performances.

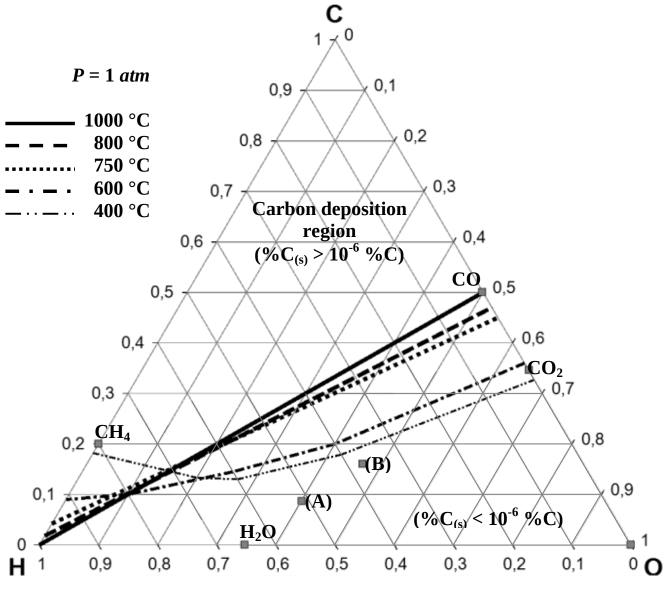

Figure 2-1: Ternary C-O-H diagram at 1 *atm* [66] with typical co-electrolysis inlet compositions: (A) 65/25/10 *vol.%* and (B) 45/45/10 *vol.%* of $H_2O/CO_2/H_2$.

## 2.3. Modeling Studies

Computational simulation appears to be one efficient approach to analyze the coupled mechanisms of HTSE. Indeed, the cell response depends on entangled multi-physics phenomena such as electrochemical reactions, as well as mass and energy transport in the electrolyzer. Furthermore, all chemical and electrochemical source terms are linked to the local temperature field throughout the SOEC. Steam electrolysis has been widely modeled because this approach allows the identification of governing factors within the deeply interconnected phenomena occurring inside a SOC. Conversely, very few studies have been dedicated to the modeling of $CO_2$ electrolysis and/or co-electrolysis of $H_2O$ and $CO_2$. This section aims at giving an overview of the published models. It should be noted that the approach followed to simulate SOEC is usually very similar to the one used to investigate the SOFC response.

Some models were recently developed to describe the HTSE. Ni *et al.* [55, 68] proposed isothermal models taking into account the coupled mass transport and electrochemical reactions. A 2D multi-physics in-house-model has been developed by Laurencin *et al.* [69] to analyze the performances of a SRU or a stack. This model encompasses a combined electrochemical and thermal description of the electrolyzer, where the mass transport through the porous electrodes has been computed in the frame of the dusty-gas-model (DGM). More recently, Udagawa *et al.* [70, 71] developed a one dimensional dynamic model including a thermal analysis. A 2D in-house Computational Fluid Dynamic (CFD) model has been proposed by Ni [72] for a better understanding of HTSE operation. This approach can serve for design optimization and was extended to a 3D model [73, 74] by using a commercial CFD software. Grondin *et al.* [75] developed a “local” model focused on the cathode response and identified an electrochemical process that should be limited by the adsorption of water molecules. Lay *et al.* [24] also developed a “local” anode model and the authors shown that the kinetic response of a LSM-YSZ oxygen electrode could be controlled by a charge transfer followed by an $O_2$ desorption step.

In co-electrolysis mode, thermodynamic investigations have also been carried out on the effect of temperature, pressure and inlet composition on the outlet gas and performances [58, 76]. Stoots *et al.* [45] have developed a chemical equilibrium co-electrolysis model to determine the co-electrolyzer outlet composition. The simulations show remarkable agreement with experimental CO, $CO_2$ and $H_2$ contents measured by gas analyses, up to the maximum cell current density investigated of 0.24 $A.cm^{-2}$. After investigating $CO_2$ electrolysis [77], Ni *et al.* [55, 78] have recently developed a kinetic model taking into account the $CO_2$ electro-reduction and the reverse water gas shift reaction. These authors have shown that the WGS reaction can either produce or consume CO depending on the cell inlet gas stream composition, cell temperature and operating voltage.

Furthermore, based on the initial work of Hecht *et al.* [79] in a SOFC mode, some recent studies were focused on finding limiting elementary steps among extensive electrochemical pathways concerning the co-electrolysis [80, 81] or $CO_2$ electrolysis process [59]. It is worth mentioning that all these studies assume that the reaction pathway in electrolysis anodic polarization is the same than the one proposed in fuel cell cathodic polarization. The authors proposed pathways respectively divided in 10 [59], 18 [80] and 21 [81] elementary reactions. They calibrated their models on experimental polarization curves. Furthermore, Yurkiv *et al.* [82] highlighted that CO oxidation on Ni-YSZ electrodes may be subjected to a change in rate-determining step depending on CO partial pressure. Despite these findings, no clear consensus seems to emerge concerning the co-electrolysis mechanisms.

Additionally, no consensus arises from the literature concerning the influence of the WGS reaction on CO production in a co-electrolyzer. Indeed, several models are based on the hypothesis that all CO is chemically produced through the reverse WGS reaction [45, 58, 83]. Conversely, Ni *et al.* [55] shown that the WGS reaction accounts for large shifts in CO production, but that the electrochemical production remains preponderant. This lack of agreement has led Sun *et al.* [76] to combine a fast and dominant WGS kinetics along with a fixed electrochemical utilization for both $H_2O$ and $CO_2$ when simulating a co-electrolyzer.

# 2.4. References

1. M. Mori, Thermal Expansion of Nickel-Zirconia Anodes in Solid Oxide Fuel Cells during Fabrication and Operation, *J. Electrochem. Soc.* 145, 1374 (**1998**).
2. N. H. Menzler, F. Tietz, S. Uhlenbruck, H. P. Buchkremer, and D. Stöver, Materials and manufacturing technologies for solid oxide fuel cells, *J. Mater. Sci.* 45, 3109 (**2010**).
3. C.-K. Lin, T.-T. Chen, Y.-P. Chyou, and L.-K. Chiang, Thermal stress analysis of a planar SOFC stack, *J. Power Sources* 164, 238 (**2007**).
4. J. E. O'Brien, C. M. Stoots, J. S. Herring, and J. J. Hartvigsen, Performance of Planar High-Temperature Electrolysis Stacks for Hydrogen Production from Nuclear Energy, *Nucl. Technol.* 158, 118 (**2007**).
5. M. Ni, M. K. H. Leung, and D. Y. C. Leung, Technological development of hydrogen production by solid oxide electrolyzer cell (SOEC), *Int. J. Hydrog. Energy* 33, 2337 (**2008**).
6. C. Haering, A. Roosen, H. Schichl, and M. Schnoller, Degradation of the electrical conductivity in stabilised zirconia systemPart II: Scandia-stabilised zirconia, *Solid State Ion.* 176, 261 (**2005**).
7. K. Eguchi, Power generation and steam electrolysis characteristics of an electrochemical cell with a zirconia- or ceria-based electrolyte, *Solid State Ion.* 86-88, 1245 (**1996**).
8. V. Kharton, F. Marques, and A. Atkinson, Transport properties of solid oxide electrolyte ceramics: a brief review, *Solid State Ion.* 174, 135 (**2004**).
9. P. Kim-Lohsoontorn, N. Laosiripojana, and J. Bae, Performance of solid oxide electrolysis cell having bi-layered electrolyte during steam electrolysis and carbon dioxide electrolysis, *Curr. Appl. Phys.* 11, S223 (**2011**).
10. M. A. Laguna-Bercero, Recent advances in high temperature electrolysis using solid oxide fuel cells: A review, *J. Power Sources* 203, 4 (**2012**).
11. V. V. Kharton, A. L. Shaula, N. P. Vyshatko, and F. M. B. Marques, Electron-hole transport in (La0.9Sr0.1)0.98Ga0.8Mg0.2O3−δ electrolyte: effects of ceramic microstructure, *Electrochimica Acta* 48, 1817 (**2003**).
12. K. Huang and J. B. Goodenough, A solid oxide fuel cell based on Sr- and Mg-doped LaGaO3 electrolyte: the role of a rare-earth oxide buffer, *J. Alloys Compd.* 303-304, 454 (**2000**).
13. X. Zhang, Interface reactions in the NiO–SDC–LSGM system, *Solid State Ion.* 133, 153 (**2000**).
14. P. Moçoteguy and A. Brisse, A review and comprehensive analysis of degradation mechanisms of solid oxide electrolysis cells, *Int. J. Hydrog. Energy* 38, 15887 (**2013**)
15. O. Yamamoto, Solid oxide fuel cells: fundamental aspects and prospects, *Electrochimica Acta* 45, 2423 (**2000**).
16. W. Doenitz, R. Schmidberger, E. Steinheil, and R. Streicher, Hydrogen production by high temperature electrolysis of water vapour, *Int. J. Hydrog. Energy* 5, 55 (**1980**).
17. D. Simwonis, Nickel coarsening in annealed Ni/8YSZ anode substrates for solid oxide fuel cells, *Solid State Ion.* 132, 241 (**2000**).

18. J. Laurencin, G. Delette, B. Morel, F. Lefebvre-Joud, and M. Dupeux, Solid Oxide Fuel Cells damage mechanisms due to Ni-YSZ re-oxidation: Case of the Anode Supported Cell, *J. Power Sources* 192, 344 (**2009**).
19. J. Laurencin, G. Delette, O. Sicardy, S. Rosini, and F. Lefebvre-Joud, Impact of “redox” cycles on performances of solid oxide fuel cells: Case of the electrolyte supported cells, *J. Power Sources* 195, 2747 (**2010**).
20. F. Abdeljawad and M. Haataja, Microstructural coarsening effects on redox instability and mechanical damage in solid oxide fuel cell anodes, *J. Appl. Phys.* 114, 183519 (**2013**).
21. H. Yokokawa, H. Tu, B. Iwanschitz, and A. Mai, Fundamental mechanisms limiting solid oxide fuel cell durability, *J. Power Sources* 182, 400 (**2008**).
22. A. Hauch, M. Mogensen, and A. Hagen, Ni/YSZ electrode degradation studied by impedance spectroscopy: Effect of p(H2O), *Solid State Ion.* In Press, Corrected Proof (**2011**).
23. T. Matsui, R. Kishida, H. Muroyama, and K. Eguchi, Comparative Study on Performance Stability of Ni-Oxide Cermet Anodes under Humidified Atmospheres in Solid Oxide Fuel Cells, *J. Electrochem. Soc.* 159, F456 (**2012**).
24. E. Lay-Grindler, J. Laurencin, G. Delette, J. Aicart, M. Petitjean, and L. Dessemond, Micro modelling of solid oxide electrolysis cell: From performance to durability, *Int. J. Hydrog. Energy* 38, 6917 (**2013**).
25. N. Osada, H. Uchida, and M. Watanabe, Polarization Behavior of SDC Cathode with Highly Dispersed Ni Catalysts for Solid Oxide Electrolysis Cells, *J. Electrochem. Soc.* 153, A816 (**2006**).
26. O. A. Marina, L. R. Pederson, M. C. Williams, G. W. Coffey, K. D. Meinhardt, C. D. Nguyen, and E. C. Thomsen, Electrode Performance in Reversible Solid Oxide Fuel Cells, *J. Electrochem. Soc.* 154, B452 (**2007**).
27. X. Yang and J. T. S. Irvine, (La0.75Sr0.25)0.95Mn0.5Cr0.5O3 as the cathode of solid oxide electrolysis cells for high temperature hydrogen production from steam, *J. Mater. Chem.* 18, 2349 (**2008**).
28. M. Liang, B. Yu, M. Wen, J. Chen, J. Xu, and Y. Zhai, Preparation of LSM–YSZ composite powder for anode of solid oxide electrolysis cell and its activation mechanism, *J. Power Sources* 190, 341 (**2009**).
29. A. Hauch, S. D. Ebbesen, S. H. Jensen, and M. Mogensen, Highly efficient high temperature electrolysis, *J. Mater. Chem.* 18, 2331 (**2008**).
30. W. Wang and S. Jiang, A mechanistic study on the activation process of (La, Sr)MnO3 electrodes of solid oxide fuel cells, *Solid State Ion.* 177, 1361 (**2006**).
31. X. J. Chen, S. H. Chan, and K. A. Khor, Defect Chemistry of La[sub 1−x]Sr[sub x]MnO[sub 3±δ] under Cathodic Polarization, *Electrochem. Solid-State Lett.* 7, A144 (**2004**).
32. W. Wang, Y. Huang, S. Jung, J. M. Vohs, and R. J. Gorte, A Comparison of LSM, LSF, and LSCo for Solid Oxide Electrolyzer Anodes, *J. Electrochem. Soc.* 153, A2066 (**2006**).
33. M. A. Laguna-Bercero, J. A. Kilner, and S. J. Skinner, Performance and Characterization of (La, Sr)$MnO_3$ /YSZ and $La_{0.6}Sr_{0.4}Co_{0.2}Fe_{0.8}O_3$ Electrodes for Solid Oxide Electrolysis Cells $^{\dagger}$, *Chem. Mater.* 22, 1134 (**2010**).
34. V. I. Sharma and B. Yildiz, Degradation Mechanism in La 0.8Sr0.2CoO3 as Contact Layer on the Solid Oxide Electrolysis Cell Anode, *J. Electrochem. Soc.* 157, B441 (**2010**).

35. Y.-M. Kim, P. Kim-Lohsoontorn, S.-W. Baek, and J. Bae, Electrochemical performance of unsintered Ba0.5Sr0.5Co0.8Fe0.2O3−δ, La0.6Sr0.4Co0.8Fe0.2O3−δ, and La0.8Sr0.2MnO3−δ cathodes for metal-supported solid oxide fuel cells, *Int. J. Hydrog. Energy* 36, 3138 (**2011**).

36. S. Simner, J. Bonnett, N. Canfield, K. Meinhardt, J. Shelton, V. Sprenkle, and J. Stevenson, Development of lanthanum ferrite SOFC cathodes, *J. Power Sources* 113, 1 (**2003**).

37. R. Chiba, Properties of La1−ySryNi1−xFexO3 as a cathode material for a low-temperature operating SOFC, *Solid State Ion.* 152-153, 575 (**2002**).

38. S. P. Simner, J. F. Bonnett, N. L. Canfield, K. D. Meinhardt, V. L. Sprenkle, and J. W. Stevenson, Optimized Lanthanum Ferrite-Based Cathodes for Anode-Supported SOFCs, *Electrochem. Solid-State Lett.* 5, A173 (**2002**).

39. P. Hjalmarsson, M. Søgaard, and M. Mogensen, Electrochemical performance and degradation of (La0.6Sr0.4)0.99CoO3−δ as porous SOFC-cathode, *Solid State Ion.* 179, 1422 (**2008**).

40. P. Hjalmarsson, M. Søgaard, and M. Mogensen, Electrochemical behaviour of (La1−xSrx)sCo1−yNiyO3−δ as porous SOFC cathodes, *Solid State Ion.* 180, 1395 (**2009**).

41. Y. Huang, K. Ahn, J. M. Vohs, and R. J. Gorte, Characterization of Sr-Doped LaCoO[sub 3]-YSZ Composites Prepared by Impregnation Methods, *J. Electrochem. Soc.* 151, A1592 (**2004**).

42. L. Adijanto, R. Küngas, F. Bidrawn, R. J. Gorte, and J. M. Vohs, Stability and performance of infiltrated La0.8Sr0.2CoxFe1−xO3 electrodes with and without Sm0.2Ce0.8O1.9 interlayers, *J. Power Sources* 196, 5797 (**2011**).

43. F. Chauveau, J. Mougin, J. M. Bassat, F. Mauvy, and J. C. Grenier, A new anode material for solid oxide electrolyser: The neodymium nickelate Nd2NiO4+δ, *J. Power Sources* 195, 744 (**2010**).

44. W. Doenitz and R. Schmidberger, Concepts and design for scaling up high temperature water vapour electrolysis, *Int. J. Hydrog. Energy* 7, 321 (**1982**).

45. C. Stoots, J. O'Brien, and J. Hartvigsen, Results of recent high temperature coelectrolysis studies at the Idaho National Laboratory, *Int. J. Hydrog. Energy* 34, 4208 (**2009**).

46. C. M. Stoots, J. E. O'Brien, K. G. Condie, L. Moore-McAteer, J. J. Hartvigsen, and D. Larsen, *2500-Hour High Temperature Solid-Oxide Electrolyzer Long Duration Test*, Idaho National Laboratory (INL) (**2009**)

47. S. D. Ebbesen, J. Hogh, K. A. Nielsen, J. U. Nielsen, and M. Mogensen, Durable SOC stacks for production of hydrogen and synthesis gas by high temperature electrolysis, *Int. J. Hydrog. Energy* 36, 7363 (**2011**).

48. P. Kim-Lohsoontorn, N. Laosiripojana, and J. Bae, Performance of solid oxide electrolysis cell having bi-layered electrolyte during steam electrolysis and carbon dioxide electrolysis, *Curr. Appl. Phys.* 11, S223 (**2011**).

49. P. Kim-Lohsoontorn and J. Bae, Electrochemical performance of solid oxide electrolysis cell electrodes under high-temperature coelectrolysis of steam and carbon dioxide, *J. Power Sources* 196, 7161 (**2011**).

50. C. Graves, S. D. Ebbesen, and M. Mogensen, Co-electrolysis of CO2 and H2O in solid oxide cells: Performance and durability, *Solid State Ion.* 192, 398 (**2011**).

51. G. Tao, K. R. Sridhar, and C. L. Chan, Study of carbon dioxide electrolysis at electrode/electrolyte interface: Part I. Pt/YSZ interface, *Solid State Ion.* 175, 615 (**2004**).

52. Z. Zhan and L. Zhao, Electrochemical reduction of CO2 in solid oxide electrolysis cells, *J. Power Sources* 195, 7250 (**2010**).

53. S. D. Ebbesen and M. Mogensen, Electrolysis of carbon dioxide in Solid Oxide Electrolysis Cells, *J. Power Sources* 193, 349 (**2009**).
54. Z. Zhan, W. Kobsiriphat, J. R. Wilson, M. Pillai, I. Kim, and S. A. Barnett, Syngas Production By Coelectrolysis of CO2/H2O: The Basis for a Renewable Energy Cycle, *Energy Fuels* 23, 3089 (**2009**).
55. M. Ni, An electrochemical model for syngas production by co-electrolysis of H2O and CO2, *J. Power Sources* 202, 209 (**2012**).
56. Y. Zheng, Q. Li, W. Guan, C. Xu, W. Wu, and W. G. Wang, Investigation of 30-cell solid oxide electrolyzer stack modules for hydrogen production, *Ceram. Int.* (**2013**)
57. J. Schefold, A. Brisse, and F. Tietz, Nine thousand hours of operation of a solid oxide cell in steam electrolysis mode, *J. Electrochem. Soc.* 159, A137 (**2011**).
58. V. N. Nguyen, Q. Fang, U. Packbier, and L. Blum, Long-term tests of a Jülich planar short stack with reversible solid oxide cells in both fuel cell and electrolysis modes, *Int. J. Hydrog. Energy* 38, 4281 (**2013**).
59. Y. Shi, Y. Luo, N. Cai, J. Qian, S. Wang, W. Li, and H. Wang, Experimental characterization and modeling of the electrochemical reduction of CO2 in solid oxide electrolysis cells, *Electrochimica Acta* 88, 644 (**2013**).
60. W. Li, H. Wang, Y. Shi, and N. Cai, Performance and methane production characteristics of H2O–CO2 co-electrolysis in solid oxide electrolysis cells, *Int. J. Hydrog. Energy* 38, 11104 (**2013**).
61. S. D. Ebbesen, C. Graves, and M. Mogensen, Production of Synthetic Fuels by Co-Electrolysis of Steam and Carbon Dioxide, *Int. J. Green Energy* 6, 646 (**2009**).
62. A. Hauch, S. D. Ebbesen, S. H. Jensen, and M. Mogensen, Solid Oxide Electrolysis Cells: Microstructure and Degradation of the Ni/Yttria-Stabilized Zirconia Electrode, *J. Electrochem. Soc.* 155, B1184 (**2008**).
63. F. Tietz, D. Sebold, A. Brisse, and J. Schefold, Degradation phenomena in a solid oxide electrolysis cell after 9000 h of operation, *J. Power Sources* 223, 129 (**2013**).
64. K. Chen and S. P. Jiang, Failure mechanism of (La,Sr)MnO3 oxygen electrodes of solid oxide electrolysis cells, *Int. J. Hydrog. Energy* 36, 10541 (**2011**).
65. A. V. Virkar, Mechanism of oxygen electrode delamination in solid oxide electrolyzer cells, *Int. J. Hydrog. Energy* 35, 9527 (**2010**).
66. K. Girona, *Modélisation et Validation Expérimentale du Comportement Electrochimique d'une Pile à Combustible SOFC en Reformage Interne de Biocombustible*, (**2009**).
67. Y. Tao, S. D. Ebbesen, and M. B. Mogensen, Carbon Deposition in Solid Oxide Cells during Co-Electrolysis of H2O and CO2, *J. Electrochem. Soc.* 161, F337 (**2014**).
68. M. Ni, M. K. H. Leung, and D. Y. C. Leung, Mathematical modeling of the coupled transport and electrochemical reactions in solid oxide steam electrolyzer for hydrogen production, *Electrochimica Acta* 52, 6707 (**2007**).
69. J. Laurencin, D. Kane, G. Delette, J. Deseure, and F. Lefebvre-Joud, Modelling of solid oxide steam electrolyser: Impact of the operating conditions on hydrogen production, *J. Power Sources* 196, 2080 (**2011**).
70. J. Udagawa, P. Aguiar, and N. P. Brandon, Hydrogen production through steam electrolysis: Model-based steady state performance of a cathode-supported intermediate temperature solid oxide electrolysis cell, *J. Power Sources* 166, 127 (**2007**).

71. J. Udagawa, P. Aguiar, and N. P. Brandon, Hydrogen production through steam electrolysis: Model-based dynamic behaviour of a cathode-supported intermediate temperature solid oxide electrolysis cell, *J. Power Sources* 180, 46 (**2008**).
72. M. Ni, Computational fluid dynamics modeling of a solid oxide electrolyzer cell for hydrogen production, *Int. J. Hydrog. Energy* 34, 7795 (**2009**).
73. J. E. O'Brien, M. G. McKellar, C. M. Stoots, J. S. Herring, and G. L. Hawkes, Parametric study of large-scale production of syngas via high-temperature co-electrolysis, *Int. J. Hydrog. Energy* 34, 4216 (**2009**).
74. T. Boëdec, M. Reytier, D. Lhachemi, D. Tschumperlé, P. Louat, S. Di Iorio, P. Baurens, and G. Delette, A New Stack to Validate Technical Solutions and Numerical Simulations, *Fuel Cells* 12, 239 (**2012**).
75. D. Grondin, J. Deseure, P. Ozil, J.-P. Chabriat, B. Grondin-Perez, and A. Brisse, Computing approach of cathodic process within solid oxide electrolysis cell: Experiments and continuum model validation, *J. Power Sources* 196, 9561 (**2011**).
76. X. Sun, M. Chen, S. H. Jensen, S. D. Ebbesen, C. Graves, and M. Mogensen, Thermodynamic analysis of synthetic hydrocarbon fuel production in pressurized solid oxide electrolysis cells, *Int. J. Hydrog. Energy* 37, 17101 (**2012**).
77. M. Ni, Modeling of a solid oxide electrolysis cell for carbon dioxide electrolysis, *Chem. Eng. J.* 164, 246 (**2010**).
78. M. Ni, 2D thermal modeling of a solid oxide electrolyzer cell (SOEC) for syngas production by H2O/CO2 co-electrolysis, *Int. J. Hydrog. Energy* 37, 6389 (**2012**).
79. E. S. Hecht, G. K. Gupta, H. Zhu, A. M. Dean, R. J. Kee, L. Maier, and O. Deutschmann, Methane reforming kinetics within a Ni–YSZ SOFC anode support, *Appl. Catal. Gen.* 295, 40 (**2005**).
80. W. Li, Y. Shi, Y. Luo, and N. Cai, Elementary reaction modeling of CO2/H2O co-electrolysis cell considering effects of cathode thickness, *J. Power Sources* 243, 118 (**2013**).
81. Y. Xie and X. Xue, Modeling of solid oxide electrolysis cell for syngas generation with detailed surface chemistry, *Solid State Ion.* 224, 64 (**2012**).
82. V. Yurkiv, A. Utz, A. Weber, E. Ivers-Tiffée, H.-R. Volpp, and W. G. Bessler, Elementary kinetic modeling and experimental validation of electrochemical CO oxidation on Ni/YSZ pattern anodes, *Electrochimica Acta* 59, 573 (**2012**).
83. C. M. Stoots, J. E. O'Brien, K. G. Condie, and J. J. Hartvigsen, High-temperature electrolysis for large-scale hydrogen production from nuclear energy - Experimental investigations, *Int. J. Hydrog. Energy* 35, 4861 (**2010**).

# Chapter 3

# Investigation Tools

# Chapter 3

# Investigation Tools

This chapter details the tools implemented to investigate steam electrolysis, $CO_2$ electrolysis and $H_2O+CO_2$ co-electrolysis through a coupled experimental/modeling approach. In the first section, the experimental test bench is detailed, from the cell holder to the gas lines. The different apparatus used in electrochemical and gas composition measurements are also described, as well as the cell startup procedure. The second section is devoted to the model description: hypotheses and governing equations for mass transport, electrochemical and thermal phenomena are presented, along with geometries and materials used for modeling and simulations.

# 3.1. Experimental Setup for Cell Testing

## 3.1.1. Test Bench

The experimental setup used for radial cell testing is sketched in Figure 1 and Figure 2. The cell was placed in a 50 *mm* diameter alumina housing between two alumina plates providing the connections to the gas delivery system. Gold and platinum grids (with a mesh density of 100 and 3600 $meshes.cm^{-2}$ respectively) ensured the current collection at the anode side. The finer platinum grid, in contact with the electrode, provided improved contacts. A nickel grid of 50 *mm* in diameter (with a mesh density of 100 $meshes.cm^{-2}$) was used at the cathode side. Note that it was not necessary to add a finer grid at the cathode side because of the good electrical conductivity of the Ni-YSZ cermet. Four gold wires welded to the grids allow direct cell voltage measurements and current supply (Figure 3-1). Both anode and cathode gases were supplied to the cell from the center of the housing and flowed through the grid meshes (assuming the function of gas channels) according to a radial co-flow configuration. The cell holder was designed so that the pressure drop in the compartment that ensured gases collection at the cell outlet was negligible compared to the one that arises through the current collecting meshes, thus yielding a homogenous radial gas distribution. Ceramic glass sealing (Schott G018-311) was deposited on the edge of the cell to provide gas tightness between both anodic and cathodic compartments in operation. Additionally, a weighted alumina ring was positioned on the sealing agent. It acted as a casing for the ceramic glass, thus improving gas tightness. At the cathode side, gases were collected while the anodic ones were directly released in the furnace. Mechanical pressure was applied from outside of the furnace onto the grids to improve electrical contacts. The test bench control elements were managed by a Rockwell automate combined with the supervision software RSView® for collecting and archiving all data. Furthermore, some tasks were automated (*e.g.* heating ramp, current or voltage ramps, *etc.*) and security alarms were set up.

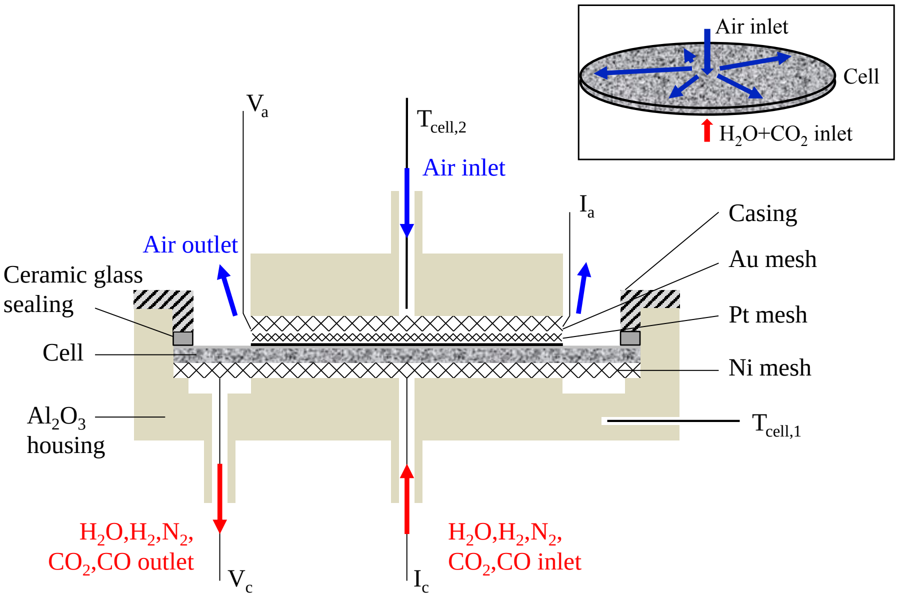

Figure 3-1: Description of the experimental setup in the vicinity of the cell.

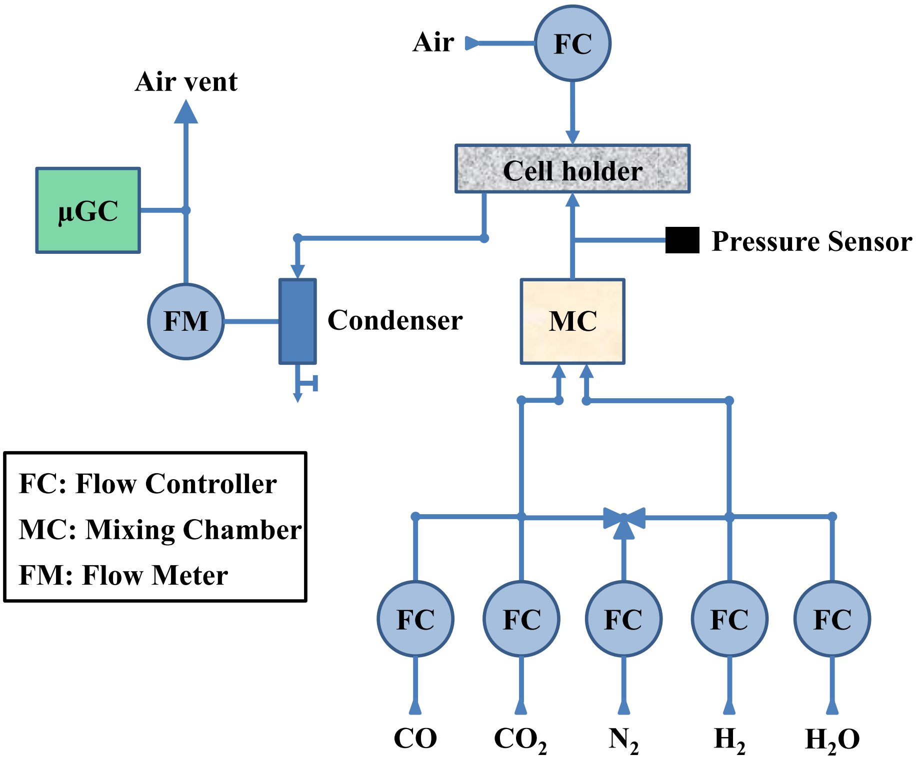

Figure 3-2: Schematic of the complete test bench.

### 3.1.2. Gas Lines, Steam Generation and Gases Purity

The test bench was designed to investigate SOFC, $H_2O$ electrolysis, $CO_2$ electrolysis and co-electrolysis operating modes. Thus, there were 6 gas lines corresponding to:

- Anode side: Air as sweeping gas
- Cathode side: $H_2$, $H_2O$, $CO_2$, CO, $N_2$

All gas lines were equipped with electrovalves and check valves and flows were controlled with mass flow controllers (Brooks Instrument 5850S).

All gases converged toward a mixing chamber, allowing for homogeneous mixing before reaching the cell. Due to some dead space in the test bench when operating in single $H_2O$ electrolysis mode, nitrogen was systematically added to the inlets.

Several studies [1, 2] have shown that impurities contained in the inlet gas can cause severe cell degradation. Thus, gas purity could be a significant factor, especially when studying cell behavior over long periods. The following Table 3-1 summarizes the characteristics of the different gases used. For all experiments carried out in this work, class 1 ISO 8573-1 pressurized air was used at the anode side.

| **Gas** | **Purity** | **Supplier** | **Impurities (*vol-ppm*)** | | | | | | | | | |
|---|---|---|---|---|---|---|---|---|---|---|---|---|
| | | | Ar | $CO_2$ | $O_2$ | $N_2$ | $H_2O$ | $H_2$ | HC ($C_1$-$C_4$) | CO | NOx | $H_2S$ |
| $H_2$ | 3.5 | Air Products | | | <10 | | <10 | | | | | |
| $N_2$ | 4.8 | Air Products | | | <5 | | <3 | | | | | |
| CO | 4.5 | Air Liquide | <7 | <1 | <5 | <10 | <3 | <1 | <2 | | | |
| $CO_2$ | 4.5 | Air Products | | | <3 | | <5 | | | <5 | <2 | <1 |

Table 3-1: Available characteristics of gases used in electrolysis investigations.

### 3.1.3. Safety Concerns Related to Gases

Several safety concerns arise from the different gases used to investigate co-electrolysis. Indeed, $H_2$ induces ATEX risks (Explosive Atmosphere). Under 600°$C$ (temperature of autoignition in air), mixtures containing between 4% and 75% of $H_2$ in air can explode. Therefore, several procedures were implemented to limit $H_2$ concentration under 3% at low temperature. Furthermore, a gas leaking in the test room could replace the oxygen and cause anoxia. Whereas there is about 21% of oxygen in the air, risk of anoxia starts when this level drops below 18.5%. Finally, CO is a colorless and odorless virulent poison, even at low concentrations. As can be seen in Figure 3-3, a few minutes of exposure to higher CO contents can be deadly.

To tackle these concerns, the test room was therefore equipped with numerous detectors (CO, $H_2$ and $O_2$). Additionally, when using or producing CO, personal portable detector were used. Finally, the room ventilation was designed to regularly replace the full volume of air, thus limiting any risks.

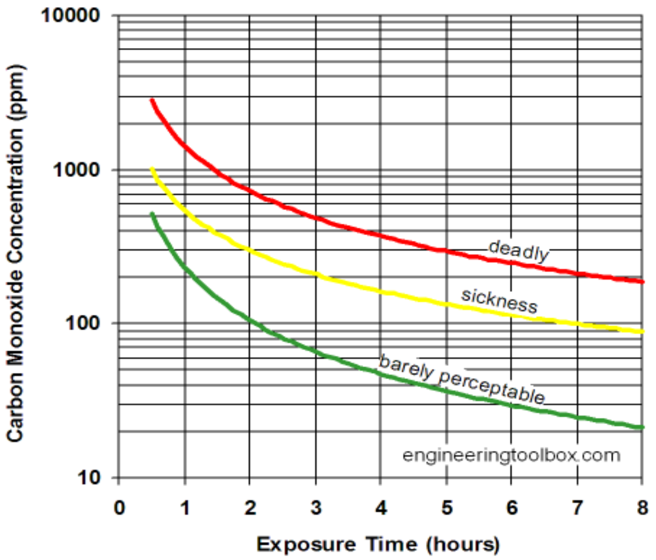

Figure 3-3:
Health effects of carbon monoxide [3].

## 3.1.4. Measuring Equipment

Most of the experimental data presented in this work are polarization curves (*i*-*V*), gas analyses and electrochemical impedance spectroscopy measurements. This section details the different apparatus used in this work.

### 3.1.4.1. Polarization curves

Electrochemical performances were studied in a galvanostatic mode using a potentiostat/galvanostat (PGSTAT-302N Autolab), equipped with a FRA2 module and a 10 *A* booster. However, when testing cells of large active areas (*e.g.* 9.08 $cm^2$ for a radial cell of 34 *mm* diameter), the current was supplied using a Xantrex XPD 33-16 DC power supply. Most of *i*-*V* curves were recorded at a sweep rate of 10 $mA.s^{-1}$. However, in order to save time, a sweep rate of 25 $mA.s^{-1}$ was set to obtain polarization curves under high cathodic flows. Initial experiments confirmed that increasing the sweep rate from 10 to 25 $mA.s^{-1}$ had no impact in the chosen conditions.

### 3.1.4.2. Gas analyses

Cell outlet compositions were determined by micro gas chromatography (μGC) using an SRA R-3000 apparatus, equipped with a thermal conductivity detector and two separating columns. The first column was equipped with a molecular sieve 10 *m*-MS5A with backflush injection and Ar as carrier gas. It allowed the identification of $H_2$, $O_2$, $N_2$, $CH_4$ and CO. The second column was a 8 *m*-Paraplot U with variable injection. Feeded with He, it detected $CO_2$, ethane, propane and other heavier hydrocarbons. Characteristics of carrier gases are given in Table 3-2. It is worth noting that exhaust gas compositions were analyzed by μGC after steam/water removal, to avoid condensation in the columns. Thus, a condenser was placed at the cathode outlet (Figure 3-2), and the chromatograph was equipped with a water filter.

| **Gas** | **Purity** | **Supplier** | **Impurities (*vol-ppb*)** | | | | | |
|---|---|---|---|---|---|---|---|---|
| | | | $CO + CO_2$ | $O_2$ | $N_2$ | $H_2O$ | $H_2$ | THC ($C_1$-$C_4$) |
| He | 6.0 | Air Products | <100 | <100 | <100 | <500 | NA | <100 |
| Ar | 6.0 | Air Liquide | <10 | <100 | <300 | <600 | <10 | <50 |

Table 3-2: Characteristics of carrier gas used in micro gas chromatography analyses.

### 3.1.4.3. Electrochemical Impedance Spectroscopy (EIS)

Table 3-3 gathers frequency range, number of frequencies and other relevant parameters used to record classic scans. It should be emphasized that all measurements were performed in the linear part of polarization curves while keeping the ratio measure to noise sufficiently high (*e.g.* typical current amplitude is 50 *mA*). The software NOVA (v. 1.10) was used as interface with the apparatus.

| **Frequency range (Hz)** | **Number of frequencies** | **Integration time** | **Integration cycle** |
|---|---|---|---|
| 20.000 - 0.01 | 99 | 2s | 1 |
| **Stabilization time** | **Frequency step** | **Wave type** | **RMS** |
| 120 s | logarithmic | Single sine | No |

Table 3-3: Classical conditions for EIS scan recording.

## 3.1.5. Cell Startup Procedures

Before any electrochemical measurements, the following procedures were systematically implemented:

- test bench tightness evaluation
- temperature changes and glass ceramic sealing procedure
- cermet reduction
- mechanical load optimization.

#### 3.1.5.1. Test bench tightness evaluation

The total test bench volume was initially determined using the ideal gas law, a pressure sensor and a chronometer: by closing the outlet gas pipe just before the air vent (Figure 3-2) and measuring the time $\Delta t$ corresponding to a pressure increase $\Delta P$ induced by a known $N_2$ flow, the bench volume could be assessed. Consequently, prior to each cell testing, the leakage rate (function of the volume) was consistently measured to evaluate the tightness of the setup. The maximum acceptable leakage was set to 1 $mbar.L.min^{-1}$ at $\Delta P = 30$ $mbars$, which corresponds roughly to 1% of total flows fed to the cathode during electrochemical measurements at $\Delta P_{operation} \approx 2$ $mbars$.

#### 3.1.5.2. Temperature changes and glass ceramic sealing procedure

Once the cell was placed in the cell holder, it was heated up above 800°$C$, while the cathode was fed with pure nitrogen and the anode with air. All heating and cooling rates were equal to 1°$C.min^{-1}$. After a step above 800°$C$, the temperature was decreased down to 800°$C$. This procedure allowed the ceramic glass to act as a seal by providing gas tightness between anodic and cathodic compartments.

#### 3.1.5.3. Cermet reduction

Once the cell temperature was stabilized at 800°$C$, the nickel oxide in the cermet cathode was reduced to metallic nickel Ni by feeding the electrode with a mixture of nitrogen and hydrogen. Step by step (10 *min* long), the amount of $H_2$ was gradually increased while reducing the $N_2$ flow, so that the total flow remained constant at 12 $NmL.min^{-1}.cm^{-2}$ from pure nitrogen to pure hydrogen. Figure 3-4 displays an example of cermet reduction by plotting the cell OCV versus the time. Changes in inlet composition can be noticed by the sudden drops (*i.e.* when the nitrogen flow is lowered) and increases in cell voltage.

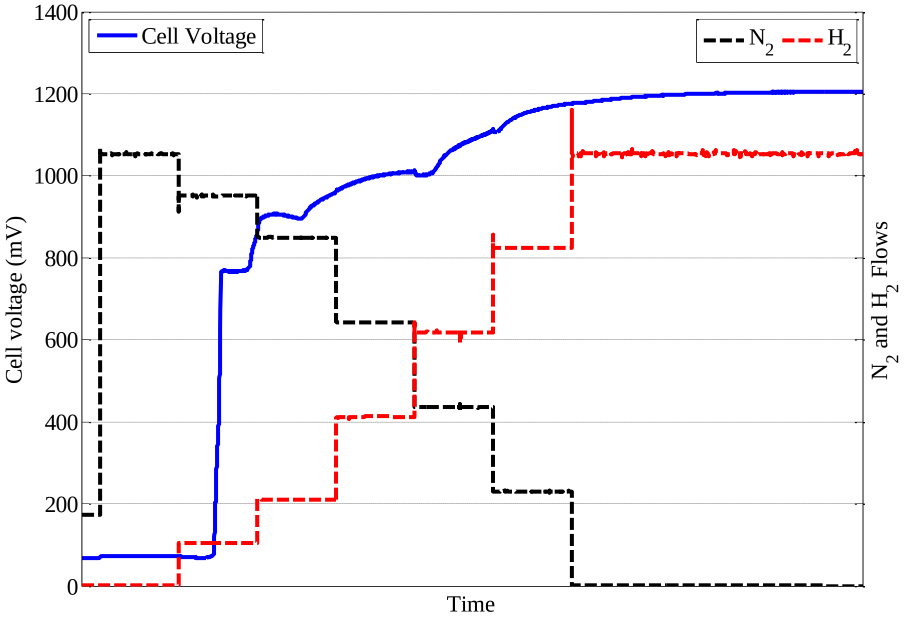

Figure 3-4:
OCV evolution
during cermet
reduction at 800°*C*.

### 3.1.5.4. Mechanical load optimization

The cell was initially loaded with 0.5 *kg* at room temperature. Then, once at 800°*C* and after reaching the defined gas conditions and checking the Open Circuit Voltage (OCV), an increasing additional load was applied while recording the cell serial Area Specific Resistance (ASR) $R_s$ by EIS. The load was increased until the serial ASR was minimized, indicating an optimization of the contact ASR. Typically, the applied weight on investigated radial cells was 0.5 $kg.cm^{-2}$, leading to a contact ASR of about 0.05 $\Omega.cm^{-2}$ at 800°*C*.

# 3.2. Modeling Approach

The proposed model describes the $H_2$ and CO production through reaction of steam (Reaction (3-1)) and carbon dioxide (Reaction (3-2)), occurring simultaneously at the cathode side, while $O_2$ is produced at the anode side (Reaction (3-3)).

$$H_2O + 2e^- \rightarrow H_2 + O^{2-} \tag{3-1}$$

$$CO_2 + 2e^- \rightarrow CO + O^{2-} \tag{3-2}$$

$$2O^{2-} \rightarrow O_2 + 4e^- \tag{3-3}$$

The WGS reaction (Reaction (3-4)) was assumed to occur in the porous cathode material:

$$CO + H_2O \leftrightarrow CO_2 + H_2 \qquad \Delta_r H\left(800°C, 1\,atm\right) = 41\,kJ.mol^{-1} \text{ [4]} \tag{3-4}$$

The electrochemical module was coupled to a thermal description of the SOC, combining both electrochemical and chemical heat sources (*cf.* section 3.2.4). The following sections detail the geometries and materials considered, and the hypotheses and boundary conditions relevant for mass transfer, electrochemical and thermal modeling. This co-electrolysis model was derived from a previous one developed for steam electrolysis [5], to take into account the simultaneous $CO_2$ electrolysis.

## 3.2.1. Geometry and Materials

The 2D model is able to describe a ‘typical’ squared and planar SRU, constituted of one cell and two half interconnects with an active area of 100 *cm²*, in either a co-flow or counter-flow configuration (Figure 3-5). This model can also be used to simulate a radial geometry (Figure 3-6), representative of the experimental test bench (Figure 3-1). $(x,y,z)$ and $(r,\theta,z)$ coordinates are used for longitudinal and radial geometries, respectively.

Most classical materials used for HTE were considered for the simulations: $La_{0.8}Sr_{0.2}MnO_{3\pm\delta}$ (LSM) for the anode, $ZrO_2$ stabilized with 8 *mol.%* $Y_2O_3$ (8YSZ) for the electrolyte and a Ni-8YSZ cermet for the cathode. A cathode supported cell configuration is considered in this study, but it is worth mentioning that the simulated cell geometry can be either an electrolyte- or a cathode-supported one.

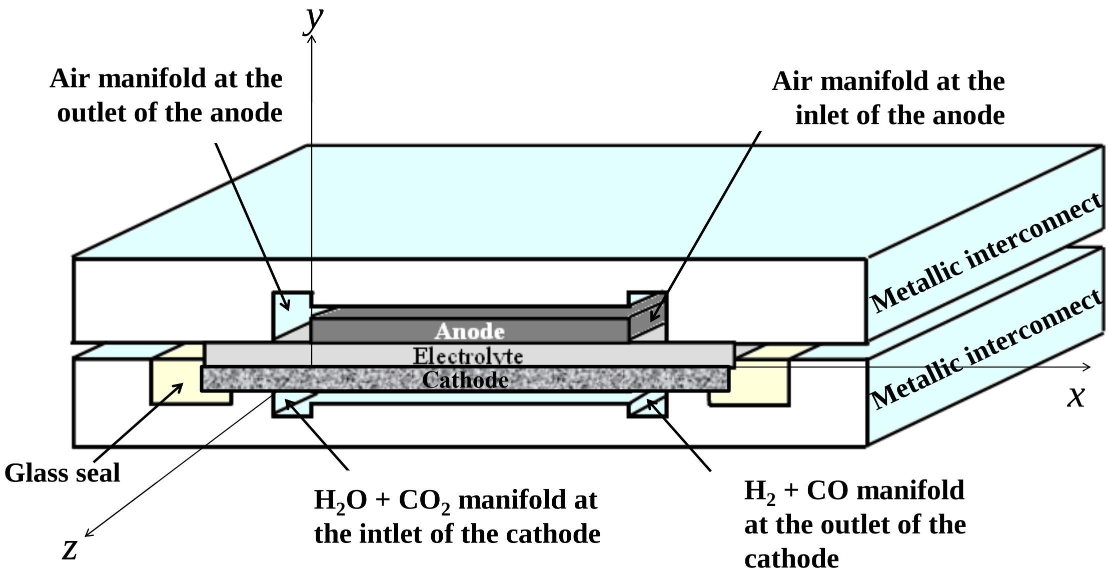

Figure 3-5: Schematic representation of the simulated SRU (cross-section view) and coordinate system used in the model considering a planar CSC in a counter-flow configuration [5].

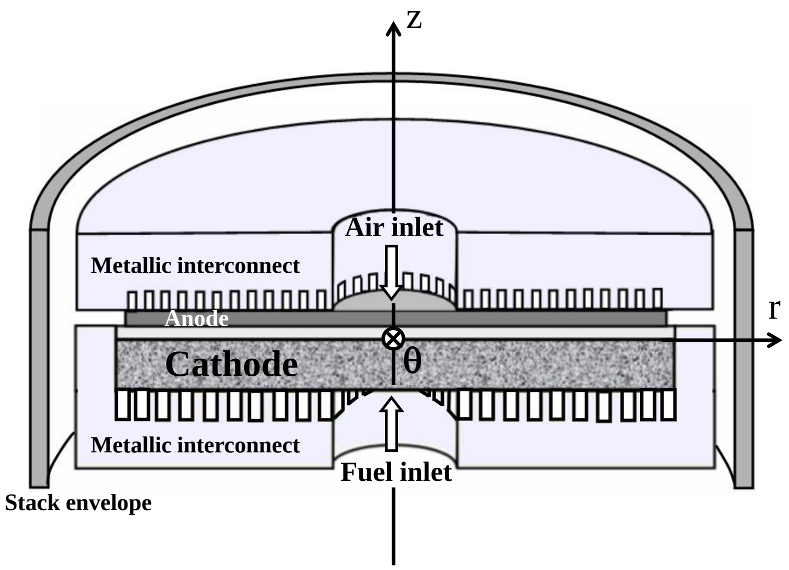

Figure 3-6: Schematic representation of the simulated SRU (cross-section view) and coordinate system used in the model considering a radial cathode-supported cell in a co-flow configuration [6].

### 3.2.2. Mass Transfer Description

The pressure drop along the gas channels was supposed to be negligible. Therefore, atmospheric conditions were assumed for the gas-phase pressure in the SRU ($P_T = 1$ *atm*).

The variation of molar fractions along the gas channels (*i.e.* in the *x* or *r* directions in Figure 3-5 and Figure 3-6, respectively) originates from molar fluxes through the porous electrodes (*i.e.* in the *y* or *z* direction, respectively). This variation was calculated by using local mass balances performed for each species along the channels:

$$\frac{dn_i}{dx} = \gamma_i e N_i \tag{3-5}$$

where $n_i$ denotes the molar flow rate in the channels for specie i, $N_i$ the molar flux through the electrode, $e$ the width of the gas channel and $\gamma_i$, a stoichiometric coefficient (equal to -1 for reactants and +1 for products).

In porous electrodes, the viscous flow, which is driven by a pressure gradient, is generally considered negligible compared to the diffusive flow [7, 8]. Such a hypothesis is especially accurate at the cathode side since reactions (3-1)-(3-4) are equimolar. Therefore, the mass transport through the porous electrodes (*i.e.* in the direction perpendicular to the gas channel axis) was described in the frame of the Dusty Gas Model (DGM), combining the Stephan-Maxwell and Knudsen diffusions [9]:

$$\frac{N_i}{D_{i,k}^{eff}} + \sum_{j=1, j \neq i}^{n} \frac{y_j N_i - y_i N_j}{D_{i,j}^{eff}} = -\frac{P_T}{RT}\left(\frac{dy_i}{dy}\right) \tag{3-6}$$

where $y_i$ is the molar fraction of specie *i* and $P_T$ the total pressure (= 1 *atm*).

The effective Knudsen and binary diffusion coefficients, $D_{i,k}^{eff}$ and $D_{i,j}^{eff}$, were determined as a function of the electrode microstructure parameters (*i.e.* the mean pore radius $\bar{r}$, the tortuosity factor $\tau$ and the porosity $\varepsilon$) [10–12]. In porous media such as electrodes, the following expressions are usually employed [13]:

$$D_{i,j}^{eff} = \frac{\varepsilon}{\tau} D_{i,j} \quad \text{and} \quad D_{i,k}^{eff} = \frac{\varepsilon}{\tau} D_{i,k} \tag{3-7}$$

The Knudsen diffusion coefficient can be assessed according to the kinetic theory of gases:

$$D_{i,k} = \bar{r}\frac{2}{3}\sqrt{\frac{8RT}{\pi M_i}} \tag{3-8}$$

where $M_i$ denotes the molecular weight for the gas i.

The binary diffusion coefficients have been expressed as follows [12]:

$$D_{i,j} = \frac{0{,}00143T^{1.75}}{P_T M_{i,j}^{1/2}(V_i^{1/3}+V_j^{1/3})^2} \text{ with } M_{i,j} = 2/\left(\frac{1}{M_i}+\frac{1}{M_j}\right) \tag{3-9}$$

where $V_i$ corresponds to the Füller diffusion volume of specie i.

At the anode side, a binary mixture of oxygen and nitrogen was considered as the electrode inlet. Using the method presented in [5], an analytical solution of the DGM (Equation (3-6)) can be found, provided that the $N_2$ flux is nil inside the electrode, and that the $O_2$ flux is imposed by the local current density *i(x)* according the Faraday law:

$$N_{O_2} = \frac{|i|}{4F} \tag{3-10}$$

The oxygen molar fraction at the anode/electrolyte interface $y_{O_2}^{int}$ can be then expressed as a function of the electrode thickness $\delta_a$, the molar fraction into the anodic gas channel $y_{O_2}^{canal}$ and the gas constant *R*:

$$y_{O_2}^{int} = \frac{D_{O_2,k}^{eff}+D_{O_2,N_2}^{eff}}{D_{O_2,k}^{eff}} + \left(y_{O_2}^{canal} - \frac{D_{O_2,k}^{eff}+D_{O_2,N_2}^{eff}}{D_{O_2,k}^{eff}}\right)\exp\left(\frac{RT}{P_T}\times\frac{-|i|}{4F}\times\frac{D_{O_2,k}^{eff}}{D_{O_2,k}^{eff}D_{O_2,N_2}^{eff}}\times\delta_a\right) \tag{3-11}$$

At the cathode side, the total current is generated by electrochemical reduction of $H_2O$ and $CO_2$ (Reactions (3-1) and (3-2)). Therefore, the local current can be split into two contributions $I_{H_2}$ and $I_{CO}$ related to $H_2O$ and $CO_2$ reduction reactions. At the electrode/electrolyte interface, the molar fluxes can be then expressed as a function of these two components:

$$I = I_{CO} + I_{H_2} \quad \text{with } N_{CO_2} = -N_{CO} = \frac{I_{CO}}{2F\times dS} \text{ and } N_{H_2O} = -N_{H_2} = \frac{I_{H_2}}{2F\times dS} \ (y{=}0) \tag{3-12}$$

Moreover, the occurrence of the WGS reaction (Reaction (4)) within the cathode can produce or consume species involved in electrochemical reactions. These source terms modify the fluxes according to the following mass balances:

$dN_i(x,y) = r_i(x,y) \times dy$ with $i = H_2, H_2O, CO$ *et* $CO_2$. (3-13)

where $r_i$ is the molar rate of formation per unit volume of the porous medium written for each gas species i.

This term is linked to the WGS reaction rate $v_{WGS}$ which is assumed to occur in the void fraction of the cermet:

$r_{H_2} = r_{CO_2} = \varepsilon \times v_{WGS}$ and $r_{H_2O} = r_{CO_2} = -\varepsilon \times v_{WGS}$ (3-14)

where ε is the cermet porosity.

The WGS reaction kinetic rate can be expressed as follows:

$$v_{WGS} = k_+ y_{CO} y_{H_2O} - k_- y_{CO_2} y_{H_2} \quad (3\text{-}15)$$

where $k_+$ and $k_-$ are the kinetic constants of forward and backward reactions.

The kinetic constants are calculated as a function of the WGS reaction activation energy $E_a^{WGS}$:

$$k_+ = f_0 \frac{kT}{\hbar} \exp\left(\frac{-E_a^{WGS}}{RT}\right) = k_0 \exp\left(\frac{-E_a^{WGS}}{RT}\right) \text{ and } k_+/k_- = K_e \quad (3\text{-}16)$$

where $K_e$ is the thermodynamic equilibrium constant for the WGS reaction.

Numerical values used to assess the WGS kinetic can be found in Table 3-4.

| $K_e$ | | | | |
|---|---|---|---|---|
| 978 *K* | 1018 *K* | 1078 *K* | 1118 *K* | 1178 *K* |
| 1.58 | 1.34 | 1.07 | 0.93 | 0.78 |
| $E_a^{WGS}$ = 103800 $J.mol^{-1}$ | | $k_0$ = 1.88 ×$10^8$ $mol.s^{-1}.bar^{-2}.m^{-3}$ | | |

Table 3-4 : Kinetic values for WGS reaction kinetics [14, 15].

In this model, the reactions of carbon deposition and methane production were not considered. Indeed, thermodynamic predictions [16] and experimental reports [17] demonstrated that methane production is negligible at atmospheric pressure and high temperature. Similarly, in a high temperature co-electrolyzer operating at atmospheric pressure, thermodynamic calculations [18] have shown that carbon deposition is not favored in presence of $H_2O$ and/or $CO_2$. However, if CO becomes largely preponderant at high $CO_2$ and $H_2O$ conversion rates, carbon formation becomes likely. In such peculiar operating conditions, the carbon deposit could yield deactivation of active sites and could be a limiting factor and a source of degradation.

### 3.2.3. Electrochemical Description

Assuming that electrodes are good electronic conductors, the electrical potential can be considered constant along the cell (*i.e.* electrodes are thus considered equipotential for the electronic phase). Since the global current density can be split in two components, $I_{H_2}$ and $I_{CO}$, the cell is assumed to be represented by the equivalent electrical circuit shown in Figure 3-7.

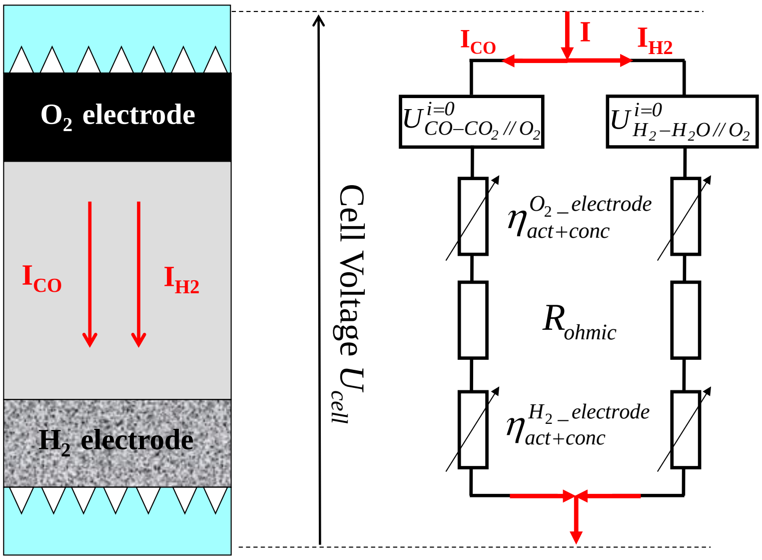

Figure 3-7: Equivalent electrical circuit for cell operation in co-electrolysis mode.

A first coupling between the two branches of the equivalent circuit (*i.e.* between the two electrochemical reactions) comes from the diffusion process through the cathode (see previous section). In addition, the active sites of the electrodes are potentially not fully available for the water molecules electrolysis because of the presence of $CO_2$. Accordingly, each elementary surface of the electrode *dS* has been split in one active surface related to $H_2O$ electrolysis and a second one associated to the electrochemical reduction of $CO_2$ [19]:

$$idS = i_{H_2}dS_{H_2O} + i_{CO}dS_{CO_2} \quad \text{with} \quad dS_{H_2O} = \beta dS \quad \text{and} \quad dS_{CO_2} = (1-\beta)dS \quad (0 \le \beta \le 1) \qquad (3\text{-}17)$$

$\beta = 1$ means that the water molecules are preferentially adsorbed on the active sites of the cathode and prevent the $CO_2$ reduction. Nevertheless, it is suggested here that the repartition of the active sites for both electrochemical reactions is directly given by the relative percentage of $H_2O$ and $CO_2$ at the cathode/electrolyte interface. In this view, the surface ratio $\beta$ can be expressed as follows [19]:

$$\beta = y_{H_2O}^{int} \Big/ \left( y_{CO_2}^{int} + y_{H_2O}^{int} \right) \tag{3-18}$$

$\beta$ represents, at the macroscopic scale, the competition between $H_2O$ and $CO_2$ electrolyses over the same active sites. In other words, it translates adsorption/desorption and charge transfer phenomena competition, and more specifically, the readiness of steam electrolysis compared to $CO_2$ electrolysis.

Considering the equivalent electrical circuit in Figure 3-7, both current densities must be determined from Equations (3-19) and (3-20), obtained from a decomposition of the general Butler-Volmer expression. These equations are written assuming that the local current densities are negative in the electrolysis mode. For each slice of cell laying between *x* and *x+dx* (Figure 3-5), the cell voltage is expressed as functions of the equilibrium potential, the ohmic losses and the different overpotentials related to the $H_2$-$H_2O$//$O_2$ and CO-$CO_2$//$O_2$ electrochemical systems:

$$U_{cell} = U_{i=0}^{H_2-H_2O//O_2} + R_{ohm}\left|i_{H_2}\right| + \left(\left|\eta_{act,H_2-H_2O//O_2}^{anode}\right| + \left|\eta_{act,H_2-H_2O//O_2}^{cathode}\right|\right) + \left(\left|\eta_{conc,H_2-H_2O//O_2}^{anode}\right| + \left|\eta_{conc,H_2-H_2O//O_2}^{cathode}\right|\right) \quad \text{(for } dS_{H_2O}\text{)} \tag{3-19}$$

$$U_{cell} = U_{i=0}^{CO-CO_2//O_2} + R_{ohm}\left|i_{CO}\right| + \left(\left|\eta_{act,CO-CO_2//O_2}^{anode}\right| + \left|\eta_{act,CO-CO_2//O_2}^{cathode}\right|\right) + \left(\left|\eta_{conc,CO-CO_2//O_2}^{anode}\right| + \left|\eta_{conc,CO-CO_2//O_2}^{cathode}\right|\right) \quad \text{(for } dS_{CO_2}\text{)} \tag{3-20}$$

where $U_{i=0}$ is the Open Circuit Voltage (OCV) computed from the Nernst equation:

$$U_{i=0}^{H_2-H_2O//O_2}(x) = U_{H_2-H_2O//O_2}^{0}(T) + \frac{RT}{2F} ln \frac{y_{H_2}^{int\_i=0}\sqrt{y_{O_2}^{int\_i=0}}}{y_{H_2O}^{int\_i=0}} \tag{3-21}$$

$$U_{i=0}^{CO-CO_2//O_2}(x) = U_{CO-CO_2//O_2}^{0}(T) + \frac{RT}{2F} ln \frac{y_{CO}^{int\_i=0}\sqrt{y_{O_2}^{int\_i=0}}}{y_{CO_2}^{int\_i=0}} \tag{3-22}$$

where $y_{i=H_2,H_2O,CO,CO_2}^{int\_i=0}$ are the molar fractions taken at the cathode/electrolyte interface and $y_{i=O_2}^{int\_i=0}$ denotes the oxygen molar fraction calculated at the anode/electrolyte interface at *i*=0.

It is worth emphasizing that the OCV evolves along the cell length because of the WGS reaction which modifies the partial pressures even at *i*=0. For both electrochemical systems, the standard potential $U_0$ depends on the temperature according to the thermodynamic data in [20], assuming a linear dependence on the temperature:

$$U^0_{H_2O-H_2//O_2} = 1.27786 - 0.0002814 \times T \tag{3-23}$$

$$U^0_{CO_2-CO//O_2} = 1.46714 - 0.0004527 \times T \tag{3-24}$$

The terms $R_{ohm} i_{H_2}$ and $R_{ohm} i_{CO}$ denote the pure ohmic losses including the ionic ASR of the electrolyte, $R_e$, the electronic ASRs of both electrodes, $R_{LSM}$ and $R_{Ni-8YSZ}$, and the total contact ASR due to the current collection between the electrodes and the interconnects, $R_c$.

$$R_{ohm} = R_{LSM} + R_{Ni-8YSZ} + R_e + R_c \tag{3-25}$$

$$with \quad R_{LSM} = \frac{\delta_a}{\sigma_{LSM}},\ R_{Ni-8YSZ} = \frac{\delta_c}{\sigma_{Ni-8YSZ}},\ R_e = \frac{\delta_e}{\sigma_{8YSZ}} \tag{3-26}$$

where $\sigma$ is the electrical conductivity of each considered material and $\delta$ the thickness of the anode, electrolyte or cathode layer.

In planar configuration, electronic ASR of the electrodes is low compared to ohmic losses due to the electrolyte and can be regarded as temperature independent within the operating conditions range [21]. Inversely, the ionic conductivity of the 8YSZ electrolyte has to be expressed as function of the operating temperature and is taken as [22]:

$$\sigma_{8YSZ}\left(\Omega.cm^{-1}\right) = 466 \times \exp\left(\frac{-9934}{T}\right) \quad \left(T \text{ in } K\right) \tag{3-27}$$

For small current densities (*i.e.* rapid mass transport), the current density is related to the activation overpotential through the Butler-Volmer equation [23]:

$$i = i_0 \left[ \exp\left(\frac{\alpha z F}{RT} \eta_{act}\right) - \exp\left(-\frac{(1-\alpha) z F}{RT} \eta_{act}\right) \right] \tag{3-28}$$

where $i$ is the current density generated by the electrochemical reaction, $i_0$ is the exchange current density, $\alpha$ is the symmetry factor, $z$ is the number of electrons exchanged during the charge transfer, $F$ the Faraday constant, $R$ the gas constant, $T$ the temperature and $\eta_{act}$ the activation overpotential.

For a co-electrolysis mode, assuming that the symmetry factor $\alpha$ is equal to 0.5, the activation overpotentials are expressed as follows:

$$\left|\eta^{anode}_{act,H_2-H_2O//O_2}\right|+\left|\eta^{cathode}_{act,H_2-H_2O//O_2}\right|=\frac{RT}{F}\left[\sinh^{-1}\left(\frac{\left|i_{H_2}\right|}{2i_{0,anode}}\right)+\sinh^{-1}\left(\frac{\left|i_{H_2}\right|}{2i^{H_2-H_2O}_{0,cathode}}\right)\right] \tag{3-29}$$

$$\left|\eta^{anode}_{act,CO-CO_2//O_2}\right|+\left|\eta^{cathode}_{act,CO-CO_2//O_2}\right|=\frac{RT}{F}\left[\sinh^{-1}\left(\frac{\left|i_{CO}\right|}{2i_{0,anode}}\right)+\sinh^{-1}\left(\frac{\left|i_{CO}\right|}{2i^{CO-CO_2}_{0,cathode}}\right)\right] \tag{3-30}$$

The exchange current density $i_0$ represents the capacity of the electrode to proceed with the electrochemical reaction. It is a measure of the forward and backward rate constants at the equilibrium. The higher the exchange current density, the higher is the electrochemical reaction rate for a given electrode overpotential. The activation overpotential thus represents the voltage loss induced by the electrochemical reactions.

It should be noted here that without introducing the phenomenological 'surface ratio' parameter $\beta$ (Equation (3-18)), the specific calculation of both activation overpotentials would lead to an overestimation of the available electroactive area by a factor 2. Indeed, solving Equations (3-29) and (3-30) would be equivalent to assuming that all active sites are simultaneously available for the reduction of both steam and $CO_2$.

The concentration overpotentials can arise because the gas composition in the vicinity of the active sites is different from the initial composition at OCV. This can be related to insufficient gas diffusion through the electrodes or insufficient gas flow rate introduced at the anode or cathode inlet. The concentration overpotentials can be expressed from the Nernst equation according to:

$$\eta^{cathode}_{conc,H_2-H_2O//O_2}=\frac{RT}{2F}ln\left(\frac{y^{int\_i=0}_{H_2}\times y^{int\_i\neq 0}_{H_2O}}{y^{int\_i\neq 0}_{H_2}\times y^{int\_i=0}_{H_2O}}\right) \tag{3-31}$$

$$\eta^{cathode}_{conc,CO-CO2//O_2}=\frac{RT}{2F}ln\left(\frac{y^{int\_i=0}_{CO}\times y^{int\_i\neq 0}_{CO_2}}{y^{int\_i\neq 0}_{CO}\times y^{int\_i=0}_{CO_2}}\right) \tag{3-32}$$

$$\eta^{anode}_{conc,H_2-H_2O//O_2}=\eta^{anode}_{conc,CO-CO_2//O_2}=\frac{RT}{4F}ln\left(\frac{y^{int\_i=0}_{O_2}}{y^{int\_i\neq 0}_{O_2}}\right) \tag{3-33}$$

In the proposed model, the molar fractions are taken at the anode or cathode active sites (*i.e.* the Triple Phase Boundary lengths), which were reduced to the anode/electrolyte or cathode/electrolyte interfaces. It is worth noting that this assumption is well verified for sufficiently thick electrodes. Indeed, numerous studies [7, 24, 25] showed that the reaction zone spreads on a limited region from the electrolyte/electrode interface within the electrode (~10-20 $\mu m$). In this work, the improvement of the electrode efficiency due to the extent of the electrochemical reactions is taken into account in the 'apparent' exchange current densities including the 'global' electrochemical process into the active layers [26].

### 3.2.4. Thermal Description

The thermal model used for co-electrolysis simulations has been adapted from a previous one developed for steam electrolysis and SOFC modes detailed in [5, 6]. The main assumptions are summarized in this section. It is worth noting that the evolutions of all variables with the geometry are taken into account (*e.g.* temperatures, partial pressures, heat transfer coefficients, surface element variation in the specific case of radial cell geometries… as functions of ($x$,$y$) or ($z$,$\theta$)). However, for the sake of clarity, some of the dependences are not expressed in following equations. Additional details and numerical input data concerning this thermal description can be found in Chapter 5 and in references [5, 6].

Adiabatic conditions were assumed for the surfaces connecting two adjacent SRUs (*i.e.* the bottom and top free surfaces of SRU as shown on Figure 3-8). This assumption is well verified only for the SRUs located in the central region of the stack where heat flux in the stacking direction can be neglected. The temperatures of gases introduced into the SRU were chosen equal to $T_{insulating}$. The temperature of the insulating envelope surrounding the stack was supposed to be controlled by $T_{insulating}$.

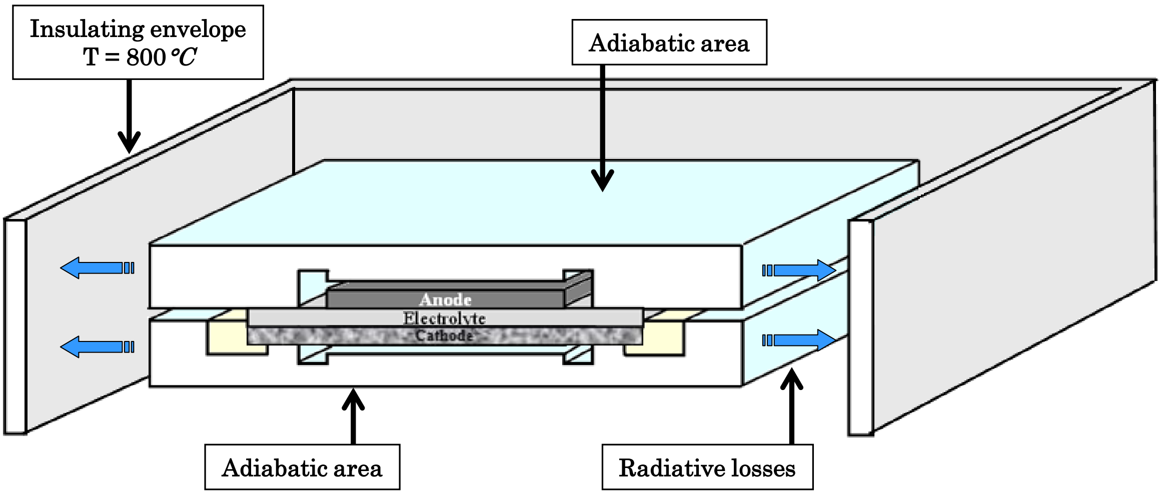

Figure 3-8: Boundary conditions assumed for the thermal simulations [5]

The governing equation to calculate the temperature field in the solids was expressed considering conduction, convection and radiation. For a solid volume *dV*, with a *dS* surface contact with a fluid, the energy balance can be written as follows:

$$\lambda\left\{div\left(grad\left(T\right)\right)\right\}dV + d\dot{Q} = h_{gas}dS\left\{T_s - T_g\right\} + d\dot{\varphi}_{rad} \tag{3-34}$$

The first term of this Equation (3-34), $\lambda\{div(grad(T))\}dV$, is related to the heat transport by conduction in the solid phases and $\lambda$ represents the thermal conductivity of the solid volume *dV*. Porous anode and cathode were modeled as a homogenous media in which only conduction was taken into account. Indeed, the Peclet number *Pe* calculated within both electrodes remains much lower than unity, meaning that the convective heat transfers are negligible in comparison with the conductive ones [8].

The second term of Equation (3-34), $d\dot{Q}$, corresponds to thermal sources related to electrochemical and chemical reactions. The first contribution to $d\dot{Q}$ is the heat generation, $d\dot{Q}_{H_2O} + d\dot{Q}_{CO_2}$, due to reductions of steam and carbon dioxide:

$$d\dot{Q}_{H_2O} = \left[\frac{i_{H_2}(x)}{2F}\Delta H_{H_2O} + U_{cell} i_{H_2}(x)\right] dS_{H_2O} \tag{3-35}$$

$$d\dot{Q}_{CO_2} = \left[\frac{i_{CO}(x)}{2F}\Delta H_{CO_2} + U_{cell} i_{CO}(x)\right] dS_{CO_2} \tag{3-36}$$

where $\Delta H_i$ corresponds to the enthalpies for $H_2O$ and $CO_2$ formation.

The location within the SRU of source terms due to the electrochemical reactions is discussed in reference [5].

The second contribution to $d\dot{Q}$, $d\dot{Q}_{WGS}$, is due to the heat generation of the WGS chemical reaction. Corresponding heat source terms were located within the porous cathode and are expressed as a function of the reaction rate $v_{WGS}$ :

$$d\dot{Q}_{WGS} = \{v_{WGS}(x,y)\Delta H_{WGS}\}dV \tag{3-37}$$

where $\Delta H_{WGS}$ is the enthalpy of the WGS reaction (Reaction (4)).

Computation of the convective term $h_{gas}\, dS\, \{T_s - T_g\}$ (Equation (3-34)) requires to know the temperature of fluids $T_g$, which must be determined all along the gas channels. Details about the modeling of the convective heat transfer phenomena in the SRU can be found in references [5, 6]. One must remind here that energy balances are used to compute the temperature increase or decrease of gases flowing into the channels:

$$\sum_i \frac{\partial\left(n_i(x)\,C_p^i(x)\,T_g(x)\right)}{\partial x}dx = h_{cathode}(x)dS\left\{T_s(x) - T_g(x)\right\} \quad (i = H_2, H_2O, CO, CO_2, N_2) \tag{3-38}$$

$$\sum_i \frac{\partial\left(n_i(x)\,C_p^i(x)\,T_g(x)\right)}{\partial x}dx = h_{anode}(x)dS\left\{T_s(x) - T_g(x)\right\} \quad (i = O_2, N_2) \tag{3-39}$$

where $T_s$ is the wall temperature of the solid phase. The exchange surface $dS$ correspond to the contact surface between gas and solid. The heat transfer coefficients $h$ have been determined from an asymptotic value of the Nusselt number $Nu$ [5]:

$$h_{steam\,or\,air}(x) = \frac{Nu\,\lambda_i(x)}{D_H} \quad i = O_2 // N_2 \quad or \quad i = H_2O // H_2 // CO // CO_2 // N_2 \tag{3-40}$$

where $D_H$ is the hydraulic diameter of the cathode or anode channel.

It is worth noting that effective heat conductivities of fluids $\lambda_i$ were calculated for each position along the gas channel through a mixture law. Therefore, these parameters depend on both the gas composition along the cell and the intrinsic conductivities of gas species.

Accordingly, the heat transfer coefficient, which is linearly dependent of $\lambda_i$ according to Equation (3-40), will follow the same evolution.

The last term of Equation (3-34), $d\dot{\varphi}_{rad}$, corresponds to the radiative heat transfer and can be divided into two contributions. The first one, $d\dot{\varphi}_1$, corresponds to the surface-to-surface heat exchange between electrodes (anode or cathode) and interconnect plates. It was approximated in the model according to the general expression between two infinite parallel planes:

$$d\dot{\varphi}_1 = \left\{ \frac{\sigma \varepsilon_{anode/cathode} \varepsilon_{interconnect}}{1 - \left(1 - \varepsilon_{anode/cathode}\right)\left(1 - \varepsilon_{interconnect}\right)} \left(T^4_{anode/cathode} - T^4_{interconnect}\right) \right\} dS \tag{3-41}$$

where $\varepsilon$ is the emissivity of materials (for anode, cathode and interconnects) and $\sigma$ the Stefan-Boltzmann constant.

The second contribution is the radiative heat losses, $d\dot{\varphi}_2$, flowing from the SRU to the stack insulating envelope:

$$d\dot{\varphi}_2 = \left\{ \sigma \varepsilon_{interconnect} \left(T_s^4 - T^4_{insulating}\right) \right\} dS \tag{3-42}$$

where $T_s$ is the surface temperature taken on the free edge of the SRU and $T_{insulating}$ the temperature of the isolating envelope taken equal to 800°$C$ (Figure 3-8).

### 3.2.5. Numerical Architecture

Mass transfer and electrochemical descriptions were implemented using the commercial software Matlab®. Thermal calculations were solved within the frame of the finite elements code Cast3M. The computational procedures are summarized in the flowcharts given in Figures 3-9 and 3-10.

Within the electrochemical module, the cell is divided into a mesh of elementary slices. Local mass balances (Equation (3-5)) allow calculating gas flow in the channels from one elementary slice to the next one. For each slice of cell, both local electrochemical currents are determined into an iterative scheme so that Equations (3-19) and (3-20) are simultaneously verified. These calculations, along with $\beta$ (Equations (3-17) and (3-18)), encompass the determinations of local overpotentials associated to mass transfer through the porous electrodes. It can be mentioned that the set of equations describing diffusion and WGS reaction within the cathode are numerically solved by a Runge-Kutta method associated with a shooting method. For each slice of cell, the numerical solution is obtained through two main loops running until both $H_2O$ and $CO_2$ electrochemical currents (and the resulting diffusion process, molar fractions distribution and $\beta$) are stable. An external loop is added all along the cell length to ensure the convergence of the output data in a counter-flow configuration.

Once the electrochemical calculations are completed, the repartition of gas composition, fluxes and thermal sources are used as input data for the thermal module. Heat transfer by conduction and radiation are calculated according to a finite element analysis which has been coupled with a finite difference method to solve the thermal convection along the gas channel. The new temperature field throughout the SRU 2D geometry is subsequently introduced in the electrochemical module. A global iterative loop between both modules is run until the stability of model outputs is reached.

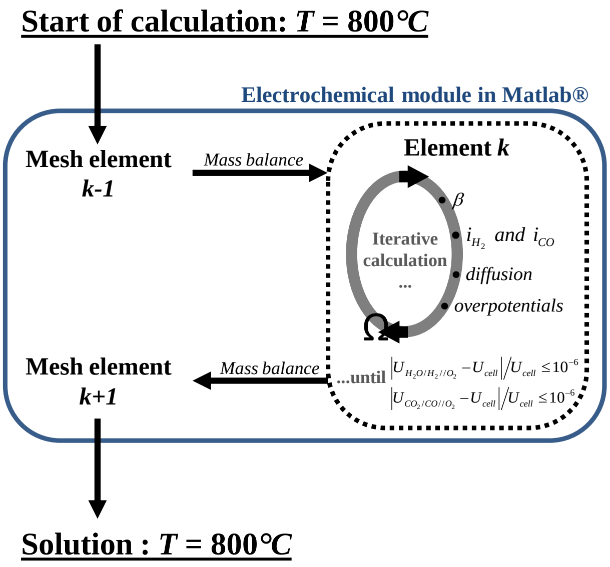

Figure 3-9:

Isothermal model summary and architecture.

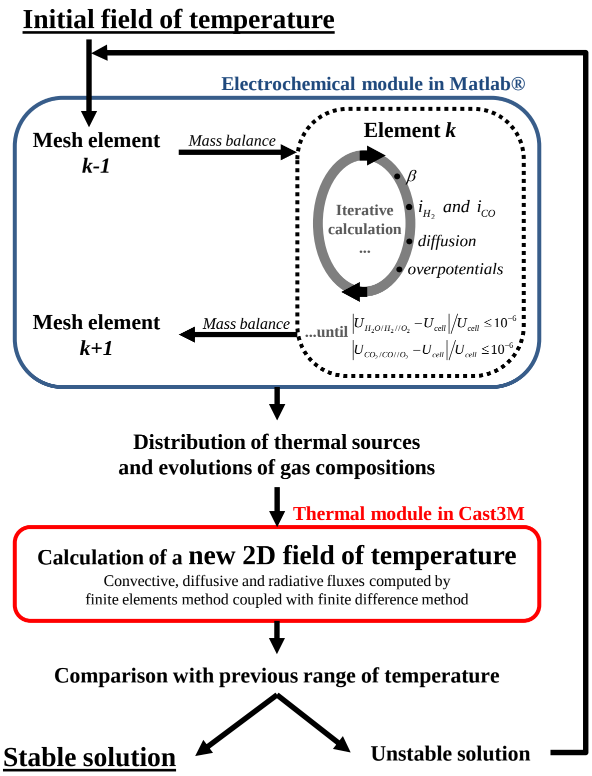

Figure 3-10:

Complete model summary and architecture.

### 3.2.6. Numerical Reliability

As detailed in previous sections, the model is constituted by several entangled loops. They run until a preset condition is satisfied (*i.e.* the computed error is smaller than the maximum acceptable error). These acceptable errors are detailed in this section in order to explicit the numerical accuracy.

#### 3.2.6.1. Loops on each current density

Both current densities were determined so that the computed cell voltage equals the set voltage (Equations (3-19) and (3-20)) within a margin of relative error of $5\times10^{-5}$ $V.V^{-1}$. This amounts to a maximum error of 0.1 *mV* at 1.5 *V*.

### 3.2.6.2. Loop on global current density stability

Once both current densities were determined, a new value for the surface ratio $\beta$ was computed from the resulting molar fractions. Even small variations of $\beta$ can lead to significant changes for $i_{H_2}$ and $i_{CO}$. Hence, before performing calculations on the adjacent mesh, the relative change between two consecutive global current densities determined iteratively has to be lower than 1% (*i.e.* <0.02 $A.cm^{-2}$ if the absolute local current density is 2 $A.cm^{-2}$).

### 3.2.6.3. Loop on counter flow

When simulating a counter-flow configuration, the outlet air flow is assumed. Calculations follow the cathodic flow, thus the computed oxygen content in the anodic flow decreases element after element through local mass balances resulting from local electrochemical production. When reaching the last element of the cell length (*i.e.* cathodic outlet and anodic inlet), the resulting oxygen flow is compared to the known inlet one. The loop is exited when this relative error is lower than 2%.

The maximum acceptable error was adjusted from calculations done with the analytical steam reduction model. Indeed, most of the calculation time can be linked to the numerical solving of the DGM, which is only done in co-electrolysis simulations. A 2% relative error results in an acceptable number of iterations and has a limited influence on the resulting global current (*i.e.* the difference between the global current densities obtained within a $10^{-6}$ and a 2% relative error is lower than 0.01 $A.cm^{-2}$).

## 3.2.7. Model Positioning in International Literature

Recent efforts in co-electrolysis investigations have led to the development of multiple electrochemical models (*cf.* 2.3) aiming at predicting both the performances and the outlet gas compositions of an operating cell. Due to the fast WGS reaction kinetics, the vast majority of these models assume that steam is the sole electrochemically active specie, whereas CO is produced through the reverse WGS reaction. Conversely, M. Ni et al. [20] have proposed a model taking into the $CO_2$ reduction as well as the chemical reaction. However, to the best of my knowledge, no models prior to this work have described the macroscopic co-electrolysis mechanism through a splitting approach (*cf.* Equation (3-17)).

As already mentioned, the model described in this chapter is based on previous ones developed to simulate SRUs or stacks operated first in SOFC mode [6], then in HTE mode [5]. Nevertheless, the proposed model differs from these predecessors mainly by the description of the diffusion, which now considers up to 5 species, and by two hereby introduced and strong hypotheses that are an approach based on a parallel equivalent electrical circuit and a coupling of the two branches through a surface ratio parameter.

## 3.3. Conclusion

The experimental and modeling tools detailed in this chapter have been used to investigate the cell responses in steam electrolysis, carbon dioxide electrolysis and co-electrolysis modes. Single electrolysis measurements were devoted to determining the unknown parameters before simulating co-electrolysis operations. Throughout this work, no parameters have been adjusted using co-electrolysis data. Experimental results and corresponding simulations are presented in the following chapters, intended for model validation and simulations results.

## 3.4. References

1. S. D. Ebbesen, C. Graves, and M. Mogensen, Production of Synthetic Fuels by Co-Electrolysis of Steam and Carbon Dioxide, *Int. J. Green Energy* 6, 646 (**2009**).
2. S. D. Ebbesen, C. Graves, A. Hauch, S. H. Jensen, and M. Mogensen, Poisoning of Solid Oxide Electrolysis Cells by Impurities, *J. Electrochem. Soc.* 157, B1419 (**2010**).
3. *http://www.engineeringtoolbox.com/carbon-monoxide-d_893.html*
4. J. Xu and G. F. Froment, Methane steam reforming, methanation and water-gas shift: I. Intrinsic kinetics, *AIChE J.* 35, 88 (**1989**).
5. J. Laurencin, D. Kane, G. Delette, J. Deseure, and F. Lefebvre-Joud, Modelling of solid oxide steam electrolyser: Impact of the operating conditions on hydrogen production, *J. Power Sources* 196, 2080 (**2011**).
6. J. Laurencin, F. Lefebvre-Joud, and G. Delette, Impact of cell design and operating conditions on the performances of SOFC fuelled with methane, *J. Power Sources* 177, 355 (**2008**).
7. J.-W. Kim, Polarization Effects in Intermediate Temperature, Anode-Supported Solid Oxide Fuel Cells, *J. Electrochem. Soc.* 146, 69 (**1999**).
8. T. Ackmann, L. G. J. de Haart, W. Lehnert, and D. Stolten, Modeling of Mass and Heat Transport in Planar Substrate Type SOFCs, *J. Electrochem. Soc.* 150, A783 (**2003**).
9. R. Suwanwarangkul, E. Croiset, M. W. Fowler, P. L. Douglas, E. Entchev, and M. A. Douglas, Performance comparison of Fick’s, dusty-gas and Stefan–Maxwell models to predict the concentration overpotential of a SOFC anode, *J. Power Sources* 122, 9 (**2003**).
10. Y. Shi, N. Cai, and C. Li, Numerical modeling of an anode-supported SOFC button cell considering anodic surface diffusion, *J. Power Sources* 164, 639 (**2007**).
11. L. Andreassi, G. Rubeo, S. Ubertini, P. Lunghi, and R. Bove, Experimental and numerical analysis of a radial flow solid oxide fuel cell, *Int. J. Hydrog. Energy* 32, 4559 (**2007**).
12. B. Todd and J. B. Young, Thermodynamic and transport properties of gases for use in solid oxide fuel cell modelling, *J. Power Sources* 110, 186 (**2002**).
13. T. Boëdec, M. Reytier, D. Lhachemi, D. Tschumperlé, P. Louat, S. Di Iorio, P. Baurens, and G. Delette, A New Stack to Validate Technical Solutions and Numerical Simulations, *Fuel Cells* 12, 239 (**2012**).
14. W. Lehnert, J. Meusinger, and F. Thom, Modelling of gas transport phenomena in SOFC anodes, *J. Power Sources* 87, 57 (**2000**).
15. B. Morel, J. Laurencin, Y. Bultel, and F. Lefebvre-Joud, Anode-Supported SOFC Model Centered on the Direct Internal Reforming, *J. Electrochem. Soc.* 152, A1382 (**2005**).
16. X. Sun, M. Chen, S. H. Jensen, S. D. Ebbesen, C. Graves, and M. Mogensen, Thermodynamic analysis of synthetic hydrocarbon fuel production in pressurized solid oxide electrolysis cells, *Int. J. Hydrog. Energy* 37, 17101 (**2012**).
17. W. Li, H. Wang, Y. Shi, and N. Cai, Performance and methane production characteristics of H2O–CO2 co-electrolysis in solid oxide electrolysis cells, *Int. J. Hydrog. Energy* 38, 11104 (**2013**).

18. W. Y. Lee, J. Hanna, and A. F. Ghoniem, On the Predictions of Carbon Deposition on the Nickel Anode of a SOFC and Its Impact on Open-Circuit Conditions, *J. Electrochem. Soc.* 160, F94 (**2012**).
19. J. Aicart, J. Laurencin, M. Petitjean, and L. Dessemond, Experimental Validation of Co-Electrolysis Modeling, *Proc. 2013 FDFC Congr.* (**2013**).
20. M. Ni, An electrochemical model for syngas production by co-electrolysis of H2O and CO2, *J. Power Sources* 202, 209 (**2012**).
21. C. Stiller, B. Thorud, S. Seljebø, Ø. Mathisen, H. Karoliussen, and O. Bolland, Finite-volume modeling and hybrid-cycle performance of planar and tubular solid oxide fuel cells, *J. Power Sources* 141, 227 (**2005**).
22. A. Weber and E. Ivers-Tiffée, Materials and concepts for solid oxide fuel cells (SOFCs) in stationary and mobile applications, *Eighth Ulm. Electrochem. Tage* 127, 273 (**2004**).
23. W. G. Bessler, J. Warnatz, and D. G. Goodwin, The influence of equilibrium potential on the hydrogen oxidation kinetics of SOFC anodes, *Solid State Ion.* 177, 3371 (**2007**).
24. S. B. Adler, Mechanism and kinetics of oxygen reduction on porous La1−xSrxCoO3−δ electrodes, *Solid State Ion.* 111, 125 (**1998**).
25. S. Primdahl and M. Mogensen, Oxidation of hydrogen on Ni/yttria-stabilized zirconia cermet anodes, *J. Electrochem. Soc.* 144, 3409 (**1997**).
26. F. Usseglio-Viretta, J. Laurencin, G. Delette, J. Villanova, P. Cloetens, and D. Leguillon, Quantitative microstructure characterization of a Ni–YSZ bi-layer coupled with simulated electrode polarisation, *J. Power Sources* 256, 394 (**2014**).

# Chapter 4

# Model Validation

# Chapter 4

# Model Validation

The aim of this chapter is to present experimental validation of the model developed and previously detailed. The overall methodology (Chapter 1) was applied on two commercial cathode supported cells (*i.e.* adjustment of 'apparent' exchange current densities for steam and $CO_2$ electrolysis on single electrolysis experimental polarization curves, before simulating co-electrolysis operation). The electrochemical protocols implemented highlight the different overpotentials through composition and flow changes, allowing for exchange current densities numerical evaluation. Using these values, the global validity of the co-electrolysis model was then assessed by comparing experimental polarization curves to simulated ones obtained in the same conditions. In addition, gas analyses were carried out to validate the expression of the 'surface ratio' parameter $\beta$. Finally, a sensitivity analysis was also performed to better understand co-electrolysis mechanisms.

The first cell was supplied by the Jülich research center (FZJ - Forschungszentrum *Jülich*, Germany). The cell microstructure was investigated prior to this work by Usseglio-Viretta and Laurencin (*cf.* [1, 2] and F. Usseglio-Viretta PhD thesis, 2014), so that the actual microstructure parameters could be inputted in the model.

The second tested cell was a commercial high performances CSC, enabling to achieve higher current densities than the FZJ cell. However, the cell microstructure was relatively unknown. Therefore, the corresponding microstructure parameters were numerically adjusted along with exchange current densities using single electrolyzes polarization curves.

## 4.1. Model Version

As stated in Chapter 3, the model can simulate a planar SRU integrated in a stack environment. However, it is also well adapted to describe a single radial cell operating in isothermal mode. Radial cells of 50 *mm* diameter and up to 34 *mm* active surface diameter could be characterized in the test bench used (Chapter 3), where the cell temperature is mostly controlled by the large oven in which it is placed. Such statement is corroborated by the maximum temperature variations, experimentally measured by thermocouples placed near the cell, which did not exceed ±2*°C*. Accordingly, simulations presented in this chapter were performed considering the isothermal radial co-flow version of the model. It implies that a uniform temperature equal to 800*°C* was assumed.

The thermal module (*cf.* Figure 3-9 and 3-10) was therefore not used to obtain the simulations presented in this chapter. The influence of temperature on the cells performances and SRU operation will be described in Chapter 5.

## 4.2. Investigations of a CSC with a Known Microstructure (FZJ)

Single electrolysis experiments and models served to assess the 'apparent' exchange current densities for both $H_2O$ and $CO_2$ single electrolyzes. Then, the co-electrolysis model was used to simulate the cell operating in this mode, and the simulations were compared to experimental data as means of model validation.

### 4.2.1. Cell

Initial performances were recorded at 800°*C* in single electrolysis and co-electrolysis modes. The investigated radial cell was composed of a 1 *mm* thick Ni-8YSZ cathodic substrate supporting a 10 $\mu m$ thick electrolyte and a 50 $\mu m$ thick anode. The oxygen electrode was constituted by a functional layer of LSM-YSZ on which pure LSM was deposited to ensure current collection. The cell active area was equal to 9.1 $cm^2$. The actual microstructural parameters of the cathode support were determined by Laurencin *et al.* [1, 2], using X-ray nanotomography and 3D reconstructions (Figure 4-1), and are reported in Table 4-1. The anode microstructure was modeled using the same values for the porosity and mean pore radius while the anodic tortuosity factor that was set equal to 4 [3, 4].

| **Electrode** | **Porosity ($\varepsilon$)** | **Tortuosity factor ($\tau$)** | **Mean pore radius ($\bar{r}$)** |
|---|---|---|---|
| Cermet - Cathode | 0.43 | 2.8 | 1.2 $\mu m$ |

Table 4-1: Actual cermet microstructure obtained by X-ray nanotomography [1, 2].

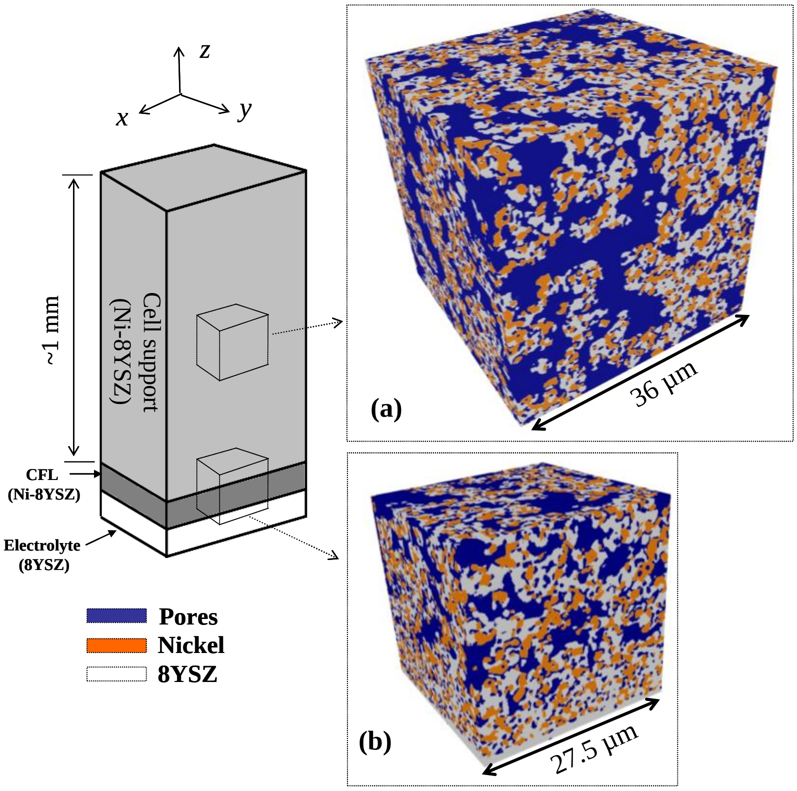

Figure 4-1: Representation of the three-dimensional reconstructed microstructure of the studied Ni-8YSZ support [1, 2].

### 4.2.2. Experiments

The experimental conditions used for steam and carbon dioxide single electrolyzes, as well as co-electrolysis, are reported in Table 4-2. Gas flows and compositions were chosen to highlight the cathodic concentration overpotentials (*i.e.* conversion and/or diffusion) at high faradaic conversion rates. The inlet flows of $H_2O$ and $CO_2$ were kept constant in experiments A1 to A4 and A5 to A8 respectively. The ratios of steam to hydrogen and $CO_2$ to CO were set to 50/50, 65/35 and 80/20 *vol.%* in experiment A1/A5, A2/A6 and A3/A7 respectively. The influence of the dilution ratio was investigated through experiments A1 and A4 for $H_2O$ electrolysis, and experiments A5 and A8 for $CO_2$ electrolysis. Co-electrolysis experimental conditions have been obtained by setting the $H_2O/H_2$ and $CO_2/CO$ ratios to 80/20 and changing the H/C ratio from 1/1 (experiment A9) to 4/1 (experiment A10), while respecting a dilution ratio of 10 *vol.%* $N_2$. Finally, the air flow at the anode side was set twice as much as the total flow at the cathode side, in order to limit cell temperature variations and maintain isothermal conditions during operation.

The experimental protocol was carried out within 36 *h* to avoid degradation of the investigated cell. To check this assumption, the polarization curve in the conditions of experiment A1 was recorded several times throughout the protocol.

| **Experiment** | **[$H_2O$]** | **[$H_2$]** | **[$CO_2$]** | **[CO]** | **[$N_2$]** | **$F_{tot\ cath}$** |
|---|---|---|---|---|---|---|
| - | *vol.%* | *vol.%* | *vol.%* | *vol.%* | *vol.%* | *$NmL.min^{-1}.cm^{-2}$* |
| **A1** | 45 | 45 | 0 | 0 | 10 | 13.34 |
| A2 | 59 | 32 | 0 | 0 | 10 | 10.23 |
| A3 | 72 | 18 | 0 | 0 | 10 | 8.31 |
| A4 | 25 | 25 | 0 | 0 | 50 | 23.94 |
| **A1** | 45 | 45 | 0 | 0 | 10 | 13.34 |
| A5 | 0 | 0 | 45 | 45 | 10 | 10.20 |
| A6 | 0 | 0 | 59 | 32 | 10 | 7.84 |
| A7 | 0 | 0 | 72 | 18 | 10 | 6.37 |
| A8 | 0 | 0 | 25 | 25 | 50 | 18.36 |
| A9 | 36 | 9 | 36 | 9 | 10 | 16.62 |
| A10 | 58 | 14 | 14 | 4 | 10 | 10.39 |
| **A1** | 45 | 45 | 0 | 0 | 10 | 13.34 |

Table 4-2: Gas feeding conditions tested on the commercial FZJ CSC at $T = 800°C$.

### 4.2.3. Cell Stability

To use single electrolyzes experiments to estimate apparent exchange current densities, the cell should not suffer major degradation throughout the entire electrochemical protocol (Table 4-2). Indeed, all exchange current densities adjusted onto degraded polarization curves would be underestimated. Moreover, the comparison of co-electrolysis experiments to the simulations would be irrelevant since apparent exchange current densities evolve with degradations.

Experiment A1 was taken as a reference experiment to detect any degradation of the investigated cell. It was not recorded after $CO_2$ electrolysis to avoid the influence of modifying the electrolysis mode (Table 4-2). As shown in Figure 4-2, successive measurements did not significantly alter the cell performances. However, limited degradations are evidenced after $CO_2$ electrolysis and co-electrolysis modes. The modifications of the *i*-*V* curve are very slight so that it does not have an impact on the determination of the exchange current density related to $CO_2$ electrolysis, as discussed hereafter (see section 4.2.5).

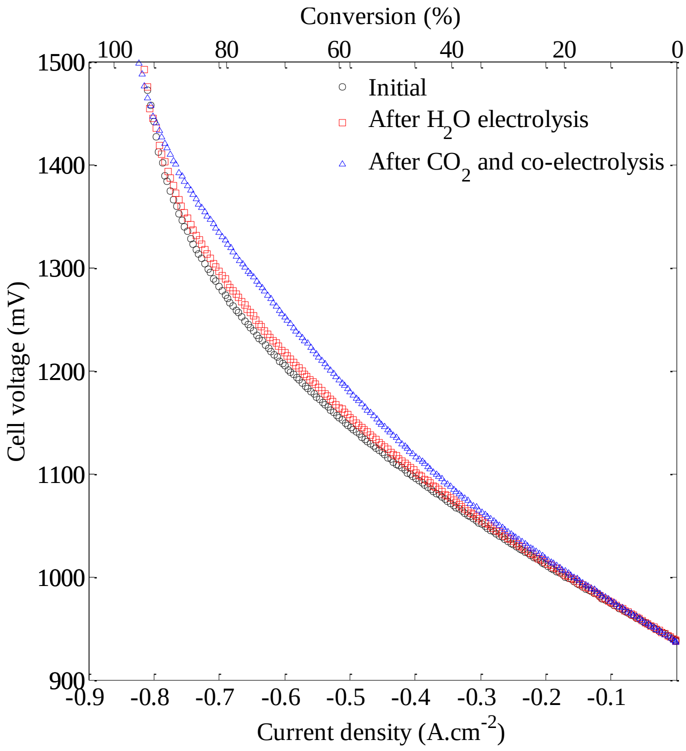

Figure 4-2:
Evolution of the reference polarization curve for Experiment A1 throughout the electrochemical protocol.

(o) initial
(□) at the end of $H_2O$ electrolysis measurements
(Δ) after $CO_2$ electrolysis and co-electrolysis measurements.

### 4.2.4. Polarization Curves for $H_2O$ and $CO_2$ Single Electrolyzes

Figures 4-3 and 4-4 display polarization curves recorded in both single electrolysis modes. All measured OCV values are within 1% of theoretical predictions based on the Nernst Law (Equations (3-21) and (3-22)). From impedance spectroscopy measurements, the total contact ASR of the investigated cell was estimated to $1.3\times10^{-2}$ $\Omega.cm^2$ at OCV. These results confirm the gas tightness between anodic and cathodic compartments, and highlight the good electrical contacts between the cell and the current collectors at the beginning of the test protocol.

Gas inlets at the cathode side were adapted to achieve suitable conversion rates so that the concentration overpotentials become predominant. Therefore, the steam conversion rate reached 95% at 1.5 $V$ on experiment A3 (Figure 4-3) and the $CO_2$ conversion rate was equal to 94% at 1.35 $V$ on experiment A7 (Figure 4-4). In order to avoid rapid cell degradation, polarization curves were stopped before the $H_2O$ or $CO_2$ conversion rate exceeded roughly 95%.

In agreement with literature reports [5–7], the performances for $CO_2$ electrolysis are lower than for $H_2O$ reduction (Figures 4-3 and 4-4). For instance, at 1.1 $V$ and for similar faradaic conversion rate, the calculated ASR values for $CO_2$ electrolysis (0.6-0.7 $\Omega.cm^2$) are higher than the ones for $H_2O$ reduction (0.4-0.5 $\Omega.cm^2$). The conversion rate at 1.5 $V$ changes little for steam to hydrogen ratio varying from 1 to 4, whereas a more significant increase is recorded for $CO_2$ electrolysis at 1.35 $V$ for equivalent $CO_2$/CO ratios. These results agree with those of Fan *et al.* [8] for nearly similar ratios, and Bidrawn *et al.* [9]. For both $H_2O$ and $CO_2$ electrolysis, the performances are enhanced by increasing the total flow at the cathode side, as already reported [10]. Therefore, at this stage, the increase in ASR for $CO_2$ electrolysis compared to $H_2O$ electrolysis can be partly related to the lower gas flow (Table 4-2). Regardless the reduction reaction, increasing the nitrogen content yields an increase of the cell voltage even if the total gas flow increases. This is explained by a lower effective gas diffusivity when increasing the diluent content [11].

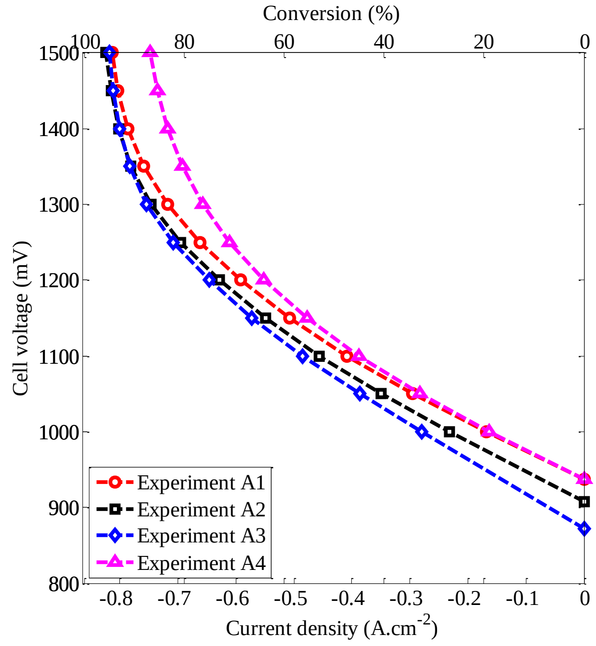

Figure 4-3: Experimental polarization curves for experiments A1 to A4 ($H_2O$ electrolysis).

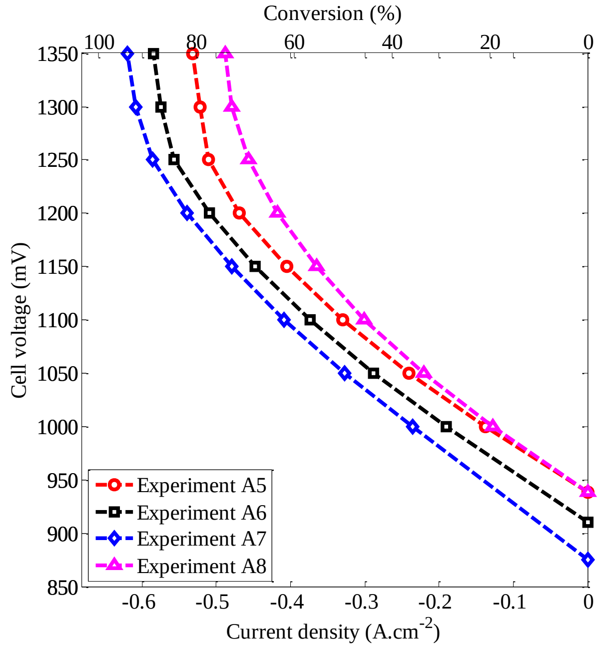

Figure 4-4: Experimental polarization curves for experiments A5 to A8 ($CO_2$ electrolysis).

### 4.2.5. Determination of Cathodic 'Apparent' Exchange Current Densities $i_{0,cathode}^{H_2-H_2O}$ and $i_{0,cathode}^{CO-CO_2}$

Single electrolysis models were used to determine the 'apparent' cathodic exchange current density for both $H_2O$ and $CO_2$ electrolysis. For this purpose, the actual microstructural parameters of the tested cell were used in the simulations (Table 4-1) and the 'apparent' anodic exchange current density was set to 200 $mA.cm^{-2}$. This value has been widely used in SOFC and SOEC studies [12–14] for typical electrodes operated with air at 800°$C$. In these conditions, the apparent cathode exchange current densities (related to steam and carbon dioxide single electrolyzes) remain the only free variables.

#### 4.2.5.1. Steam Electrolysis

Several studies have assessed or used a value in the order of 530 $mA.cm^{-2}$ [3, 15–17] for the cathodic exchange current density in case of a typical Ni-YSZ electrode operated in steam electrolysis conditions at 800°C. Using this input value, the steam electrolysis model becomes entirely predictive. Figure 4-5 displays all simulated polarization curves related to the $H_2O$ electrolysis experimental protocol (experiments A1 to A4) and Figure 4-6 compares experimental data and simulations for experiment A4. A fair global agreement is found: the model successfully anticipates OCV, ASR and limiting current densities as well as variations between the different experimental conditions. As a consequence, the global behavior of the simulated cell response tends to validate the electrolysis model.

However, a slight difference can be noticed between experimental curves and simulated data for high current densities ($|i| > 0.5$ $A.cm^{2}$), corresponding to high conversion rates (> 60%). This discrepancy could be due to inaccuracies on the amount of steam effectively reaching the cell for these experiments. Indeed, uncertainties of 5% have been estimated on steam flow rates introduced at the cell inlet. That could explain a main part of the difference between simulated and experimental limiting current densities. Moreover, the mass transfer calculation across the thick cathode depends on its microstructural properties and gas diffusion coefficients. A slight error on these parameters could also introduce a bias in the simulations.

The single steam electrolysis model can also be used to adjust any parameter on experimental data. In order to study the cell response sensitivity on the cathode exchange current density, a modeling-based approach was developed to fit this parameter on the experimental polarization curves. It was computed by coupling the single electrolysis model with an error minimization algorithm focusing solely on the low current density sections of the experimental data. In this condition, the cell response is mainly governed by activation overpotentials and not by concentration overpotentials. For each suggested value of $i_{0,cathode}^{H_2-H_2O}$, the complete electrochemical module was run iteratively and the corresponding least squares error was computed and minimized.

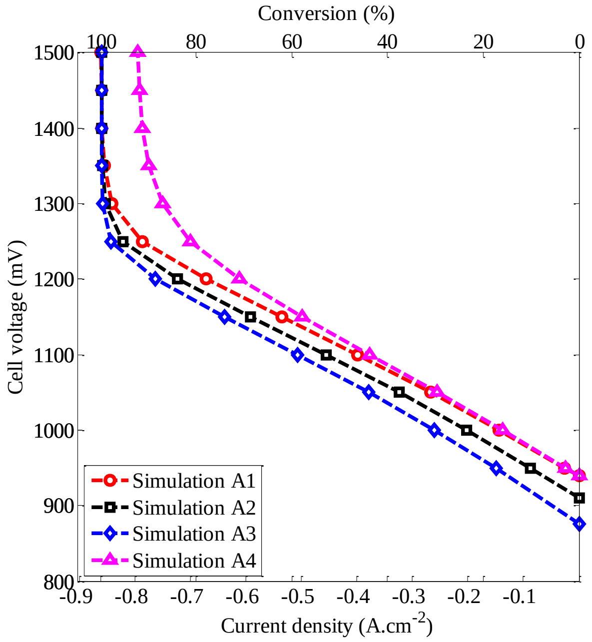

Figure 4-5: Simulated polarization curves for experiments A1 to A4 ($H_2O$ electrolysis) with all model inputs set ($i_{0,cathode}^{H_2-H_2O}$ = 530 $mA.cm^{-2}$).

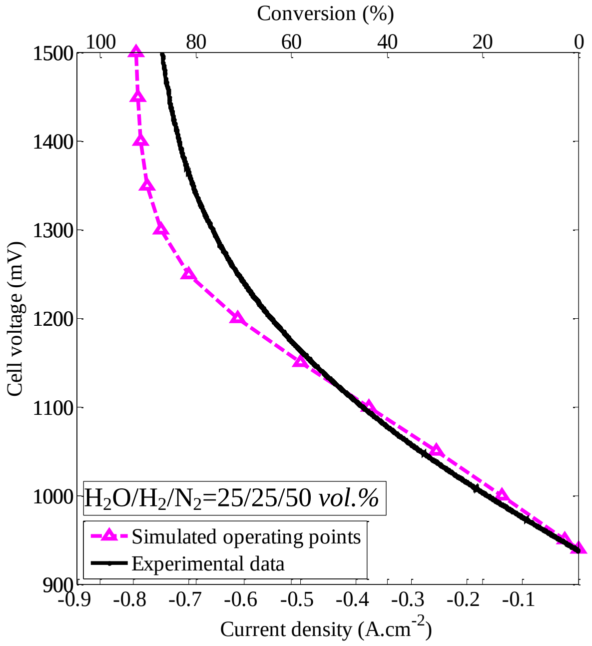

Figure 4-6: Experimental and simulated polarization curves for experiment A4.

Table 4-3 summarizes the simulated values for $H_2O$ exchange current density computed from experiments A1-A4. Only limited variations are observed and the results average at 560 $mA.cm^{-2}$, in agreement with previously published reports [3, 15–17] (*i.e.* 530 $mA.cm^{-2}$). The as-obtained slight difference inclines to endorse the numerical method developed to assess $i_0$. Moreover, this slight discrepancy can probably be attributed to the effect of electrode microstructure on exchange current density. It should be noted that, as expected, adjusting the exchange current density did not improve the gap observed at high polarizations.

| **Experiment** | A1 | A2 | A3 | A4 |
|---|---|---|---|---|
| $i_{0,cathode}^{H_2-H_2O}$ $(mA.cm^{-2})$ | 584 | 572 | 546 | 551 |

Table 4-3: Values for $i_{0,cathode}^{H_2-H_2O}$ adjusted on experimental data.

### 4.2.5.2. Carbon Dioxide Electrolysis

Carbon dioxide electrolysis on nickel cermet-based cells has received a growing but limited attention compared to steam electrolysis. Therefore, the modeling based approach developed in the previous section was applied to $CO_2$ electrolysis in order to assess the corresponding exchange current density (Figure 4-7). The $i_0^{CO-CO_2}$ parameters fitted on A5-A8 experimental polarization curves are reported in Table 4-4, with values averaging at 370 $mA.cm^{-2}$.

As expected, the exchange current density is lower for $CO_2$ electrolysis compared to $H_2O$ electrolysis. It is worth emphasizing that this computed average $i_0^{CO-CO_2}$ is in the same range than those usually reported in SOFC modes [12–14]. A good agreement is found between experimental and simulated data (Figure 4-8). Similarly to steam electrolysis simulation results (Figure 4-6), the model successfully predicts variations in ASR, maximum currents and OCV for carbon dioxide.

| **Experiment** | A5 | A6 | A7 | A8 |
|---|---|---|---|---|
| $i_{0,cathode}^{CO-CO_2}$ ( $mA.cm^{-2}$) | 398 | 376 | 337 | 381 |

Table 4-4: Values of apparent exchange current density fitted on $CO_2$/CO experimental data.

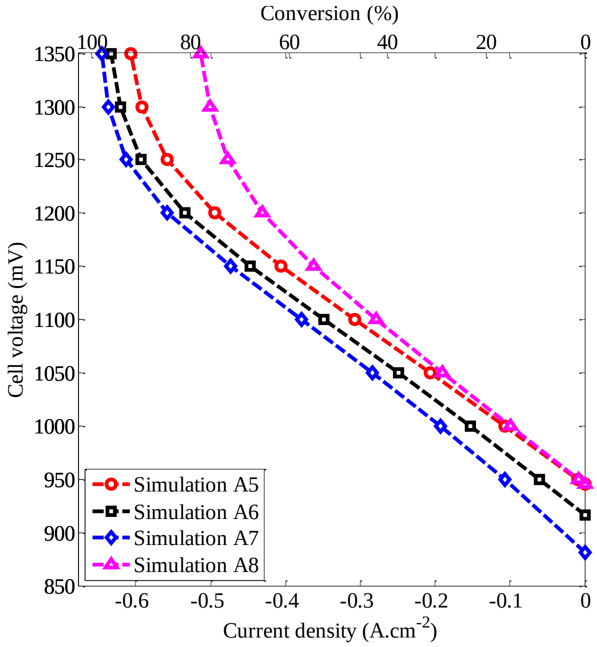

Figure 4-7: Simulated polarization curves for experiments A5 to A8 ($CO_2$ electrolysis) with computed $i_{0,cathode}^{CO-CO_2}$.

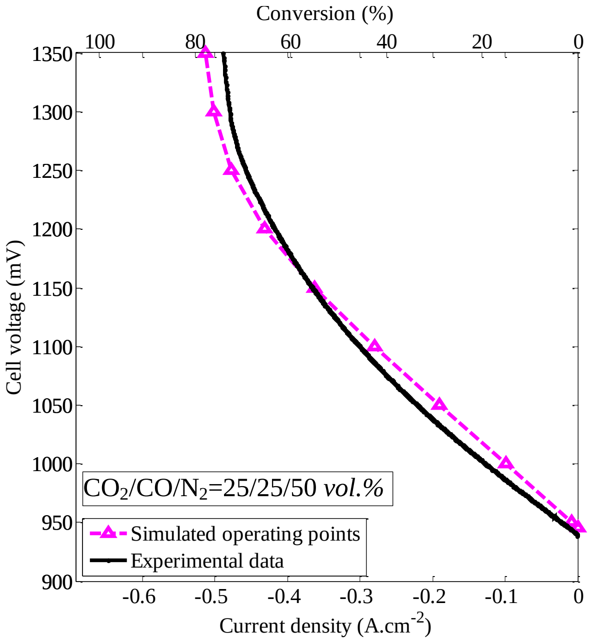

Figure 4-8: Experimental and simulated polarization curves for experiment A8.

In comparison with the simulation of $H_2O$ electrolysis (Figure 4-6), no significant discrepancy between experimental data and simulations arises for high current densities and high conversion rates (Figure 4-8). This suggests that diffusional process and associated $CO_2$ electrolysis concentration overpotentials were well calculated in the corresponding model. As a consequence, the gap obtained in $H_2O$ electrolysis between simulated and experimental data is likely to arise from the experimental setup and/or steam flow rather than uncertainties on the microstructural model inputs. Besides, this result could mean that the DGM and its associated diffusion coefficients are especially well adapted to describe the $CO/CO_2$ diffusion through porous electrodes. But it could also suggest that the DGM is not fully predictive at high conversion for $H_2/H_2O$ feedings, even if this model remains, at the time of writing, the most relevant to calculate the diffusional process across porous SOEC/SOFC electrodes.

### 4.2.6. Prediction of Cell Behavior in Co-Electrolysis Mode

Based on the above results, the average values for $i_{0,cathode}^{H_2-H_2O}$ and $i_{0,cathode}^{CO-CO_2}$ were implemented in the co-electrolysis model. Thus, corresponding simulations were performed without any neither free nor adjusted parameters.

Polarization curves were computed in the same operating conditions than experiments A9 and A10 (Table 4-2). A fair agreement is found between simulated results and experimental polarization curves as shown in Figures 4-9 and 4-10. This confirms the ability of the developed model to predict the cell global behavior in co-electrolysis conditions, especially at low current densities. Accordingly, this model appears representative and could give insights on the co-electrolysis process and its parametric evolutions.

As could be expected, a slight difference between experimental data and simulation is evidenced at the highest current densities. These last conditions correspond to high conversion rates for both electroactive species. This is consistent with the results obtained in steam electrolysis mode (Figure 4-6).

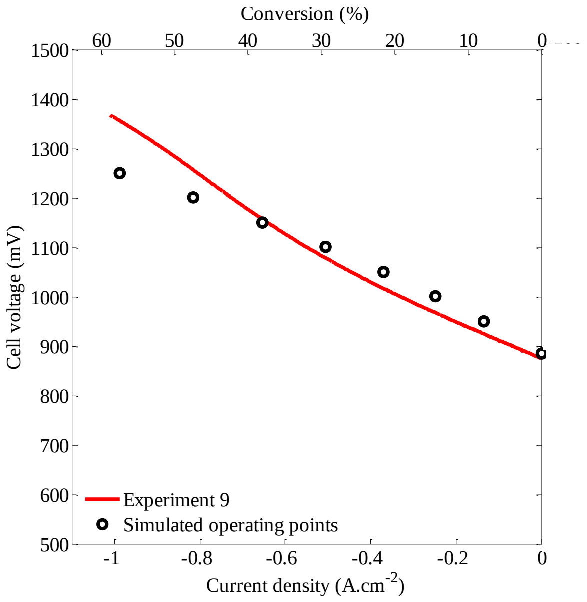

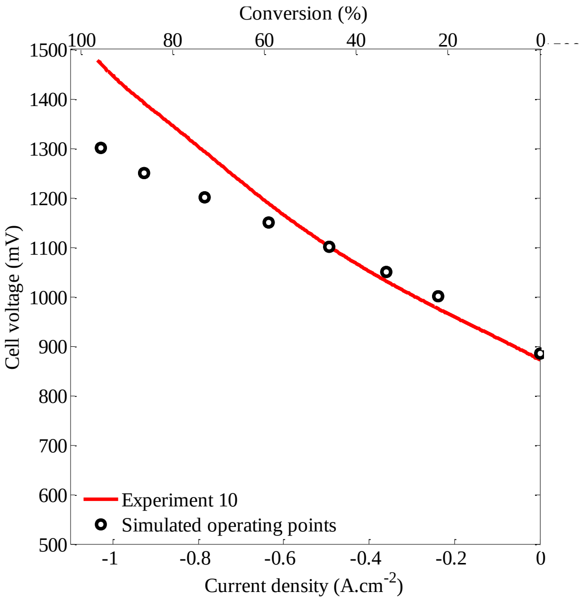

Figure 4-9: Experimental and simulated polarization curves for experiment A9.

Figure 4-10: Experimental and simulated polarization curves for experiment A10.

## 4.2.7. Steam Outlet Mass Balance in Co-Electrolysis Operation

A steady state estimation of the steam content in the outlet flow was performed on the FZJ cell. The condenser (Figure 3-2) was emptied before the beginning of the experiment, and the cell operated at a constant current density of -0.96 *A.cm*$^{-2}$ during 191.5 *h*. The cathode was fed with the inlet of experiment A9 (Table 4-2).

At the end of the experiment, 177.8 *g* of water was weighted using a high precision balance. This corresponds to a constant Steam Conversion (SC) equal to 64.6% (Table 4-5). This hypothesis was experimentally validated through gas analyses performed in galvanostatic operation and presented in section 4.3.8. Considering the saturation vapor pressure at the condenser temperature, the outlet gas stream still contained about 10 *mbars* of water vapor and thus, the experimental SC should be decreased by ≈1%. In the chosen conditions, simulations predict a global SC of 60.4%. The good agreement between experimental and simulated SC represents an additional validation element for the co-electrolysis model.

| Parameter | Value | Unit | Parameter | Value | Unit |
|---|---|---|---|---|---|
| Total time | 191.5 | *h* | Weighted water | 177.8 | *g* |
| Inlet steam flow | 3.26 | *NL.h*$^{-1}$ | Water recovered | 35.4 | *%* |
| | 1.455×10$^{-1}$ | *mol.h*$^{-1}$ | **Experimental SC** | **64.6 %** | |
| $M_{H_2O}$ | 18 | *g.mol*$^{-1}$ | | | |
| Total steam sent to the cell | 27.87 | *mol* | **Simulated SC** | **60.4 %** | |
| | 501.7 | *g* | | | |

Table 4-5: Summary of steam outlet mass balance experiment.

## 4.2.8. Intermediate Conclusions

At this stage, the fair agreement between experimental and simulated data emphasizes the ability of the developed model to describe the different phenomena involved in a SOC in electrolysis modes. The model hypotheses seem therefore appropriate to predict the cell global behavior (*i.e.* polarization curves).

Nevertheless, not all parameters have been validated, as for instance the surface ratio $\beta$ (Equation (3-18)) influencing the outlet gas composition. Moreover, the gaps between experimental data and simulated *i-V* curves evidenced at high current densities in steam electrolysis (Figure 4-6) and co-electrolysis (Figure 4-10) modes are likely to originate from inaccuracies on the amount of steam reaching the cell. The degradation observed on cells tested with the chosen experimental protocol (Table 4-2) could be related to $CO_2$ electrolysis. To overcome these discrepancies, some modifications of the experimental test bench and protocols were made. The cathode outlet gas was analyzed by gas chromatography. A pressure sensor was added to the cathode compartment of the test bench, and the gas tightness evaluation procedure (Chapter 3) was implemented. The path and flow of $N_2$ were optimized to ensure that all steam produced was available for the chemical reactions. Finally, polarization curves for $CO_2$ electrolysis were recorded after co-electrolysis measurements. All commercial cells were subsequently studied using this modified experimental framework.

## 4.3. Investigations of a CSC with Unknown Microstructure (Optimized Cell)

### 4.3.1. Methodology

A second commercial CSC was tested to further validate the co-electrolysis model. However, contrary to the previous FZJ cell, the electrodes microstructure was unknown. Therefore, Scanning Electron Microscopy (SEM) examinations were performed and polarization curves were recorded in single electrolysis modes to assess the cathode support layer microstructure parameters (porosity, tortuosity factor and mean pore diameter) and 'apparent' exchange current densities ($i_{0,cathode}^{CO-CO_2}$, $i_{0,cathode}^{H_2O-H_2}$ and $i_{0,anode}$).

### 4.3.2. Cell

The cell consisted of a thick Ni-8YSZ cathode (thickness 500 *µm*, diameter 50 *mm*), a thin 8YSZ electrolyte (5 *µm*), an intermediate layer of CGO (2 *µm*), and a LSC anode (20 *µm*). The anode was 20 *mm* in diameter so that the electroactive cell area was 3.14 $cm^2$.

The cermet porosity was evaluated to 0.46 by manual segmentation (with ImageJ software) of a polished cross section image (Figure 4-11). It was obtained with a Scanning Electron Microscopy in Back Scattering Electron mode using a Philips XL30 scanning electron microscope complemented by a Si-Li Oxford Instruments Detector. Additionally, the mean pore radius was estimated to about 1.2 *µm*.

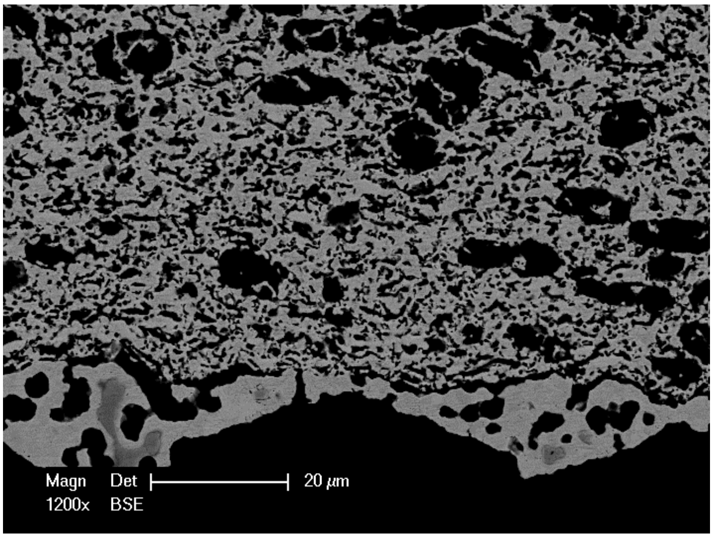

Figure 4-11:
SEM cross-section examination of the commercial cermet.
A thin Ni layer, probably used to improve electrical contact, is observed on this micrograph.

### 4.3.3. Experiments

Initial performances of the investigated CSC were recorded at 800*°C* in steam electrolysis, co-electrolysis and $CO_2$ electrolysis modes. Experimental conditions of the chosen protocol are given in Table 4-6. For each experiment, the corresponding polarization curve was recorded. All low and high flow rates experiments display respectively the same initial amount of oxidized species (*i.e.* $H_2O$ and/or $CO_2$). Thus, performances in the different modes can be directly compared since gas conversions will be equal at a given current density. The overall protocol was carried out in 12 *h* to limit cell degradation. To check the cell performance stability, the polarization curve corresponding to Experiment B1 was recorded after each mode change. It should be emphasized that the maximum variation recorded between experimental OCV and Nernst law predictions was merely 0.4%.

The cathode outlet gas composition corresponding to Experiment B3* was investigated by µGC as a function of the current density. Therefore, the molar fractions of $H_2$, $N_2$, $O_2$, $CH_4$, CO and $CO_2$ were measured at OCV, -0.48, -0.96, -1.43 and -1.75 $A.cm^{-2}$, respectively. Additionally, the WGS reaction kinetics implemented in the model was validated through gas analyses at OCV. Finally, the evolution of the outlet composition in steady state operation was investigated over 288 *h*.

| **Exp.** | **$H_2O$**<br>*vol.%* | **$H_2$**<br>*vol.%* | **$CO_2$**<br>*vol.%* | **CO**<br>*vol.%* | **$N_2$**<br>*vol.%* | **$F_c$**<br>*$NmL.min^{-1}cm^{-2}$* | **$F_a$** |
|---|---|---|---|---|---|---|---|
| **B1** | 40% | 40% | | | 20% | 12.5 | 25 |
| B2 | 64% | 16% | | | 20% | 12.5 | 25 |
| B2* | 64% | 16% | | | 20% | 30 | 60 |
| B3* | 48% | 16% | 16% | | 20% | 30 | 60 |
| B4* | 32% | 16% | 32% | | 20% | 30 | 60 |
| **B1** | 40% | 40% | | | 20% | 12.5 | 25 |
| B5 | | | 40% | 40% | 20% | 12.5 | 25 |
| B6 | | | 64% | 16% | 20% | 12.5 | 25 |
| B6* | | | 64% | 16% | 20% | 30 | 60 |
| **B1** | 40% | 40% | | | 20% | 12.5 | 25 |

Table 4-6: Electrochemical experimental protocol. $F_c$ and $F_a$ correspond to cathodic and anodic inlet flow rates respectively. * highlights high flows.

### 4.3.4. Cell Stability

Figure 4-12 shows the evolution of the cell response under steam electrolysis (Experiment B1) throughout the electrochemical protocol. As it can be observed, the co-electrolysis protocol had no noticeable impact on the reference curve. However, reaching the $CO_2$ electrolysis limiting current seems to have slightly degraded the cell response. Indeed, the ASR calculated in the linear part of the polarization curve increased from 0.26 $\Omega.cm^2$ to 0.29 $\Omega.cm^2$ during the tests. Despite this slight degradation, one can infer that the global cell response remained nearly stable throughout the electrochemical measurements. Thus, all experimental data were used for modeling and simulations.

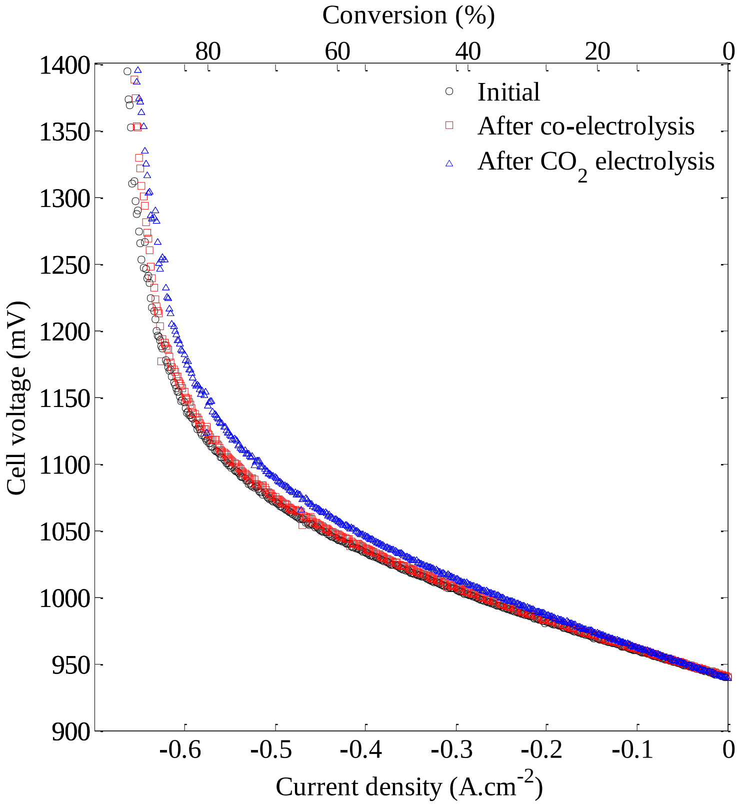

Figure 4-12:
Evolution of the reference polarization curve (experiment B1, $H_2O$ electrolysis) throughout the electrochemical protocol.

(o) initial
(□) after co-electrolysis
(Δ) after $CO_2$ electrolysis.

### 4.3.5. Experimental and Simulated Single Electrolyzes Polarization Curves

The polarization curves obtained for $CO_2$ electrolysis (Experiments B5, B6 and B6*) and in $H_2O$ electrolysis (Experiments B1, B2 and B2*) modes are presented in Figures 4-13 and 4-14, respectively. It is worth noting that the behavior of the cell as a function of operating parameters agrees with those previously published in the literature. When the concentration of reactants ($CO_2$ or $H_2O$) increases, the OCV decreases as expected from the Nernst law [18]. As shown on Figure 4-13, the cell performances for $CO_2$ reduction increase with $CO_2$ flow rate, (*i.e.* decrease of the total cell overpotential and total polarization resistance) [8, 9, 19]. This is well in agreement with the recorded behavior of the FZJ cell (Figure 4-4). If one refers to the single $H_2O$ electrolysis (Figure 4-14), an increase of steam concentration in the feed gas yields enhanced performances as already reported [20–22]. In agreement with theoretical predictions [23], increasing the oxidant flow rate favors higher performances at a given current density [10, 24]. Finally, the comparison of results in Figures 4-13 and 4-14 further confirms that lower current densities are recorded for $CO_2$ electrolysis compared to $H_2O$ electrolysis, which agrees with literature reports [5–7], and previous results obtained with the FZJ cell (*cf.* section 4.2).

The following aims at assessing the electrokinetic parameters of all three electrochemical reactions (Equations (3-1) to (3-3)) related to the cell considered, as well as the unknown microstructure parameters.

The anode was modeled using usual values of microstructural parameters, as reported in the literature [3] and already implemented in section 4.2. It should be noted that these parameters have a limited influence on the cell global response. Indeed, under air sweeping (*i.e.* $y_{O_2}^{int\_i=0}$), if the produced oxygen transport through the electrode were to be extremely hindered by the microstructure so that $y_{O_2}^{int\_i\neq 0}=1$, the corresponding concentration overpotential should be limited to 36 $mV$ (*cf.* Equation (3-32)).

#### 4.3.5.1. Determination of Cathode Tortuosity Factor and $i_{0,cathode}^{CO-CO_2}$

Since the cathode porosity and mean pore radius were assessed (*cf.* section 4.3.2), only the cathodic tortuosity factor, which largely controls the limiting currents, remains to be adjusted on experimental data at high cell polarization. Since the model can accurately predict the $CO_2$ electrolysis response (Figure 4-8), $\tau_c$ was firstly determined by fitting simulations on polarization curves of experiments B5 and B6 to grasp limiting currents.

The 'apparent' exchange current densities $i_{0,cathode}^{CO-CO_2}$ and $i_{0,anode}$ were then tuned to be representative of the cell ASR (Table 4-7). It is worth mentioning that the as-obtained values are higher by a factor 4 than literature reports [15, 25, 26]. However, one must keep in mind that these values are 'apparent' macroscopic descriptions of microscopic mechanisms which strongly depend on microstructure. Consequently, a higher exchange current density can be expected for an optimized functional layer exhibiting a higher density of TPBl. For the investigated cell, a sensitivity analysis was performed to quantify the influence of $i_0$ on the simulated response (*cf.* section 4.3.10).

As can be seen in Figure 4-13, a good agreement is found for experiments B5 and B6, and the complete set of parameters ($\tau_c$, $\overline{r}_c$, $i_{0,cathode}^{CO-CO_2}$, $i_{0,anode}$) stands to accurately simulate the polarization curve at higher inlet gas flow (Experiment B6*). Conversion rates obtained at 1.4 *V* for these experiments are 83%, 82% and 53% respectively.

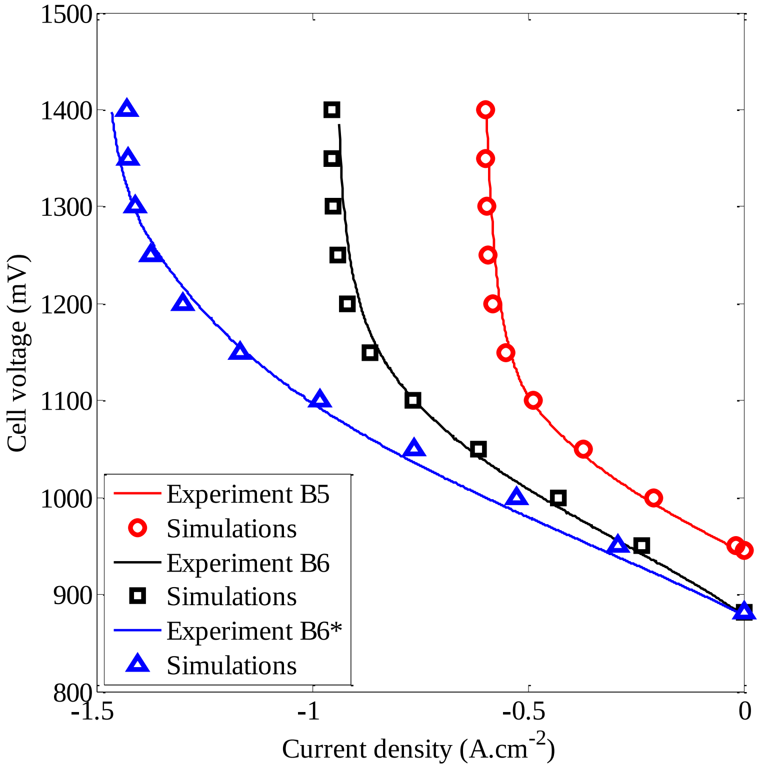

Figure 4-13: Experimental and simulated polarization curves for experiments B5, B6 and B6* ($CO_2$ electrolysis).

| | | | |
|---|---|---|---|
| **Microstructural parameters** | $\tau_c$ (a) | $\overline{r}_c$ (b) | $\varepsilon_c$ (b) |
| | 7.8 | 1.2 $\mu m$ | 0.46 |
| | $\tau_a$ (d) | $\overline{r}_a$ (d) | $\varepsilon_a$ (d) |
| | 4 | 1.2 $\mu m$ | 0.43 |
| **'Apparent' exchange current densities** ($mA.cm^{-2}$) | $i_{0,cathode}^{H_2O-H_2}$ (c) | $i_{0,cathode}^{CO-CO_2}$ (a) | $i_{0,anode}$ (a) |
| | 4×560 | 4×370 | 4×520 |

Table 4-7: Microstructure parameters and 'apparent' exchange current densities

(a) Numerical adjustment, (b) from SEM examinations,

(c) assuming $i_{0,cathode}^{H_2O-H_2} / i_{0,cathode}^{CO_2-CO} = 1.51$ (section 4.2.5), (d) section 4.2.1.

#### 4.3.5.2. Determination of $i_{0,cathode}^{H_2-H_2O}$

The ratio of electrochemical oxidation rates of $H_2$ to that of CO was reported to be in the range of 2-2.5 at $800°C$ [27]. It was then suggested to use such values to express $R_0 = i_{0,cathode}^{H_2O-H_2} / i_{0,cathode}^{CO_2-CO_2}$ [25]. As done for the FZJ cell (section 4.2), $R_0$ was evaluated to 1.51 from experimental polarization curves. This value was thus kept constant in this section, leading to $i_0^{H_2-H_2O} = 4 \times 560\ mA.cm^{-2}$. Therefore, no further adjustments were made to simulate steam electrolysis.

As for carbon dioxide electrolysis (Figure 4-13), a global agreement is evidenced between experimental and simulated results (Figure 4-14). Modeling predicts both OCV and ASR variations when the inlet composition and/or flow are modified. However, the simulations seem to overestimate limiting current densities for $H_2O$ electrolysis, as previously observed for the FZJ cell (Figure 4-6). The gap is evidenced at high conversion rates when hydrogen becomes predominant in the gas phase. This could be partly related to uncertainties concerning the amount of steam effectively reaching the cell. But on may also evoke the ability of the DGM relevance to model $H_2/H_2O$ transport in SOEC at high polarizations, when $H_2$ is preponderant. Indeed, the effective Knudsen diffusion of hydrogen is 3-5 times larger than for the other components, and the effective binary diffusion coefficient of steam in hydrogen is 5.5 times higher than that of $CO_2$ in CO [28, 29]. In other words, in the as-modeled $H_2O$ electrolysis (*i.e.* constant $i_0^{H_2-H_2O}$), diffusion of $H_2$ (*i.e.* through DGM, diffusion coefficients, *etc.*) is largely enhanced compared to the other gaseous components.

Nevertheless, it can be concluded that both single electrolysis models can simulate the global cell response with the set of microstructure parameters and 'apparent' exchange current densities implemented.

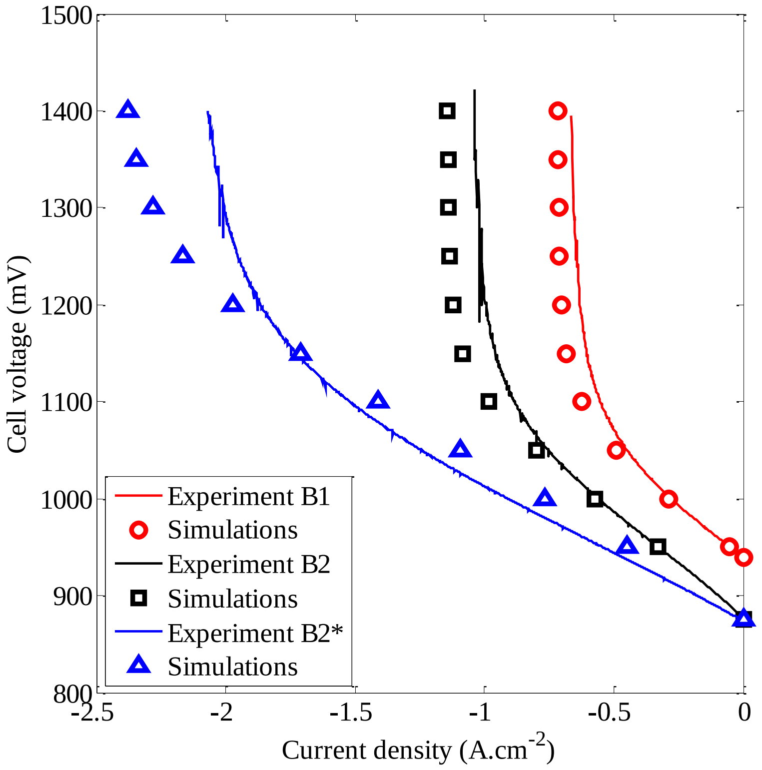

Figure 4-14: Experimental and simulated polarization curves for experiments B1, B2 and B2* ($H_2O$ electrolysis).

## 4.3.6. Comparison of Experimental and Simulated Co-Electrolysis *i*-*V* Curves

The former parameters were inputted in the co-electrolysis model, which thus became entirely predictive as no further adjustment on parameters was made. As expected, the model can simulate the ASR increase and decrease of limiting current density when introducing $CO_2$ (Figures 4-15 and 4-16). The higher the $CO_2$ content, the lower is this limiting current density. Moreover, a gap is observed at high polarization but its magnitude is lowered compared to $H_2O$ electrolysis (Figure 4-14), due to the presence of $CO_2$/CO.

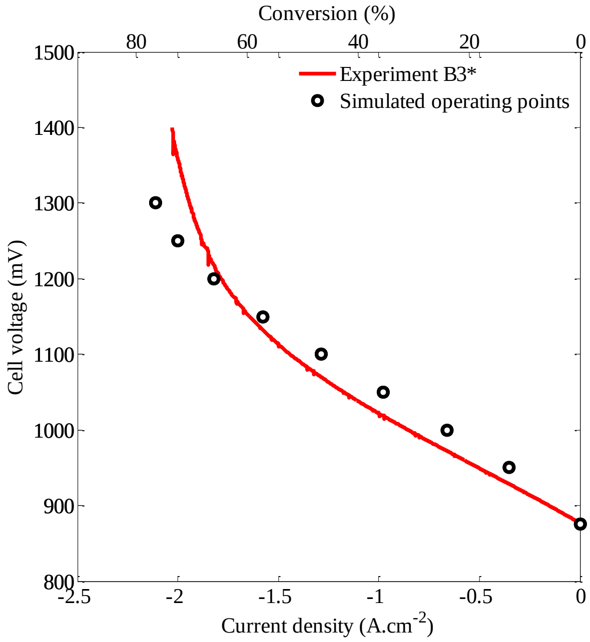

Figure 4-15: Experimental and simulated polarization curves for experiment B3*.

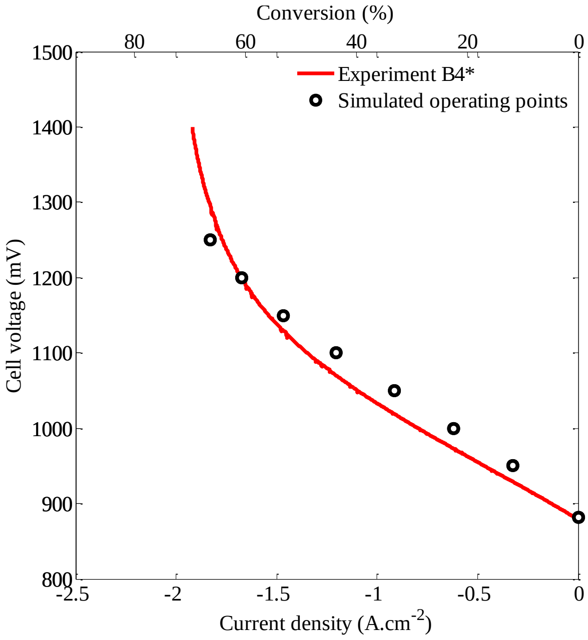

Figure 4-16: Experimental and simulated polarization curves for experiment B4*.

This first step of model validation is based on comparisons between experimental and simulated polarization curves. Therefore, only the global cell response is compared to the simulations. Additional experiments are thus required to further extend the range of use of the co-electrolysis model. Consequently, the following sections aim at validating, on one hand, the WGS reaction kinetics implemented in the model and, on the other hand, the model ability to predict co-electrolysis outlet compositions under operation.

### 4.3.7. Gas Analyses – WGSR Kinetics Validation

Four water gas Shift reaction Experiments (SExp., Table 4-8) were performed to validate the kinetics of the WGS reaction implemented in the model (*cf.* Table 3-4). In order to increase the experimental accuracy, the inlet gas flows were significantly higher than those used in the previous protocols (Tables 4-2 and 4-6). Gas analyses were carried out on the gaseous outlets at OCV and 800°*C*. Compositions for SExp.1 to 3 were compatible with a co-electrolysis process, whereas the composition for SExp.4 was the furthest from the chemical equilibrium that could be achieved without risking the cermet deactivation.

Considering the radial co-flow configuration of the experimental test bench (Figure 4-17), one can expect variations of gas composition inside the volume of the cathode [25], and along the cell radius [29]. The last assumption becomes meaningful if one considers the catalytic effect of nickel on the WGS reaction [30]. Accordingly, simulations corresponding to SExp.4 were initially performed to quantify the volume required to be representative of experimental measurements, and thus evaluate the rate of the WGS reaction. For this purpose, the simulations were carried out for cermet volumes comprised between 10 *mm* radius (*i.e.* $\pi \times (10\,mm/2)^2 \times 0.5\,mm \times 0.46 = 18.1\,mm^3$) and an infinite radius. Note that the real available volume at the cathode side arguably corresponds to a radius of 22.5 *mm* (*i.e.* 91.4 $mm^3$).

No nitrogen was detected in the cathode outlet gas for SExp.4 (Table 4-8). This ensured gas tightness of the investigated cell. The as-obtained results were compared to simulations considering an infinite radius (*i.e* thermodynamic equilibrium).

As can be seen in Figure 4-18, a very good agreement between experimental and calculated outlet composition for SExp.4 is obtained for a radius at least equal to 22.5 *mm*. Accordingly, all other simulations were performed considering a radius of 22.5 *mm*. In this condition, the agreement is preserved, since the difference between experimental and simulated partial pressures $\left|y^*_{i,exp} - y^*_{i,sim}\right|$ (*i* = $H_2$, $O_2$, $N_2$, CO or $CO_2$, * indicates the removal of $H_2O$) peaks at 2.9% and averages at 1.1% for SExp.1 to 4 (Figure 4-19).

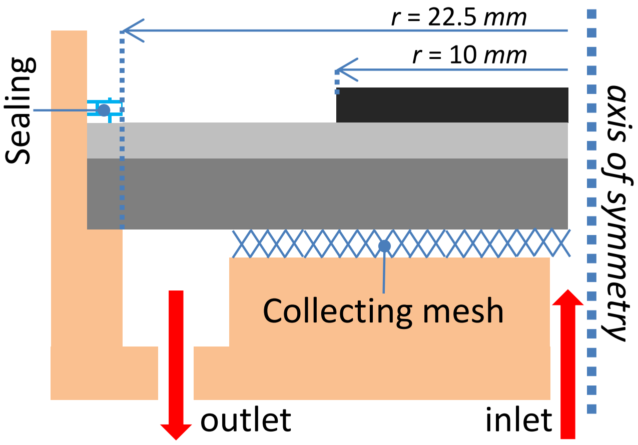

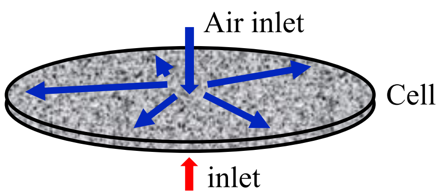

Figure 4-17:
Diagram of the test bench in the cell vicinity.

**Experimental protocol**

| SExp. | $H_2O$<br>*vol.%* | $H_2$<br>*vol.%* | $N_2$<br>*vol.%* | CO<br>*vol.%* | $CO_2$<br>*vol.%* | $F_c$<br>$NmL.min^{-1}cm^{-2}$ |
|---|---|---|---|---|---|---|
| 1 | 36.0 | 12.0 | 40.0 |  | 12.0 | 40.0 |
| 2 | 52.9 | 17.7 | 11.8 |  | 17.6 | 40.8 |
| 3 | 45.0 | 15.0 | 10.0 |  | 30.0 | 48.0 |
| 4 | 42.9 | 14.3 |  | 42.9 |  | 37.2 |

**µGC outlet simulations vs. radius**

| SExp. | $H_2$<br>*vol.%* | $N_2$<br>*vol.%* | CO<br>*vol.%* | $CO_2$<br>*vol.%* | *r*<br>*mm* |
|---|---|---|---|---|---|
| 4 | 37.5 |  | 45.9 | 16.6 | 10 |
| 4 | 43.5 |  | 31.8 | 24.7 | 22.5 |
| 4 | 43.6 |  | 31.6 | 24.8 | ∞ |

**µGC outlet measurements**

| SExp. | $H_2$<br>*vol.%* | $N_2$<br>*vol.%* | CO<br>*vol.%* | $CO_2$<br>*vol.%* | Raw total<br>*vol.%* |
|---|---|---|---|---|---|
| 1 | 15.0 | 65.8 | 3.4 | 15.5 | 99.7 |
| 2 | 30.2 | 29.2 | 7.1 | 32.8 | 99.3 |
| 3 | 18.9 | 20.9 | 8.8 | 51.9 | 100.5 |
| 4 | 42.1 | 0.0 | 30.9 | 27.3 | 100.3 |

**µGC outlet simulations (*r* = 22.5 *mm*)**

| SExp. | $H_2$<br>*vol.%* | $N_2$<br>*vol.%* | CO<br>*vol.%* | $CO_2$<br>*vol.%* | *r*<br>*mm* |
|---|---|---|---|---|---|
| 1 | 15.9 | 64.7 | 3.5 | 15.9 | 22.5 |
| 2 | 32.8 | 26.9 | 7.5 | 32.8 | 22.5 |
| 3 | 20.6 | 19.8 | 9.2 | 50.4 | 22.5 |
| 4 | 43.5 |  | 31.8 | 24.7 | 22.5 |

Table 4-8: Micro gas chromatography experimental protocol, results and simulations. Outlet measurements and simulations take into account the removal of water prior to entering the µGC apparatus.

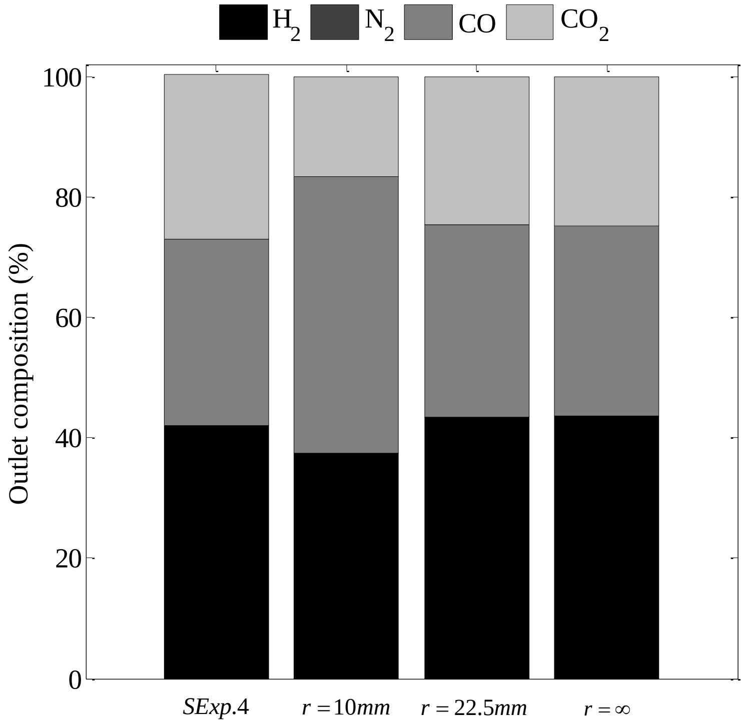

Figure 4-18:
Experimental and simulated gas composition corresponding to SExp.4.
Influence of the available volume for the WGS reaction on the outlet composition.

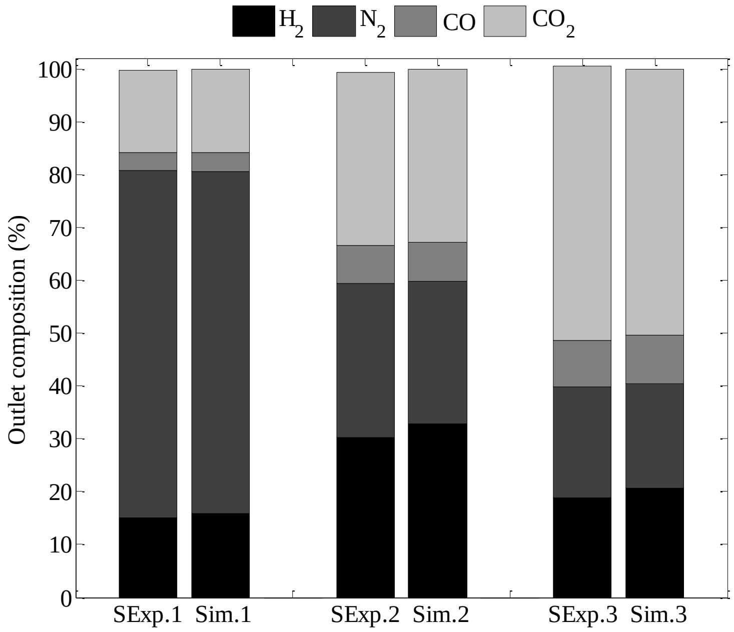

Figure 4-19: Experimental and simulated gas compositions for SExp.1 to 3. The reaction is assumed to occur in the pores of the cermet ($\varepsilon_c = 0.46$ and cathode thickness of 500 *µm*) over a surface of 22.5 *mm* radius.

These results clearly show that the WGS reaction kinetics used in the co-electrolysis model are fast enough to reach a chemical equilibrium state at the cell outlet. Since these gas compositions depend on the temperature, the good correlation between simulations and chromatography analyses also indicates that the WGS reaction only occurs in the cathode volume.

### 4.3.8. Gas Analyses – Galvanostatic Operation

As mentioned above, the reliability of the co-electrolysis model depends on the relevance of the surface ratio $\beta$ (Equation (3-17)), describing the readiness of the cathode for $H_2O$ electrolysis compared to $CO_2$ electrolysis. In order to determine the governing parameters for co-electrolysis processes, gas analysis of the cathode outlet was performed during 288 *h*, in isothermal operation, at 800°*C* and -0.67 $A.cm^{-2}$. The inlet gas composition corresponds to experiment B3* (Table 4-6) and the faradaic conversion is equal to 24.3% in the chosen conditions.

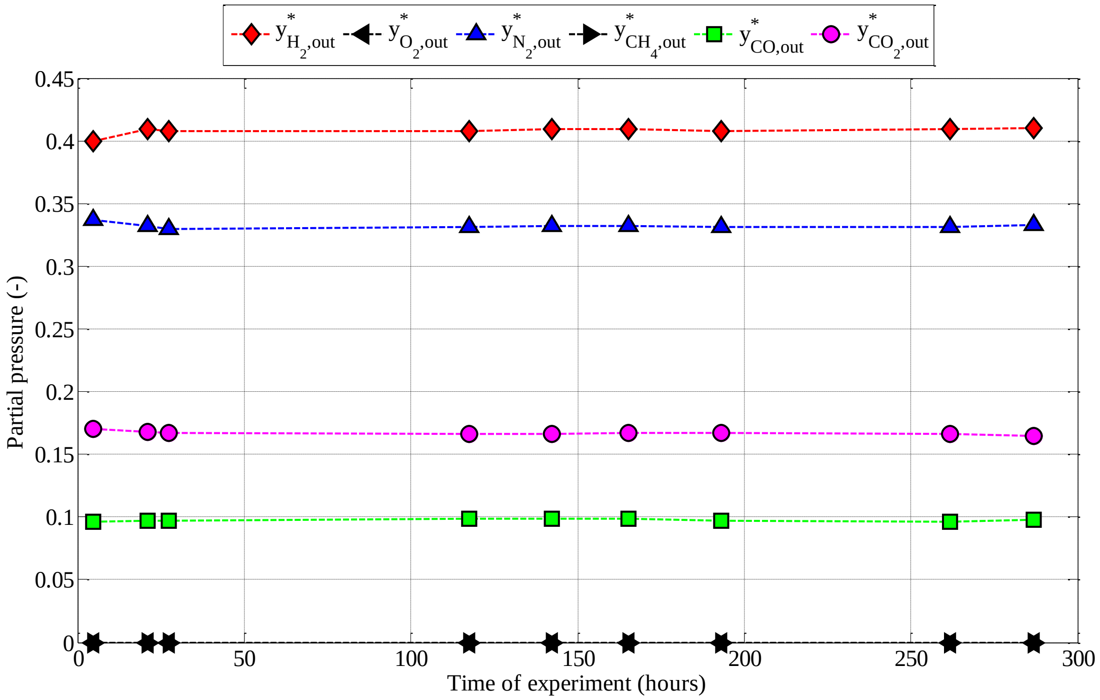

Figure 4-20: Gas chromatography results in stationary conditions over 288 *h* (B3$^*$,48/16/16/20 *vol.%* $H_2O/CO_2/H_2/N_2$, -0.67 $A.cm^{-2}$ – 24.3% faradaic conversion). $y^*$ are the molar fractions after removal of $H_2O$.

Similarly to the results presented in the previous section, the sum of gas volume fractions for each analysis displays a raw total equal to 100% ±1%. This is a good indicator of the measurements accuracy and apparatus calibration. In agreement with thermodynamic predictions [31], no $CH_4$ was detected. No significant evolution of $H_2$, $N_2$, CO and $CO_2$ partial pressures in the cathodic outlet flow was recorded during the galvanostatic operation (Figure 4-20). Similar results were obtained over 230 *h* by Nguyen *et al.* [32]. The stability of all measured partial pressures during this experiment induces that the steam molar fraction at the cell outlet remained also nearly constant. It was estimated to 38-40 *vol.%* from µGC measurements, assuming gas tightness of the complete cathode path (the method of calculation is presented in the following paragraph). However, the cell voltage steadily increased from its initial value of 1.3 *V* (Figure 4-21). Assuming a linear variation versus time, one can calculate an increasing rate of the cell potential equal to +0.506 $mV.h^{-1}$, amounting to ≈150 *mV* over 288 *h*.

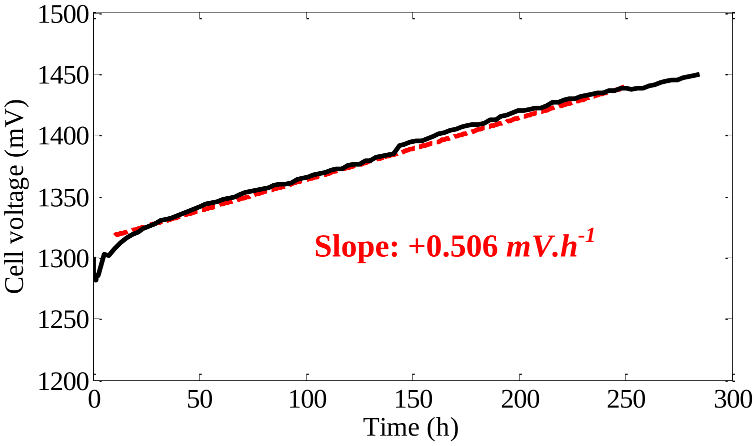

Figure 4-21:
Evolution of the cell voltage during the 288 *h* steady state experiment at -0.67 *A.cm*$^{-2}$ and 24.3% faradaic conversion

No outlet composition evolution was detected in this experiment. Therefore, the phenomenological approach developed in this work is validated, as the co-electrolysis mechanism stability was demonstrated through nearly 300 *h*. Furthermore, if the cathode microstructure is not deeply modified (due to massive nickel particles agglomeration or catalyst passivation), surface and interface phenomena should not be altered. In this case, the competition between $H_2O$ and $CO_2$ electrolyzes should also remain unchanged. Such hypothesis is corroborated by the fact that the cell voltage increase did not affect the outlet gas composition. This remark suggests that the underlying co-electrolysis mechanism could be controlled by surface phenomena, such as gas molecule adsorption/desorption, since these phenomena, in general, do not involve charged species. Then, at a given current density, the repartition of surface activities for $H_2O$ and $CO_2$ electrolyzes would be independent of the local electrical field. Consequently, all further comparisons between simulations and gas analyses by µGC were performed as a function of the current crossing the SOEC.

### 4.3.9. Gas Analyses – Effect of Current

Gas chromatography measurements and simulations were compared for different current densities in order to fully validate the expression of the surface ratio $\beta$. Gas analyses were performed by µGC on the cell cathodic outlet at OCV, 0.48, 0.96, 1.43 and 1.75 *A.cm*$^{-2}$. The cell operated in the conditions of experiment B3* (Table 4-6) at 800°*C*. Experimental results and simulations are compared in Figure 4-22. One must remind that the molar fractions reported in Figure 4-22 correspond to the outlet gas composition after steam condensation.

A remarkable agreement is highlighted over a wide range of conversion rates (from OCV up to 64 % Faradaic conversion). Experimental and simulated $N_2$ outlet partial pressures at OCV are identical. As this gas is chemically and electrochemically neutral, it is a rigorous indicator of the complete cathodic gas line tightness. Additionally, it should be noted that $N_2$ partial pressure behaves as expected. Indeed, because the µGC apparatus does not measure water contents, the relative importance of nitrogen decreases when $H_2$ is produced.

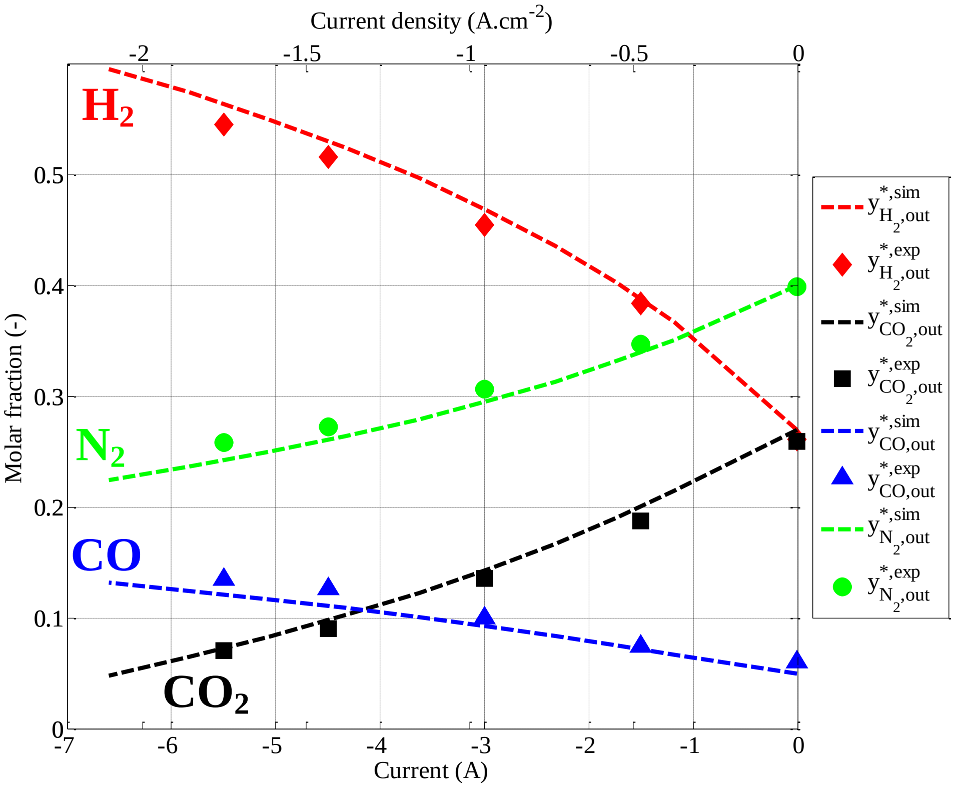

Figure 4-22: Gas chromatography analyses and simulated outlet compositions (48/16/16/20 *vol.%* $H_2O/CO_2/H_2/N_2$) at OCV, -0.48, -0.96, -1.43 and -1.75 $A.cm^{-2}$. $y^*$ are the molar fractions after condensation of $H_2O$.

All chemical reactions occurring at the cathode side are equimolar and conserve the total amount carbon atoms. Furthermore, since complete cathodic gas line tightness was evidenced, the amount of nitrogen is also preserved. Consequently, it is possible to compute the cell outlet steam molar fraction from µGC measurements through conservation of nitrogen and carbon atoms, using following equations (4-1) and (4-2):

$$y_{H_2O}^{cell\ outlet}\left(y_{N_2}^{*,\mu GC,i\neq 0}\right)=1-\frac{y_{N_2}^{inlet}}{y_{N_2}^{*,\mu GC,i\neq 0}} \tag{4-1}$$

$$y_{H_2O}^{cell\ outlet}\left(y_{C}^{*,\mu GC,i\neq 0}\right)=1-\frac{y_{CO_2}^{inlet}+y_{CO}^{inlet}}{y_{CO_2}^{*,\mu GC,i\neq 0}+y_{CO}^{*,\mu GC,i\neq 0}} \tag{4-2}$$

where $y_j$ is the usual molar fraction of specie j, and $y^*$ the molar fraction after removal of $H_2O$.

It should be noted that these equations amount to dilute µGC results with steam so that N and C atoms are conserved.

Figure 4-23 reports the comparison between simulated steam molar fraction at the cell outlet and the ones computed using equations (4-1) and (4-2). A good global agreement is established, since maximum variations of the order of 5% between simulated and experiment based data are obtained. However, it should be emphasized that equations (4-1) and (4-2) respectively assume that $CO_2$+CO and $N_2$ molar fractions are exact. Consequently, these methods amplify the error on the steam outlet molar fraction, which could explain for the most part the correlations difference between Figures 4-22 and 4-23.

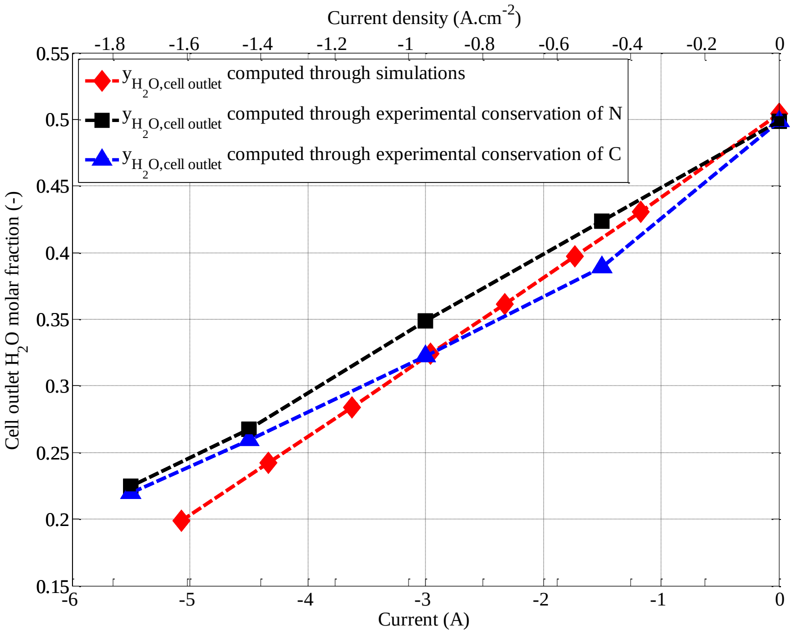

Figure 4-23: Evolution of steam molar fraction at the cell outlet with polarization (48/16/16/20 *vol.%* $H_2O/CO_2/H_2/N_2$).

As the modeled electrochemical processes and thus outlet composition are greatly dependent on the "surface ratio" $\beta$, the reported results would tend to validate its definition. Furthermore, this brings additional model validation elements, and strengthens our previous conclusions.

### 4.3.10. Sensitivity Analysis

In order to evaluate the respective influence of the "surface ratio" $\beta$, WGS reaction, and ratio of 'apparent' exchange current densities on the cell simulated response, a sensitivity analysis was performed. Inlet composition and flows correspond to experiment B3* (Table 4-6). The sensitivity is related to the response of the complete model (Chapter 3). The chosen parameters are given in Table 4-9. $\beta = 0.5$ means that both reduction reactions of $H_2O$ and $CO_2$ proceed on equal active surfaces (case D). $\beta = 1$ corresponds to a full hindering of $CO_2$ electrolysis and thus CO is solely produced by the reverse WGS reaction (case E). $\beta = 0.25$ represents the case where $CO_2$ electrolysis is favored compared to $H_2O$ electrolysis (case C). The influence of the WGS reaction was studied by nullifying its kinetic (case B). Finally, the impact of $R_0 = i_{0,cathode}^{H_2O-H_2} / i_{0,cathode}^{CO_2-CO_2}$ was determined by setting $i_{0,cathode}^{H_2O-H_2} = i_{0,cathode}^{CO_2-CO_2}$ (case A).

The different simulated polarization curves are shown in Figure 4-24. Figures 4-25 and 4-26 present the sensitivity analysis results at -1 and -1.5 *A.cm*$^{-2}$, respectively.

| **Study Case** | A | B | C | D | E |
|---|---|---|---|---|---|
| **Condition** | $R_0 = i_{0,cathode}^{H_2O-H_2} / i_{0,cathode}^{CO_2-CO_2} = 1$ | no WGS reaction | $\beta$=0.25 | $\beta$=0.5 | $\beta$=1 |

Table 4-9: Study cases for the sensitivity analysis.

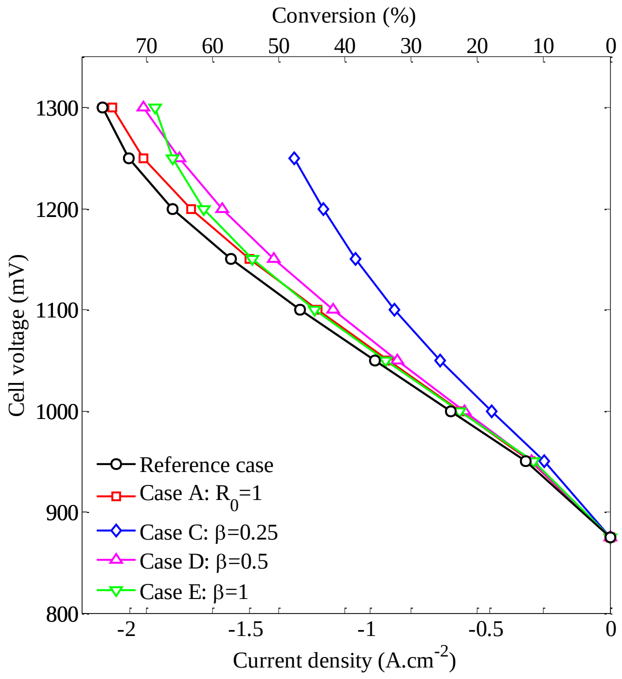

Figure 4-24:

Simulated polarization curves at 800°*C*

for all study cases A, C, D and E.

(30 *NmL.min$^{-1}$.cm$^{-2}$* of

48/16/16/20 *vol.%* $H_2O/CO_2/H_2/N_2$).

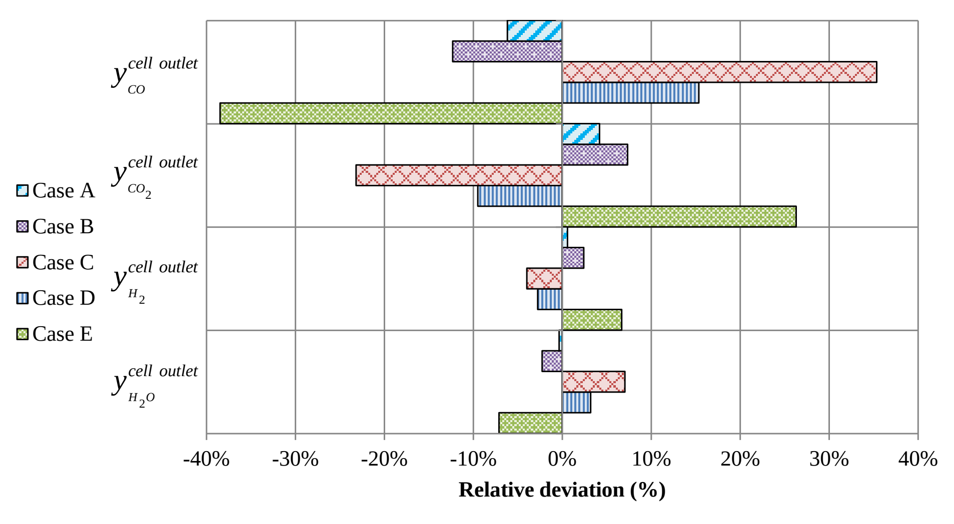

Figure 4-25:

Sensitivity

analysis results

at -1 *A.cm$^{-2}$*.

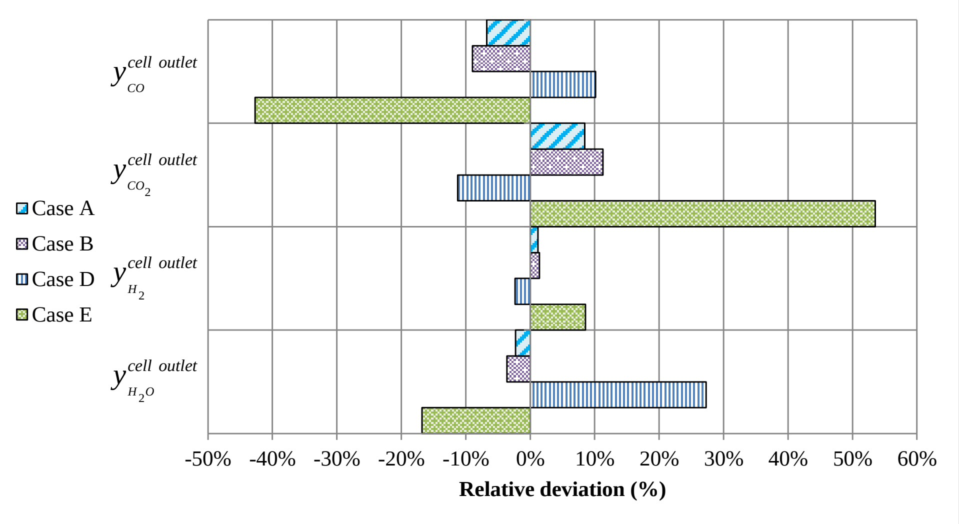

Figure 4-26:

Sensitivity

analysis results

at -1.5 *A.cm$^{-2}$*.

Polarization curves show limited deviations from the reference case, except for case C (Figure 4-24). Indeed, in these conditions, mass transfer limitations arising in $CO_2$ electrolysis mode prevented reaching higher current densities. Furthermore, assuming that 3/4 of the active surface participate to the reduction of $CO_2$ although $H_2O$ is the main component in the inlet stream obviously induces considerable changes in the overpotentials distribution, thus affecting the cell global response.

As shown in Figures 4-25 and 4-26, all studied cases display larger relative variations for $CO_2$/CO partial pressures compared to $H_2O/H_2$. This is mostly due to the inlet composition investigated, with no CO and characterized by a high ratio of hydrogen to carbon. However, since industrial co-electrolyzers are likely to rely on similar inlets with low to no CO contents, errors on estimations of outlet CO partial pressure would have extensive consequences on scale design.

Study case A ($R_0$=1) shows little variations of the polarization curve (+10 *mV*), and limited deviations concerning outlet compositions (<10%). Indeed, even if the $H_2O$ electrolysis kinetic is slowed down, steam remains the main component in the inlet gas, and diffuses faster than $CO_2$ through the porous cathode. Hence, the surface ratio definition (Equation (3-18)) insures that $H_2$ would still be produced to a greater extent than CO. Consequently, an error in determining the 'apparent' exchange current densities would have a confined impact on the cell simulated response.

When the WGS reaction kinetics is nil (case B), no influence on the polarization curve is evidenced, apart for at OCV. The error on outlet partial pressures, although moderate both at -1 and -1.5 $A.cm^{-2}$, decreases with higher polarization/current density. Both observations seem to lean toward a weak influence of the reverse WGS reaction under current and conversely confirm the predominance of electrochemical reduction of $CO_2$ on the CO production. The relative impact of chemistry and electrochemistry over CO production will be detained in Chapter 5.

Cases C, D and E investigate the influence of the 'surface ratio' definition. Case C (*i.e.* $\beta$ = 0.25) corresponds to the furthest value of $\beta$ from the reference case (which is roughly equal to 0.8 when calculated with local partial pressures at the electrolyte interface). Since the limiting current appears at much lower current density, comparisons are not possible at -1.5 $A.cm^{-2}$. As can be expected when $CO_2$ electrolysis is favored, CO production and thus $CO_2$ consumption are widely overestimated. Indeed, observed deviations are in the 30% range. Conversely, if CO is only produced by the reverse WGS reaction (case E, $\beta$ = 1), $CO_2$

depletion is extensively underestimated. This last case displays the largest variations concerning partial pressures (*e.g.* $\Delta P_{CO_2}^{out} / P_{CO_2}^{ref} \simeq +55\%$ at -1 $A.cm^{-2}$). Finally, sensitivity results for case D ($\beta = 0.5$) appear somewhat in between those of cases C and E, with partial pressures variations in the range of 10-30%. As could be expected, outlet gas compositions depend on the "surface ratio" definition. Indeed, cases C, D and E all lead to significant variations concerning one or more gas components.

This sensitivity analysis highlights the impact of several relevant parameters on the cell simulated response. The limited influence of case A strengthens the methodology implemented on the optimized cell. Indeed, numerical and/or experimental uncertainties could have led to misestimate the 'apparent' exchange current densities. However, since the electrochemical competition between $H_2O$ and $CO_2$ electrolyzes is biased by mass transfer limitations, the influence of both cathodic exchange current densities appear to be limited. Additionally, as was highlighted in the previous section, a very good correlation has been obtained between experimental and simulated outlet partial pressures. Hence, if cases C, D and E had physical bases, the significant molar fraction variations obtained here when $\beta$ is not expressed by Equation (3-18) should have been picked up by the µGC analyses, especially at high current density. This leans toward validating further its definition and its uniqueness at the macroscopic scale.

## 4.4. Conclusion

The isothermal model was validated using polarization curves obtained on two types of commercial cathode supported cells. A numerical method for computing 'apparent' exchange current densities was detailed. Additionally, outlet gas composition measurements in galvanostatic operation over nearly 300 *h* confirmed that the co-electrolysis process could be described by a phenomenological 'surface ratio'. Finally, the proposed definition for this parameter (*i.e.* interfacial partial pressures ratio of electroactive species) was corroborated by the good agreement between simulated and experimental outlet partial pressures under current, as well as by the sensitivity analysis. These experiments have shown that, in the range of cell polarization and gas compositions investigated, the cathodic outlet composition only depends on current density and temperature. Indeed, no voltage dependence was highlighted.

## 4.5. References

1. J. Laurencin, R. Quey, G. Delette, H. Suhonen, P. Cloetens, and P. Bleuet, Characterisation of Solid Oxide Fuel Cell Ni–8YSZ substrate by synchrotron X-ray nano-tomography: from 3D reconstruction to microstructure quantification, *Journal of Power Sources* 198, 182 (**2012**).
2. F. Usseglio-Viretta, J. Laurencin, G. Delette, J. Villanova, P. Cloetens, and D. Leguillon, Quantitative microstructure characterization of a Ni–YSZ bi-layer coupled with simulated electrode polarisation, *Journal of Power Sources* 256, 394 (**2014**).
3. J. Laurencin, D. Kane, G. Delette, J. Deseure, and F. Lefebvre-Joud, Modelling of solid oxide steam electrolyser: Impact of the operating conditions on hydrogen production, *Journal of Power Sources* 196, 2080 (**2011**).
4. J. Laurencin, F. Lefebvre-Joud, and G. Delette, Impact of cell design and operating conditions on the performances of SOFC fuelled with methane, *Journal of Power Sources* 177, 355 (**2008**).
5. P. Kim-Lohsoontorn, N. Laosiripojana, and J. Bae, Performance of solid oxide electrolysis cell having bi-layered electrolyte during steam electrolysis and carbon dioxide electrolysis, *Current Applied Physics* 11, S223 (**2011**).
6. J. E. O'Brien, M. G. McKellar, C. M. Stoots, J. S. Herring, and G. L. Hawkes, Parametric study of large-scale production of syngas via high-temperature co-electrolysis, *International Journal of Hydrogen Energy* 34, 4216 (**2009**).
7. C. Graves, S. D. Ebbesen, and M. Mogensen, Co-electrolysis of CO2 and H2O in solid oxide cells: Performance and durability, *Solid State Ionics* 192, 398 (**2011**).
8. C. Fan, T. Iida, K. Murakami, T. Matsui, R. Kikuchi, and K. Eguchi, Investigation on the Power Generation and Electrolysis Behavior of Ni-YSZ⁄YSZ⁄LSM Cell in Reformate Fuel, *Journal of Fuel Cell Science and Technology* 5, 031202 (**2008**).
9. F. Bidrawn, G. Kim, G. Corre, J. T. S. Irvine, J. M. Vohs, and R. J. Gorte, Efficient Reduction of CO[sub 2] in a Solid Oxide Electrolyzer, *Electrochemical and Solid-State Letters* 11, B167 (**2008**).
10. X. Yue and J. T. S. Irvine, (La,Sr)(Cr,Mn)O3/GDC cathode for high temperature steam electrolysis and steam-carbon dioxide co-electrolysis, *Solid State Ionics* 225, 131 (**2012**).
11. Y. Jiang and A. V. Virkar, Fuel Composition and Diluent Effect on Gas Transport and Performance of Anode-Supported SOFCs, *Journal of The Electrochemical Society* 150, A942 (**2003**).
12. S. H. Chan, K. . Khor, and Z. . Xia, A complete polarization model of a solid oxide fuel cell and its sensitivity to the change of cell component thickness, *Journal of Power Sources* 93, 130 (**2001**).
13. M. Ni, Modeling of a solid oxide electrolysis cell for carbon dioxide electrolysis, *Chemical Engineering Journal* 164, 246 (**2010**).
14. M. Ni, Modeling of SOFC running on partially pre-reformed gas mixture, *International Journal of Hydrogen Energy* 37, 1731 (**2012**).
15. S. H. Chan and Z. T. Xia, Polarization effects in electrolyte/electrode-supported solid oxide fuel cells, *Journal of Applied Electrochemistry* 32, 339 (**2002**).
16. P.-W. Li and M. K. Chyu, Simulation of the chemical/electrochemical reactions and heat/mass transfer for a tubular SOFC in a stack, *Journal of Power Sources* 124, 487 (**2003**).
17. M. Ni, An electrochemical model for syngas production by co-electrolysis of H2O and CO2, *Journal of Power Sources* 202, 209 (**2012**).

18. W. Li, Y. Shi, Y. Luo, and N. Cai, Elementary reaction modeling of CO2/H2O co-electrolysis cell considering effects of cathode thickness, *Journal of Power Sources* 243, 118 (**2013**).
19. Y. Shi, Y. Luo, N. Cai, J. Qian, S. Wang, W. Li, and H. Wang, Experimental characterization and modeling of the electrochemical reduction of CO2 in solid oxide electrolysis cells, *Electrochimica Acta* 88, 644 (**2013**).
20. O. A. Marina, L. R. Pederson, M. C. Williams, G. W. Coffey, K. D. Meinhardt, C. D. Nguyen, and E. C. Thomsen, Electrode Performance in Reversible Solid Oxide Fuel Cells, *Journal of The Electrochemical Society* 154, B452 (**2007**).
21. M. A. Laguna-Bercero, R. Campana, A. Larrea, J. A. Kilner, and V. M. Orera, Steam Electrolysis Using a Microtubular Solid Oxide Fuel Cell, *Journal of The Electrochemical Society* 157, B852 (**2010**).
22. C. Jin, C. Yang, F. Zhao, D. Cui, and F. Chen, La0.75Sr0.25Cr0.5Mn0.5O3 as hydrogen electrode for solid oxide electrolysis cells, *International Journal of Hydrogen Energy* 36, 3340 (**2011**).
23. M. Ni, M. Leung, and D. Leung, Energy and exergy analysis of hydrogen production by solid oxide steam electrolyzer plant, *International Journal of Hydrogen Energy* 32, 4648 (**2007**).
24. J. S. Herring, J. E. O’Brien, C. M. Stoots, G. L. Hawkes, J. J. Hartvigsen, and M. Shahnam, Progress in high-temperature electrolysis for hydrogen production using planar SOFC technology, *International Journal of Hydrogen Energy* 32, 440 (**2007**).
25. M. Ni, An electrochemical model for syngas production by co-electrolysis of H2O and CO2, *Journal of Power Sources* 202, 209 (**2012**).
26. R. Maric, S. Ohara, T. Fukui, H. Yoshida, M. Nishimura, T. Inagaki, and K. Miura, Solid Oxide Fuel Cells with Doped Lanthanum Gallate Electrolyte and LaSrCoO3 Cathode, and Ni-Samaria-Doped Ceria Cermet Anode, *Journal of The Electrochemical Society* 146, 2006 (**1999**).
27. Y. Matsuzaki and I. Yasuda, Electrochemical Oxidation of H 2 and CO in a H 2-H 2 O-CO-CO 2 System at the Interface of a Ni-YSZ Cermet Electrode and YSZ Electrolyte, *Journal of the Electrochemical Society* 147, 1630 (**2000**).
28. B. Todd and J. B. Young, Thermodynamic and transport properties of gases for use in solid oxide fuel cell modelling, *Journal of Power Sources* 110, 186 (**2002**).
29. J. Laurencin, D. Kane, G. Delette, J. Deseure, and F. Lefebvre-Joud, Modelling of solid oxide steam electrolyser: Impact of the operating conditions on hydrogen production, *Journal of Power Sources* 196, 2080 (**2011**).
30. J. Xu and G. F. Froment, Methane steam reforming, methanation and water-gas shift: I. Intrinsic kinetics, *AIChE Journal* 35, 88 (**1989**).
31. P. J. Lunde and F. L. Kester, Carbon dioxide methanation on a ruthenium catalyst, *Industrial & Engineering Chemistry Process Design and Development* 13, 27 (**1974**).
32. V. N. Nguyen, Q. Fang, U. Packbier, and L. Blum, Long-term tests of a Jülich planar short stack with reversible solid oxide cells in both fuel cell and electrolysis modes, *International Journal of Hydrogen Energy* (**2013**)

# Chapter 5

# Simulation Results & Discussion

# Chapter 5

# Simulation Results and Discussion

Simulations obtained with the co-electrolysis model, validated in Chapter 4, are presented in this part. The corresponding results were obtained using input parameters corresponding to the FZJ cell. Indeed, as stated in Chapter 4, the model is entirely predictive when the cathode microstructure parameters and electrochemical properties are known. Moreover, it is expected that the thick cermet (*i.e.* 1 *mm*) should enhance concentration overpotentials.

Results first refer to a single radial cell of 9.08 $cm^2$ of active surface area operated in isothermal co-flow conditions. These simulations were performed to investigate the co-electrolysis mechanism and the relative influence of the WGS reaction over CO production. Then, a planar SRU was simulated, integrating a cell of 100 $cm^2$ of active surface area and fed in a counter-flow configuration. In addition, the influence of temperature on this relevant geometry for technological implementation was highlighted. Finally, co-electrolysis operating maps were computed over a wide range of inlet gas flow rates.

## 5.1. Investigation of Co-Electrolysis Mechanism

### 5.1.1. High Faradaic Conversion

The co-electrolysis model was applied to simulate the behavior of a radial CSC. It was operated in isothermal conditions at 800°*C* and 99% Faradaic Conversion (FC, Equation (5-1)), corresponding to a cell voltage of 1300 *mV*. These working conditions were chosen in order to enhance mass transport and concentration overpotentials. The simulated cathode was fed in accordance to Experiment A10 of Table 4-2 (*i.e.* 10.4 $NmL.min^{-1}.cm^{-2}$ of 58/14/14/4/10 *vol.%* of $H_2O/H_2/CO_2/CO/N_2$).

$$FC = \frac{N_{H_2O}^{electrolyzed} + N_{CO_2}^{electrolyzed}}{N_{H_2O}^{0} + N_{CO_2}^{0}} = \frac{1}{N_{H_2O}^{0} + N_{CO_2}^{0}} \frac{|i|}{2F} \tag{5-1}$$

where $N_j^0$ is the molar flux of specie j in the inlet and *i* the global current density.

Regardless of the operating point on a polarization curve, the model is able to provide the variations of any of its variables within the two dimensional geometry. The following sections describe the longitudinal (*i.e.* along the cell radius, *r* axis) and axial (*i.e.* along the cathode thickness, *z* axis) evolutions obtained in the investigated radial geometry (Figure 3-6).

#### 5.1.1.1. Evolutions Along the Cell Radius

Figure 5-1 shows the evolution of molar fractions of active species in the gas channel while Figure 5-2 shows the current densities for $H_2O$ and $CO_2$ electro-reductions along the cathode/electrolyte interface. The profiles are plotted from the cell inlet to the cell outlet. The $H_2$ molar fraction exhibits a steep elevation whereas the CO content increases gently along the cell radius. Conversely, the $H_2O$ and $CO_2$ molar fractions decrease along the cell. Indeed, $H_2O$ and $CO_2$ species are consumed by electrochemical reduction to produce $H_2$ and CO. Difference in molar fractions gradients between $H_2/H_2O$ and $CO/CO_2$ reveals that steam reduction rate is faster than $CO_2$ consumption. This result is consistent with the fact that $H_2O$ reduction is kinetically faster than the $CO_2$ one (*i.e.* $i_{0,cathode}^{H_2-H_2O}$ greater than $i_{0,cathode}^{CO-CO_2}$).

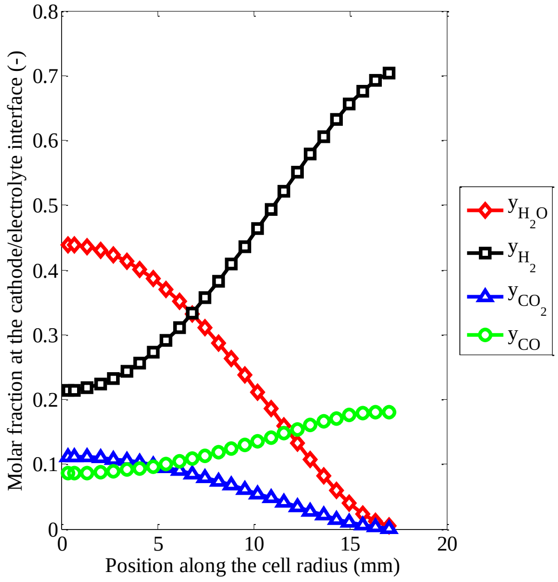

Figure 5-1: Molar fractions along the cathode/electrolyte interface for simulated experiment A10 (co-electrolysis) at 1300 *mV*.

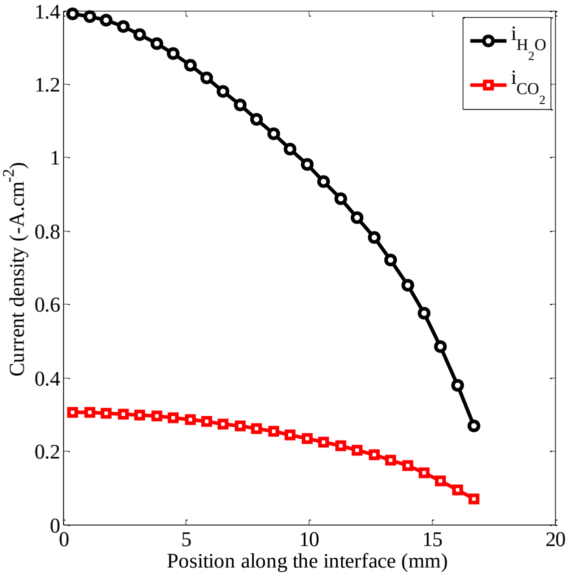

Figure 5-2: Current densities along the cell radius for simulated experiment A10 (co-electrolysis) at 1300 *mV*.

As shown in Figure 5-2, local current densities decrease steeply from the cell center to the cathode outlet. Indeed, $H_2O$ and $CO_2$ are highly converted along the cell, yielding lower amounts of reactants available at the electrode/electrolyte interface for reduction. This supports the high global faradaic conversion rate of 99% computed.

It is worth noting that the average electrochemical production rate of $H_2$ is here roughly three times higher than that of CO at the cathode/electrolyte interface. This confirms that $CO_2$ electrolysis can occur in parallel of $H_2O$ electrolysis, which is consistent with the CO/$CO_2$ single electrolysis experimental feasibility, presented in Chapter 4.

Figure 5-3 illustrates the Nernst potential and the overpotentials related to steam electrolysis in co-electrolysis operation, plotted along the cell radius. It can be noticed that the sum of all the overpotentials to the Nernst potential is equal to the cell voltage of 1300 *mV* (Equation (3-19)). This result highlights the reliability of overpotential calculations along the cell radius (*cf.* section 3.2.6).

Ohmic and activation overpotentials are decreasing functions of the distance from the center as they directly depend on the current density (*cf.* Equations (3-19) and (3-28)). In agreement with the chosen values for anode and cathode exchange current densities ($i_{0,cathode}^{H_2/H_2O} = 560\ mA.cm^{-2}$ and $i_{0,anode}^{LSM-YSZ} = 200\ mA.cm^{-2}$), it is found that the anode activation overpotential is higher than cathode activation contribution.

It is also shown that the anodic concentration overpotential remains negligible regardless of the position along the cell. This can be related to the thin anode that does not significantly contribute to the mass transport limitation. Let us recall that even if the oxygen molar fraction rises up to $y_{O_2}^{\mathrm{int}\_i\neq 0} = 1\ atm$, according to Equation (3-32) with $y_{O_2}^{\mathrm{int}\_i=0} = 0.21\ atm$, the anode concentration overpotential would only be equal to 36 *mV*. As the global steam conversion rate is higher than 94%, the steam molar fraction falls close to zero at the cell outlet (Figure 5-1). Accordingly, the cathode concentration overpotential increases strongly along the cell to account for up to 77% of the total voltage at the outer cell boundary (Figure 5-3). It is worth noting that very similar responses are predicted concerning $CO_2$ reduction. However, the ohmic overpotential is lower because of a low current density related to $CO_2$ electrolysis (Figure 5-2).

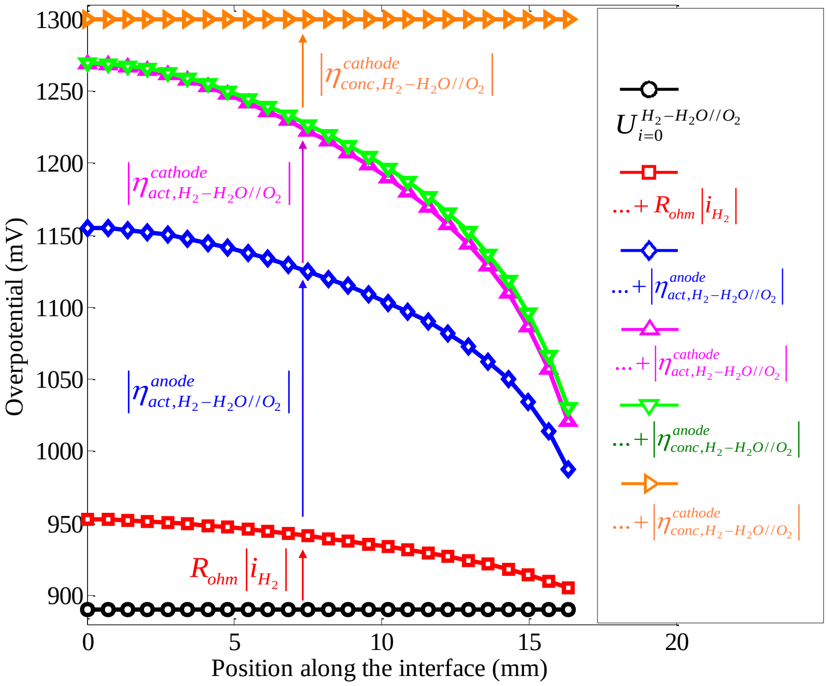

Figure 5-3: Overpotentials for $H_2O$ electrolysis along the cell radius for simulated experiment A10 (co-electrolysis) at 1300 *mV*.

Figure 5-4 shows the evolution of the resulting local rate of the WGS reaction, $R_{WGS}$, computed along the cell radius using Equation (5-2). $R_{WGS}$ is positive when CO is consumed and negative when the reverse WGS reaction is favored.

$$R_{WGS}(r) = \frac{\varepsilon_c}{\delta_c} \int_{z=0}^{z=\delta_c} v_{WGS}(r,z)\, dz \qquad (5\text{-}2)$$

where $\delta_c$ is the cathode thickness, $\varepsilon_c$ the cathode porosity and $v_{WGS}$ the rate of the WGS reaction.

It can be noticed that $R_{WGS} > 0$ at the cell inlet. Indeed, initial composition of the cathodic flow imposes the WGS reaction to consume CO. Conversely, at the cell outlet, the large production of $H_2$ along the cell (Figure 5-1) reverses the WGS reaction to produce CO ($R_{WGS} < 0$). In the investigated conditions, the resulting rate of the WGS reaction is nil at about 11 *mm* of cell radius. It is worth emphasizing that in radial geometry, elementary surfaces increase with the radius. Therefore, elementary volumes in which the chemical reaction occur also increase, and Figure 5-4 might not reflect the resulting global production of the WGS reaction.

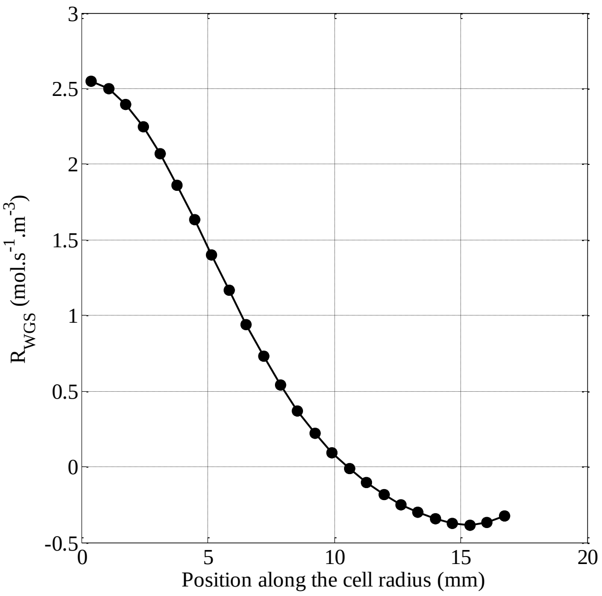

Figure 5-4:
Resulting local rate of the WGS reaction along the cell radius for simulated Experiment A10 (co-electrolysis) at 1300 *mV* and 99% FC.

$R_{WGS}$ is positive when CO is consumed

#### 5.1.1.2. Evolutions Along the Cathode Thickness

Variations of molar fractions and WGS reaction rate as functions of the cathode thickness are shown in Figures 5-5 and 5-6, respectively. These plots have been computed at 8.5 *mm* away from the center of the cell, which corresponds to the middle of the cell radius. All molar fractions appear to vary nearly linearly through the cermet. The consumption of steam and carbon dioxide at the cathode/electrolyte interface increases the contents of $H_2$ and CO in the cathode.

In the conditions of Experiment A10, and for the chosen cell geometry and potential, it is found that, at the middle of the cell radius, CO is consumed at the cathode/electrolyte interface, and produced at the external interface. This observation arises from the variation of the WGS reaction rate within the cathode (Figure 5-6). Furthermore, the absolute values for the WGS reaction rate are found low compared to the rate of the electrochemical reduction reaction. Thus, for the slice of cell located in the middle of the cell radius, the WGS reaction does not significantly influence the molar fractions gradients across the electrode (Figure 5-5). Finally, the WGS reaction is reversed around the middle of the electrode thickness.

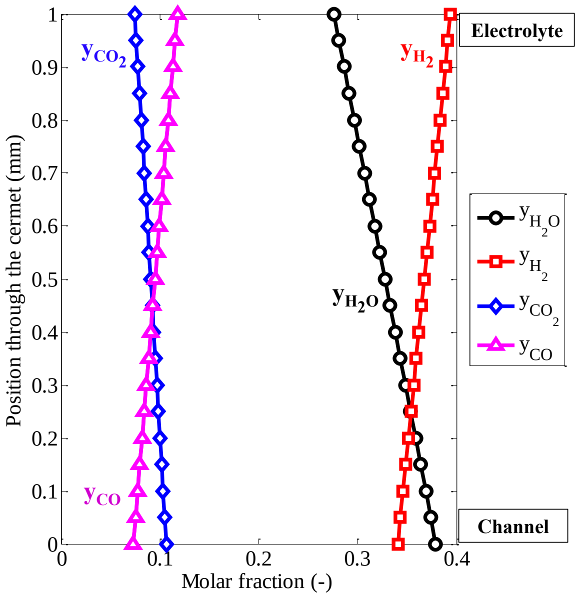

Figure 5-5: Molar fractions in the cathode thickness, at 8.5 *mm* (middle) of cell radius, for simulated Experiment A10 (co-electrolysis) at 1300 *mV* and 99% FC.

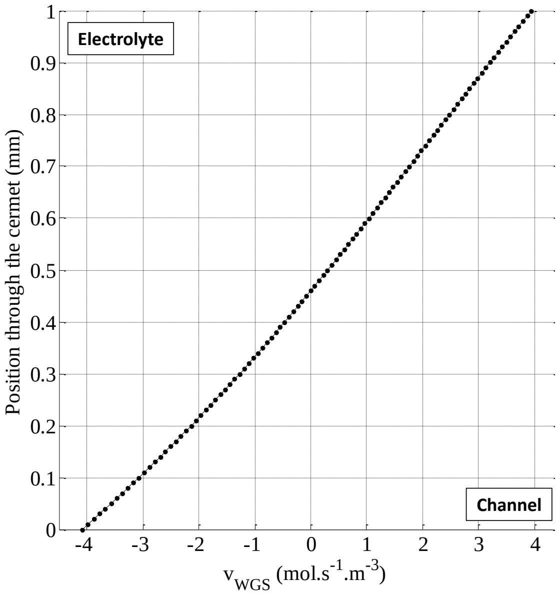

Figure 5-6: WGS reaction production rate in the cathode thickness, at 8.5 *mm* (middle) of cell radius, for simulated Experiment A10 (co-electrolysis) at 1300 *mV* and 99% FC. $v_{WGS}$ is positive when CO is consumed.

## 5.1.2. Effect of Polarization

One of the main issues in steam and carbon dioxide co-electrolysis investigations is to assess the effect of the WGS reaction on CO production to predict the real efficiency of the whole process. In this view, the relative global CO production through the reverse WGS reaction compared to $CO_2$ electrolysis, $\zeta_{CO}$, was defined as follows:

$$\zeta_{CO} = \frac{\iiint\limits_{cermet\ volume} -\varepsilon_c v_{WGS} dV}{\frac{1}{2F}\iint\limits_{cell\ active\ area} i_{CO} dS + \iiint\limits_{cermet\ volume} -\varepsilon_c v_{WGS} dV} \tag{5-3}$$

where $\varepsilon$ is the cathode porosity, $v_{WGS}$ the rate of the WGS reaction, $i_{CO}$ the current density related to $CO_2$ electrolysis, $F$ the Faraday's constant, $dS$ and $dV$ the elementary surface and volume, respectively. Note that the numerator in Equation (5-3) represents the amount of CO produced through the reverse WGS reaction, whereas the denominator refers to the CO production by both chemical and electrochemical processes.

At 800°*C*, the WGS reaction globally consumes CO for cell voltages lower than 1200 *mV*, as indicated by the negative values of $\zeta_{CO}$ (Figure 5-7). At high polarization the calculated values are low, meaning that carbon monoxide in the outlet gas mainly originates from the electrochemical reduction of $CO_2$. At an intermediate cell voltage of 1100 *mV*, the CO production is decreased by roughly 6% due to the WGS reaction, and $\zeta_{CO}$ is positive (*i.e.* +2%) at 1300 *mV*. Thus, in this last case, the chemical reaction barely produces CO. Therefore, in the chosen conditions, one can deduce that the WGS reaction does not prevail on the global co-electrolysis mechanism as soon as the cell voltage exceeds 1000-1100 *mV*.

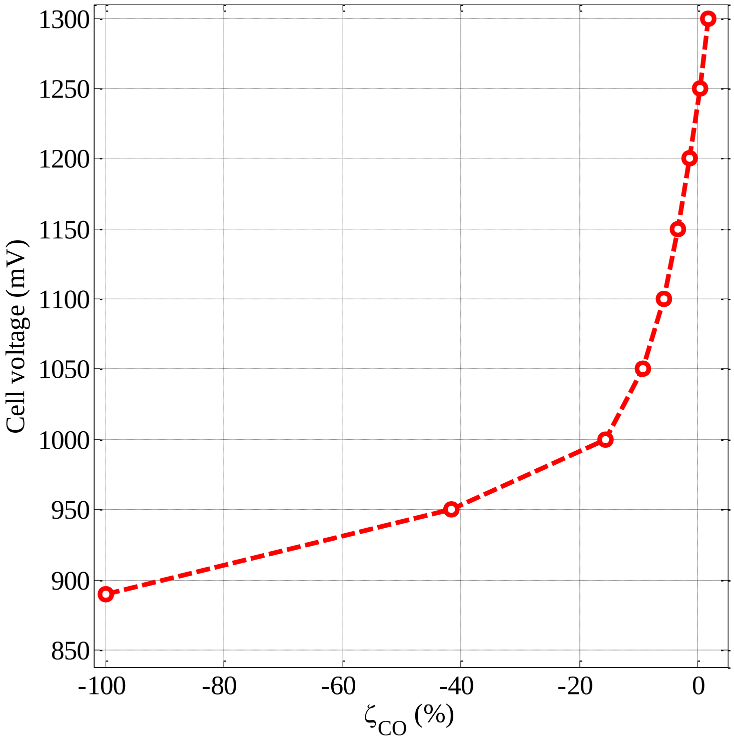

Figure 5-7:
CO relative production by the reverse WGS reaction for simulated experiment A10 (co-electrolysis) as a function of polarization.

Negative values indicate that CO is globally consumed.

The resulting overpotentials $\eta$ have also been computed by averaging the local overpotentials along the cell, according to Equation (5-4) expressed in polar coordinates for the radial version of the model.

$$\eta_i^* = \int_{\theta=0}^{2\pi}\int_{r=0}^{cell\ radius} \eta_i\left(r\right).dS\left(r,\theta\right) \Big/ S_{cell} = \int_{\theta=0}^{2\pi}\int_{r=0}^{cell\ radius} \eta_i\left(r\right).rdrd\theta \Big/ S_{cell} \qquad (5\text{-}4)$$

where $S_{cell}$ is the cell active electrode area, and $(r,\theta)$ the polar coordinates.

The simulated behaviors of each contribution to the polarization curve (Figure 5-8) are similar to those previously described in Figure 5-3. The concentration overpotential of the anode is low while the cathodic one increases with the conversion rate. The main polarization loss is due to the anodic activation, which is consistent with the values of exchange current densities used as input parameters (*i.e.* $i_{0,cathode}^{H_2-H_2O} > i_{0,anode}$).

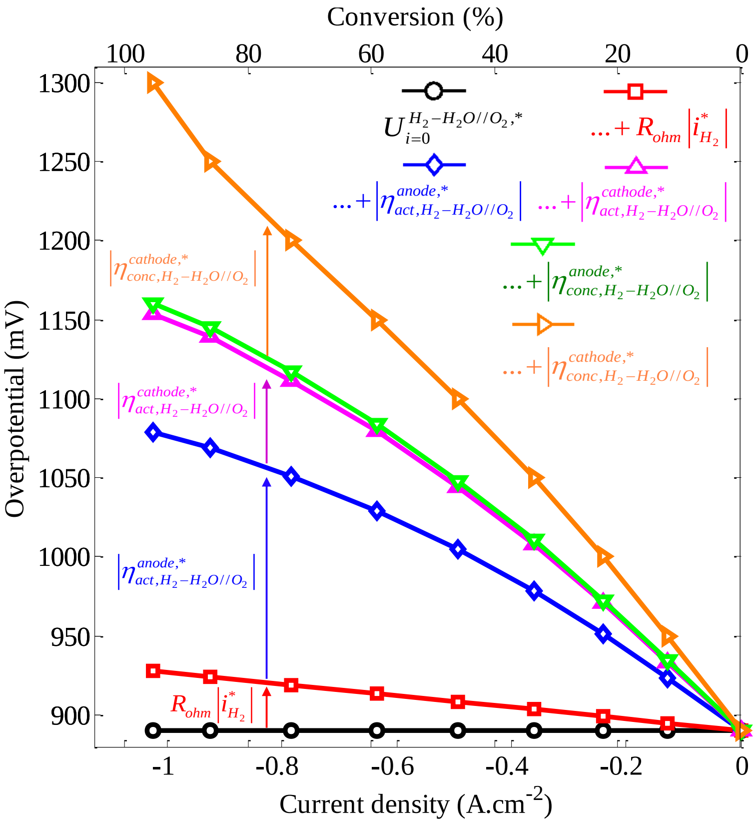

Figure 5-8: Overpotentials of $H_2O$ electrolysis for simulated Experiment A10 (co-electrolysis).

### 5.1.3. Co-electrolysis Simulated Performances at 800°*C*

Simulations were performed in order to compare the expected performances of both single electrolyzes and co-electrolysis process (Figures 5-9 and 5-10). The polarization curves were computed considering a single cell in a radial and co-flow configuration at 800°*C* for two inlet cathodic flow rates (6 and 12 $NmL.min^{-1}.cm^{-2}$), the inlet anodic flow rate being twice the cathodic one. Simulations were performed considering different cathode inlet gas mixtures: $H_2O/H_2$ or $CO_2/CO$ = 90/10 *vol.%* and $H_2O/CO_2/H_2$ = 65/25/10 *vol.%*. This co-electrolysis composition was chosen since it should yield a $H_2/CO$ outlet ratio of about 3 [1], technologically relevant for methane production (*cf.* Table 1-5). It is worth reminding that, at a given cathode flow rate, performances and conversion rates can be compared since the three gas mixtures investigated contain the same amount of oxidized species (*i.e.* that can potentially participate to the electrolysis reaction(s)). In agreement with literature data [2–4], the performances of steam electrolysis and co-electrolysis are rather close and these modes display higher conversion rates than in $CO_2$ electrolysis mode. As expected, conversion rates decrease with higher inlet flow rates, evidencing mass transfer limitations at higher current densities.

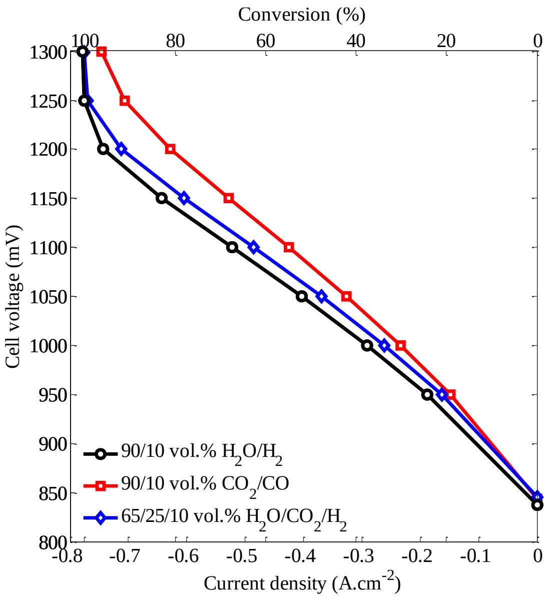

Figure 5-9: Simulated polarization curves for all electrolysis modes at 800°*C* (6 $NmL.min^{-1}.cm^{-2}$).

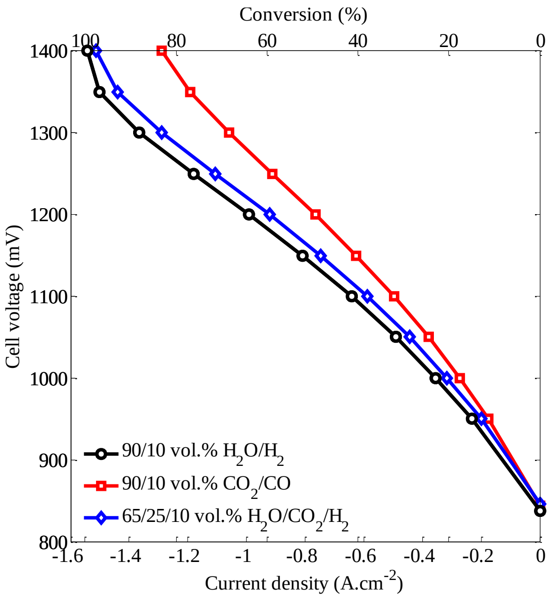

Figure 5-10: Simulated polarization curves for all electrolysis modes at 800°*C* (12 $NmL.min^{-1}.cm^{-2}$).

As shown in Figure 5-11, for the chosen co-electrolysis gas mixture, a positive value of $\zeta_{CO}$ is computed whatever the cell voltage. The sign of $\zeta_{CO}$ indicates that the reverse WGS reaction is globally favored at 800°*C* (*cf.* section 5.1.2). This result is explained since the gas feeding contains no CO. If one refers to Figure 5-7, one can thus deduce that the global direction of the WGS reaction depends on experimental conditions. Although here the WGS reaction globally contributes to the production of CO, $\zeta_{CO}$ is a decreasing function of the cell voltage regardless of the total inlet flow rate. For instance, only 10% of the CO contained in the outlet gas stream is produced by the reverse WGS reaction at 1200 *mV* and 800°*C*. It is worth noting that the contribution of the chemical reaction increases with the total gas flow rate. However, throughout all investigated compositions, the WGS reaction does not prevail over the global production of syngas.

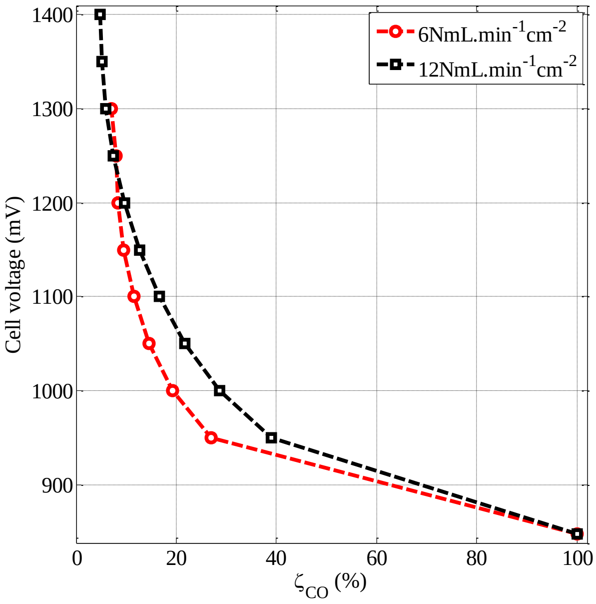

Figure 5-11:
CO relative production by the reverse WGS reaction for simulated composition 65/25/10 *vol.%* of $H_2O/CO_2/H_2$ and cathodic inlet flow rates of 6 and 12 $NmL.min^{-1}.cm^{-2}$.

Positive values indicate that CO is globally produced.

However, this last conclusion, obtained for inlets somewhat compatible with a potential industrial use of co-electrolysis (*cf.* Table 1-5), greatly depends on inlet composition and flow rate. Therefore, isothermal simulations were performed at 1.3 *V* (*i.e.* close to the thermoneutral voltage) to quantify the amounts of $H_2$ or CO chemically produced with gas inlets favoring the WGS or reverse WGS reactions, respectively (Table 5-1). When the cell is fed with 50/50 *vol.%* $H_2/CO_2$ and $H_2O/CO$, respectively, it is found that electrolysis is still responsible for more than 60% of the global production of CO and $H_2$, respectively (Table 5-1). The as-obtained values can be considered as maximum contributions of the chemical reaction that can be achieved within the set of investigated parameters (*i.e.* cell, microstructure, flow rate, voltage, temperature, *etc.*).

| **Cell** | $F_{cathode}$<br>$NmL.min^{-1}.cm^{-2}$ | **Cell Voltage**<br>*V* | **Inlet Composition**<br>*vol.%* | **Chemical Production**<br>*%* |
|---|---|---|---|---|
| FZJ | 12 | 1.3 | 50/50 $H_2/CO_2$ | **33% of CO** |
| | | | 50/50 $H_2O/CO$ | **39% of $H_2$** |

Table 5-1: Maximum simulated influence of the WGS reaction over CO or $H_2$ production.

## 5.2. Intermediate Conclusion

The influence of the chemical WGS reaction over global CO production has been investigated through simulations. First, this paragraph aims at gathering and summarizing these findings. It is reminded that no consensus on this question has been achieved in the literature, leading to multiple simplifying assumptions (*cf.* section 2.3 and, more recently, [5]).

First, the simulated influence of the WGS reaction is governed by the kinetic parameters inputted. However, its kinetics and location of occurrence were experimentally validated through gas analyses. Indeed, good correlations between outlet gas composition measurements and simulations were obtained at OCV for multiple high flow inlets (*cf.* 4.3.7).

In section 4.3.10, a sensitivity analysis was presented to evaluate the influence of the WGS reaction, among other relevant parameters. By nullifying its kinetic, it was shown that the chemical reaction had no noticeable impact on the polarization curve, apart from OCV. Furthermore, its influence on outlet molar fractions was found to be limited, in the 10% range at higher current densities.

Finally, Figures 5-7 and 5-11 both showed that within the investigated conditions, and regardless of its global direction, the WGS reaction only accounted for less that 10% of the total outlet CO at high cell polarization (*i.e.* $U_{cell} > 1100\ mV$). Even by favoring the chemical reaction, co-electrolysis still yielded more than 60% of the syngas production (Table 5-1).

These findings highlight a limited influence of chemistry over electrochemistry concerning co-electrolyzer syngas production at 800°*C*. It would seem that it is mostly due to the chemical reaction reversing direction in the cathode thickness, so that its global production is roughly balanced. In conclusion, the WGS reaction is not likely to prevail in the co-electrolysis process for the investigated conditions. Accordingly, neglecting the chemical reaction instead of assuming it accounts for all of the produced CO seem therefore mostly appropriate if simplifications are needed (*eg.* for modeling purposes, simulating a large scale process, *etc.*).

## 5.3. SRU Operation

Simulations presented in this section were performed to estimate the technological relevance of the co-electrolysis process, by establishing operating maps. In this objective, a SRU integrating a CSC in a counter-flow configuration was simulated (Figure 5-12) for a cathodic inlet gas composition of 65/25/10 *vol.%* $H_2O/CO_2/H_2$, and temperature dependences were taken into account. Indeed, such composition should lead to a ratio $H_2/CO$ in the outlet gas of about 3/1 REF, and could in turn be utilized to produce synthetic methane (Table 1-5).

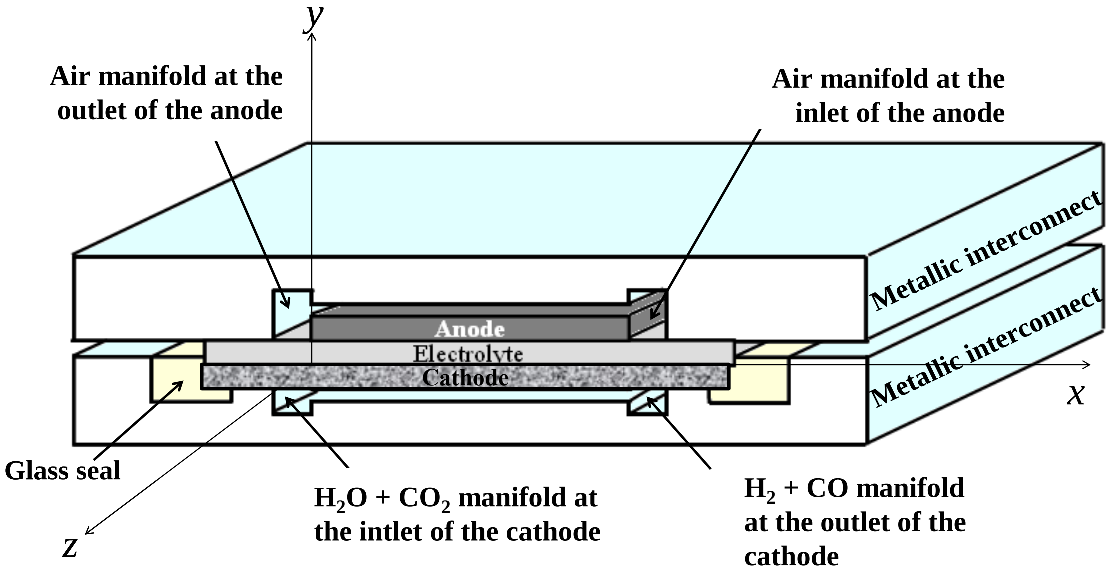

Figure 5-12: Geometry of the simulated SRU – CSC in counter-flow configuration.

### 5.3.1. Simulation Parameters

The influence of the temperature on co-electrolysis polarization curve was investigated at the SRU level based on the classical geometry of Figure 5-12 [6] (planar CSC in counter-flow feeding), integrating a 10×10 *cm*$^2$ FZJ cell, and by coupling the electrochemical and thermal modules (*cf.* 3.2.5). According to the results obtained for a radial configuration is isothermal conditions, the previous sections, the composition of the cathode inlet gas stream was 65/25/10 *vol.%* $H_2O/CO_2/H_2$, while the anode was fed with air (Table 5-2). A wide range of flow rates, and thus conversion rates, was examined, from 12 to 48 $NmL.min^{-1}.cm^{-2}$.

The influence of temperature on exchange current densities was taken into account through corresponding activation energies (Table 5-2), according to an Arrhenius type behavior:

$$i_0\left(T\right)=i_0^0\exp\left(-E_a\big/RT\right) \tag{5-5}$$

where $i_0$ is the exchange current density, $i_0^0$ the pre-exponential factor and $E_a$ the activation energy.

Pre-exponential factors were tuned to obtain 530, 356 and 200 $mA.cm^{-2}$ for $i_{0,cathode}^{H_2-H_2O}$, $i_{0,cathode}^{CO-CO_2}$ and $i_{0,anode}$, respectively, at 800°*C*. All remaining numerical values concerning the thermal description can be found in references [6–8].

The following sections highlight some of the results obtained with simulated conditions C2 (Table 5-2), before presenting the computed operating maps for co-electrolysis operation.

| | **Denomination** | **C1** | **C2** | **C3** | **C4** |
|---|---|---|---|---|---|
| $F_{cathode}$ | $NmL.min^{-1}.cm^{-2}$ | 12 | 20 | 31 | 48 |
| $F_{air}$ | $NmL.min^{-1}.cm^{-2}$ | 12 | 20 | 31 | 48 |
| Cathode | | $H_2O$ | $CO_2$ | $H_2$ | |
| | *vol.%* | 65 | 25 | 10 | |
| Anode | | $N_2$ | $O_2$ | | |
| | *vol.%* | 79 | 21 | | |

| **Single Repeating Unit (SRU) and Cell** | | | | | |
|---|---|---|---|---|---|
| Dimensions | | | Microstructure | | |
| $\delta_{cathode}$ | 1000 | *μm* | $\tau_c$ | 2.8 | - |
| $\delta_{electrolyte}$ | 10 | *μm* | $\varepsilon_c$ | 0.43 | - |
| $\delta_{canode}$ | 50 | *μm* | $\tau_c$ | 1.2 | *μm* |
| Cell total length | 118 | *mm* | $\tau_a$ | 4 | - |
| Cell active length | 100 | *mm* | $\varepsilon_a$ | 0.5 | - |
| Interconnect plate thickness | 10 | *mm* | $\tau_a$ | 1 | *μm* |
| Gas channel width | 1 | *mm* | $T_S^*$ | 800 | *°C* |

[*] Temperature of the insulating envelope.

| **Electrochemical and electrical parameters** | | | | | |
|---|---|---|---|---|---|
| $E_a^{H_2-H_2O}$ | 120 [8] | $kJ.mol^{-1}$ | $i_{0,cathode}^{H_2-H_2O}(800°C)$ | 530 [8] | $mA.cm^{-2}$ |
| $E_a^{CO-CO_2}$ | 120 [9] | $kJ.mol^{-1}$ | $i_{0,cathode}^{CO-CO_2}(800°C)$ | 356 $^{**}$ | $mA.cm^{-2}$ |
| $E_a^{anode}$ | 190$^*$ | $kJ.mol^{-1}$ | $i_{0,anode}(800°C)$ | 200 | $mA.cm^{-2}$ |
| | | $R_{contact}$ | 0.05 | $\Omega.cm^2$ | |

Table 5-2: Thermal simulations inputs. All other numerical values can be found in [6–8].

[*] Internal research to be published.

[**] Section 4.2, $R_0 = i_{0,cathode}^{H_2O-H_2} / i_{0,cathode}^{CO_2-CO_2} = 1.51$.

### 5.3.2. Polarization Curve at 20 $NmL.min^{-1}.cm^{-2}$

The effect of temperature on the polarization curve of the simulated SRU operating in conditions C2 (Table 5-2) is shown in Figure 5-13.

At OCV, the cell temperature is about 797.5°*C* (*i.e.* 3°*C* less than the temperature of the insulating envelope as described in Chapter 3). Indeed, the inlet cathodic composition corresponds roughly to the thermodynamic equilibrium of the WGS reaction at 800°*C*. Thus, the thermal sources related to the chemical reaction have a barely noticeable impact on both cell temperature and gases composition along the cell at OCV. A more significant influence can be anticipated by changing the inlet composition.

Figure 5-13A compares the polarization curves of the SRU obtained with the complete model (*i.e.* taking into account the thermal module) and in isothermal conditions, respectively. It also reports the temperature taken at the middle of the cell length (Figure 5-13B). It can be noted that because of $CO_2$ parallel electrolysis and WGS reaction, the thermoneutral voltage is shifted compared to single steam electrolysis. This phenomenon has been experimentally observed by following cell temperature slight changes during co-electrolysis *i-V* curves recording. In the simulated conditions considered, the thermoneutral voltage is assessed at about 1.32 *V*. As expected [1], the co-electrolysis thermoneutral voltage is comprised between those of steam electrolysis (1.29 *V*) and $CO_2$ electrolysis (1.46 *V*).

Similarly to observations in single steam electrolysis [6] (*cf.* Figure 1-9), the three operating thermal modes can be detected. For cell voltages bellow the thermoneutral voltage, the endothermicity of electrolysis reactions is not balanced by heat sources and thus, the cell temperature drops below the one at OCV. Accordingly, the current density is lower than in isothermal operation since local temperatures influence the ionic conductivity of the electrolyte, the chemical and electrochemical kinetics, *etc*. Conversely, above the thermoneutral voltage (*i.e.* exothermic operation), cell performances are enhanced. For example, at 1400 *mV*, the cell current density rises from -1.62 to -2.09 $A.cm^{-2}$ when the exothermicity is taken into account. Furthermore, the distribution of thermal fluxes reveals that about 75% of the produced heat is dissipated through radiative flow along this polarization curve. Conversely, the remaining 25% is evacuated through gas convection. These values are consistent with the ones reported on a CSC in steam electrolysis mode [6].

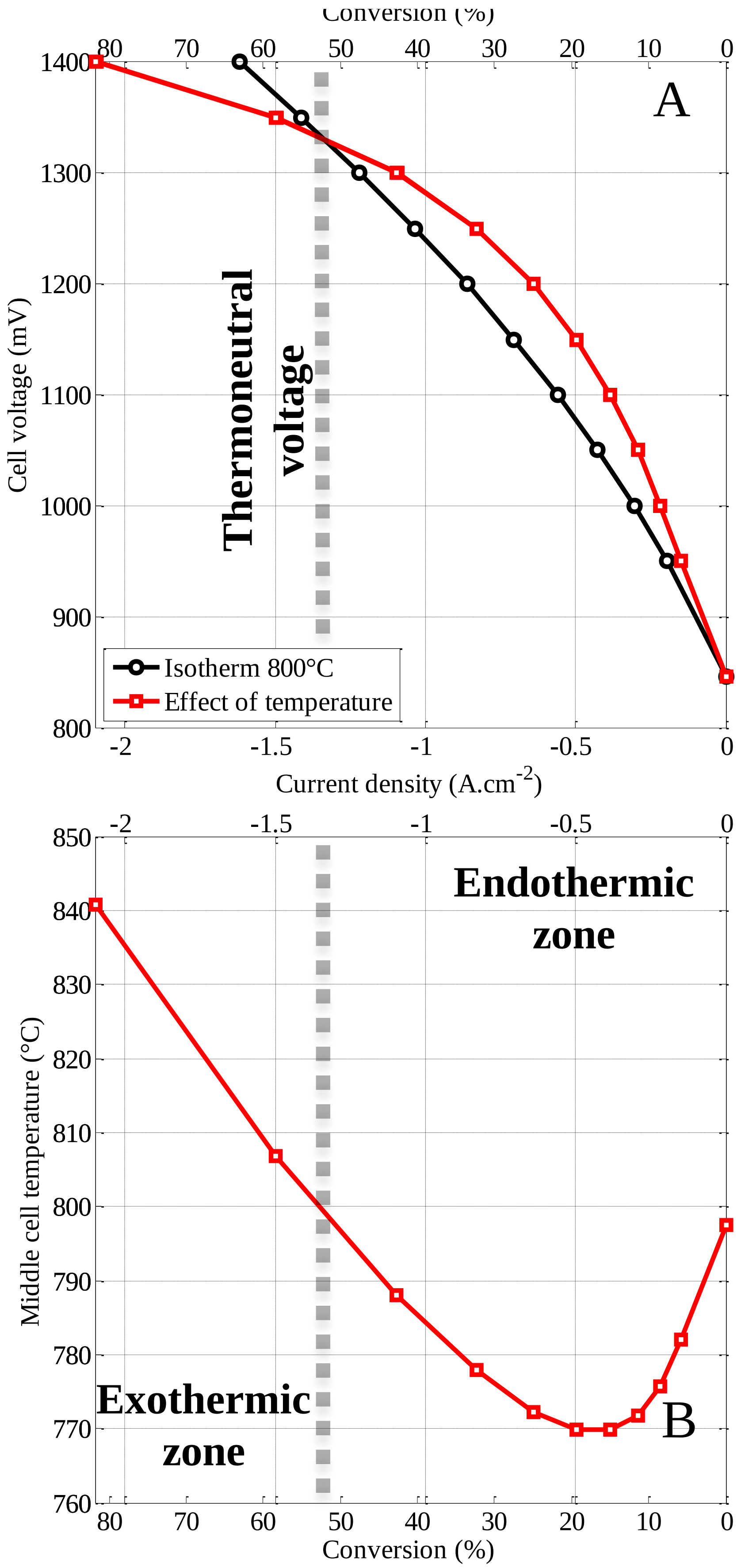

Figure 5-13: Influence of the operating temperature on the SRU performances for conditions C2. Cathode fed with 20 $NmL.min^{-1}cm^{-2}$ of 65/25/10 *vol.%* $H_2O/CO_2/H_2$. Anode fed with 20 $NmL.min^{-1}cm^{-2}$ of air.

### 5.3.3. Overpotentials Decomposition

The decomposition of C2 previous polarization curve (Figure 5-13A) into overpotentials is detailed in Figure 5-14. As for the isothermal overpotential decomposition (Figure 5-8), activation overpotentials mainly contribute to the cell voltage at low current densities, especially anode activation (Figure 5-14). It can be seen that although activation still accounts for most of the voltage elevation, its relative proportion decreases at higher current densities. Indeed, the temperature elevation in the exothermic section of the *i-V* curve accelerates the electrochemical kinetics, decreasing the influence of activation (Equation (5-5)).

Furthermore, the contribution of ohmic losses is here higher than for the single cell. Indeed, the contact ASR was adapted to be representative of the SRU geometry, and the chosen value was experimentally assessed from SRU ASR measurements.

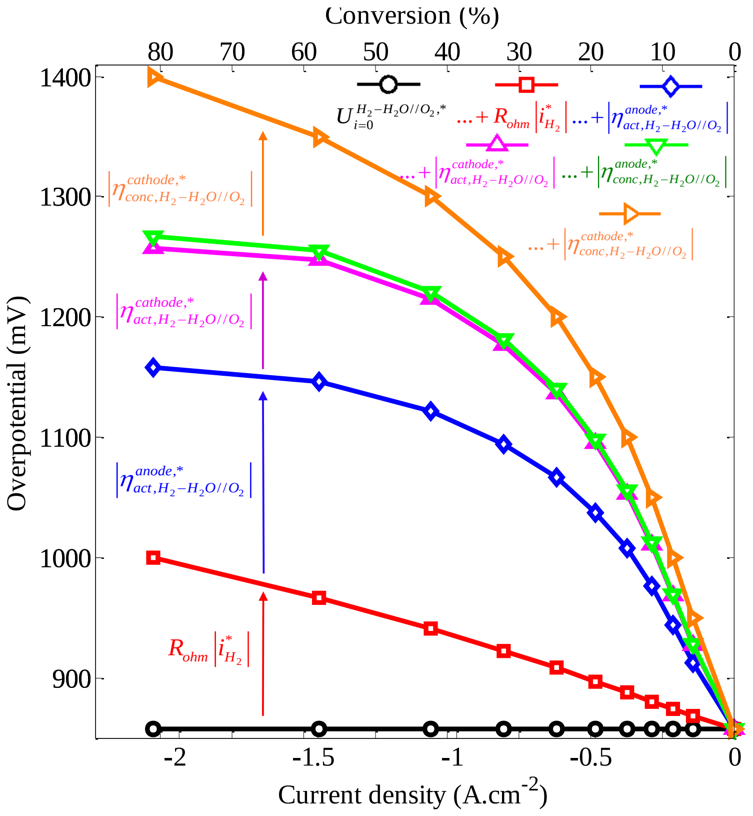

Figure 5-14: Overpotential for conditions C2 (20 *NmL.min*$^{-1}$.*cm*$^{-2}$ of 65/25/10 *vol.%* $H_2O/CO_2/H_2$).

### 5.3.4. Longitudinal Evolutions of Cell Temperature

Figure 5-15 shows the temperature profiles along the cell length simulated as functions of the cell voltage for operating conditions C2 (Table 5-2). In the investigated conditions, the thermoneutral voltage was estimated at about 1.32 *V* (*cf.* Figure 5-13). For cell voltages up to 1.3 *V* (*i.e.* below the thermoneutral voltage), cell temperatures are lower than 800*°C*, which is consistent with endothermic operation. Conversely, cell temperatures increase above 800*°C* at 1.4 *V* when the cell operates exothermically.

These results can be directly compared to those obtained in steam single electrolysis with 20 $NmL.min^{-1}.cm^{-2}$ of cathode gas flow rate (*cf.* Appendix 7.4). Indeed, in these conditions, computed current densities are very similar. Such comparison leads to several obvious observations:

- Temperature elevations taken in the middle of the cell are less pronounced in co-electrolysis mode than in $H_2O$ electrolysis. Indeed, at 1.4 *V*, the temperature in the middle of the cell length is found to be about 840*°C*, whereas 870*°C* is reached in $H_2O$.
- Longitudinal temperature gradients appear to be flattened in co-electrolysis mode. In Figure 5-15, they are all lower than 10*°C*.

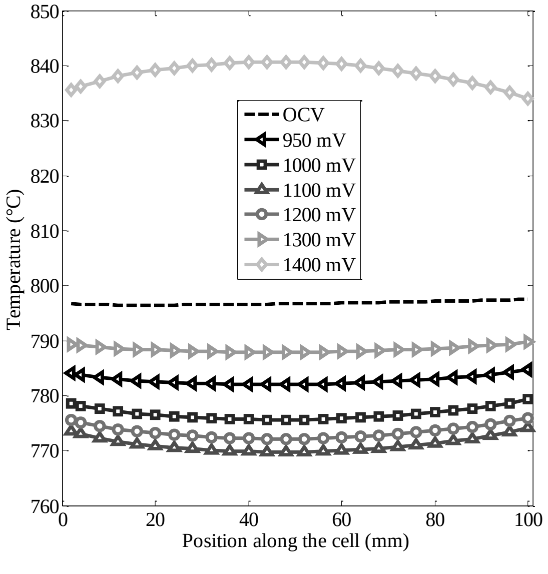

Figure 5-15:
Longitudinal evolutions of cell temperature as a function of the cell voltage when the cell is fed with 20 $NmL.min^{-1}.cm^{-2}$ of 65/25/10 *vol.%* $H_2O/CO_2/H_2$ (conditions C2).

The differences in cell temperatures and thermal profiles between co-electrolysis and $H_2O$ electrolysis modes could be explained by several factors. First, the volumetric heat capacity of the cathode gas mixture is increased in co-electrolysis operation. Indeed, both CO and $CO_2$ display greater $C_p$ (33.7 and 55.4 $J.mol^{-1}.K^{-1}$ respectively) than $H_2$ and $H_2O$ (30.3 and 42.4 $J.mol^{-1}.K^{-1}$), respectively. Thus, cathode gas flows are able to evacuate more heat in co-electrolysis than in $H_2O$ electrolysis. Also, the reverse WGS reaction, which is favored in the chosen conditions, is slightly endothermic. Therefore, it alleviates the temperature increase when the cell operates exothermically.

Besides the obvious advantage of co-electrolysis that is syngas generation, this simulated SOC operating mode suggests an easier thermal management, especially crucial in stack environment. Co-electrolysis could thus exhibit a wider range of acceptable operating conditions compared to $H_2O$ electrolysis, since high thermal gradient have been shown to cause mechanical stress, potentially leading to cell failure [10].

### 5.3.5. Longitudinal Evolutions of molar fractions and $\beta$

The profiles of molar fractions along the cathode/electrolyte interface, obtained with C2 inputs (Table 5-2) at 1.4 $V$, are shown in Figure 5-17. As they are being consumed, $H_2O$ and $CO_2$ molar fractions decrease along the cell, while those of $H_2$ and CO increase, as expected. In comparison with a radial geometry (Figure 5-1), molar fractions follow here a quasi linear evolution. This arises from the longitudinal geometry in which every elementary cell active areas are equivalent, whereas in radial geometries, elementary surfaces are a function of the cell radius. However, the influence of conversion rates (*i.e.* higher concentration overpotentials) can be seen here toward the cell outlet, where the consumption rates of oxidized species are slower (*i.e.* the molar fraction evolutions digress from linear behaviors).

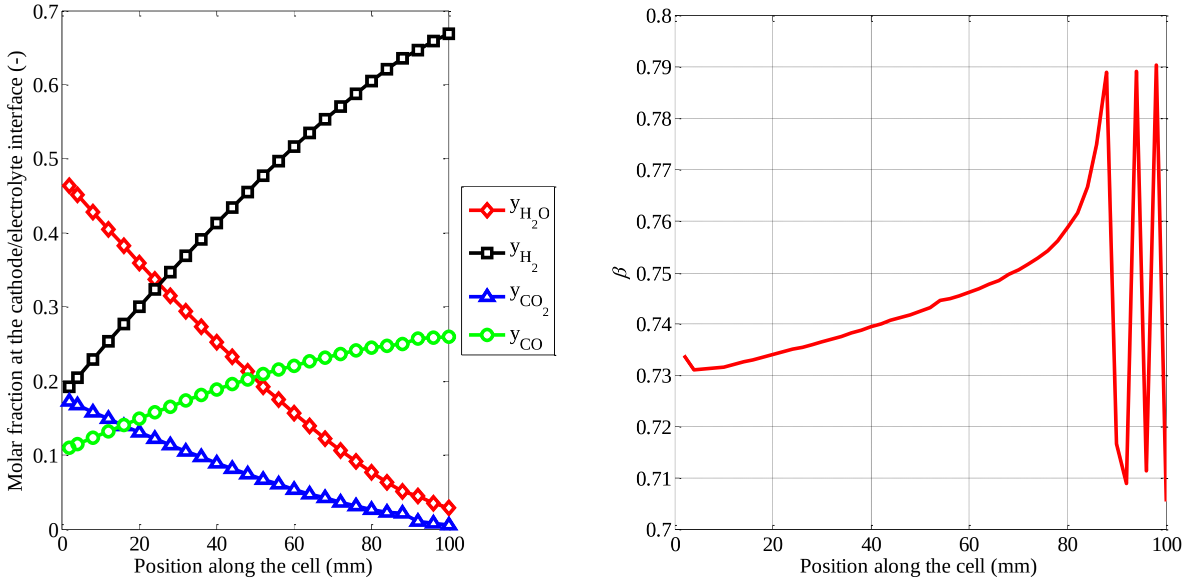

Figure 5-17: Molar fractions along the cathode/electrolyte interface (left) and $\beta$ (right) longitudinal evolutions at 1.4 *V* when the cell is fed with 20 $NmL.min^{-1}.cm^{-2}$ of 65/25/10 *vol.%* $H_2O/CO_2/H_2$ (conditions C2)

Since the surface ratio depends on interfacial $H_2O$ and $CO_2$ molar fractions (Equation (3-18)), $\beta$ evolves along the cell (Figure 5-17). In the chosen conditions, it increases along the cell length ($\beta = 0.73$ at the cell inlet and 0.79 at the outlet). This means that, progressively, more $H_2O$ is electrolyzed compared to $CO_2$ (*i.e.* in other words, the ratio $i_{H_2}/i_{CO}$ increases). This observation is attributed to the reverse WGS reaction, which consumes $CO_2$ and produces $H_2O$ at high $H_2$ contents (Figure 5-17), in turn favoring $H_2O$ electrolysis.

As can be seen in Figure 5-17, simulating $\beta$ can cause instabilities in the numerical resolution. Indeed, at high conversion rates, slight relative variations of $H_2O$ and $CO_2$ interfacial molar fractions can largely influence the value of the surface ratio parameter. This can be avoided in the current co-electrolysis model by increasing the longitudinal mesh density, which is highly computational time consuming. However, it should be emphasized that this phenomenon may only be observed in the limiting current density (*i.e.* very high conversion rates), which is not an interesting operating point from a technological point of view. Furthermore, the observed oscillations display limited amplitude, and only affect about 10% of the cell active surface. Thus, the variations of $\beta$ can be regarded as meaningless.

### 5.3.6. Co-electrolysis Operating Maps

This section presents the complete set of simulations detailed in Table 5-2. These operating maps present the main parameters that characterize the co-electrolysis process, and should as such be helpful to determine relevant conditions for co-electrolysis operation. In this view, maps of current densities (Figure 5-18A) and conversion rates (Figure 5-18B) were plotted as a function of cell voltage and inlet cathode gas flow rates. Note that these inlets correspond to a mixture of 65/25/10 *vol.%* $H_2O/CO_2/H_2$, while the anode is swept with the same flow rate of air (Table 5-2). Additional relevant maps are given in Figures 5-19, 5-20 and 5-21.

At a given cell voltage, increasing the cathodic flux yields higher current densities due to lower concentration overpotentials (Figure 5-18A), which can be attributed to lower conversion rates, as shown in Figure 5-18B. Because the WGS reaction is conservative of oxidized and reduced species, $H_2$+CO production profiles follow those of current densities (Figure 5-19A). The ratio of $H_2$+CO production to electrical power is plotted in Figure 5-19B. It is a combination of Figures 5-18A and 5-19A. It can be seen that this ratio increases with lower cell voltages. Global heat source terms (Figure 5-20A) and resulting cell temperatures (Figure 5-20B) are slightly dependent of inlet fluxes. Very similar observations can be made concerning single $H_2O$ electrolysis operating maps, presented in Appendix 7.4. These last maps were computed in similar conditions (same SRU geometry and cathode inlets composed of 90/10 *vol.%* $H_2O/H_2$) [10].

Comparing $H_2O$ and co-electrolysis operating maps highlights several striking differences. First, a maximum current density of about -2.2 $A.cm^{-2}$ is obtained in co-electrolysis, whereas about -6 $A.cm^{-2}$ was calculated in steam electrolysis (Appendix 7.4). Such difference in current density is mainly explained by a higher SRU temperature elevation in $H_2O$ electrolysis. This stem from mass transport limitations due to CO and $CO_2$ in the thick porous cathode, and could be an overall limitation of the co-electrolysis process. However, such lower current densities have positive repercussions on the SRU thermal management. Indeed, the maximum temperature elevation obtained in co-electrolysis is limited to +40*°C* compared to 800*°C*, which is significantly lower than for $H_2O$ electrolysis (Appendix 7.4). Furthermore, in comparable conditions, temperature elevations are lowered in co-electrolysis than in $H_2O$ electrolysis, so that this parameter does not appear here to be limiting.

Figure 5-21A presents the global influence of the WGS reaction on the co-electrolysis process. As already evidenced for low inlet flow rates (Figure 5-11), the amount of CO produced by the reverse WGS reaction increases with the cathodic flow rate (*i.e.* lower faradaic conversion rate), but the contribution of the chemical reaction is a decreasing function of the cell voltage. For instance, only a fourth of the produced CO originates from the reverse WGS reaction at 1200 *mV*, even by increasing the cathodic flow rate up to 48 $NmL.min^{-1}.cm^{-2}$. One can thus assert that electrochemical reductions of steam and carbon dioxide prevail on syngas production.

These operating maps can be used to determine optimal operating conditions regarding the complete "Power to Gas" process. In co-electrolysis operation, the minimum acceptable conversion rate is likely to be the most relevant parameter. Thus, within the investigated range, one could argue that 20 $NmL.min^{-1}.cm^{-2}$ at 1.35 *V* could be a middle ground for practical operations, yielding -1.5 $A.cm^{-2}$ and 60% conversion rate. This co-electrolyzer would then operate at about 810 *°C* in a slightly exothermic mode, with therefore limited degradation of the cell efficiency (*cf.* 1.3.1), and allowing preheating inlet gases. Using these values, one can evaluate the global output of a 25 10×10 $cm^2$ stack. Such co-electrolyzer would correspond to a 5 *kW* electrical power, and would produce 1.63 $Nm^3.h^{-1}$ of syngas with a ratio $H_2/CO = 3.3$.

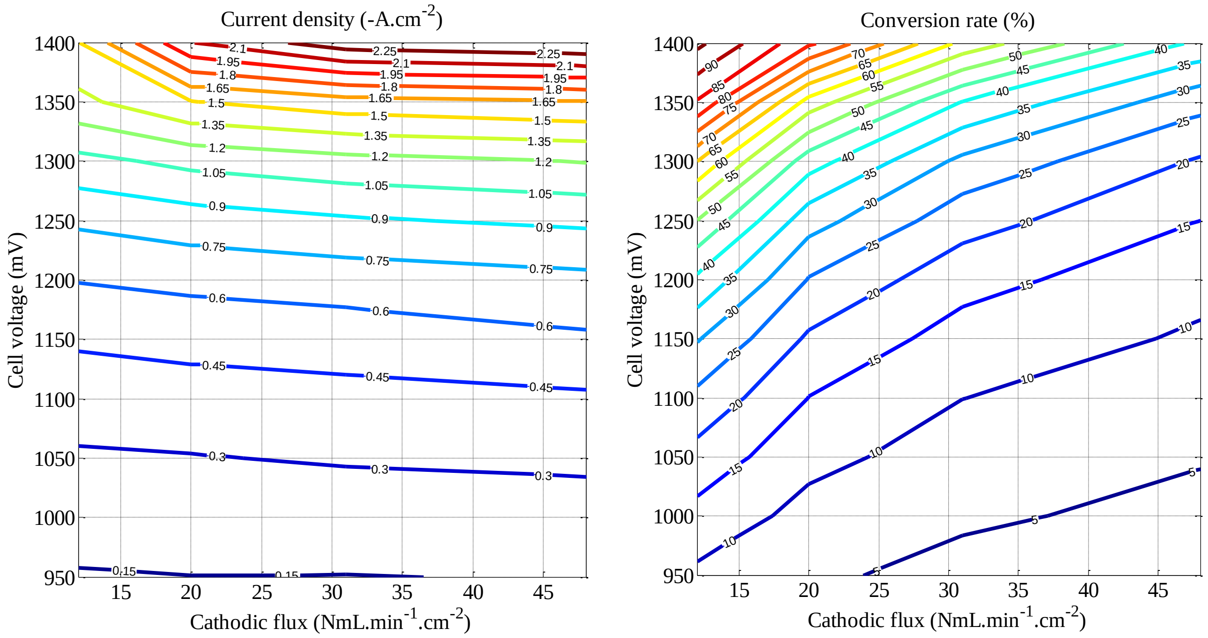

Figure 5-18: Co-electrolysis operating maps (1/4): Current densities (A-left) and corresponding Faradaic conversion rates (B-right).

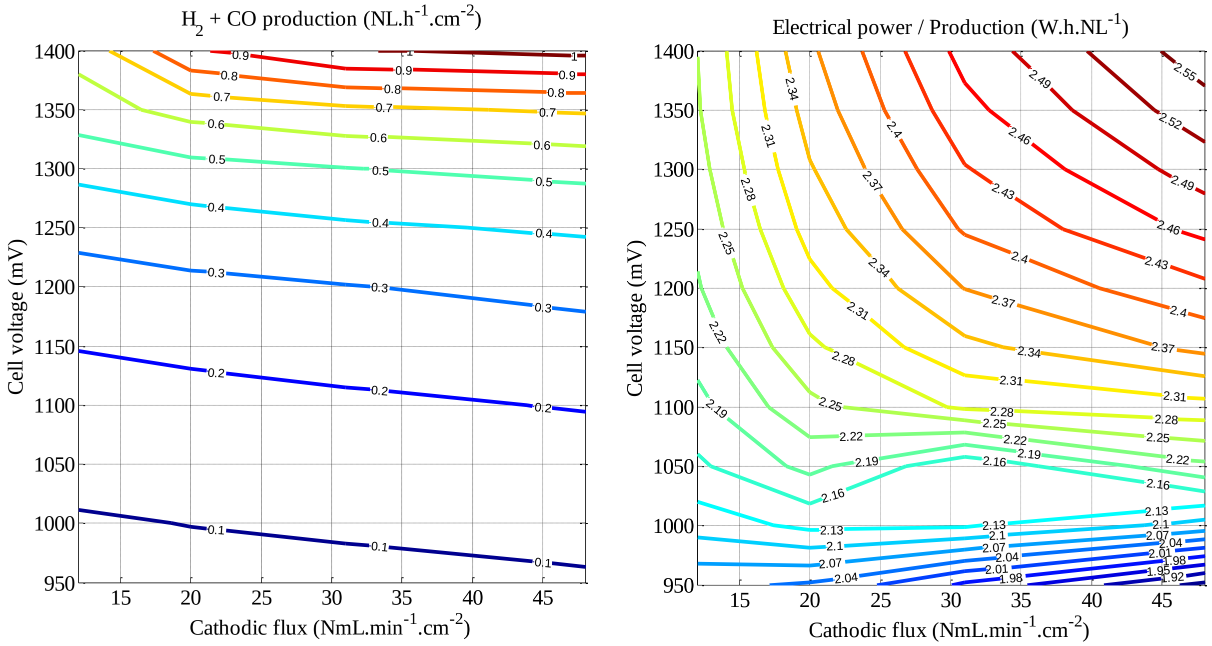

Figure 5-19: Co-electrolysis operating maps (2/4): Production of $H_2$ and CO (A-left) and Efficiency defined as the ratio of production over electrical power required (B-right).

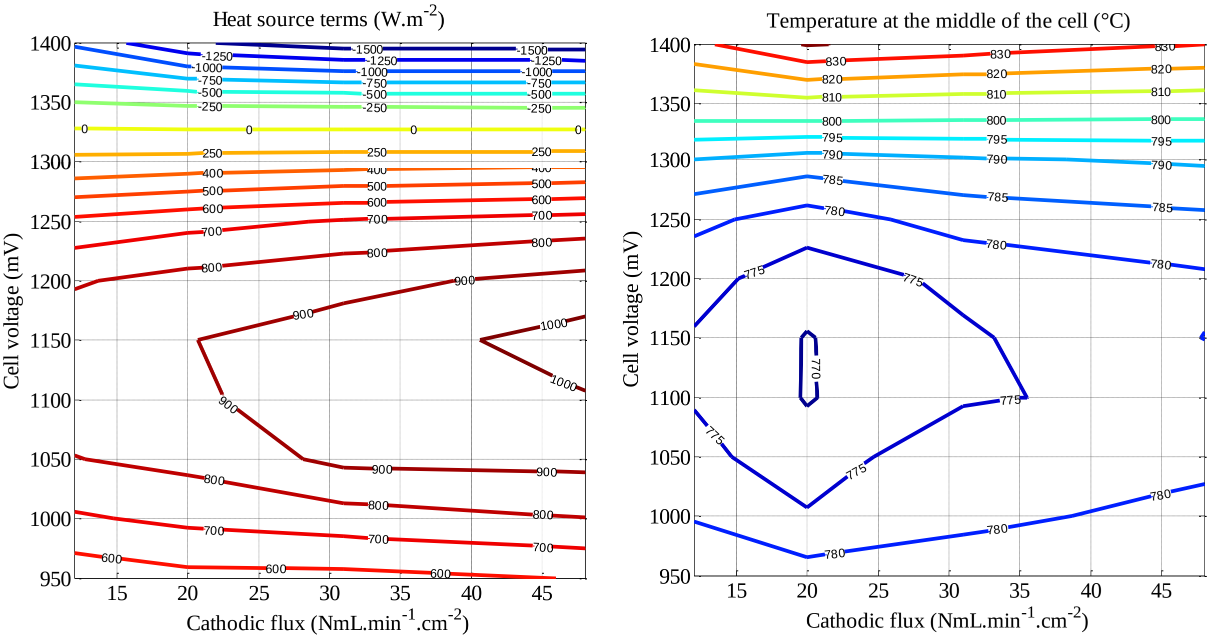

Figure 5-20: Co-electrolysis maps (3/4): Heat source terms (A-left) and Temperature taken at the middle of the cell length (B-right).

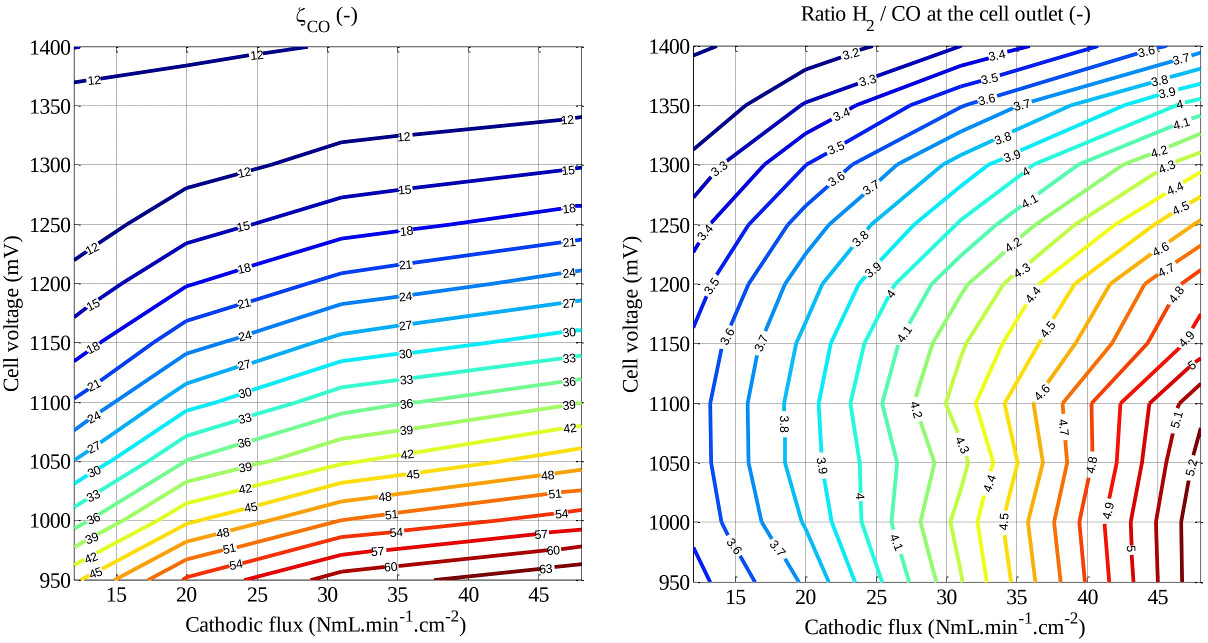

Figure 5-21: Co-electrolysis operating maps (4/4): CO produced by the reverse WGS reaction compared to $CO_2$ electrolysis (left) and $H_2/CO$ ratio at the cell outlet (right).

### 5.3.7. Influence of Inlet Ratio $CO_2/H_2O$

The influence of the $CO_2/H_2O$ ratio in the gas inlet on the gas outlet composition was investigated for ratios varying between 0.1 and 3. Simulations were performed at 1.3 *V* (*i.e.* close to the thermoneutral operating cell voltage), for both 12 and 24 $NmL.min^{-1}.cm^{-2}$ inlet cathodic flow rates. All inlet compositions were diluted with 10 *vol.%* $H_2$ (*i.e.* $CO_2/H_2O = 1$ is equivalent to 45/45/10 *vol.%* $H_2O/CO_2/H_2$). Corresponding outlet compositions are reported in Figure 5-22.

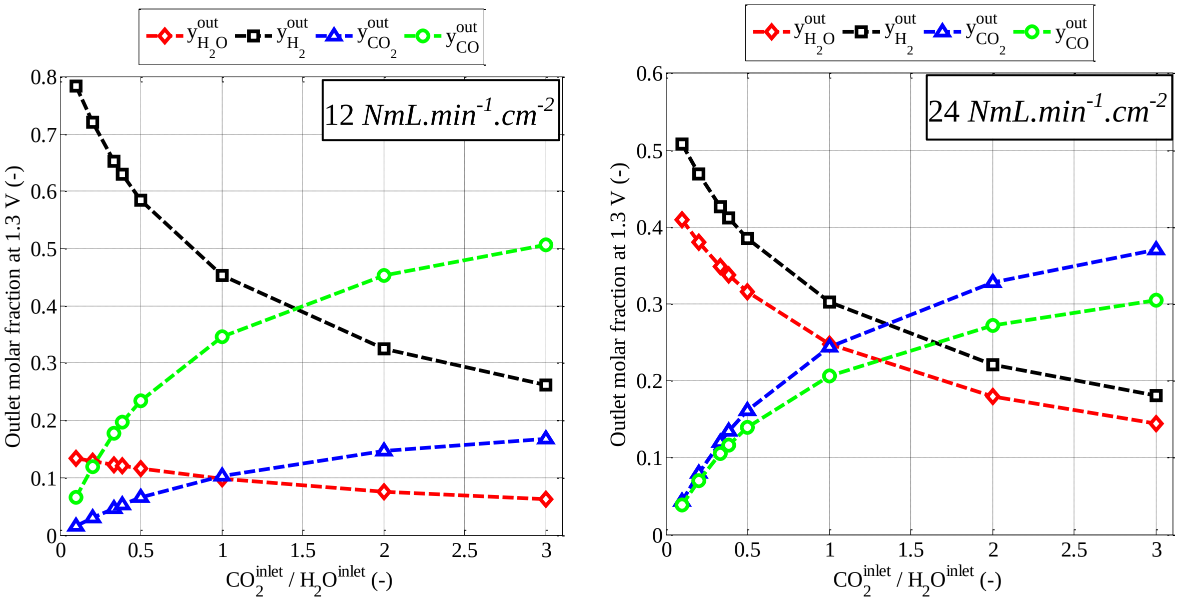

Figure 5-22: Outlet compositions simulated at 1.3 *V* with the isothermal model, as a function of the inlet ratio $CO_2/H_2O$. Inlet cathodic flow rates are 12 (left) and 24 (right) $NmL.min^{-1}.cm^{-2}$.

As could be expected, the production of CO increases with the $CO_2$ content in the inlet gas flow. Conversely, $H_2$ is mainly produced when $H_2O$ is the majority inlet component. In agreement with previous results, conversion rates, that can be assessed from outlet $H_2O$ and $CO_2$ outlet molar fractions, decrease with higher flow rates. Conversion rates also decrease when larger amounts of $CO_2$ are fed to the cell. This agrees with the lower performances obtained in $CO_2$ electrolysis mode compared to $H_2O$ electrolysis (cf. Figures 4-13 and 4-14), and highlight more severe mass transfer limitations in the cathode.

This approach could serve to identify optimal inlet composition for a specific process (*e.g.* co-electrolysis followed by methanation or Fisher-Tropsch process). Within the range of simulations performed in this section, the inlet compositions leading to the production of a specific syngas, as determined by the outlet ratio $H_2$/CO, were identified and gathered in Table 5-3.

| | **Optimum inlet compositions (*vol.%* $H_2O$/*vol.%* $CO_2$/*vol.%* $H_2$)** | | | | | |
|---|---|---|---|---|---|---|
| **$H_2$/CO,outlet** | $F_c = 12\ NmL.min^{-1}.cm^{-2}$ | | | $F_c = 24\ NmL.min^{-1}.cm^{-2}$ | | |
| 1 | 36 | 54 | 10 | 34 | 56 | 10 |
| 2 | 53 | 37 | 10 | 51 | 39 | 10 |
| 3 | 62 | 28 | 10 | 62 | 28 | 10 |

Table 5-3: Optimum inlet compositions for specific syngas production at 1300 *mV*.

## 5.4. Conclusion

The three models used in this work (*i.e.* $H_2O$ electrolysis, $CO_2$ electrolysis and co-electrolysis) allowed predicting polarization curves in all modes. In accordance with literature reports [2, 11, 12] and experimental observations (*cf.* Chapter 4), co-electrolysis performances were found to be in between those of $H_2O$ and $CO_2$ single electrolyzes in similar conditions.

Studying the cell voltage decomposition showed that at lower conversion rates, both anodic and cathodic activation account for most of the global overpotential. Therefore, an improvement of exchange current densities by optimizing microstructure and/or new electrode materials could be a way toward vastly increasing both performances and efficiencies. Moreover, cathode concentration overpotentials become prevalent at high current density due to the CO/$CO_2$ mass transfer limitation. In addition, the temperature dependence on a SRU was investigated. It was found that longitudinal thermal gradients are lower in co-electrolysis compared to $H_2O$ electrolysis, limiting the resulting mechanical stresses. In the exothermic part of the computed co-electrolysis polarization curves, the benefits from higher temperature, which could have yielded higher current densities, are hindered by higher mass transfer limitations than in $H_2O$ electrolysis. Indeed, a maximum current density was simulated (*i.e.* about $-2.2\ A.cm^{-2}$), resulting in large drops of conversion rates when the cathodic flow rate was increased. Therefore, studies devoted to microstructure optimization of the cell support to enhance $CO/CO_2$ gas transport should constitute a promising way to improve cell efficiency in co-electrolysis operation.

Results showed that $CO_2$ can be electrochemically reduced in presence of $H_2O$, in agreement with experimental evidence of $CO_2$ electrolysis feasibility (*cf.* Chapter 3). In the chosen, the influence of the WGS reaction in CO production was elucidated. It is found that the chemical reaction does not prevail over electrochemistry in conditions compatible with a Power-to-Gas process at about 800°*C*. Even if inlets were chosen to favor the WGS reaction, it still did not account for the majority of the global syngas production.

Co-electrolysis operating maps were computed for inlet composition 65/25/10 *vol.%* $H_2O/CO_2/H_2$. These highlight that optimal operating conditions could be mainly determined by the conversion rate. In addition, the outlet ratio $H_2/CO$ depends on current density, inlet cathodic flow rate and temperature. These parameters, to which one could add the cermet thickness and general cell dimensions, could all be adjustable variables to obtain a specific outlet gas composition, for a coupling with a specific process (*e.g.* Methanation reaction).

Finally, the co-electrolysis model proved to be an excellent tool to investigate the complex and entangled phenomena occurring in an operating SOC.

# 5.5. References

1. X. Sun, M. Chen, S. H. Jensen, S. D. Ebbesen, C. Graves, and M. Mogensen, Thermodynamic analysis of synthetic hydrocarbon fuel production in pressurized solid oxide electrolysis cells, *Int. J. Hydrog. Energy* 37, 17101 (**2012**).
2. P. Kim-Lohsoontorn, N. Laosiripojana, and J. Bae, Performance of solid oxide electrolysis cell having bi-layered electrolyte during steam electrolysis and carbon dioxide electrolysis, *Curr. Appl. Phys.* 11, S223 (**2011**).
3. P. Kim-Lohsoontorn and J. Bae, Electrochemical performance of solid oxide electrolysis cell electrodes under high-temperature coelectrolysis of steam and carbon dioxide, *J. Power Sources* 196, 7161 (**2011**).
4. S. H. Jensen, P. H. Larsen, and M. Mogensen, Hydrogen and synthetic fuel production from renewable energy sources, *Int. J. Hydrog. Energy* 32, 3253 (**2007**).
5. P. Kazempoor and R. J. Braun, Model validation and performance analysis of regenerative solid oxide cells: Electrolytic operation, *Int. J. Hydrog. Energy* 39, 2669 (**2014**).
6. J. Laurencin, D. Kane, G. Delette, J. Deseure, and F. Lefebvre-Joud, Modelling of solid oxide steam electrolyser: Impact of the operating conditions on hydrogen production, *J. Power Sources* 196, 2080 (**2011**).
7. J. Laurencin, F. Lefebvre-Joud, and G. Delette, Impact of cell design and operating conditions on the performances of SOFC fuelled with methane, *J. Power Sources* 177, 355 (**2008**).
8. F. Usseglio-Viretta, J. Laurencin, G. Delette, J. Villanova, P. Cloetens, and D. Leguillon, Quantitative microstructure characterization of a Ni–YSZ bi-layer coupled with simulated electrode polarisation, *J. Power Sources* 256, 394 (**2014**).
9. R. Suwanwarangkul, E. Croiset, E. Entchev, S. Charojrochkul, M. D. Pritzker, M. W. Fowler, P. L. Douglas, S. Chewathanakup, and H. Mahaudom, Experimental and modeling study of solid oxide fuel cell operating with syngas fuel, *J. Power Sources* 161, 308 (**2006**).
10. F. Usseglio-Viretta, *Optimisation des performances et de la robustesse d’un électrolyseur à hautes températures*, (**2014**).
11. J. E. O’Brien, M. G. McKellar, C. M. Stoots, J. S. Herring, and G. L. Hawkes, Parametric study of large-scale production of syngas via high-temperature co-electrolysis, *Int. J. Hydrog. Energy* 34, 4216 (**2009**).
12. C. Graves, S. D. Ebbesen, and M. Mogensen, Co-electrolysis of CO2 and H2O in solid oxide cells: Performance and durability, *Solid State Ion.* 192, 398 (**2011**).

# Chapter 6

# Conclusion

# Chapter 6

# Conclusion

This work investigated the high temperature co-electrolysis of steam and carbon dioxide in SOCs, and the relevance of this operating mode to produce storage units for carbon-free electricity overproduction as well as $CO_2$ valorization devices. Indeed, co-electrolysis should enable the conversion of $H_2O$ and $CO_2$ emitted by industries (such as nuclear power plants and cement, energy, chemical, steel industries respectively) into syngas ($H_2$+CO) and oxygen. The syngas can, in turn, be converted into high added value storable products, such as methane or synthetic liquid fuels (methanol or DME), while oxygen can be valorized and used in industrial sites. To better understand the entangled phenomena occurring in a SOC operated in co-electrolysis mode, the chemical and electrochemical response of typical commercial cells was investigated using a coupled experimental and modeling approach.

An in-house co-electrolysis model was adapted from a previous one developed in steam electrolysis. The model takes into account mass transfer, chemical, electrochemical and thermal phenomena occurring inside the operating SOC. Furthermore, it was duplicated to consider both radial and planar cell geometries, needed to be respectively representative of experimental data acquired on a single cells as well as stack environments. Additionally, a macroscopic representation of the electrochemical mechanism was proposed through the introduction of a surface ratio parameter $\beta$. This parameter, which was expressed as a function of local steam and carbon dioxide partial pressures, encompasses the coupled mechanisms related to the simultaneous $CO_2$ and $H_2O$ electro-reductions within the same cathodic active layer.

In parallel to the numerical approach, numerous experimental tools were set up in this investigation. A test bench dedicated to co-electrolysis measurements was designed based on the laboratory feedbacks. After putting the test rig into service, its reliability was optimized. Finally, a micro gas chromatograph was coupled to the test bench to analyze cell outlet compositions.

Experimental polarization curves obtained in all electrolysis modes displayed typical behaviors consistent with literature reports. Co-electrolysis performances were shown to lie between those of $H_2O$ and $CO_2$ single electrolyzes. Additionally, current densities as high as -1.5 $A.cm^{-2}$ were achieved in $CO_2$ electrolysis on optimized cells. This result confirms the possibility to electrochemically reduce $CO_2$ in standard SOCs.

Single electrolysis and co-electrolysis models were experimentally validated on two types of commercial Cathode Supported Cells (CSC), one of which had a well-known microstructure. Experimental protocols were developed to highlight variations in cathodic overpotentials through feeding composition and flow changes. Complete polarization curves were investigated and compared to the simulation over a large range of cell voltages (from open circuit voltages to steep limiting currents). A special attention was paid to avoid any significant degradation during the protocols.

The good agreement between simulations and experiments in all electrolysis modes has allowed confirming the models ability to predict polarization curves. In addition, gas analyses were performed at OCV and in operation in order to respectively validate both the Water Gas Shift (WGS) reaction kinetics and the expression of the surface ratio as a combination of local $H_2O$ and $CO_2$ partial pressures.

A good consistency between simulated and experimental cell outlet compositions was highlighted over the complete range of current densities. Furthermore, a sensitivity analysis was performed by changing the expression of $\beta$. It has been found that any modifications in the definition of this parameter lead to a large disagreement between model predictions and experimental gas composition analysis. In such conditions, the co-electrolysis model loses its relevance. In other words, only one expression of the surface ratio is liable to accurately model and predict the co-electrolysis experiments. This result tends to prove the underlying physical meanings of $\beta$ and shows that the model can be used over a large range of gas composition with a high level of confidence.

Detailed analyses of numerous simulations led to assess the relative influence of the WGS reaction over CO production in co-electrolysis operations. It was demonstrated that, within the range of this study, the chemical reaction does not prevail over $CO_2$ electrolysis, as long as the cell current density is sufficiently high. Since such currents were obtained for cell voltages as low as 1.1 $V$, this statement would apply to realistic co-electrolysis operation. Such conclusion was also shown to stand with inlet compositions favoring the WGS reaction. It should be emphasized here that a limited influence of the WGS reaction contradicts some literature reports. Indeed, most of these studies have concluded that $CO_2$ electrolysis is negligible since they have focused their investigation on low current densities. According to the simulation analysis, the limited influence of the WGS reaction is believed to arise from the reaction changing direction within the cathode 2D geometry so that its production is globally balanced

Further analysis of the simulations highlighted that, due to the presence of $CO/CO_2$ in $CO_2$ and co-electrolysis modes, mass transfer through the porous cathode is a limiting process that induces large concentration overpotentials. This was confirmed by the decreased in cell performances experimentally evidenced in these modes of operation compared to single $H_2O$ electrolysis. Therefore, a cathode microstructure specifically optimized for co-electrolysis operation seems to be a major way toward improved performances. Additionally, it was shown that over the range of realistic co-electrolysis operation, activation overpotentials account for the majority of the cell voltage increase. Such issue could be mitigated through triple phase boundary lengths density increase and/or more electroactive electrode materials.

Once validated, the co-electrolysis model was used to determine operating maps for a technologically relevant inlet composition (*i.e.* 65/25/10 *vol.%* $H_2O/CO_2/H_2$). The simulations were carried out over a wide range of inlet flows and cell polarizations. This investigation evidenced that inlet composition, flow rate, temperature and current density are the most contributing factors that governs the outlet gas composition. Consequently, by taking advantages of the simulated cartographies, optimal operating conditions were identified. Additionally, global temperature variations and longitudinal thermal gradients were found to be limited in co-electrolysis operation, compared to $H_2O$ electrolysis. From this statement, it has been claimed that the range of acceptable operating conditions in co-electrolysis mode could be wider than the one previously identified in steam electrolysis, and might simplify the thermal management of the co-electrolyzer.

Many different research paths could complete this work. First, several additional series of studies could be performed to improve the model range of applicability. For instance, the thermal dependence of key parameters such as the surface ratio $\beta$ could be investigated. Moreover, thanks to the micro modeling approach depicted in [1], the dependence of the "apparent" current densities with electrode microstructure, atmosphere or even polarization could be estimated.

Besides, the underlying mechanisms of co-electrolysis process included in the macroscopic parameter $\beta$ needs to be clarified. For this purpose, the elementary reactions pathway and the associated rate-determining steps for co-electrolysis should be established. It could be propose to identify the most plausible mechanisms by coupling the microscopic modeling approach with electrochemical measurements performed on symmetrical cells in a 3 electrodes configuration (polarization curves and impedance diagrams investigations in co-electrolysis and single electrolysis modes).

Also, the WGS kinetics constants (pre-exponential and activation energy) implemented the model, could be further validated through accurate chemical rates measurements, based on non-equilibrium outlet compositions. These could not be done in this work due to test bench limitations.

Furthermore, the gaps obtained in $H_2O$ electrolysis at high current densities could probably be improved through $H_2$ diffusion coefficients optimization and/or by taking into account some of the potential dependences already evoked. In addition, the evolution in time of co-electrolysis performances must be investigated. Indeed, this technology cannot become viable if degradation rates are too high. Such optimization requires a better comprehension of the microscopic co-electrolysis electrochemical mechanism.

Finally, a deep investigation on the influence of pressurized co-electrolysis must be conducted. Indeed, it has been proposed in an industrial flow-chart to associate a co-electrolyzer with a methanation reactor, which operates at high pressure. Technical assessments of this industrial process have suggested that large gains in efficiency and cost could be achieved when both devices have similar operating conditions. Nonetheless, the beneficial or detrimental effect of pressure on the co-electrolysis process has to be carefully estimated. For this purpose, the effect of pressure should be taken into account in the co-electrolysis model. It is expected that pressure could impact the electrochemistry as well as the gas mass transfer. Moreover, the catalytic reaction of methane formation in the cathode should be implemented in the model. Also, the risk of carbon should constitute an important issue that should be studied.

1. E. Lay-Grindler, J. Laurencin, G. Delette, J. Aicart, M. Petitjean, and L. Dessemond, Micro modelling of solid oxide electrolysis cell: From performance to durability, *Int. J. Hydrog. Energy* 38, 6917 (**2013**).

# Chapter 7

# Appendix

# Chapter 7

# Appendix

# 7.1. Hysteresis on Optimized Cell

On most of the tested cells, some of the polarization curves displayed a hysteresis: the performances are lower during the "Return" (R) to OCV that during the "Initial" (I) sweep. The following sections illustrate such phenomenon, and investigate the effect of composition, time and limiting current density on both shape and size of the hysteresis (Figure 7-1).

## 7.1.1. Influence of Composition and Time

No hysteresis is observed for single $H_2O$ electrolysis, whereas the largest ones are observed for single $CO_2$ one. Additionally, in a co-electrolysis mode, the voltage gap between initial and return polarization curves increases when $CO_2$ inlet content increases from 20 to 40 *vol.%*. Similar measurements were obtained on all optimized cells tested. The higher the inlet $CO_2$ content, the higher is the magnitude of the hysteresis.

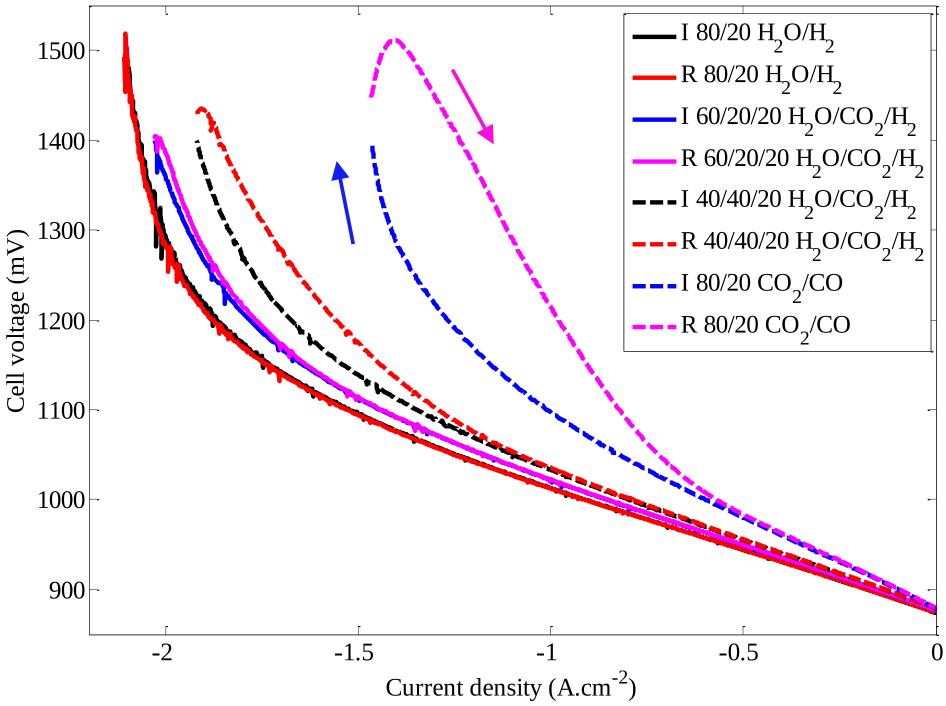

Figure 7-1: Effect of inlet composition of hysteresis in all electrolysis modes at 800°*C*.

Furthermore, it should be noted that this phenomenon is mostly reversible. Indeed, recording the same polarization curve twice led to the same set of initial and return curves. Similarly, as can be seen in Figure 7-2, the same experiment performed on two different optimized cells from the same batch also yielded the same results. Finally, it should be mentioned that recording the initial polarization curve and then maintaining a galvanostatic condition in the hysteresis area led the cell voltage to increase up to its “return value” within a few minutes. These results unambiguously show that the recorded hysteresis originates from $CO_2$ reduction and is not likely to originate from the electrode microstructure.

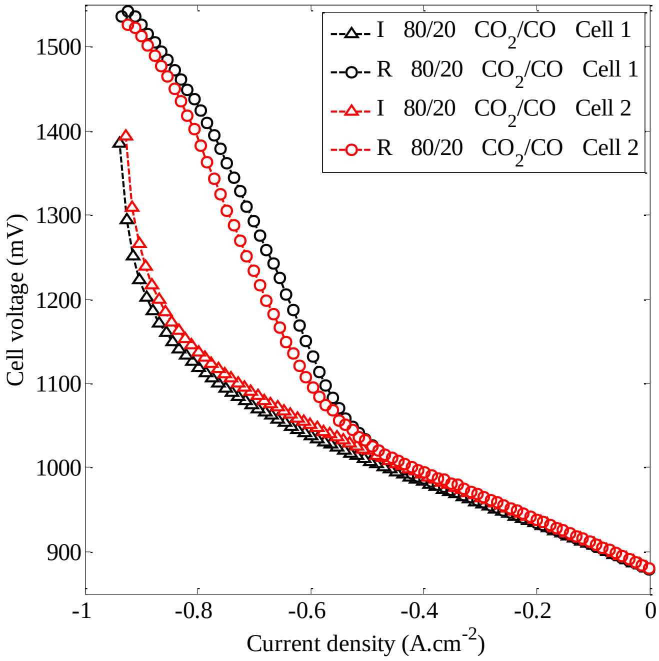

Figure 7-2:
Hysteresis resulting from $CO_2$ electrolysis obtained at 800°C on 2 cells from the same batch.

### 7.1.2. Influence of Limiting Current

The obtained hysteresis does not only dependent on the inlet gas composition investigated. Indeed, it is only recorded if the limiting current is reached, even in $CO_2$ electrolysis (Figure 7-3). Moreover, when electrolyzing $CO_2$ at 1300 *mV*, a hysteresis was initially always observable at 800°*C*, which disappeared at 850°*C*.

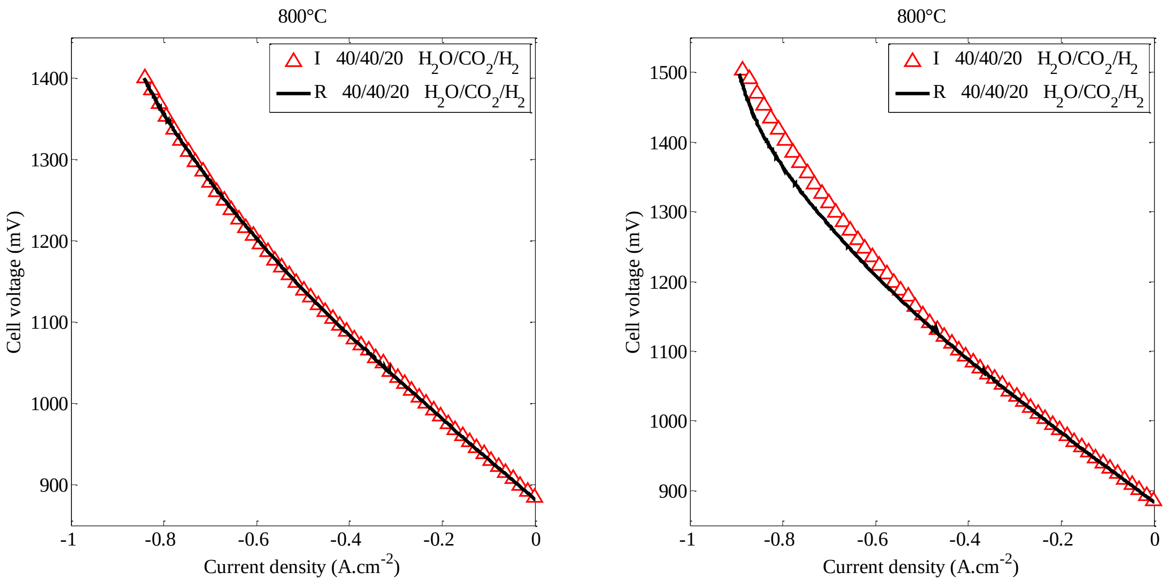

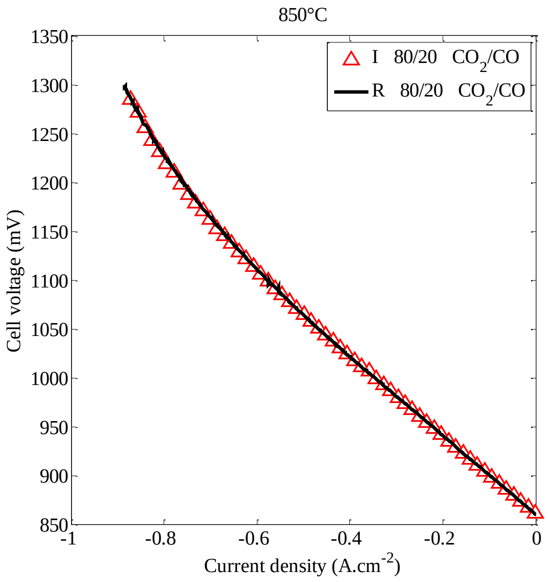

Figure 7-3:
Influence of reaching the limiting current density on *i*-*V* hysteresis.

### 7.1.3. Conclusion

Since the hysteresis is observed once the limiting current is be reached, this $CO_2$ related phenomenon is likely to be independent of diffusion processes through the porous electrode. Indeed, the temperature variation investigaetd has a limited impact on gaseous diffusion, whereas this phenomenon vanished by increasing the temperature by 50°*C*.

To the best of my current knowledge, there are limited experimental reports concerning $CO_2$ electrolysis, none of which display return curves. However, the literature is much more extensive about CO oxidation. Indeed, Holtappels *et al.* [1] have reported a highly dynamical CO oxidation, with multiple and periodically changing reaction rates, believed to be related to passivation and reactivation of active sites. These observations could be coherent with reports of changes in number of relaxation times [2] and mechanism [3] depending on $P_{CO_2} / P_{CO}$ ratios. Accordingly, a change $CO_2$ adsorption and/or CO desorption processes at high CO contents (*i.e.* limiting current density) could explain the observed hysteresis. Such slower mechanism, becoming limiting as $P_{CO}$ increases, could also explain the time dependence observed.

Additional experiments in the hysteresis section of polarization curves are required to further understand this dynamic phenomenon. For example, EIS measurements under polarization could give insights on a variation of elementary steps in electrolysis mode. However, it should be emphasized that this phenomenon does not affect the predictive ability of the co-electrolysis model developed in this work (*cf.* Chapter 3). Indeed, from a technological point of view (*cf.* Chapter 5), imposing a limiting current is not optimal since degradation rates should be increased, and performances should suffer from higher cathodic concentration overpotential. In addition, special interest is currently given to inlet composition 65/25/10 *vol.%* $H_2O/CO_2/H_2$, as it can lead to methane production. As previously showed (Figure 7-1), only a very limited hysteresis could sometimes be observed in these conditions.

## 7.2. Cell Degradation in Co-Electrolysis

### 7.2.1. Durability Experiment : 900 *h* at -1 $A.cm^{-2}$

One of the optimized cells (*cf.* Chapter 4) operated in $H_2O$ electrolysis and $H_2O+CO_2$ co-electrolysis modes to assess the corresponding degradation rates. After initial start-up procedures (*cf.* Chapter 3), polarization curves were recorded. Subsequently, the cell was operated in a galvanostatic mode at -1 $A.cm^{-2}$ and 24 $NmL.min^{-1}.cm^{-2}$ cathodic flow, first during 259 *h* with 90/10 *vol.%* $H_2O/H_2$ (+20% $N_2$), then 643 *h* with 65/25/10 *vol.%* $H_2O/CO_2/H_2$. Additional evaluations of performances were performed between both modes and at the end of the experiment. The voltage increase was deduced from the time evolution of the cell voltage, and the extrapolation of these results led to assess degradation rates per *kh* (Figure 7-4).

Excluding the initial voltage jump, operating the cell in $H_2O$ electrolysis mode lead to a quasi linear degradation rate of +8.8 $\%.kh^{-1}$. Conversely, the slope of the cell voltage evolution changes abruptly in co-electrolysis mode, leading to 2 very different degradation rates: +19.3 and 8.4 $\%.kh^{-1}$ respectively. Many additional experiments are required to further investigate degradation rates in co-electrolysis mode, and to draw any meaningful conclusions. In addition, there are very few related literature reports, and none at such a high current density. However, the as-recorded results suggest that co-electrolysis could result in higher but comparable degradation rates compared to $H_2O$ electrolysis.

During the 643 *h* of co-electrolysis operation, steam outlet mass balance was performed (see 4.2.7 for additional details), as well as µGC measurements. Results shown in Table 7-1 highlight yet again the agreement between simulated and experimental data, and therefore the model ability to predict outlet composition in operating conditions. It is worth noting here that in the specific case of this experiment, computing the $H_2O$ and $CO_2$ conversions from Faraday’s law and the model gives the same result. Such observation arises from the specific set of operating conditions investigated here, and has not been observed anywhere else is this work.

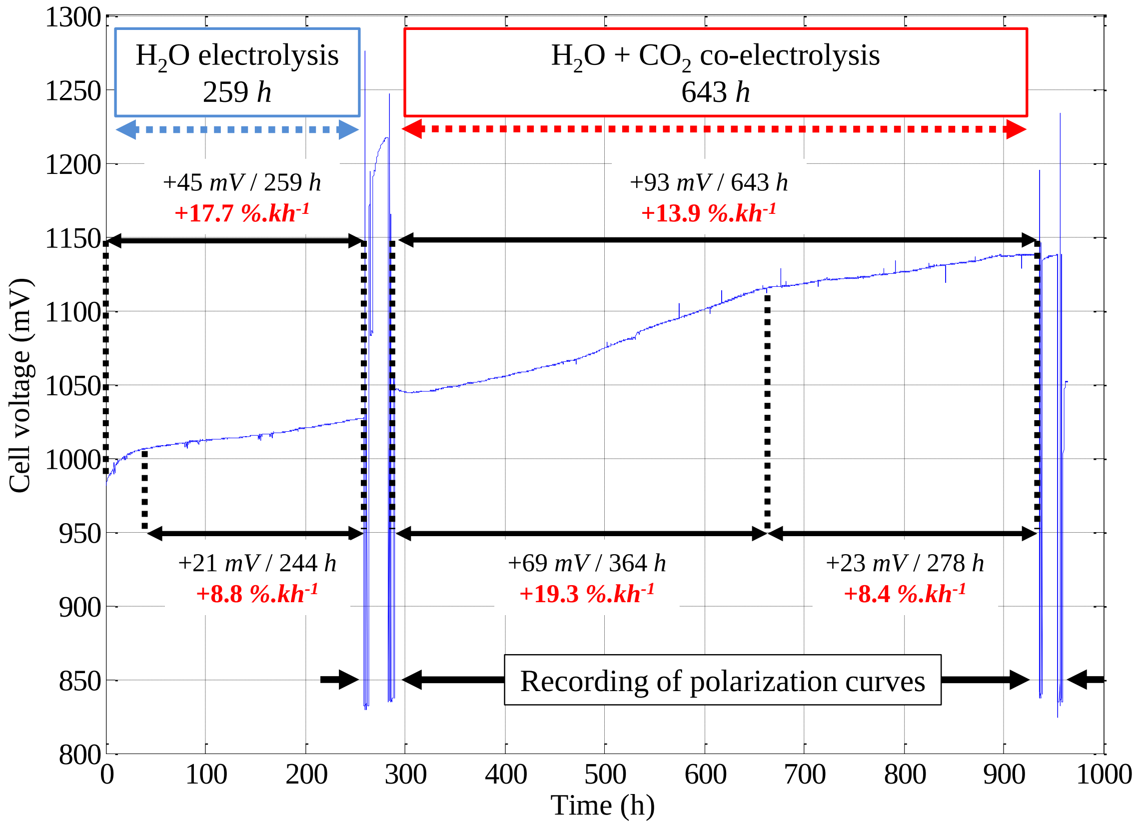

Figure 7-4: Durability experiment in $H_2O$ and co-electrolysis modes over nearly 1000 *h* in galvanostatic operation (-1 $A.cm^{-2}$, 24 $NmL.min^{-1}.cm^{-2}$, 90/10 *vol.%* $H_2O/H_2$ (+20% $N_2$) and 65/25/10 *vol.%* $H_2O/CO_2/H_2$)

| **Steam outlet mass balance experiment** | | **µGC measurements** | | |
|---|---|---|---|---|
| Experimental SC | Simulated SC | Component | $y^{*,\exp}$ | $y^{*,sim}$ |
| 31.9% | 32.0% | $CO_2$ | 30.3% | 30.6% |
| | | CO | 16.7% | 14.4% |
| | | $H_2$ | 53.3% | 55.1% |

Table 7-1: Steam outlet mass balance experiment and µGC measurements in co-electrolysis operation during the durability test. Comparison simulated and experimental data.

### 7.2.2. MEB Analysis

Scanning Electrons Microscope (SEM) and Energy Dispersive Spectrometry (EDS) cartographies were performed on three optimized cell: a reference cell with a fully reduced cermet (referred to as cell 1 here), the cell used in section 4.3 (cell 2), and the cell presented in the previous paragraph that was operated during 9000 *h* (cell 3). Contrary to both latter cells, the reference cell was not operated before examinations. The vicinity of the cathode/electrolyte interface was observed in order to investigate carbon deposition. Fractographies of the cells were examined using a SEM FEG (LEO 1530) equipped with a high resolution INLENS detector. Results obtained on cell 1, 2 and 3 are displayed on Figures 7-5, 7-6 and 7-7, respectively.

First, no explicit carbon deposition could be detected through the MEB examinations and chemical analyses. However, this does not necessarily means that such phenomenon did not occur. Indeed, late polarization curves in $H_2O$ electrolysis performed on cell 2 and 3 could have oxidized any potential solid carbon.

Furthermore, although they were operated during ≈ 400 *h* and ≈ 900 h respectively, cell 2 and 3 seem to display similar microstructures, significantly different from the reference observations. Indeed, Nickel particles seem bigger and their distribution less homogeneous in operated cell compared to initial examinations. This could be sign of Ni aggregation, an identified degradation phenomenon [4]. In addition, these modified microstructures also appear to change from the center of the cell (*i.e.* inlet) to the active area outlet.

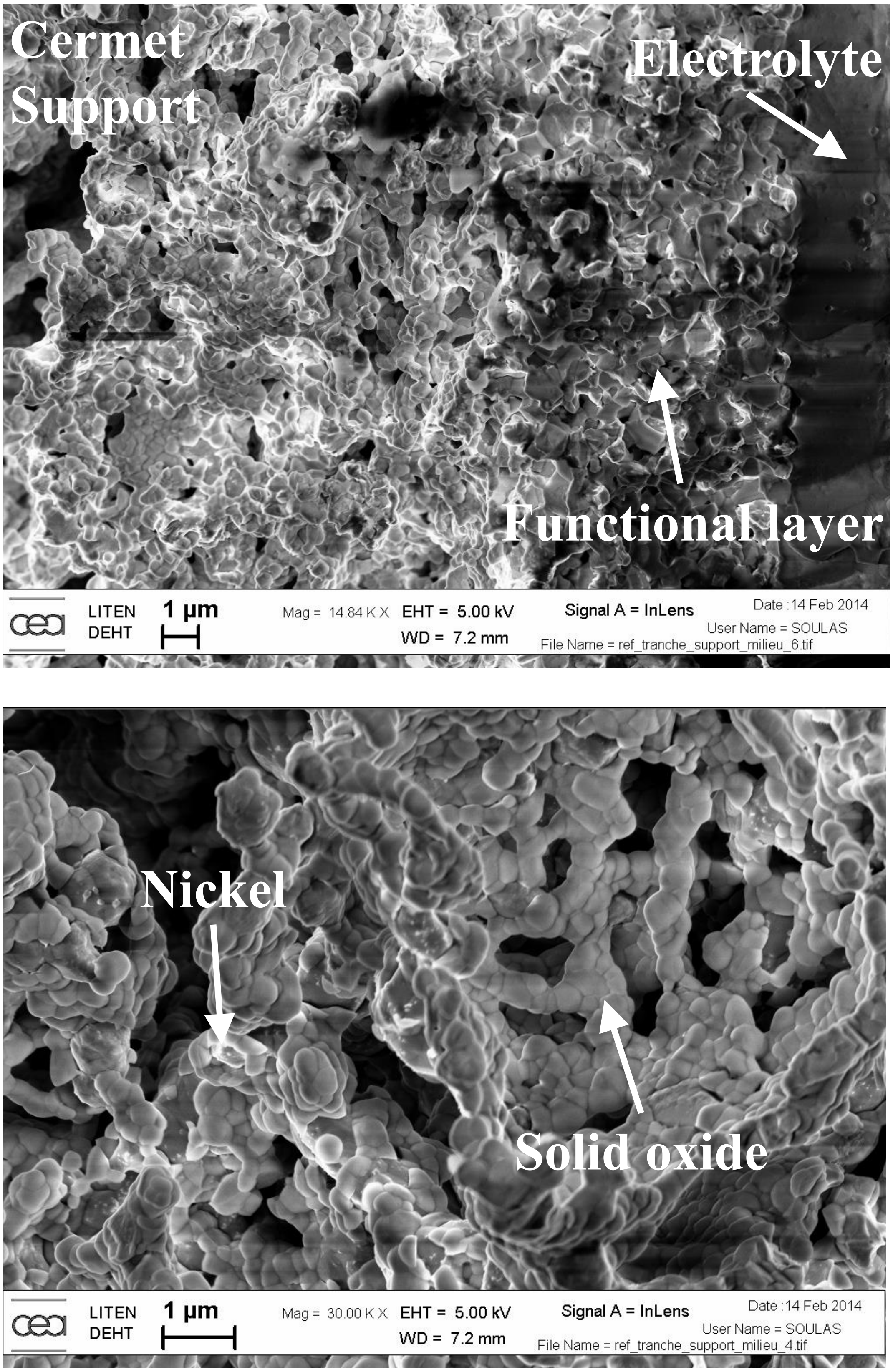

Figure 7-5: MEB examinations of the reference reduced cermet.

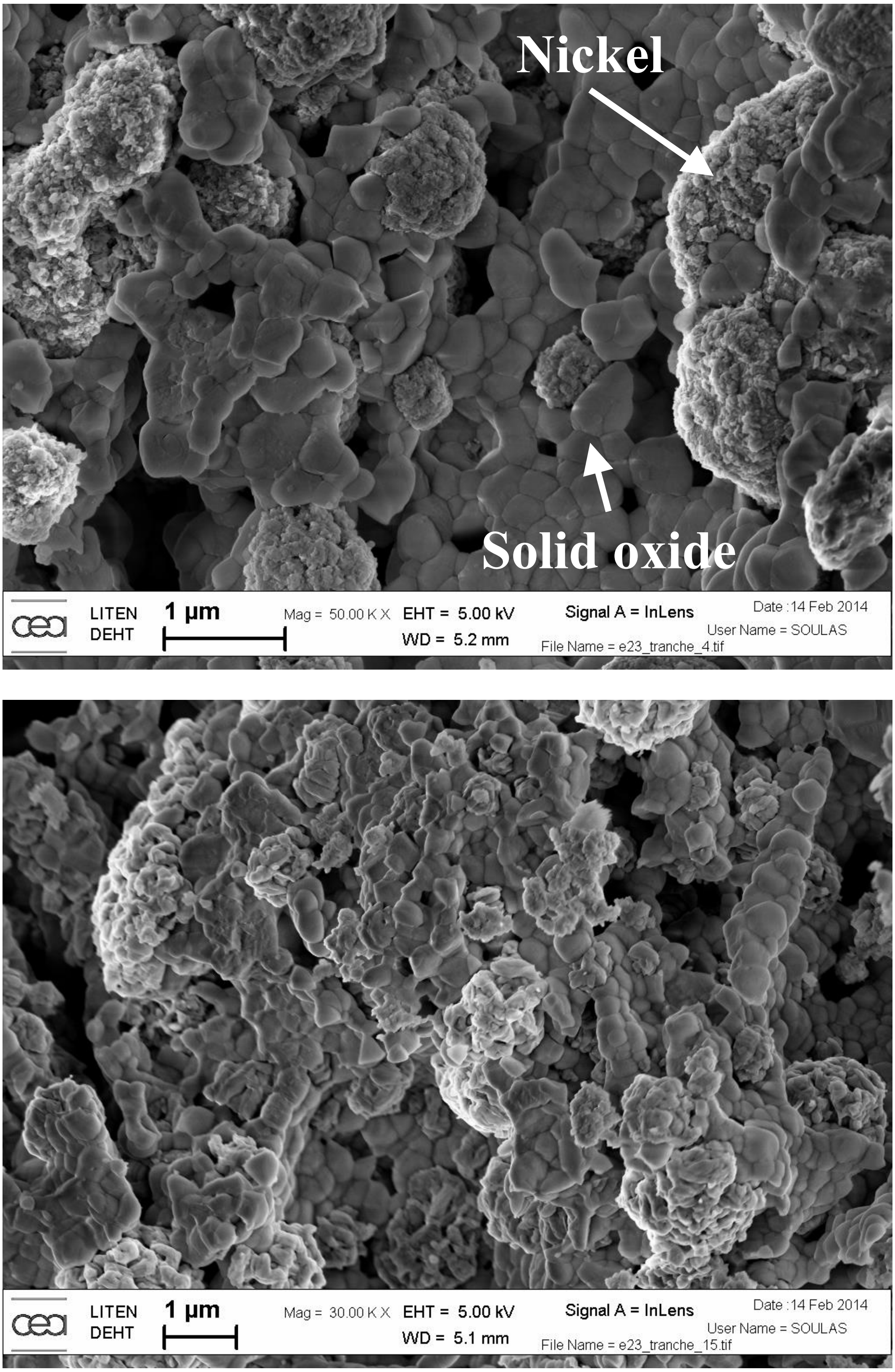

Figure 7-6: MEB examinations of the cathode/electrolyte interface vicinity of the cell used in section 4.3.

(up) at the center of the cell (radius = 0)

(down) at the active area outlet (radius ≈ 10 *mm*)

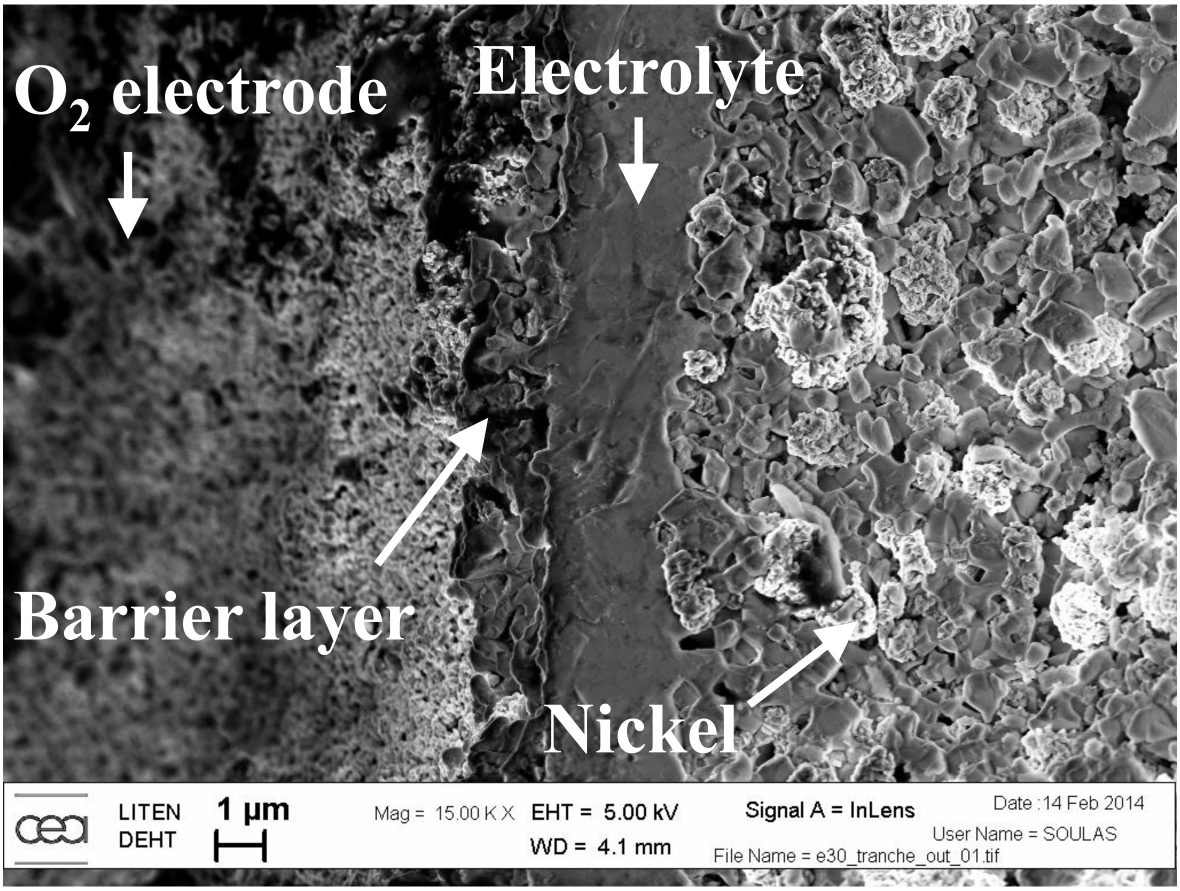

Figure 7-7: MEB examination of the cell used in the durability experiment, at the active area outlet (radius ≈ 10 *mm*).

In conclusion, these preliminary results did not highlight carbon deposition subsequent to $CO_2$ electrolysis and/or co-electrolysis operations. In addition, cell degradation during operation could be linked to a modification of the cathode microstructure, as Ni aggregation seems to be observed. Finally, as these microstructure modifications appear to evolve from the center of the cell to the outlet of the active area, they could to be influenced by operating parameter. Indeed, as was shown in Chapter 5, current density and partial pressures also evolve along the cell radius.

## 7.3. Steam Electrolysis Operating Maps

$H_2O$ electrolysis operating maps in conditions comparable to section 5.3.6 (same cell, SRU geometry, flow, inlet content of oxidized species – 90/10 *vol.%* $H_2O/H_2$) have been simulated as part of upcoming F. Usseglio-Viretta PhD thesis [5]. Some of the results are presented here as a basis of comparison for co-electrolysis operating maps presented in Chapter 5.

These $H_2O$ electrolysis operating maps lead to the following main observations, given below each figure.

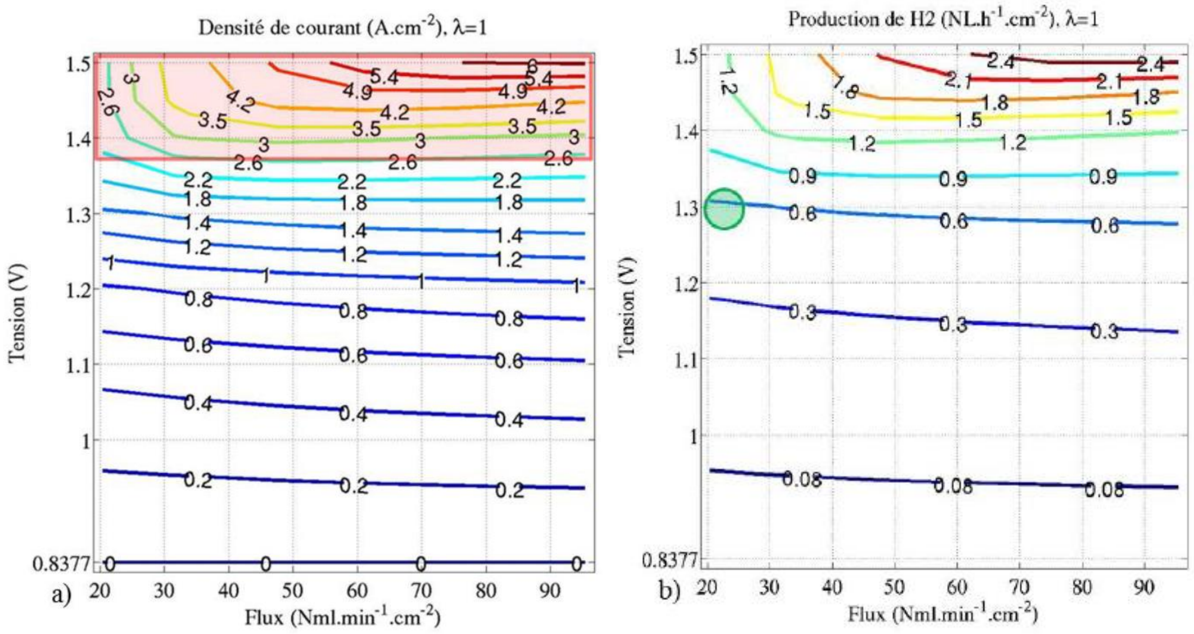

Figure 7-8: Steam electrolysis operating maps (1/3): Current density (left) and $H_2$ production (right).

- Current density increases with higher cathodic flows.
- Within the range of inlet flows investigated, a maximum current density of -6 $A.cm^{-2}$ is computed.
- Production of $H_2$ directly proportional to the current density.

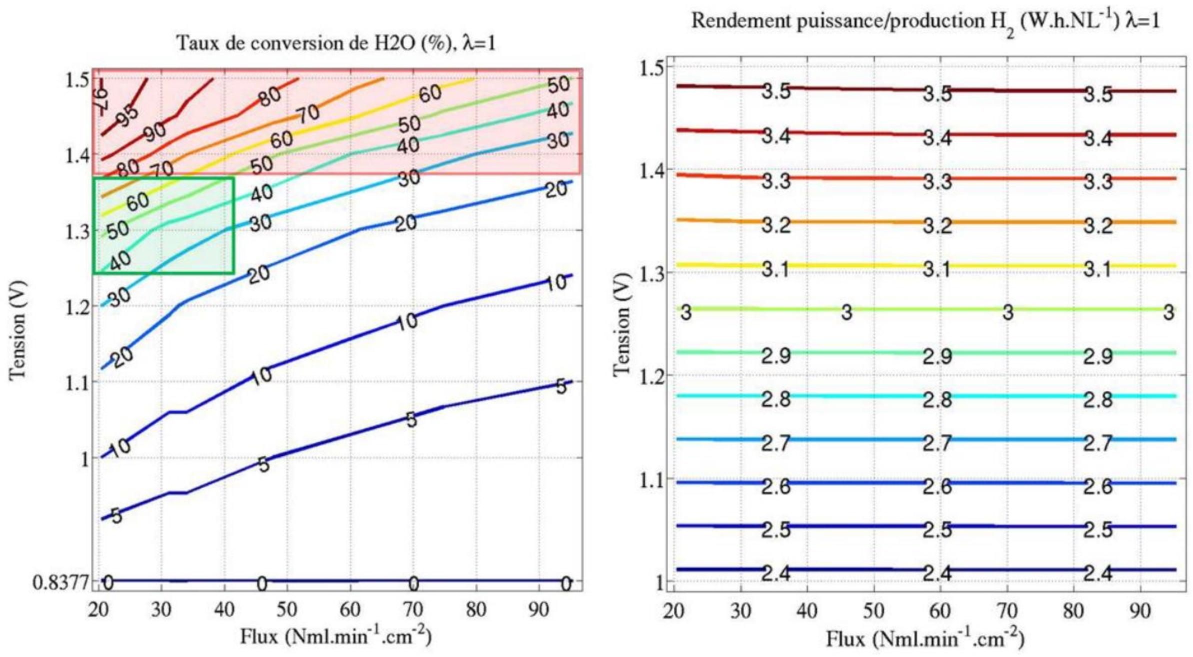

Figure 7-9: Steam electrolysis operating maps (2/3): Conversion rate (left) and Efficiency defined as electrical power to $H_2$ production ratio (right).

- Maximum computed conversion rate is greater than 97%.
- Conversion rate decreases with higher cathodic flows.
- The ratio Electrical power over $H_2$ production is solely dependent on the cell voltage.

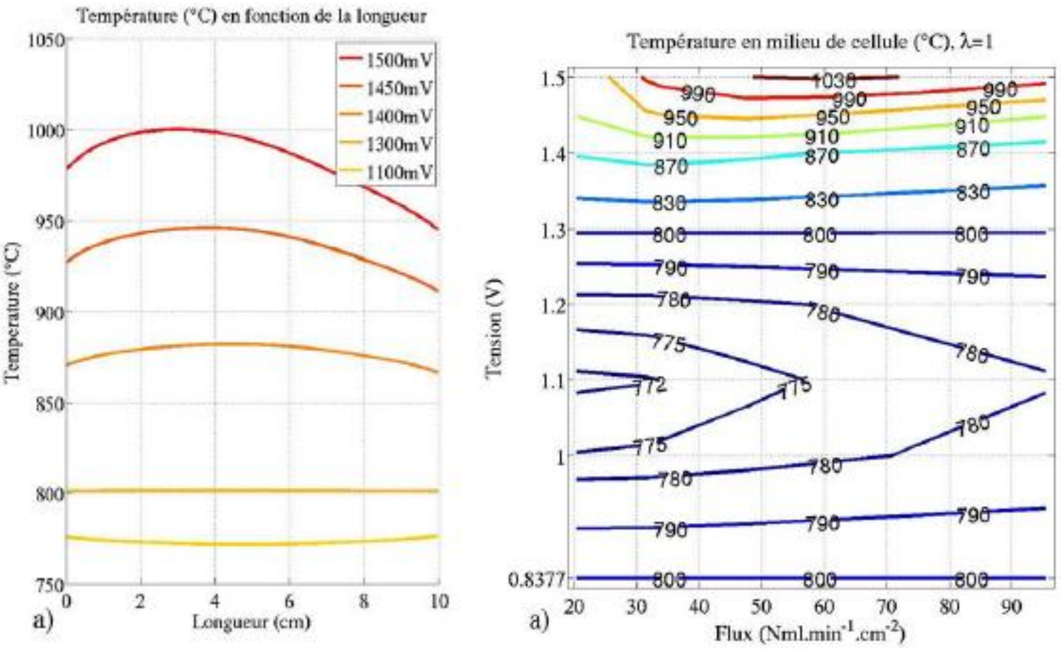

Figure 7-10: Steam electrolysis operating maps (3/3): Longitudinal cell temperature at 30 *NmL.min*$^{-1}$*.cm*$^{-2}$ (left) and Temperature at the middle of the cell (right).

- Steep longitudinal temperature gradients computed for cell voltages above 1300 *mV*, greater than 50°*C* at 1500 *mV*.
- Significant temperature elevations computed in the exothermic regime compared to 800°C at OCV, greater than 1030°C at 1500 mV and 60 *NmL.min*$^{-1}$*.cm*$^{-2}$ inlet cathodic flow.

- Cell temperature considerations led to the exclusion of the red zone in Figure 7-9.
- Conversion rate considerations identified the green zone as optimal in Figure 7-9.

## 7.4. References

1. P. Holtappels, L. G. J. De Haart, U. Stimming, I. C. Vinke, and M. Mogensen, Reaction of CO/CO2 gas mixtures on Ni–YSZ cermet electrodes, *J. Appl. Electrochem.* 29, 561 (**1999**).
2. F. Boulenouar, K. Yashiro, M. Oishi, A. Kaimai, Y. Nigara, T. Kawada, and J. Mizusaki, Electrochemical Oxidation of CO in a CO-CO2 System at the Interface of Ni Grid Electrode/YSZ Electrolyte, *Electrochem Soc Ser.* 759 (**2001**).
3. V. Yurkiv, A. Utz, A. Weber, E. Ivers-Tiffée, H.-R. Volpp, and W. G. Bessler, Elementary kinetic modeling and experimental validation of electrochemical CO oxidation on Ni/YSZ pattern anodes, *Electrochimica Acta* 59, 573 (**2012**).
4. P. Moçoteguy and A. Brisse, A review and comprehensive analysis of degradation mechanisms of solid oxide electrolysis cells, *Int. J. Hydrog. Energy* 38, 15887 (**2013**).
5. F. Usseglio-Viretta, *Optimisation des performances et de la robustesse d'un électrolyseur à hautes températures*, (**2014**).

# Abstract

This work investigates the high temperature co-electrolysis of $H_2O$ and $CO_2$ in Solid Oxide Cells. A detailed model was developed, encompassing electrochemical, chemical, thermal and mass transfer phenomena, and introducing a macroscopic representation of the co-electrolysis mechanism. This model allows predicting the performances and outlet compositions in single cell and stack environments. An experimental validation protocol was implemented on two types of commercial Cathode Supported Cells, ranging from polarization curves, obtained in single and co-electrolysis modes, to micro gas analyses. These tests aimed both at determining the different exchange current densities, representative of the kinetics of electrochemical reactions, and validating the simulated cell global behavior and mechanism proposed. Comprehensive analysis of the simulations led to the identification of limiting processes and paths for optimization, as well as to the establishment of co-electrolysis operating maps.

# Résumé

Cette étude porte sur la co-électrolyse de $H_2O$ et $CO_2$ à $800°C$ dans une cellule à oxydes solides. Un modèle détaillé a été développé afin de rendre compte des phénomènes électrochimiques, chimiques, thermiques et de transferts de matière, et introduisant une représentation macroscopique du mécanisme de co-électrolyse. Il permet d'estimer les performances et les compositions en sortie de cellule. Un protocole expérimental, visant à valider les principales hypothèses de ce modèle, a été appliqué à deux types de cellule commerciale à cathode support. À partir de courbes de polarisations, obtenues en électrolyse et en co-électrolyse, ainsi que d'analyses gaz, les densités de courant d'échange, illustrant les cinétiques électrochimiques, ont pu être estimées, et le mécanisme proposé a pu être validé. L'analyse des simulations a permis l'identification des processus limitant la co-électrolyse, la proposition de voies d'optimisation et l'établissement des cartographies de fonctionnement.